

Easing a COVID-19 lockdown without
risking a resurgence p. 218

How one error muddles the
cancer genome pp. 240 & 282

Illuminating palladium
catalysis pp. 242 & 318

Science

\$15
17 APRIL 2020
SPECIAL ISSUE
sciencemag.org

 AAAS

DROUGHT



Cottrell Scholars 2020: the Future of Science

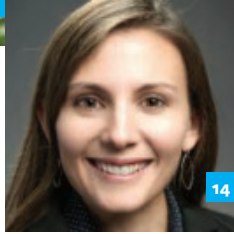
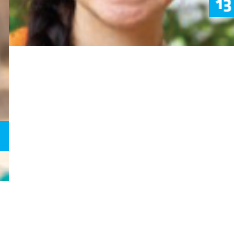
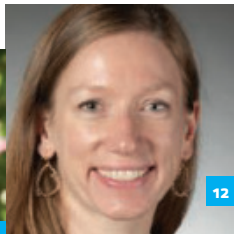
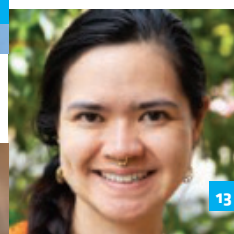
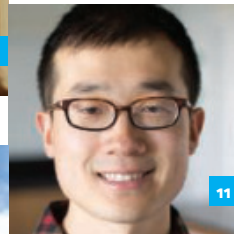
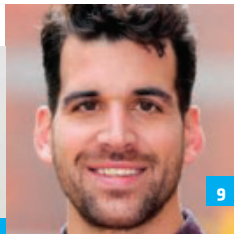
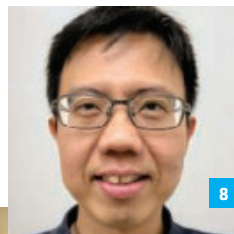
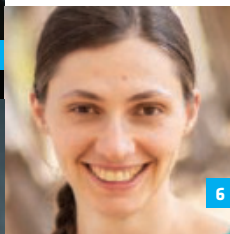
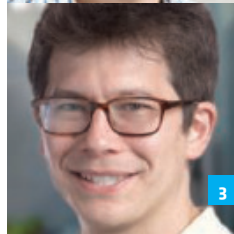
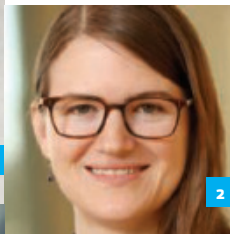
Research Corporation for Science Advancement, America's first foundation dedicated wholly to science, has named 25 early-career scholars in chemistry, physics, and astronomy as its 2020 Cottrell Scholars. Each awardee receives \$100,000. Recipients are recognized for high-quality research, innovative educational initiatives, and academic leadership.

Three accomplished Cottrell Scholars (far right) further along in their careers have also received recognition for their achievements. The IMPACT Award is given for national impact in science through leadership and service. STAR Awards reward excellence in science teaching and research.

For additional information visit rescorp.org or call 520.571.1111.

Cottrell Scholar Awardees

1. **Carlos R. Baiz**, chemistry, University of Texas at Austin / Molecular Dynamics at Heterogeneous Oil-Water Interfaces and a New Approach to Addressing the Mental Health Needs of Graduate Students
2. **Kateri H. DuBay**, chemistry, University of Virginia / Teaching Entropy and Modeling the Sequence-Determinants of Surface-Initiated Copolymerizations
3. **Keary M. Engle**, chemistry, Scripps Research Institute / Catalytic Difunctionalization of Alkenes Using Transient Directing Groups
4. **Pengfei Huo**, chemistry, University of Rochester / Enabling New Chemical Reactivities through Polariton Photochemistry
5. **Catherine Kealhofer**, physics, Williams College / Nonequilibrium Phonon Dynamics in Two-dimensional Materials
6. **Elena F. Koslover**, physics, University of California, San Diego / Physics of Cellular Distribution Networks: Morphology and Transport in the Endoplasmic Reticulum
7. **Kristin S. Koutmou**, chemistry, University of Michigan / Chemical Modifications to mRNA Nucleosides: A New Frontier in Gene Regulation
8. **Kah Chun Lau**, physics, California State University, Northridge / Data-Driven Solubility Model Development of Concentrated Non-aqueous Electrolytes
9. **Frank A. Leibfarth**, chemistry, University of North Carolina at Chapel Hill / Organocatalytic Kinetic Resolution Polymerization of Lactones
10. **Huey-Wen Lin**, physics, Michigan State University / Unveiling the Three-Dimensional Structure of Nucleons
11. **Song Lin**, chemistry, Cornell University / New Catalytic Methods for Enantioselective Electrosynthesis and Introducing Electrosynthesis to College and Graduate Curricula
12. **Britt F. Lundgren**, astronomy, University of North Carolina Asheville / Shedding Light on Star Formation Driven Galaxy Outflows across Cosmic Time
13. **Elisabetta Matsumoto**, physics, Georgia Institute of Technology / Knotty Knits: Using Topological Constraints to Program Geometry and Elastic Response in Knitted Textiles with Lattice Defects
14. **Sharon R. Neufeldt**, chemistry, Montana State University / Combined Experimental and Computational Approach to Improving Nickel and Palladium-Catalyzed Cross-Couplings



15. Glen D. O'Neil, chemistry, Montclair State University / Neurotransmitter Detection using Light-Addressable Electrochemical Sensors: Investigating the Role of Metal Morphology and Coverage on Sensor Response using Scanning Electrochemical Methods

16. Peter P. Orth, physics, Iowa State University / Probing Fractionalization and Entanglement in Quantum Spin Liquids: Theory of Two-dimensional Spectroscopy

17. Cedric Owens, chemistry, Chapman University / Constructing a Better Nitrogenase by Uncovering Protein-protein Interactions That Protect the Enzyme and Expand its Chemistry **18. Dennis V. Perepelitsa**, physics, University of Colorado Boulder / Next-Generation Experimental Probes of Hot and Dense Nuclear Matter **19. Leslie A. Rogers**, astronomy, University of Chicago / Searching for Water in Distant Worlds: Connecting the Atmospheric and Bulk Compositions of Sub-Neptune-Size Planets

20. Brenda M. Rubenstein, chemistry, Brown University / Advancing Chemistry through Data Science: Catalyst Design via Data-Enabled Quantum Chemistry and Integrating Data Science into the Chemistry Curriculum

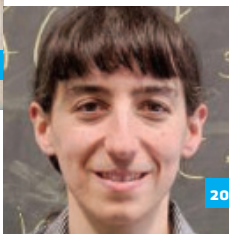
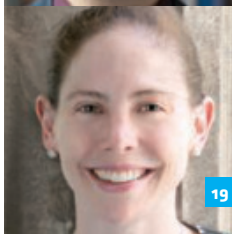
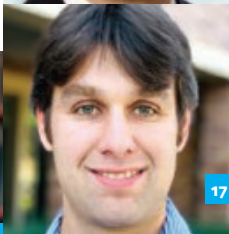
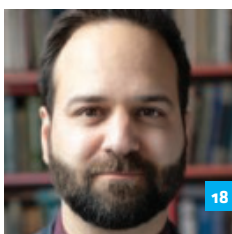
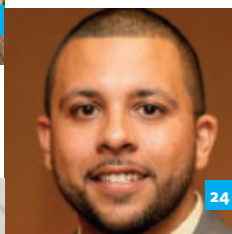
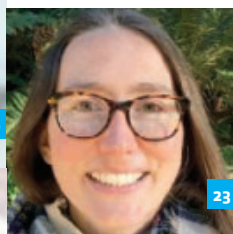
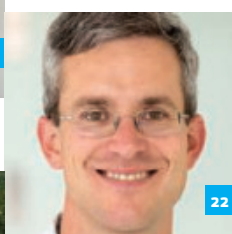
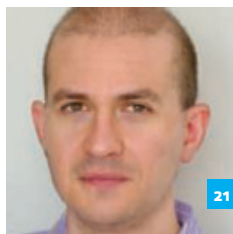
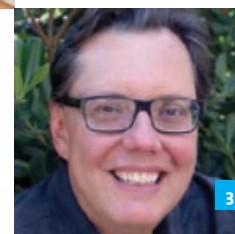
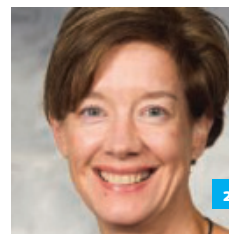
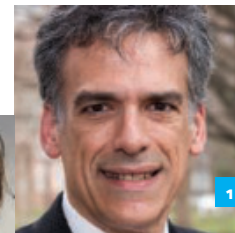
21. Lorenzo Sironi, astronomy, Columbia University / To B or Not to B: The Birth and Death of Magnetic Fields in the Universe **22. David A. Strubbe**, physics, University of California, Merced /

Light-induced Structural Dynamics in Materials: New Theoretical Insight into Ultrafast Phenomena **23. Claire P. Till**, chemistry, Humboldt State University / Scandium and Iron: Parallels in Chemical Reactivity, and Reducing the Opportunity Gap in the HSU Chemistry Department and Beyond **24. Jesus M. Velazquez**, chemistry, University of California, Davis / Achieving Energy Conversion Functionality through Compositional Modification: The Role of Metal Promotion in Chalcogenide Frameworks

25. Jessica K. Werk, astronomy, University of Washington / The Observational Signatures of Cosmic Gas Flows in a Hydrodynamic Framework

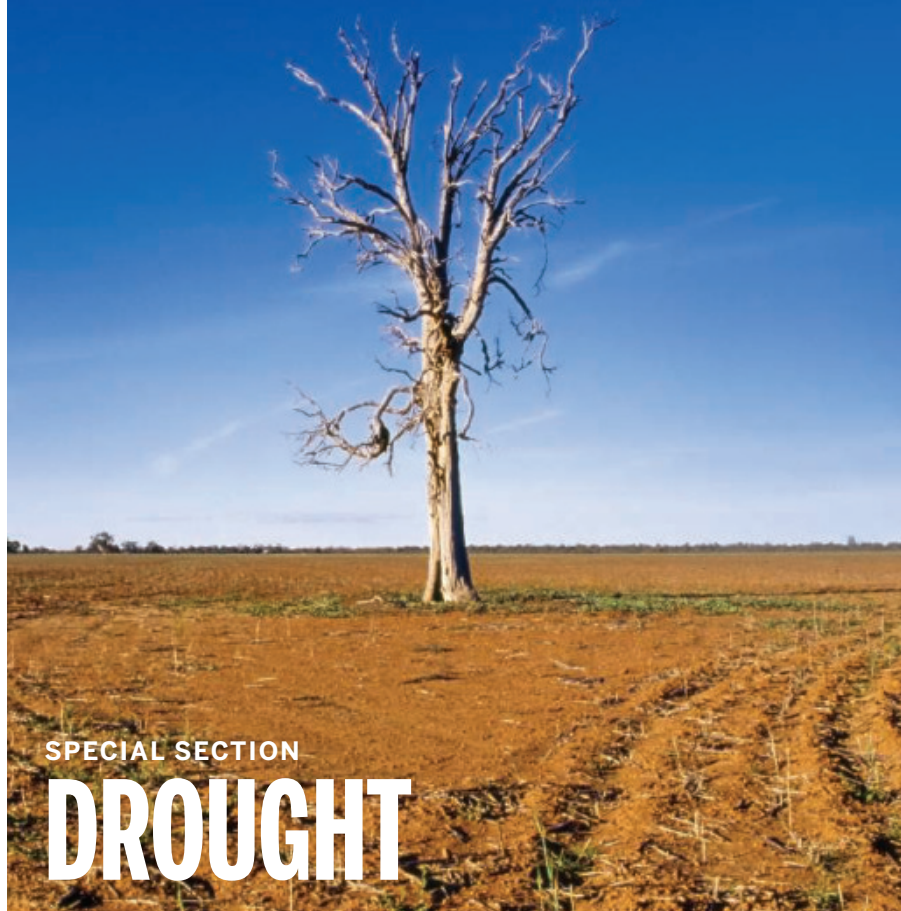
IMPACT and STAR Awardees

1. IMPACT awardee Rigoberto Hernandez, chemistry, Johns Hopkins University / Cottrell Scholar 1999 **2. STAR awardee Helen Blackwell**, chemistry, University of Wisconsin, Madison / Cottrell Scholar 2005 **3. STAR awardee Julio de Paula**, chemistry, Lewis and Clark College / Cottrell Scholar 1994



CONTENTS

17 APRIL 2020 • VOLUME 368 • ISSUE 6488



SPECIAL SECTION

DROUGHT

INTRODUCTION

254 Dry times

NEWS

226 The hunger forecast *P. Voosen*

VIDEO

230 Deep deficit *E. Stokstad*

234 Engineering an empire *L. Wade*

PODCAST

REVIEWS

256 On the essentials of drought in a changing climate *T. R. Ault*

261 Hanging by a thread? Forests and drought *T. J. Brodribb et al.*

266 The physiology of plant responses to drought *A. Gupta et al.*

270 Harnessing rhizosphere microbiomes for drought-resilient crop production *F. T. de Vries et al.*

274 The effects of drinking water service fragmentation on drought-related water security *M. Mullin*

ON THE COVER



Famines related to droughts can take a heavy toll. In 2011, dry conditions exacerbated hardships for some 430,000 refugees fleeing violence in Somalia. Here, Somali refugees seek aid in a camp near Dadaab, Kenya. Scientists are using new monitoring tools to identify regions at risk of famine and help ward off hunger before it is too late. See page 254. *Photo: Jacky Ghossein/The Sydney Morning Herald/Fairfax Media via Getty Images*

PERSPECTIVE p. 238 BOOKS ET AL. p. 250
LETTERS pp. 251 & 252 REPORT p. 314

NEWS

QQ群: 970508760

IN BRIEF

216 News at a glance

IN DEPTH

218 The lockdowns worked—but what comes next?

Easing the rules while keeping the virus at bay will be a process of trial and error

By K. Kupferschmidt

220 Pandemic carves gaps in long-term field projects

2020 is becoming the year of missing data for ecological projects and oceanographic cruises *By E. Pennisi*

221 From mice to monkeys, animals studied for coronavirus answers

Infected lab animals can assess drugs and vaccines *By J. Cohen*

223 Top EU scientist ousted over plans for coronavirus research

European Research Council president resigns over spat about agency's role in guiding funding to specific fields *By N. Wallace*

224 Ice monitor delivers a bonus: seafloor maps

Laser aboard NASA ICESat-2 satellite probes reefs and shallows near coastlines

By P. Voosen

INSIGHTS

PERSPECTIVES

238 Anthropogenic megadrought

Human-driven climate warming worsens an otherwise moderate drought *By D. W. Stahle*

DROUGHT SECTION p. 254; REPORT p. 314

240 Burning bridges in cancer genomes

Cytoskeletal forces break chromosomal fusions and trigger mutational avalanches

By J. Paiano and A. Nussenzweig

RESEARCH ARTICLE p. 282

241 Probing metabolism in time and space

Mass spectrometry imaging detects hotspots of metabolite production within cells

By T. Alexandrov

RESEARCH ARTICLE p. 283

242 Light expands a catalyst's repertoire

Visible light helps a Pd carbonylation catalyst both break and make carbon-halogen bonds

By P. Kathe and I. Fleischer

REPORT p. 318

244 Robots with insect brains

A literal approach to mechanistic explanation provides insight in neuroscience *By B. Webb*

246 Daniel S. Greenberg (1931–2020)

Incisive science journalist and commentator *By C. Norman*

POLICY FORUM

247 Deep flaws in a mercury regulatory analysis

The U.S. EPA ignores scientific evidence, economic best practice, and its own guidance *By J. Aldy et al.*

EDITORIAL p. 215

BOOKS ET AL.

249 Repairing damaged brains

Stem cell therapies slowly gain traction as viable treatments for brain disorders *By A. Woolfson*

250 What tree rings can tell us

From ancient timbers to mountaintop forests, trees hold important climate clues *By L. Daniels*

DROUGHT SECTION p. 254

LETTERS

251 Protect Indigenous peoples from COVID-19

By L. Ferrante and P. M. Fearnside

251 Ecosystem aridity and atmospheric CO₂

By T. F. Keenan et al.

DROUGHT SECTION p. 254

252 Response

By M. Berdugo et al.

DROUGHT SECTION p. 254

252 Technical Comment abstracts

RESEARCH

IN BRIEF

278 From *Science* and other journals

RESEARCH ARTICLES

281 Biochemistry

The Ccr4-Not complex monitors the translating ribosome for codon optimality *R. Buschauer et al.*

RESEARCH ARTICLE SUMMARY; FOR FULL TEXT:

DX.DOI.ORG/10.1126/SCIENCE.AAY6912

282 Cancer genomics

Mechanisms generating cancer genome complexity from a single cell division error *N. T. Umbreit et al.*

RESEARCH ARTICLE SUMMARY; FOR FULL TEXT:

DX.DOI.ORG/10.1126/SCIENCE.ABA0712

PERSPECTIVE p. 240

283 Biosynthetic enzymes

Metabolomics and mass spectrometry imaging reveal channeled de novo purine synthesis in cells *V. Pareek et al.*

PERSPECTIVE p. 241

290 Gene editing

Unconstrained genome targeting with near-PAMless engineered CRISPR-Cas9 variants *R. T. Walton et al.*

297 Gas storage

Balancing volumetric and gravimetric uptake in highly porous materials for clean energy *Z. Chen et al.*

REPORTS

303 Sex determination

Temperature-dependent sex determination is mediated by pSTAT3 repression of *Kdm6b* *C. Weber et al.*

307 Coral reefs

Meeting fisheries, ecosystem function, and biodiversity goals in a human-dominated world *J. E. Cinner et al.*

311 Topological optics

Topological funneling of light *S. Weidemann et al.*

314 Drought

Large contribution from anthropogenic warming to an emerging North American megadrought *A. P. Williams et al.*

PERSPECTIVE p. 238; DROUGHT SECTION p. 254

318 Catalysis

A dual light-driven palladium catalyst: Breaking the barriers in carbonylation reactions *G. M. Torres et al.*

PERSPECTIVE p. 242

DEPARTMENTS

214 Editorial

The moment to see the poor *By Joachim von Braun, Stefano Zamagni, and Marcelo Sánchez Sorondo*

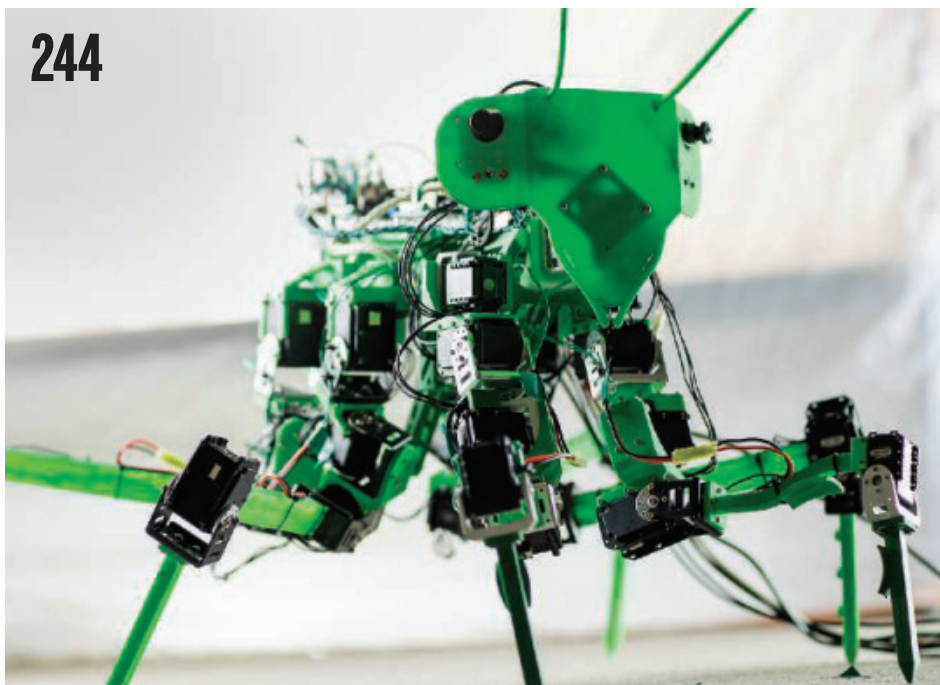
215 Editorial

Earth Day at 50 *By James Morton Turner and Andrew C. Isenberg*
POLICY FORUM p. 247

330 Working Life

My career earthquake *By Caitlyn A. Hall*

New Products324
Science Careers325



SCIENCE (ISSN 0036-8075) is published weekly on Friday, except last week in December, by the American Association for the Advancement of Science, 1200 New York Avenue, NW, Washington, DC 20005. Periodicals mail postage (publication No. 484460) paid at Washington, DC, and additional mailing offices. Copyright © 2020 by the American Association for the Advancement of Science. The title SCIENCE is a registered trademark of the AAAS. Domestic individual membership, including subscription (12 months): \$165 (\$74 allocated to subscription). Domestic institutional subscription (51 issues): \$2148; Foreign postage extra: Air assist delivery: \$98. First class, airmail, student, and emeritus rates on request. Canadian rates with GST available upon request. GST #125488122. Publications Mail Agreement Number 1069624. Printed in the U.S.A.

Change of address: Allow 4 weeks, giving old and new addresses and 8-digit account number. Postmaster: Send change of address to AAAS, P.O. Box 96178, Washington, DC 20090-6178. Single-copy sales: \$15 each plus shipping and handling available from backissues.science.org; bulk rate on request. Authorization to reproduce material for internal or personal use under circumstances not falling within the fair use provisions of the Copyright Act can be obtained through the Copyright Clearance Center (CCC), www.copyright.com. The identification code for Science is 0036-8075. Science is indexed in the Reader's Guide to Periodical Literature and in several specialized indexes.

The moment to see the poor

Joachim von Braun

is president of the Pontifical Academy of Sciences, Vatican City, and is Professor for Economic and Technological Change, University of Bonn Center for Development Research, Bonn, Germany. jvonbraun@uni-bonn.de

Stefano Zamagni

is president of the Pontifical Academy of Social Sciences, Vatican City; professor of Economics at the Johns Hopkins University School of International Studies, Bologna; and professor of Political Economics, Università di Bologna, Bologna, Italy. stefano.zamagni@unibo.it

Marcelo Sánchez Sorondo

is Bishop Chancellor of the Pontifical Academies of Sciences and of Social Science, Vatican City. pas@pas.va

The coronavirus disease 2019 (COVID-19) pandemic has illuminated inequities that have put poor people—in both low-income nations and in rich countries—at the greatest risk of suffering. Pope Francis recently pointed to that in an interview: “This is the moment to see the poor.”

Until science finds appropriate drugs and a vaccine to treat and prevent COVID-19, today's paradox is that everybody needs to cooperate with others while simultaneously self-isolating as a protective measure. Yet, whereas social distancing is quite feasible for wealthy people, poor people crowded in urban slums or refugee camps do not have that option and lack face masks and hand-washing facilities. To address the risks in large, crowded cities in developing countries, we must support prevention by testing, providing access to protective equipment, and launching a big effort to build provisional hospitals to isolate infected people.

In addition, the digital divide between the rich and poor may be costing lives. Inequitable distribution of technology and online resources means that crucial information on COVID-19, particularly early warnings and recommended early responses, are not timely, if received at all, in low-income communities. Without access to responsible, transparent, and current information, a cacophony of unproven assumptions can instead spread through poor communities. This gap in access to technology also translates into a lack of opportunities for distance learning while schools are closed, and teleworking during societal lockdown is infeasible for millions of low-income workers because of the nature of their jobs and lack of access to communications infrastructure. What COVID-19 is teaching us is that universal access to internet and communication technologies should be a human right.

Unfortunately, these inequities lead to yet others in poor communities. COVID-19 is adversely affecting national economies and is destroying small businesses and farmers. The disruptive consequences for food systems, especially, hurt poor people, who spend most of their income on food. This is increasing hunger and exacerbating the public health threat of the pandemic. The global agenda to advance the United Nations (UN) sustainability goals—particularly those related to poverty, hunger, health, decent work, and economic growth—will be undermined by COVID-19,

unless the world cooperates and includes the rescue of small businesses and farmers as it seeks to avoid a global economic crisis.

COVID-19 has also exposed the fragility of interconnectedness. Increasing global economic interactions have opened the world to massive cross-border flows of goods, services, money, ideas, and people. That allowed many to move out of poverty. However, curbing the rapid spread of severe acute respiratory syndrome–coronavirus 2 (SARS-CoV-2) requires closing borders around infection hotspots. These closings must be temporary only, and they must not hinder cooperation between nations to handle the pandemic. Human resources, equipment, knowledge about treatments, and supplies, as well as nonmarket and spiritual goods, must be shared, including with poor countries. The pandemic initially inspired nations to look inward. Seeking a solution to COVID-19 through

national isolation would be counterproductive. SARS-CoV-2 does not recognize borders. Rich nations need to support transnational and UN organizations in their global efforts to control spread of this contagion.

Science capacity in general, and specifically related to infectious diseases, is highly unequal around the world. This contributes to a greater risk of suffering in poor nations. Root causes and prevention of infectious diseases caused by bacteria, viruses, or parasites that spread from animals to humans, for example, require co-

operative research that is close to potential risk areas, including in poor nations. Now is the time for the developed world to commit to improving this. If this gap in science capacity continues to grow, the interest of rich nations will become more limited and further leave disease burden among the poor.

Other major global crises, such as climate change and biodiversity loss, demand cooperative global responses that don't leave out the poor. Once COVID-19 is under control, the world cannot return to business as usual. A thorough review of worldviews, lifestyles, and the problems of short-term economic valuation must be carried out. A more responsible, more sharing, more caring, more inclusive, and fairer society is required if we are to survive in the Anthropocene.

—Joachim von Braun, Stefano Zamagni,
Marcelo Sánchez Sorondo

“...inequities
lead to
yet others
in poor
communities.”

Earth Day at 50

The spring of 2020 will be remembered for the coronavirus pandemic. But at this moment, it is worth remembering that 50 years ago, the United States confronted a very different crisis. That April, millions of Americans participated in Earth Day “teach-ins” across the nation. These events galvanized Democrats and Republicans into action: President Nixon and Congress worked together to pass a blitz of science-based policies that aimed to protect public health and the environment—including the Clean Air Act, Clean Water Act, and Endangered Species Act—with large bipartisan majorities.

These laws elevated science above economics or special-interest politics to inform public policy. They specified the role of science in evaluating environmental impacts, setting air pollution standards, and deciding when a species needed protection. Political scientist Roger Pielke has called this “tornado politics,” because like people heeding meteorologists’ advice to take shelter during a tornado, in the face of the mounting environmental crisis, Americans looked to science to guide policies that would protect the environment and public health.

A half-century of investment in those laws has paid tremendous dividends. Although inequities persist in environmental exposures and new environmental challenges have arisen, Americans have witnessed dramatic improvements in environmental quality since the 1970s. By the early 1980s, the Clean Air Act had extended the life of the average American by 1 year. In 2010, the Clean Air Act and its 1990 amendments were estimated to prevent 3.2 million lost school days, 13 million lost workdays, and 160,000 premature deaths. The Clean Water Act is responsible for substantial declines in most major water pollutants. Scientists estimate that the Endangered Species Act has prevented the extinction of 291 species and helped 39 species to a full recovery.

The U.S. government’s uneven response to the coronavirus pandemic shows how much has changed since the early 1970s. Although millions of Americans have followed the advice of infectious disease experts this spring—sheltering at home and practicing social distancing—President Donald Trump often eschewed tornado politics, especially in the early weeks of the crisis, questioning the advice of scientific experts. Instead, he

followed his hunches and went with his gut—an approach that contributed to the nation’s slow response to the pandemic and the scale of the outbreak.

Although it may be tempting to chalk up Trump’s disregard for science to his mercurial leadership, his uneasy relationship to scientific expertise has deep roots in conservative politics. The shift away from science-based policy-making began during the 1980 presidential campaign, when Ronald Reagan not only endorsed the idea of teaching creationism in public schools, but cheerfully mocked environmental laws and projected a blithe nonchalance toward environmental problems. In the years after Reagan’s presidency, conservative leaders have often elevated values above science when it comes to environmental policy and public health.

What are these values? On the environment, conservatives have consistently turned to three themes: a belief in American exceptionalism; an unwavering faith in the market and an abundance of natural resources; and a deep skepticism of science. When the United States withdrew from the Paris climate accord in June 2017, Trump and his then Environmental Protection Agency Administrator, Scott Pruitt, emphasized what they saw as the agreement’s unfair demands on the United States and the ability of American business to solve the climate challenge without government intervention. Neither mentioned climate science, because conservatives had been characterizing climate change as a “hoax” for decades.

In the half-century since Earth Day, anti-scientism has metastasized as conservatives have successfully wedded it to core conservative values: Science is dismissed as the province of liberal elites, anti-religious in its secularism and anti-capitalist in its support for science-based regulation. What today’s coronavirus pandemic makes clear is the grave cost of delay and inaction in the face of urgent scientific warnings. In January 1970, Richard Nixon explained that it was “now or never” for the environment. That warning is even more true today. Meeting challenges like the coronavirus and climate change will require policy actions that match the scale and scientific-based rigor of those from the 1970s.

—James Morton Turner and Andrew C. Isenberg

James Morton Turner

is an associate professor of environmental studies at Wellesley College, Wellesley, Massachusetts, USA. jturner@wellesley.edu

Andrew C. Isenberg

is the Hall Distinguished Professor of American History at the University of Kansas, Lawrence, Kansas, USA. isenberg@ku.edu

“... it is worth remembering that 50 years ago, the United States confronted a very different crisis.”

NEWS

IN BRIEF

Edited by Jeffrey Brainard
DISPATCHES FROM THE PANDEMIC

A man in Stamford, Connecticut, heads to the hospital with symptoms of COVID-19 as his daughter says goodbye. Some black communities have been hit especially hard.

France embraces divisive therapy

POLITICS | The highly politicized debate about the use of hydroxychloroquine and chloroquine to treat COVID-19 infections reached an extreme last week in France, the home of microbiologist Didier Raoult, who has led three controversial studies purporting to show the drugs' benefit. More than half a million people signed an online petition to make the antimalarials more widely available; polls show the drugs are particularly popular among voters on the far right and far left. President Emmanuel Macron, a centrist, met with Raoult on 9 April but didn't mention the drugs in a televised address 4 days later in which he announced that France's lockdown would be extended until 11 May. The petition was started by former Minister of Health Philippe Douste-Blazy—France's candidate to lead the World Health Organization in 2017—and Christian Perronne, head of infectious diseases at the renowned Raymond Poincaré University Hospital. Researchers have pointed out that the drugs have side effects and that patients' demand for them may stymie efforts to test their efficacy.

Treatments for under \$1 a day

BIOMEDICINE | Most drugs now in clinical trials with COVID-19 patients could be manufactured for less than \$1 a day per patient, an analysis has found—although international programs may need to negotiate affordable retail prices. Andrew Hill of the University of Liverpool and colleagues based the estimates in part on cost data for the drugs' ingredients reported in India, a major hub for generic drug production. Most are off patent, but their retail prices run much higher than the

Read additional *Science* coverage of the pandemic at [sciencemag.org/tags/coronavirus](https://www.sciencemag.org/tags/coronavirus).

Featured interview

▲ Minority groups bear heavy toll

A grim drumbeat of reports last week revealed that COVID-19 is devastating many minority communities disproportionately. For example, black people make up 32% of Louisiana's population—but a startling 70% of the coronavirus deaths. In its first release of racial data, New York City reported that Hispanics died from COVID-19 at a rate of 22 per 100,000—double the rate of white people.

Studies of past epidemics show the same tragic patterns, which could be ameliorated by better health care policies, says Sandra Crouse Quinn, a public health expert at the University of Maryland, College Park. During the H1N1 epidemic of 2009, "for African Americans, the burden of chronic disease made them much more susceptible."

What is more, many members of minority groups said in surveys at the time that their jobs would not permit them to self-isolate at

home during a health emergency. "Sixty-one percent of Spanish-speaking Latinos could only do their job in their workplace because they work in service jobs, for example cleaning hospitals and homes." Providing them paid sick leave would help, Quinn says.

The full interview is at scim.ag/COVIDrace.

More headlines

For survivors of severe COVID-19, beating the virus is just the beginning. Illness and disability loom after weeks on a ventilator.

Social scientists scramble to study pandemic, in real time. But "natural experiments" may not yield useful results because the impacts are so widespread and messy.

South Africa hopes its battle with HIV and TB helped prepare it for COVID-19.

But those infections could also worsen the pandemic's impact.

Early-career scientists at critical career junctures brace for impact. For some, university closures will delay graduation and hiring.

Smell loss studied for warnings

SENSORY RESEARCH | Scientists have formed a group to investigate the rapid loss of smell and taste reported by some people infected by the COVID-19 virus, a possible early warning sign. The Global Consortium for Chemosensory Research includes 500 clinicians, neurobiologists, and cognitive scientists in 38 countries. They are starting to survey people who have experienced such sensory losses.

WORKPLACE

Under fire, NIH scientist drops McGill job

Facing accusations of gender bias, Constantine Stratakis, the geneticist who for 10 years has directed intramural science at the U.S. National Institute of Child Health and Human Development (NICHD), withdrew on 8 April from a position he was to have taken in June leading a large Canadian research institute. The day before, the Board of Directors of the Research Institute of the McGill University Health Centre had received a letter signed by more than 500 institute staff, faculty members, and students asking them to revoke the hiring of Stratakis, 54, who was to have become the institute's executive director and chief scientific officer. *Science* had reported on 2 April that Stratakis had been named in eight equal employment opportunity complaints by female professionals at NICHD, and that the ranks of women running labs fell disproportionately during his tenure. He has countered that he actively hired, promoted, and sought the advice of women.

Salmon restoration moves ahead

CONSERVATION | California regulators last week granted environmental permits to remove three dams on the Klamath River in what would be the nation's largest such demolition aimed at wildlife restoration, providing migrating salmon access to nearly 500 kilometers of rivers and streams. Oregon had already issued a similar permit to remove a fourth dam on the river. The Federal Energy Regulatory Commission must still decide whether to allow the dam licenses to be transferred from the energy

company PacifiCorp, their longtime owner, to a nonprofit created to demolish the dams. PacifiCorp, which faces expensive required upgrades to the dams, supports the transfer. The commission's final verdict is expected to take months. The \$446 million removal would occur in 2022.

Congo Ebola victory delayed

PUBLIC HEALTH | Plans to declare the end of the long-running Ebola outbreak in the Democratic Republic of the Congo (DRC) were dashed on 10 April when a

new case was confirmed in the city of Beni. The country was only 2 days away from the expiration of a 42-day countdown that started in March, when the last known patient at that time was released from the hospital. Countries must wait for two 21-day incubation periods after the last known case of Ebola before officially pronouncing an outbreak finished. The World Health Organization says health care workers have continued to investigate and rule out thousands of suspected Ebola cases every day across the DRC, even as they gear up to respond to the COVID-19 pandemic.

Neutrinos hint at matter's origin

PARTICLE PHYSICS | Nearly massless particles called neutrinos behave differently from their antimatter counterparts, antineutrinos, physicists with the T2K experiment in Japan report. The finding could help explain how the newborn universe generated more matter than antimatter. Neutrinos and antineutrinos each come in three types—electron, muon, and tau—and T2K researchers have been firing muon neutrinos from an accelerator in Tokai to the SuperKamiokande underground detector 295 kilometers away. The researchers look for rare instances in which the particles turned into electron neutrinos along the way through so-called neutrino oscillations. Data collected from 2009 to 2018 show with 95% probability that muon neutrinos change their identity more often than muon antineutrinos do, researchers report this week in *Nature*. Bigger experiments under construction aim to precisely measure the effect.

A dazzling stellar explosion

ASTRONOMY | A supernova first spotted in 2016 has proved to be the brightest ever observed and the most persuasive sighting yet of a rare type of boosted blast. SN2016aps erupted 3.6 billion light-years from Earth. At 500 times the brightness of a typical dying star, it quickly outshone the galaxy it resided in. In *Nature Astronomy* this week, astronomers report the exploding star was a giant, possibly 100 times heavier than the Sun; typical supernovae come from stars of a dozen solar masses. The researchers, using data from the Hubble Space Telescope and several ground-based instruments, think that in its last years the star shed lots of gas into nearby space; when the supernova blast hit that shell of gas it lit up with extraordinary brightness.



The 40-meter-tall Copco 1 Dam, completed in 1922, is one of four on the Klamath River that would be removed.



A priest in Innsbruck, Austria, views photographs of his absent congregation. Austria eased social distancing on 14 April.

IN DEPTH

COVID-19

The lockdowns worked—but what comes next?

Easing the rules while keeping the virus at bay will be a process of trial and error

By **Kai Kupferschmidt**

The world is holding its breath.

After the novel coronavirus made its way around the world, one country after another adopted harsh measures to stop SARS-CoV-2 from spreading and overwhelming hospitals. They have hit the pause button on their economies and their citizens' lives, stopping sports events, religious services, and other social gatherings. School closures in 188 countries affect more than 1.5 billion students. Borders are closed and businesses shuttered. While some countries are still seeing daily case numbers increase, others—first in Asia but increasingly in Europe—have managed to bend the curve, slowing transmission of COVID-19.

But what is the exit strategy? “We’ve managed to get to the life raft,” says epidemiologist Marc Lipsitch of the Harvard T.H. Chan School of Public Health (HSPH). “But I’m really unclear how we will get to the shore.”

As they seek a path forward, governments around the world must triangulate the health of their citizens, the freedoms of their population, and economic constraints. Could schools be reopened? Restaurants? Bars? Can people go back to their offices? “How to relax the lockdown is not something around which there is a scientific consensus,” says Caroline Buckee, an epidemiologist at HSPH. Most researchers agree that reopening society will be a long haul, marked by trial and

error. “It’s going to have to be something that we’re going to have to take baby steps with,” says Megan Coffee, an infectious disease researcher at New York University.

The number to watch in the next phase may no longer be the actual number of cases per day, but what epidemiologists call the effective reproduction number, or R , which denotes how many people the average infected person infects in turn. If R is above 1, the outbreak grows; below 1 it shrinks. The goal of the current lockdowns is to push R well below 1. Once the pandemic is tamed, countries can try to loosen restrictions while keeping R hovering around 1, when each infected person on average infects one other person, keeping the number of new cases steady.

To regulate R , “Governments will have to realize that there are basically three control knobs on the dashboard,” says Gabriel Leung, a modeler at the University of Hong Kong: isolating patients and tracing their contacts, border restrictions, and social distancing.

TURNING THE KNOBS

Singapore, Hong Kong, and South Korea have all managed to keep their epidemics in check through aggressive use of the first control. They identify and isolate cases early and trace and quarantine their contacts, while often imposing only light restrictions on the rest of society. But this strategy depends

on massively scaling up testing, which has been hampered by a scarcity of reagents and other materials everywhere. Contact tracing is also labor-intensive. Massachusetts is hiring 500 contact tracers, but a recent report by researchers at Johns Hopkins University estimated the United States as a whole needs to train about 100,000 people.

Mobile phone apps could help by automatically identifying or alerting people who recently had contact with an infected person. But Western countries have yet to implement these systems. Google and Apple have teamed up to incorporate a contact tracing app in their operating systems. Germany, France, and other countries are developing apps based on a protocol called Pan-European Privacy Preserving Proximity Tracing. It relies on short-range Bluetooth signals to gauge the proximity between two devices without logging their exact locations, which helps sidestep some privacy concerns.

But short of making these technologies compulsory, as China has done, how can a country ensure that enough people download an app for it to provide reliable information and influence the spread of disease? And what exactly counts as a contact? “If I live in a big apartment block, am I going to be getting dozens of notifications a day?” asks epidemiologist Nicholas Davies of the London School of Hygiene & Tropical Medicine (LSHTM).

Science’s COVID-19 coverage is supported by the Pulitzer Center.

Davies adds that widespread use of the apps will further drive up the demand for testing.

As to the second control knob, border restrictions, most countries have already banned entry to almost all noncitizens. Quarantining returning citizens, as New Zealand and Australia began to do in the past few weeks, further minimizes the risk of new introductions of the virus. Such measures are likely to remain in place for a while; the more a country reduces transmission domestically, the greater the risk that any new outbreaks will originate with travelers. And foreign visitors are generally harder to trace than citizens and more likely to stay at hotels and visit potential transmission hot spots, says Alessandro Vespignani, a disease modeler at Northeastern University. "As soon as you reopen to travelers, that could be something that the contact tracing system is not able to cope with," he says.

The third dashboard dial, social distancing, is the backbone of the current strategy, which has slowed the spread of the virus. But it also comes at the greatest economic and social cost, and many countries hope the constraints can be relaxed as case isolation and contact tracing help keep the virus in check. In Europe, Austria took the lead by opening small shops on 14 April. Other stores and malls are scheduled to follow on 1 May, and restaurants maybe a few weeks later. A 13 April report from the German National Academy of Sciences argued for slowly reopening schools, starting with the youngest children, while staggering break times and making masks mandatory. But French President Emmanuel Macron has said France's lockdown will remain in place until 11 May.

Choosing a prudent path is difficult, Buckee says, in part because no controlled experiments have compared the effectiveness of different social distancing measures. "Because we don't have really strong evidence," she says, "it's quite hard to make evidence-based policy decisions about how to go back." But Lipsitch says that as authorities around the world choose different paths forward, comparisons could be revealing. "I think there's going to be a lot of experimentation, not on purpose, but because of politics and local situations," he says. "Hopefully the world will learn from that."

Finding out how any particular measure affects R is not straightforward, because infections that occur today can take weeks to show up in disease reports. In 2004, mathematician Jacco Wallinga of the Dutch National

Institute for Public Health and the Environment and colleagues published a statistical method to estimate R in real time, which is now used around the world. Researchers are also incorporating data on mobility patterns and people's behavior to make the estimates more accurate. Having real-time estimates of R is important, says Adam Kucharski, a modeler at LSHTM: "If governments put a measure in or lift it, they can get a sense of what the immediate implications are, rather than having to wait," he says.

There's one other, unknown factor that will determine how safe it is to loosen the reins: immunity. Every single person who becomes infected and develops immunity makes it harder for the virus to spread. "If we get 30% or 40% of the population immune, that really starts to change that whole picture, it helps us a lot," because it would

bring R down by the same percentage, says Michael Osterholm, director of the Center for Infectious Disease Research and Policy at the University of Minnesota, Twin Cities.

Immunity will inevitably build up as more people become infected, but some researchers argue for ramping up immunity more quickly, by letting the virus spread in younger people, who are less susceptible to severe illness, while "cocooning" more at-risk patients, such as the elderly. The United Kingdom floated this "herd immunity" idea in February but backed away from it, as did the Netherlands. Some scientists say other countries should consider it once the strain that the first wave of cases has put on their health care systems eases. "Is it better to have a controlled burn in younger populations right now than it is to prevent it? I think that's a very important conversation to have," Osterholm says.

Skeptics doubt that vulnerable populations could really be protected. In many countries, multiple generations live under one roof, and young people work at nursing homes. Nor are scientists certain that COVID-19 produces robust, long-lasting immunity. Several studies seek to address these questions.

EXIT STRATEGY

For now, the most likely scenario is one of easing social distancing measures when it's possible, then clamping down again when infections climb back up, a "suppress and lift" strategy that both Singapore and Hong Kong are pursuing. Whether that approach can strike the right balance between keeping the virus at bay and easing discontent and economic damage remains to be seen.

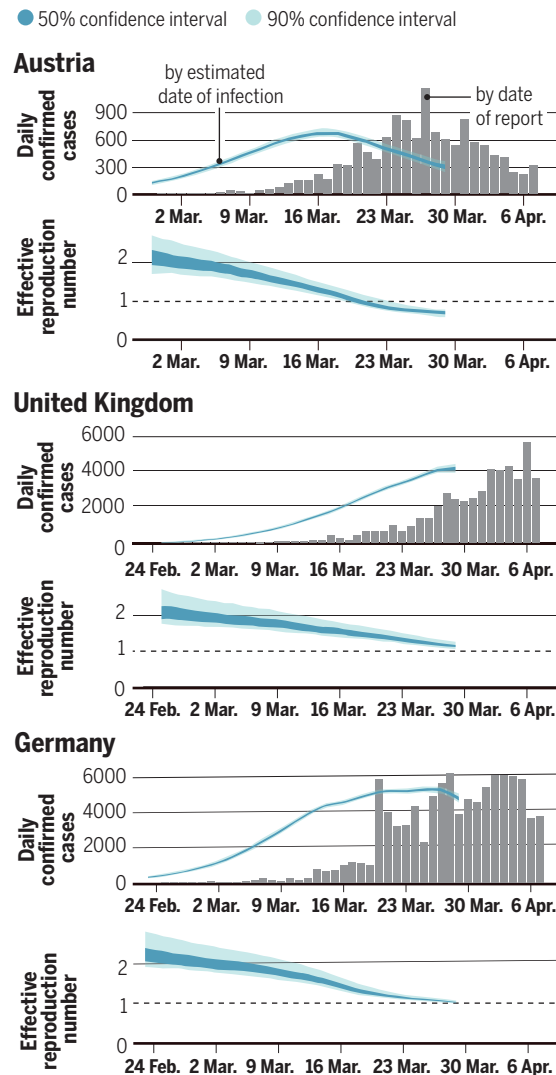
Even Singapore and Hong Kong have had to toughen some social distancing measures in recent weeks after a surge of cases, Lipsitch notes; Singapore's social distancing regime is no longer very different from that in New York City or London. And both cities' strategies are much harder to implement across a big country like the United States. "We have to have every single town and city and county be as good as Singapore for this to work," he says.

Ultimately, says Jeremy Farrar, head of the Wellcome Trust, a path out of the dilemma now facing the world will come from research. It might take the form of an effective treatment for severely ill patients, or a drug that can prevent infections in health care workers, or—ultimately—a vaccine. "Science is the exit strategy," Farrar says. ■

With reporting by Kelly Servick.

The number to watch

Lockdowns lower the number of new cases as well as R , the effective reproduction number. If R drops below 1, the epidemic shrinks.





COVID-19

Pandemic carves gaps in long-term field projects

2020 is becoming the year of missing data for ecological projects and oceanographic cruises

By Elizabeth Pennisi

When Jane Goodall witnessed a chimpanzee troop split into two bands in 1974, she called the event a “once in a lifetime” opportunity. Now, a group of chimp researchers fears missing its own once-in-a-lifetime moment because of the coronavirus pandemic. Two years ago, they, too, witnessed a chimp group fission at Kibale National Park in Uganda. The consequences surprised them: Males of one group recently attacked the other and beat up the females. “I would have never predicted that males that have grown up together would be at each other’s throats,” says John Mitani, a primatologist at the University of Michigan, Ann Arbor. But he and his colleagues are likely to remain ignorant about how this power struggle plays out over the coming months or even the next year.

Because of the coronavirus pandemic, most of the research team has left the country. Mitani says such precautions make sense for both humans and chimps,

who are likely vulnerable to COVID-19, too, according to an 11 April preprint on bioRxiv. But he and his colleagues may miss the rare events that structure chimpanzee society.

From the tropics to the poles, field researchers are abandoning study sites because of travel restrictions and fears of catching or spreading the new coronavirus. Project leaders are making hard decisions about canceling field projects and are scrambling to help students stay productive. Fleets of research vessels have been grounded and crews quarantined. As a result, researchers are steeling themselves for potentially devastating gaps in long-term data sets on the world’s flora, fauna, climate, and chemistry. Even automated surveys are in peril, as many expensive instruments need human tenders. “There’s never been another time in history where we’ve seen an essentially global cessation of surveys and data collection about species and ecosystems,” says Ben Halpern, an ecologist at the National Center for Ecological Analysis and Synthesis at the University of California, Santa Barbara.

Cruises to update instruments measuring North Atlantic Ocean currents may not happen this year.

This year’s data gap is coming just as the pandemic itself offers observers a once-in-a-lifetime moment. With business and travel almost at a standstill, pollution and other human impacts have diminished across the globe, offering a rare chance to see how the world works with a fainter human footprint. “It’s like sending a spacecraft to Saturn for a flyby survey of the planet, only to have all the instrumentation stop working right when the spacecraft flies by,” Halpern says.

Last month, Peter Marra, a conservation biologist at Georgetown University, conducted an informal Twitter survey of field scientists. Only 8.5% of the 450 responders, mostly ecologists, were going ahead with their planned fieldwork. One-third had canceled their field seasons. Even the North American Breeding Bird Survey, a massive, 54-year-old citizen science project that keeps tabs on birds across the Northern Hemisphere, was put on hold. Researchers fear losing track of reproduction and population trends in animals they’ve followed for decades.

Russell Hopcroft, a biological oceanographer at the University of Alaska, Fairbanks, remains optimistic. As he has done for decades, he was supposed to set sail this month to catch the annual plankton bloom in the Gulf of Alaska and collect data from automated instruments that tracked water conditions leading up to the bloom. Plankton, at the base of the marine food web, offer a bellwether for the productivity of this important fishing ground, which can vary dramatically year to year. “It sets the stage for how we expect the whole year to play out,” Hopcroft says. The North Pacific Fishery Management Council depends on these and other data to set catch quotas for the season.

State and federal agencies have sidelined the research vessels that collect the data. Yet Hopcroft is scheming to get special permission for a much-reduced cruise before mid-May. His ship’s crew is in quarantine after arriving from Washington, a COVID-19 hot spot, and Hopcroft and two volunteers will isolate themselves starting this week to be sure they are not infected. They want to be ready to hop on board should Alaska’s 30-day clampdown loosen on 1 May. “We aren’t ready to throw in the towel,” he says.

Oceanographer Fiammetta Straneo of the Scripps Institution of Oceanography is less hopeful about her planned cruise in June for the Overturning in the Subpolar North Atlantic Program, which has deployed

underwater instruments to continuously track temperature, salinity, and current velocity at various depths across the North Atlantic Ocean for 4 years. The goal of this joint U.S.-European effort, planned to run for 10 years, is to understand how ocean circulation is changing, which in turn will affect how climate change plays out. The instruments take data automatically, but if Straneo doesn't update them, they'll likely stop recording after this summer. "Having a 1-year gap will be a major loss," she says.

This year is also a missed opportunity for one of ecology's biggest data projects, the National Ecological Observatory Network (NEON). Decades in the making, NEON aims to monitor environmental changes in a range of North American ecosystems (*Science*, 25 September 2015, p. 1436), and 2019–20 was to be the first full year when it could gather standardized physical, chemical, environmental, and biological data from all its 81 U.S. sites. Some sites are new, but others have been operational for almost 10 years.

But on 23 March, NEON ceased all in-person and onsite work, such as trapping mammals and insects and sampling soil and water. Automated instruments collect much of NEON's data. But Paula Mabee, NEON's scientific director, says she was surprised by how many automated instruments need human tenders for calibration or to manage hazardous chemicals. Of the 73 data products on autopilot, "we proactively shut down" 24, including measurements of carbon dioxide and rainfall, she says.

The missing data will have short- and long-term implications, says Michael Dietze, an ecologist at Boston University. For example, data on tick and mammal populations are key to his team's annual predictions about when and how many nymphs of the deer tick that transmits Lyme disease will emerge.

One of the biggest blows is the grounding of NEON's airplanes. They are outfitted with cameras and remote sensing equipment to keep tabs on such variables such as the heights of trees and the chlorophyll and nitrogen content of plants, which are important for calculating carbon uptake. Philip Townsend, an ecologist at the University of Wisconsin, Madison, has been working to turn those measurements into easy-to-use maps. He'd planned to groundtruth his efforts by collecting leaves this season. But this spring, there will be both airborne measurements and leaf collection are on hold.

Yet as disappointed as he and others are, delaying or shutting down such operations "is clearly the right decision," Townsend says. "You want people to be safe." ■

With reporting by Ann Gibbons and Paul Voosen.

COVID-19

From mice to monkeys, animals studied for coronavirus answers

Infected lab animals can assess drugs and vaccines

By **Jon Cohen**

Beloved as pets, Syrian hamsters are winning another kind of attention from scientists trying to understand and defeat COVID-19. Fifteen years ago, scientists found the hamsters could readily be infected with the coronavirus that causes severe acute respiratory syndrome (SARS). Their symptoms were subtle, so the animals didn't get much traction as a model for the disease. But with COVID-19, caused by a related virus, SARS-CoV-2, the model's prospects appear brighter.

When physician scientist Jasper Fuk-Woo Chan of the University of Hong Kong (HKU) and co-workers recently infected eight hamsters, the animals lost weight, became lethargic, and developed ruffled fur, a hunched posture, and rapid breathing. High levels of SARS-CoV-2 were found in the hamsters' lungs and intestines, tissues studded with the virus' target, a protein receptor called angiotensin-converting enzyme 2 (ACE2). These findings "closely resemble the manifestations of upper and lower respiratory tract infection in humans," Chan and co-authors wrote in a 26 March paper in *Clinical Infectious Diseases*.

That team is but one of dozens of groups racing to develop animal models that can help find effective COVID-19 vaccines and treatments and clarify precisely how SARS-CoV-2 causes disease. The teams are often short-handed because of the pandemic's shelter-in-place restrictions, but they are collaborating intensively. Each Thursday, the World Health Organization arranges a video conference of nearly 100 scientists, regulators, and funders who are collectively working with a menagerie of lab animals, including mice, ferrets, and several species of monkeys. "A lot of the traditional silos of information are really coming down," says the group's co-chair, William Dowling, who works on vaccine development at the Coalition for Epidemic Preparedness Innovations.

The group swaps the latest data and tips,

such as the efficiency of different infection routes and the most likely places to find the pathogen in animals. "Everybody has been thrown into a rush to get an animal model that's faithful to the human condition and reproducible," says Chad Roy of the Tulane National Primate Research Center.

One monkey study has already delivered an encouraging result, suggesting that infection produces at least short-lived immunity. But a wide range of species may be an asset. "You need the right model for the right question," says Vincent Munster of the Rocky Mountain Laboratories branch of the U.S. National Institute of Allergy and Infectious Diseases, whose team focuses on monkeys. He cautions against dismissing an animal model simply because SARS-CoV-2 produces an effect, such as death from a brain infection, that doesn't reflect typical disease in humans.

"That's a big misunderstanding," he says, noting that "humans don't have a tail, either."

A top priority is to test experimental vaccines by immunizing animals and then "challenging" them with the virus—experiments that must be done in biosafety level 3 labs. Animal models could also warn of dangers of COVID-19 vaccines and drugs; some experimental vaccines against the related SARS virus, for example, triggered antibodies that enhanced disease severity when

test animals were challenged. Furthermore, experiments with animals may explain why children rarely develop symptoms, how readily SARS-CoV-2 transmits through fine aerosolized particles, and whether host genetic factors make some people more susceptible to severe disease.

Mice—easy to handle and breed—have long been the mainstay of biomedicine, and a good mouse model would be a boon for COVID-19 research. But mice shrug off infection with SARS-CoV-2, because the mouse ACE2 has key differences from the human one. "It's funny how the virus can have such devastation in humans, and then you can give a million particles to a mouse and it's inert," says Timothy Sheahan, who is developing mouse

"Everybody has been thrown into a rush to get an animal model that's faithful to the human condition and reproducible."

Chad Roy,
Tulane National Primate
Research Center

COVID-19 models at the University of North Carolina (UNC), Chapel Hill.

Chan, working with HKU's microbiologist Kwok-Yung Yuen and others, pinpointed the problem by doing a cross-species comparison of the region of ACE2 to which SARS-CoV-2 first attaches. In the mouse, 11 of 29 amino acids of this domain differed from the human version. (Rats had 13 differences, but hamsters only had four.)

One way around the roadblock is to engineer mice that express both the mouse and the human versions of the receptor's gene, *ACE2*. In 2007, Stanley Perlman of the University of Iowa did just that to study SARS. Although the SARS coronavirus can infect mice through their ACE2, they only develop mild symptoms. Equipped with the human ACE2, mice succumb to a lethal brain disease. This model helped evaluate potential SARS vaccines and treatments, and also teased out the impact of different immune responses.

But demand for the modified animals dwindled after the SARS outbreak subsided in 2003, and Perlman gave them to Jackson Laboratory (JAX), the mammoth nonprofit mouse supplier. It froze the animals' sperm, and since SARS-CoV-2 surfaced, has raced to breed the mouse again. "We've had over 1000 requests at this point," says Nadia Rosenthal, JAX's scientific director.

A Chinese team that also engineered mice to express the human ACE2 protein to study SARS kept some of the transgenic animals and has already infected them with SARS-CoV-2. They lost weight and showed signs of pneumonia but little else, Qin Chuan of Peking Medical Union College and colleagues reported in a preprint published on bioRxiv 28 February. "That's really very, very, very mild disease," Perlman says.

Perlman is waiting for JAX to supply the modified mice, but as a stopgap measure he stitched the human gene for ACE2 into an adenovirus, which he used to infect mice so that some of their lung cells made the receptor. When infected with SARS-CoV-2, the mice lost 20% of their weight—more than twice what Qin's team saw—but none died.

To create what Rosenthal calls a more "authentic" mouse model, researchers at JAX are using the genome editor CRISPR to change the sequence of the native mouse ACE2 so that the encoded protein is recognized by the virus. Sheahan, in collaboration with UNC's Ralph Baric, is instead tailoring the virus to the mouse, genetically tweaking its surface protein so that it can infect unaltered mice.

Other SARS-CoV-2 researchers are turning to rats. They are no more susceptible to COVID-19 than mice, but their larger size

is an advantage. "You often want to do repetitive bleeding in an experiment, and you can't do that with mice," says Prem Premsrirut of Mirimus, a company that is collaborating with an academic group to engineer a rat model by altering its ACE2 receptor. Vaccine studies, for example, often assess how different doses affect antibody responses over several days. Premsrirut notes that "most toxicology studies" of drugs also start in rats. "If you can study a drug directly in rats, you're a step ahead."

Ferrets are a mainstay of research on another respiratory disease, influenza, because the flu virus not only infects them, but produces symptoms that mimic the human disease. Infected ferrets even sneeze, readily spreading flu through the air. The animals may not prove as faithful a model for COVID-19, however. The virus does infect them and causes increases in body temperature, Young Ki Choi of Chungbuk National



Syrian hamsters are relatively easy to infect with the new coronavirus and develop mild, but easily detected, symptoms.

University and colleagues reported online on 6 April in *Cell Host & Microbe*. But it did not replicate to high levels and the ferrets didn't develop other symptoms.

The team did find evidence that ferrets might mimic one aspect of COVID-19: respiratory transmission. The animals they infected not only spread SARS-CoV-2 to cage mates, but to two of six ferrets in adjoining cages. Although researchers suspect SARS-CoV-2 primarily transmits through relatively large respiratory droplets that quickly fall to surfaces, this finding suggests finer particles, able to drift in the air for longer periods and over longer distances, can also carry infectious virus. "Aerosol infection is not as highly efficient as direct contact, but it's possible," concludes co-author Jae Jung of the University of Southern California.

The animals likely to carry the most weight in assessing potential drugs and vaccines are monkeys. Although they are expensive and difficult to handle, their close genetic rela-

tionship to humans often makes monkeys the gate keeper to clinical trials of drugs and vaccines. "This is going to be our near clinical model that we're going to rest heavily on," Roy says. Intense efforts to infect four different monkey species with SARS-CoV-2 began shortly after the isolation of the virus from people. "There's not been an emergent species that leads me to say, 'Oh wow, this is it,'" says Roy, who is testing African greens and rhesus macaques, and has looked closely at infection data from cynomolgus monkeys. (Marmosets are also being examined.)

In a Dutch study of eight cynomolgus monkeys inoculated with SARS-CoV-2, the four oldest ones developed higher levels of the virus in nose and throat swabs than younger animals. None developed symptomatic disease, but autopsies found some lung damage in two of four animals. "This looks like what you see in mild cases of humans," says Bart Haagmans from Erasmus University Medical Center, whose team published its data on 17 March on bioRxiv.

Monkey studies have also begun to explore questions about immune protection. Two rhesus monkeys that recovered from being infected with SARS-CoV-2 at Peking Union Medical College were resistant to reinfection 4 weeks later. The finding provides a hint of good news, as it suggests both natural infections and vaccine-triggered immunity will provide at least some subsequent protection.

Like ferrets, monkeys are being used to address the controversial issue of how much risk people face from aerosol transmission of SARS-CoV-2, which could inform debates about the value of homemade face masks. Roy and, separately, Douglas Reed at the University of Pittsburgh are staging experiments in air chambers that attempt to infect monkeys through this route. Humans who suffer from severe COVID-19 often have underlying diseases, such as hypertension or diabetes, and Roy says researchers may have to find or create monkeys with these comorbidities to develop the most meaningful model.

The list of animal models likely will grow rapidly. A study published online on 8 April by *Science*, for example, reported that the virus can infect cats. Autopsies showed the infection led to "massive" lesions in their nasal passages, trachea, and lungs.

Dave O'Connor of the University of Wisconsin, Madison, who is studying SARS-CoV-2 in cynomolgus monkeys, says the field will ultimately winnow down models. "It might turn out that some models are not really worth pursuing after we do this sort of foundational work, but I just don't think we're there yet. We need to let the data guide us." ■



Mauro Ferrari left the European Research Council on 7 April after its scientific council called for his ouster.

SCIENCE FUNDING

Top EU scientist ousted over plans for coronavirus research

European Research Council president resigns over spat about agency's role in guiding funding to specific fields

By **Nicholas Wallace**

Last week's noisy resignation of Mauro Ferrari as president of the €2.2 billion European Research Council (ERC)—the European Union's foremost funder of basic research—revealed a rift over its approach to research on the coronavirus pandemic. Ferrari's departure, just 3 months into the job, also showed the limits of an ERC president's power to influence the course of a funding agency that prides itself on its independence.

On 7 April, the same day Ferrari stepped down as ERC president and chair of its Scientific Council, he released a statement to the *Financial Times*, saying he had “lost faith in the system” and was upset by ERC's unwillingness to set up a “special program” to address the COVID-19 pandemic. But the next day, the 19 other members of the science council hit back. In a sharp statement, the council said Ferrari “displayed a complete lack of appreciation for the *raison d'être* of the ERC.” It also suggested that Ferrari had neglected his duties to attend to personal projects in the United States. It said the council unanimously called for his resignation on 27 March.

Although the European Union has allocated other R&D money for coronavirus research, ERC is required by EU law to exclusively support bottom-up basic research proposals without favoring particular fields. In mid-March, the science council rejected Ferrari's call for action on coronavirus research. Around that time, Ferrari was also discussing his ideas with European Commission President Ursula von der Leyen. For council member Michael Kramer, a director at the Max Planck Institute for Radio Astronomy, Ferrari seemed to be going behind the council's back. “When he started his initiative within the Commission, we were not told,” he says. It was “the last drip in the bucket.”

In an interview, Ferrari says he had no intention of violating the rule prohibiting specific research calls, but he believes ERC ought to be part of a coordinated research initiative on the virus, along with funders such as the European Innovation Council. “I was advocating a team approach,” Ferrari says.

Ferrari began the job in January as a relative outsider to EU politics. Born in Italy, he has spent most of his career working on nanomedicine in the United States, where he is a naturalized citizen. He headed the Hous-

ton Methodist Research Institute for 9 years before retiring in 2019.

The job of ERC president is a part-time, 180-day-a-year appointment. But science council members felt he was spending too much time on academic and commercial activities in the United States. Ferrari sits on the board of Arrowhead Pharmaceuticals, and is a part-time affiliate professor at the University of Washington, Seattle. He says his external activities were approved in advance by the Commission and argues his predecessors kept academic positions, too.

But Janet Thornton, an ERC vice president and former director of the European Bioinformatics Institute, says Ferrari skipped important meetings, including one on 26 February with Commission staff to discuss matters affecting ERC's autonomy and flexibility. “This particular meeting was a really important one,” she says. That evening, he gave a speech for a charity event at a London hospital whose chairman is a board member of BrYet, a biotech firm founded by Ferrari.

Ferrari says he had committed to the charity event much earlier, and that he did join the ERC meeting, by phone. He says no one ever told him his attendance or his other activities were a problem, and that he put in more work than his contract required. He denies that he was spending too much time in the United States, pointing to a house he bought in Brussels. “My wife now wants to kill me because we are leaving that house!”

Ferrari was one of three names recommended by an independent search committee to Carlos Moedas, the EU research commissioner at the time. Helga Nowotny, a former ERC president who served on the search committee, says Ferrari showed promise. After he was picked in May 2019, Ferrari came to talk with her about the job. “He was asking a lot of good questions,” she says. But, “He comes from the outside, and I think he thought that [ERC] is now his, like having a company.”

Some research leaders wonder why Ferrari didn't walk away from the job quietly. “I think he's harmed his reputation now by doing what he did,” says Anne Glover, head of the Royal Society of Edinburgh and the former EU chief science adviser. But Ferrari remains adamant that European science funders ought to be doing more about the pandemic. And he wasn't going to explain his departure with the cliché about wanting to spend more time with his family, he says. “Leaving with a flimsy excuse, when people are in the biggest crisis of a generation?” ■

Nicholas Wallace is a journalist in Brussels.

REMOTE SENSING

Ice monitor delivers a bonus: seafloor maps

Laser aboard NASA ICESat-2 satellite probes reefs and shallows near coastlines

By Paul Voosen

Late in 2018, just after its arrival in orbit, NASA's ICESat-2 satellite passed over an iconic site from the atomic age. By chance, its laser altimeter, used mostly to measure the changing height of polar ice, bounced light off the exposed rocks of Bikini Atoll in the South Pacific Ocean, home to 23 nuclear weapons tests. Then, mission scientists looked closer: To their surprise, the laser was also generating underwater reflections. "We were not just seeing the atoll," recalls Adrian Borsa, a geodesist at the Scripps Institution of Oceanography. "We were seeing this huge reef system underneath it."

Sparked by this discovery, last week mission scientists began to map the shallow sea floors that hug the world's coastlines. The satellite's green laser, penetrating up to 40 meters into the ocean, will generate bathymetric data that could be "game changing," especially for mapping coral reefs and monitoring their health, says Greg Asner, an ecologist at Arizona State University, Tempe.

ICESat-2 will fill a critical gap, says Christopher Parrish, a geographical engineer on the project from Oregon State University, Corvallis. It may be no surprise that much of the deep ocean remains unmapped, but sea floors less than 5 meters deep are also unexplored because they are off limits to ships and their sonar beams. That leaves what sailors call a "white ribbon" draped around coastlines on nautical charts. "It's just blank," Parrish says. "The fact that there's a term for it tells you how prevalent that data gap is."

ICESat-2 splits its laser to scan the globe along three parallel tracks, each one crossing every spot on Earth four times a year (*Science*, 14 September 2018, p. 1058). Its laser fires 10,000 times per second, and each shot generates up to 60 reflected photons detected by the satellite's telescope, says Tom Neumann, the mission's project scientist at NASA's Goddard Space Flight Center. "That's literally trillions of new elevation measures," he says. "The amount of data is mind boggling." The travel time of the photons reveals the surface height—and any changes—to within millimeters. Those abilities have

convinced the European Space Agency to adjust the orbit of its aging radar altimeter, CryoSat-2, in August, so its data can be compared with ICESat-2's more easily.

ICESat-2's engineers knew its green laser would delve deeper into the ocean than the infrared beam of its predecessor, ICESat. But they expected it to penetrate only 1 or 2 meters—not worth planning for. Then data started to come in that revealed far deeper reefs—not just near Bikini but also in St. Thomas and the Bahamas. "I would describe ICESat-2 as an accidental bathometer," Parrish says.



The coral reefs of Bikini Atoll can be mapped by a NASA satellite's green laser, which penetrates up to 40 meters underwater.

The new data will help with coastal navigation, and the Coast Guard and National Geospatial-Intelligence Agency have already expressed interest, says Lori Magruder, a remote sensing scientist at the University of Texas, Austin, who will lead the new bathymetry product. "There's also a rich opportunity to understand the before and after of natural disasters," she says, including how hurricanes reshape sediments. The data will also capture changes to major features of the shallows, such as mangrove roots or kelp forests, that could show whether they are succumbing to

invasive species and how their carbon storage capacity is changing as the climate warms.

But perhaps the biggest gain will be for coral reefs, says Asner, a leader of the Allen Coral Atlas, another mapping effort. Rising ocean temperatures are killing off corals worldwide, so identifying resilient species is important. Yet mapping them, from space or by drone or airplane, is expensive and challenging. "We don't know the geography of the living parts of coral reefs today, and we're unable to keep up," Asner says.

For the coral atlas, Asner and his colleagues are analyzing millions of images from satellite company Planet, looking for the green light reflecting off underwater objects. But different viewing angles and light conditions make it hard to compare images, and they struggle to capture underwater features deeper than 5 meters. "It's nice to know we can turn to ICESat-2 and use it for calibrating our work."

On its own, ICESat-2 will be able to say much about reefs. It could reveal a reef's slope and depth, indicators of the habitat it provides, and knobby textures that signal a more complex reef, with many intertwining coral species. Long term, ICESat-2 could measure which reefs are growing or receding, perhaps a sign that their corals have died. "You can compare the health of reefs across the globe," says Jenn Dijkstra, a marine ecologist at the University of New Hampshire, Durham.

Waves could limit the precision of those measurements, cautions Ved Chirayath, a remote sensing scientist at NASA's Ames Research Center. Chirayath developed FluidCam, which images the shallow sea floor using astronomical techniques to correct for wave distortions. The camera will be tested this month on a drone flight from New Mexico to Hawaii, and could end up mounted on the International Space Station.

While the ICESat-2 team continues to explore its unexpected capability, the coronavirus pandemic has opened a new avenue of research. Normally, active harbors and rivers are opaque to the space-borne laser because of sediment stirred up by boats. The global standstill has unveiled a new realm, Neumann says. "You can measure the canal depths of Venice from space." ■

PHOTO: THE ASAHI SHIMBUN/GETTY IMAGES



CALL FOR NOMINATIONS

AAAI Squirrel AI Award for Artificial Intelligence for the Benefit of Humanity

\$1,000,000 Prize

The AAAI Squirrel AI Award for Artificial Intelligence for the Benefit of Humanity recognizes positive impacts of artificial intelligence to protect, enhance, and improve human life in meaningful ways with long-lived effects. The award will be given for the first time in 2021.

The award will be given annually at the conference for the Association for the Advancement of Artificial Intelligence (AAAI) in February, and is accompanied by a prize of \$1,000,000 plus travel expenses to the conference.

Candidates may be individuals, groups, or organizations that are directly connected with the main contribution stated in the nomination. Qualifications and technical knowledge in artificial intelligence are not requirements for nominations. The emphasis is on the significance and impact of the work.

The award is administered by AAAI, with support from the European Artificial Intelligence Association (EurAI) and the Chinese Association for Artificial Intelligence (CAAI). Financial support for the award is provided by Squirrel AI.

DEADLINE for 2021 Award Nominations: May 24, 2020

<https://www.aaai.org/Awards/Squirrel-AI/>



THE HUNGER FORECAST

How a team of scientists studying drought helped build the world's leading famine prediction model

FEATURES

By Paul Voosen

The Indian Ocean seemed ready to hit Africa with a one-two punch. It was September 2019, and the waters off the Horn of Africa were ominously hot. Every few years, natural swings in the ocean can lead to such a warming, drastically altering weather on land—and setting the stage for flooding rains in East Africa. But at the same time, a second ocean shift was brewing. An unusually cold pool of water threatened to park itself south of Madagascar, leading to equally extreme, but opposite, weather farther south on the continent: drought.

Half a world away, at the Climate Hazards Center (CHC) of the University of California, Santa Barbara (UCSB), researchers took notice. Climate models, fed by the shifting ocean data, pointed to a troubling conclusion: By year's end, that cold pool would suppress evaporation that would otherwise fuel

rains across southern Africa. If the prediction held, rains would fizzle across southern Madagascar, Zambia, and Mozambique at the beginning of the growing season in January, the hungriest time of year. Zimbabwe, already crippled by inflation and food shortages, seemed particularly at risk. “We were looking at a really bad drought,” says Chris Funk, a CHC climate scientist. It was a warning of famine.

The CHC team, led by Funk and geographer Greg Husak, practice what they call “humanitarian earth system science.” Working with partners funded by the U.S. Agency for International Development (USAID), they have refined their forecasts over 20 years from basic weather monitoring to a sophisticated fusion of climate science, agronomy, and economics that can warn of drought and subsequent famines months before they arise. Their tools feed into planning at aid agencies around the world, including USAID, where they are the foundation of the agency's Famine Early Warning Systems Network (FEWS

NET), which guides the deployment of \$4 billion in annual food aid. Increasingly, African governments are adopting the tools to forecast their own vulnerabilities. “They’ve been absolutely key” to improving the speed and accuracy of drought prediction, says Inbal Becker-Reshef, a geographer at the University of Maryland, College Park, who coordinates a monthly effort to compare drought warnings for nations at risk of famine. “Every single group we work with is using their data.”

The forecasts are needed more than ever. From 2015 to 2019, the global number of people at risk of famine rose 80% to some 85 million—more than the population of Germany. Wars in Yemen, Syria, and Sudan are the biggest driver of the spike. Global warming, and the droughts and storms it encourages, also plays a role. The pace and severity of storms and droughts in Africa seem to be increasing, Funk says. “Both extremes are going to get more intense.”

The consequences of drought can be catastrophic, but it is hard to detect. Unlike tem-

PHOTO: JIKESAI NUIKIZANA/AFP VIA GETTY IMAGES



Models had predicted a drought that, by late January, was stunting the growth of maize in Zimbabwe.

perature, rainfall is spotty and local, heavily influenced by terrain. Three important clues that drought is coming—low accumulated rainfall, a lack of soil moisture, and high air temperatures—are difficult to measure from space. Satellites can see when green fields turn brown, but that often comes too late to inform a large-scale aid response. In Africa, researchers cannot rely on data from ground stations, either. Zimbabwe, for example, only has a few weather stations, and sometimes those don't even measure rainfall. This “reporting crisis” is pervasive across the continent; over the past 30 years, the number of stations with usable public data has dropped by 80% to only 600 or so.

Forecasting drought months into the future is even harder. Weather forecasts stretch out only a few weeks. Moving beyond that requires an understanding of large-scale climate patterns that influence weather over months or years. The banner example is the El Niño–Southern Oscillation, a pattern of winds and surface temperatures in

the tropical Pacific Ocean that shifts every few years, altering global weather in myriad ways. Weather in Africa is influenced by other oscillations, including the two Indian Ocean shifts CHC was watching, known as the Indian Ocean Dipole and the Subtropical Indian Ocean Dipole. But the “teleconnections” between the ocean and distant weather patterns are poorly understood, and aid agencies can be leery of relying on them for long-term drought predictions. They want evidence from real-time monitoring that drought is on the way.

The growing season in southern Africa was still months away when CHC noticed the signs of trouble—plenty of time for it and its partners, including a team of food security analysts in Washington, D.C., to refine their predictions and validate them with local observations.

The fieldwork would be led by Tamuka Magadzire, a CHC agroclimatologist based in Botswana whose analysis had shown that conditions in Zimbabwe were already ripe for famine: The previous harvest was weak, shriveled by the lowest rainfall since the early 1980s. The currency was essentially fictional, and the country's poorest had to devote 85% of their income to food. On visits in the past few years, Magadzire brought along maize for his friends and family. “It's just been really bad in terms of long dry spells,” he says.

A perfect storm was looming. Through the fall of 2019, Funk and his colleagues at FEWS NET sent a series of escalating warnings to senior officials at USAID. No one wanted to repeat what had happened a decade earlier, elsewhere in Africa. The group's forecasting record lent credibility to their warnings. But whether their call would be heeded this time would also depend on the strength of the evidence for an impending drought, political will in the United States and elsewhere—and a pandemic that had yet to rear its head.

CHC BEGAN with a dream. In 1995, Funk was a smart but directionless consultant working in Chicago for the credit card company Discover; he mined databases of personal information to identify consumers to target with ads. “It was, basically, working for the dark side,” he says. In the dream, he was standing with friends in Lake Michigan, smoking and drinking beer, when he felt the lake tug on his legs. Turning, he saw a tidal wave coming to inundate the city. But his first impulse was to rush to the office and buy stock options.

“This dream really freaked me out,” he says. “What kind of person sees the city is going to be destroyed and wants to sell options?” Funk, from an Indiana farm town, recalled how struck he was as a child by Live Aid, the 1985 charity concert for Ethiopia. He needed to make a change. He wanted to make a difference. He quit.

Funk wound up studying geography at UCSB in a group that focused on statistical climatology. He met Husak, another geography graduate student, and James Verdin, a visiting remote-sensing scientist from the U.S. Geological Survey (USGS). The three of them witnessed the record El Niño of 1997–98, in which warm waters from the western Pacific sloshed eastward toward Peru, triggering long-range atmospheric shifts that brought punishing rains to their California



Chris Funk found his calling with drought prediction at the Climate Hazards Center.

campus. El Niños also seemed to suppress rains in southern Africa, so Verdin, who now heads FEWS NET, worked with Funk to see whether greenness measures of maize fell in southern Africa during the 1997–98 event. “It was kind of mixed results,” Verdin says, “but we got it published.”

Verdin encouraged FEWS NET to sponsor Funk's and Husak's studies. By the time the next El Niño came, in 2002, the UCSB team had compiled scattered rainfall records dating back to 1961 to quantify how El Niño events dried up water resources across southern Africa. USAID used the resulting map and report to respond quickly after the 2002 El Niño, sending some \$300 million in food aid. It was the first time the agency incorporated climate forecasts into its food aid, Funk says, and it relieved some of the ensuing famine. “And we're still basically doing the same thing, better, smarter, faster.”

Funk went to work for USGS, but he remains affiliated with UCSB, where he serves as resident provocateur while Husak steers CHC's growing staff. Funk's churning mind keeps them busy, Husak says. “We lift up a lot of rocks and see what's going on underneath them.”

In the 2000s, one of those rocks led Funk back to Africa to study a different teleconnection. He and Alemu Asfaw Manni, a FEWS NET analyst in Ethiopia, gathered historical rainfall data across the country's highlands, where the soil is fertile but rain so scarce that some crops need months to germinate. Most climate models showed East Africa would get wetter with climate change.

But since the early 1990s, the team found, the highlands' long rainy season had gone into a steep decline. "This was a holy moly moment," Funk says. The trend, dubbed the "East African climate paradox," has held true to this day.

The explanation seems to lie in the ocean. Weather records indicated that many droughts in East Africa seemed to strike during strong La Niñas, El Niño's opposite number, when the western tropical Pacific heats up while the eastern Pacific cools. The UCSB team didn't understand the connection, but by August 2010, another La Niña was brewing in the Pacific. FEWS NET warned that rains across the Horn of Africa,

age of 5. As a damning U.N. report later put it: "The suffering played out like a drama without witnesses."

"It was really, really bad." Verdin sits in his austere, modern USAID office in Washington, D.C., reflecting on the Somali crisis, now nearly a decade ago. There were extenuating circumstances. Al-Shabaab, the Islamist militant group, was ascendant, and humanitarian groups feared that if their aid ended up in the wrong hands, the U.S. government might have prosecuted them, he says.

The famine warnings had been accurate—but they had also seemed insufficient. The UCSB team "didn't convey the information as

ing in satellite data. Since the late 1970s, a coalition of European countries has maintained geostationary weather satellites over Europe and Africa. Among other things, the satellites measure the temperature of clouds by the infrared light they emit. When the temperature of clouds high in the atmosphere drops below -38°C , it is likely raining lower down. By using this record to fill in rainfall between ground stations, CHIRPS assembled a continentwide rain database stretching back to 1980.

CHIRPS not only provides the historical data for climate researchers to study teleconnections, but it also collects the contemporary data for near-real-time monitoring of rainfall. "It's quite a step forward," says Felix Rembold, a drought forecaster at the European Union's Joint Research Centre. It's also in constant development: Pete Peterson, the CHC coding guru who has spearheaded CHIRPS, often woos local agencies to fill gaps in station coverage. For example, Ethiopia shares data from 50 government stations with CHC—even though its agricultural and meteorological agencies won't share their data with each other.

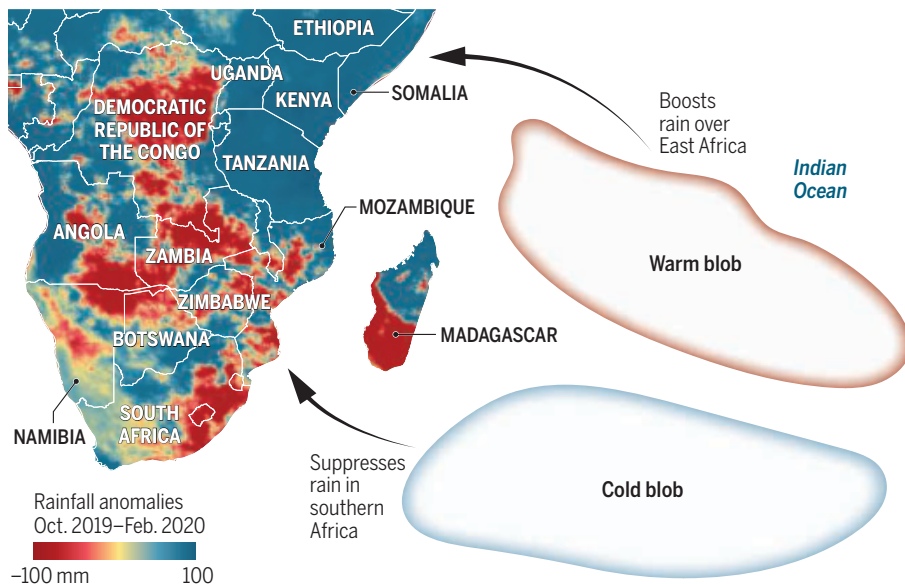
The data find their way back to Africa as CHC-affiliated field scientists train African agencies on using CHC products. For example, Kenya's Regional Centre for Mapping of Resources for Development has begun to serve up CHIRPS data to help local users forecast rains. Ideally, Funk and company hope to slip into the background, as Magadzire and his peers weave the CHC tools into the fabric of African drought response. Magadzire has had lucrative job offers, but the challenge is too compelling, he says. "My heart is in the improvement of conditions in Africa."

The long-term rainfall history in CHIRPS has enabled CHC researchers to refine their understanding of the La Niña teleconnection. By comparing global weather records and the predictions of climate models to the CHIRPS records, they have discovered the importance of the "western V," an arc of hot Pacific water that can appear during a La Niña event. Shaped like a less-than sign, it angles from Indonesia northeast toward Hawaii and southeast toward the Pitcairn Islands, and it forms as La Niña pens warm waters in the western Pacific.

It has far-reaching consequences. As water temperatures spike, energetic evaporation saturates low-level winds flowing west from the cool eastern Pacific. The moist winds dump their water over Indonesia—the wet get wetter. The winds, now high and dry, continue their march west across the Indian Ocean and drop down over East Africa, preventing the intrusion of nearby moist ocean air and breaking up rain clouds.

Double trouble

Two ocean climate patterns have aided predictions of floods and drought across Africa. A swing in the Indian Ocean Dipole pushed warm waters off East Africa, boosting rains there last winter. A shift in the Subtropical Indian Ocean Dipole left a cold pool south of Madagascar, suppressing rains across southern Africa.



including Ethiopia and Somalia, would be late, weak, and erratic.

Politicians and donors largely ignored the alarm. La Niña's threat was poorly understood, different aid groups were issuing disparate warnings, and a degree of crisis fatigue had set in about Somalia, which had been in turmoil for years. But over the next 9 months, the rains failed as predicted. Food prices tripled and malnutrition grew rampant.

In mid-2011, the United Nations finally declared a famine, and USAID ultimately delivered more than 300,000 tons of wheat, high-energy biscuits, and other staples. But the aid came too late and didn't reach enough people. Within the next year, the famine killed 260,000 people in Somalia alone. Half of them were children under the

effectively as we could," Funk says. The loss of weather stations meant their rainfall measures were getting worse, and most satellite-based estimates lacked the detail to show how dry specific crop-growing regions were getting. And their explanation of why La Niña was a threat seemed far too abstract. "You're asking somebody to open up their wallet and spend millions," Funk says. "They're not just going to do it because you say, 'Our standardized precipitation forecast is -1.2 .'"

THE FAMINE FORECASTERS needed better data. In 2015, those dreams came true when CHC released a tool called CHIRPS (which stands for Climate Hazards Center Infrared Precipitation with Station Data). It was the culmination of years of work compiling local rainfall records across Africa and fold-



Zimbabwe, crippled by inflation and weak harvests, needed food aid in 2019. This year could be far worse.

Global warming is strengthening these effects, causing them to linger even after a La Niña fades. And it appears that because of the ongoing ocean warming, they can happen without a La Niña at all, Funk says.

Armed with this new understanding, Funk in May 2016 found himself at USAID headquarters. A strong El Niño had just waned, and sea surface temperature trends suggested La Niña would follow. If it did form, he warned, FEWS NET's food analysts should prepare for sequential droughts in East Africa. A set of new seasonal climate forecasts from the National Oceanic and Atmospheric Administration echoed Funk's drought warnings. CHIRPS revealed that the October-December rains had failed. And, seeking to amplify their voices, FEWS NET and its peers at the United Nations and in Europe issued a joint alert, warning of potential famine.

By December of that year, food aid for half a million Somalis arrived. The next month, 1 million; by February 2017, 2 million. Thanks to the shipments and the many improvements East Africans had made in their own safety net, food prices didn't spike when the rains failed again. The warnings had worked.

FOUR YEARS LATER, a different teleconnection is playing out, but the picture across Africa is equally grim. In February, in a small UCSB conference room, CHC climate scientist Laura Harrison pulled up a map of Africa. Although there was no El Niño or La Niña to influence events, the two Indian Ocean oscillations she and her colleagues had been watching were going strong.

The blob of hot water off the coast of Somalia turned out to be as hot as it's ever been, a half-degree warmer than a similar state in 1997. CHC had been right to forecast extensive rains in the Horn of Africa: Moist winds from the blob fueled drenching storms. The resulting flooding and landslides ruined 73,000 hectares of crops and killed more than 350 people. The storms also saturated arid regions, feeding lush growth that lured an unpredicted hazard to the region: a locust invasion. Hundreds of billions of locusts have chewed through rich farmland in Ethiopia's Rift Valley, while stripping pastures in Kenya and Somalia.

The blob of cold water south of Madagascar was doing the opposite. Just as the team expected, it had dried up rains across southern Africa. On Harrison's screen, CHIRPS data showed a red blob of anomalous dryness across Zimbabwe—rainfall was running 80% below average for the season. Short-term forecasts called for some rain, but it looked like it would come too late, Harrison said. "The crop has failed in a lot of those areas."

On the phone from Botswana, Magadzire agreed. He had spent the day training people to use FEWS NET products, and his visiting Zimbabwean students reported lines for maize that lasted hours. To buy it, farmers were selling emaciated cows for a fraction of their value. "There is actually a huge shortage," he said. In a few days, after the team hashed out its evidence, he'd argue the same to the FEWS NET social scientists who would integrate the data with economic and security analysis.

At the end of the month, FEWS NET staff

compared their monitoring with that of their peers at the United Nations and Europe. The combined forecasts would go into the Crop Monitor for Early Warning, a monthly update provided by the University of Maryland that the G-20 group of rich nations began several years ago to unify famine warnings. Already, in response to previous reports, USAID had more than doubled its food aid to Zimbabwe, to \$86 million. But even this increase may not be enough.

On 2 April, FEWS NET sent out a rare alert, stating crisis conditions were likely in southern Africa from April to August. Maize supplies would be short, with prices 10 times their normal level. By that time, another danger had arrived: the coronavirus pandemic. The resulting lockdowns in Zimbabwe and its neighbors could exacerbate risks for the neediest, putting them out of work and unable to afford maize. By the end of this year, FEWS NET warned, Zimbabwe could find itself in emergency conditions—one step away from famine.

Reflecting on his time at CHC, Funk is proud of his team and how it has tried to lessen the toll of famines. But he is clear-eyed about a problem that isn't going away—and may be getting worse, for reasons other than natural cycles. For the past 5 years, during a time of global economic growth, famine threats were still rising, Funk points out. Now, the coronavirus pandemic has the world teetering on recession. He worries that climate change will only exacerbate the inevitable conflicts over stressed croplands. "At the end of the day," Funk says, "humanitarian crises are caused by humans." ■



DEEP DEFICIT

Droughts highlighted California's unsustainable use of groundwater. Now, the state is trying refill its aquifers

California's Central Valley—one of the richest agricultural regions in the world—is sinking. During a recent intense drought, from 2012 to 2016, parts of the valley sank as much as 60 centimeters per year. “It isn’t like an earthquake; it doesn’t happen, boom,” says Claudia Faunt, a hydrologist with the U.S. Geological Survey. But it is evidence of a slow-motion disaster, the result of the region’s insatiable thirst for groundwater.

For decades, farmers have relentlessly pumped groundwater to irrigate their crops, draining thick, water-bearing clay layers deep underground. As the clays compress, roads, bridges, and irrigation canals have cracked, causing extensive and expensive damage. In 2014, when NASA scientists flew radar equipment over the California Aqueduct, a critical piece of water infrastructure, they found that one section had dipped 20 centimeters

over 4 months. Such sagging can leave canals carrying less water—an “ultimate irony,” says Graham Fogg, a hydrogeologist at the University of California (UC), Davis, because they were built in part to slacken demand for groundwater. Excessive pumping also jeopardizes water quality, as pollutants accumulate within groundwater and the clays release arsenic. Worst of all, the persistent pumping means that, one day, aquifers might run out of usable water. “If you pump too hard,” Fogg says, “you’re playing with fire.”

Now, California has launched a landmark effort to save its groundwater. In 2014, deep in drought, the state passed a law to protect its aquifers; since then, local water managers have developed sustainability plans for those deemed the most imperiled. The plans for some particularly hard hit regions, just released

for public comment, call for ending the groundwater deficit mainly by allowing precipitation to refill aquifers, but also by curtailing demand. The state is funding scientists to gather better data on the crisis; researchers estimate that in the Central Valley, half of the aquifers are dangerously depleted, but they don’t know the extent of the damage. Meanwhile, geologists are working to identify the best places to replenish aquifers by flooding farm fields, including some with especially permeable geology.

Groundwater science is taking on a new urgency as California and other regions around the world face growing threats from drought—and are increasingly drilling wells to make up for missing rain and snow. Globally, aquifers are “highly stressed” in 17 countries that hold one-quarter of the world’s population, according to the World Resources Institute. Water and food supplies for billions of people are under threat.

By **Erik Stokstad**



California is a case study in the challenges of protecting those resources. Farm interests, which use the most groundwater, often resist limiting withdrawals, whereas environmentalists demand more water be returned to rivers and the Sacramento-San Joaquin delta; the first lawsuit challenging California's sustainability plans was filed last month. Demand for groundwater is growing where farms have expanded into areas with little surface water. Across the state, climate change is making precipitation less reliable. "A lot of people are looking to California to see how the law plays out," says Ellen Hanak of the Public Policy Institute of California (PPIC). The hope, she adds, is "there's just so much local innovation in California that it can be a model for folks elsewhere."

CALIFORNIA ONCE SERVED as a global model for another type of innovation: massive water projects. Los Angeles and other cities clamored for more water than they could get locally. The San Joaquin Valley in the southern Central Valley, the state's largest and most lucrative agricultural zone, had fertile soil and plenty of sunshine, but never enough water. Farmers had to make do with what nature provided—and what they could pump from the ground.

In the 1930s, the federal government began to build a network of dams, pipelines, and canals that moved water from the state's wetter north to farms in its semiarid south. Local projects sent water to urban centers. With the taps turned on, California's farms and cities flourished.

But the imported water didn't relieve the pressure on groundwater for long. Thanks to rural electrification, more farmers could pump as much as they wanted. There were no regulations, no limits. And pumps have become ever more powerful, with the best able to guzzle up to 5000 liters per minute from aquifers. Now, in a wet year, about 40% of the water used in the state comes out of the ground; during a drought, the proportion swells to 60%. In some farming areas, the dependence is even greater during dry years (see map, p. 232).

Rates of groundwater extraction are unsustainable in many parts of the state, says Jay Famiglietti, a hydrologist at the University of Saskatchewan. During wet years, enough water from rain and gushing streams sinks into the ground to partially refill aquifers, he says, but levels can fall even lower during the next drought. "It's like a tennis ball bouncing down the stairs, it's just going in one direction," Famiglietti says.

The trend became especially worrisome during the 2012–16 drought. In the San Joaquin Valley, deep irrigation wells lowered groundwater levels—already 250 meters below the surface in places—putting it out of reach of shallower wells that provided thousands of people with drinking water. Elsewhere, environmental groups feared that springs, streams, and rivers would run dry as groundwater levels fell.

In response, state legislators introduced proposals to regulate groundwater withdrawals. The bills were fiercely opposed by farm groups, which worried about declining land values. But the push gained mo-

Surface water moved by the California Aqueduct (left) hasn't ended overpumping of groundwater.

mentum from new satellite radar images that dramatically depicted the state's subsidence problems. "The images really drew attention to a system that's out of balance," says Rosemary Knight, a geophysicist at Stanford University.

Lawmakers were also alarmed by images of water loss (see p. 232) from NASA's Gravity Recovery and Climate Experiment (GRACE), which surveys surface and groundwater by measuring how its mass tugs on a pair of satellites. GRACE measurements, combined with other data, indicated that in 2010 Central Valley aquifers held 20 cubic kilometers less water than they had in 2003.

The Sustainable Groundwater Management Act, which became law in September 2014, was "an incredible step" for a state that had long resisted groundwater regulation, Famiglietti says. But it only requires California's some 260 groundwater sustainability agencies (new organizations set up under the law, often made up of local water districts) to stabilize, not to increase, groundwater levels. And it allows increased pumping if needed during drought, as long as no major problems result. Still, the law has forced a statewide rethink of groundwater policies. In January, the new agencies in 21 basins deemed critically overdrawn had to submit plans for achieving groundwater "sustainability" within 20 years. (Other agencies must submit their plans by 2022.)

The push to develop the plans has, in places, revealed an astounding lack of data. Many districts, for instance, aren't sure how much water is being removed from the ground because California doesn't require all pumps to have meters. (Local rules or court orders require metering in some basins to help resolve disputes.) In the absence of hard data, researchers have for years estimated flows by examining electricity records—groundwater pumps are energy hogs—and by mapping the extent and types of irrigated crops. Information on subsidence is also helpful. “It’s pretty amazing,” says hydrogeologist Andrew Fisher of

UC Santa Cruz. “We’re in a position now of not knowing what a lot of the big groundwater flows are or how they vary.”

REDUCING PRESSURE on groundwater isn’t easy or quick. One obvious tactic is to reduce demand. Some parts of California have lessened their reliance on groundwater by incentivizing efficiency and imposing requirements such as water-saving showerheads and toilets. Planting water-efficient crops helps—grapes and young almond trees use much less water than alfalfa, for example. So does leaving fields fallow, a strategy farmers have used to cope with past droughts.

But for some parts of California, such measures aren’t practical, in part because of a massive expansion of profitable vineyards and orchards—tree nut acreage alone increased 85% between 2008 and 2018. The groves and vineyards cannot be followed like other fields, although they can survive with less water than normal. And farmers are reluctant to rip them out, because they are expensive to plant, can take years to mature, and have relatively long life spans.

Still, researchers say truly protecting groundwater in California will require cutbacks in agriculture, which on average makes up about 80% of commercial and residential consumption. To stabilize groundwater in the San Joaquin Valley, farmers will likely have to reduce irrigated cropland by more than 200,000 hectares, or 10%, according to a 2019 report from PPIC. Not surprisingly, such prospects worry farmers across the state, says Chris Scheuring, a water lawyer with the California Farm Bureau Federation. “We are absolutely hoping for mitigated outcomes that get us to sustainable management without causing a lot of pain.”

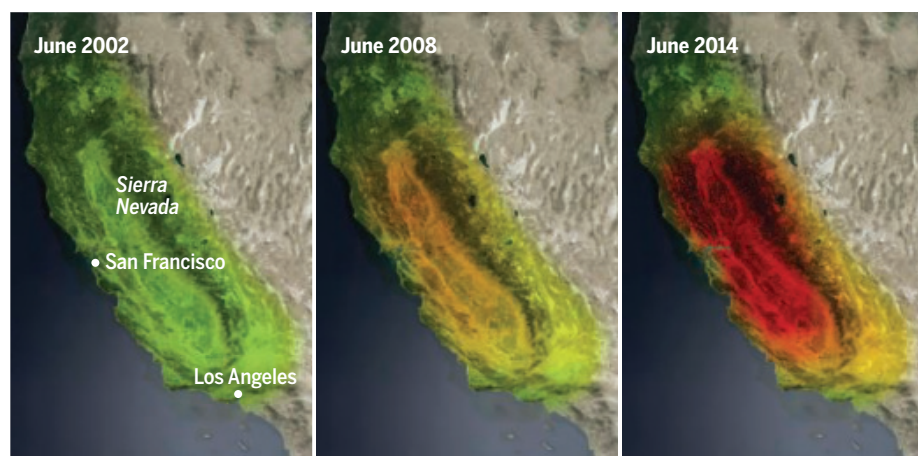
To slow the rate of depletion with less pain, a few districts are counting on proven methods for recharging aquifers. For decades, some water districts have filled dedicated ponds in wet years so that the water percolates into the ground. Others flood farm fields when water is plentiful. Vineyards can tolerate spring flooding, and some crops, like alfalfa, do well with flood irrigation. Building culverts and berms to move and hold the water can be expensive, however. In urban areas, where land is scarce or the upper layers of sediment or rock aren’t very permeable, officials pump water into the ground instead of removing it.

To expand such practices, researchers have been searching for areas ripe for recharge, based on factors such as soil type, land use, and aquifer geology. A UC Davis team identified 1.5 million promising hectares by reviewing existing data, they reported in *California Agriculture* in 2015. Some of the best places are valleys, now buried, that once existed in the Central Valley and were filled with coarse sediments during the last ice age. These sweet spots may be able to drain 60 times as much water as average sites, Fogg says. Researchers have discovered just three of these buried valleys, but Fogg says many others must exist given the region’s geological history.

Knight is using geophysical techniques to find such promising recharge areas. A helicopter-mounted instrument sends electromagnetic signals into the ground, measuring the electrical properties of bur-

California drying

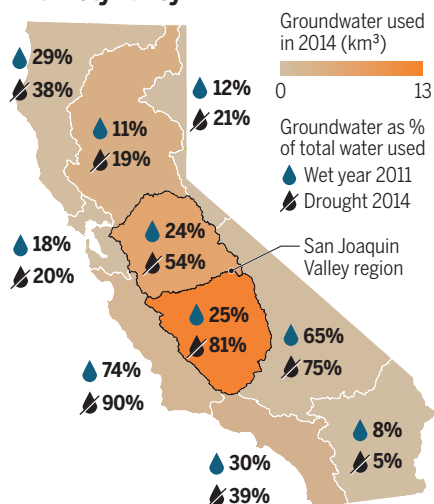
NASA’s GRACE satellites detect the gravitational pull of water masses in aquifers, reservoirs, and snowpack. In 2014, GRACE data showing water loss (below, red indicates loss) helped dramatize the draining of aquifers and galvanize state lawmakers to protect groundwater.



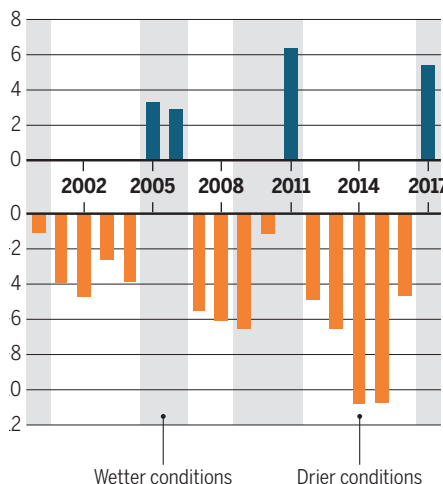
Tallying groundwater losses

California’s north receives abundant precipitation, so it relies less on groundwater during droughts than the drier farmland of the San Joaquin Valley to the south (left). In that valley, pumping has taken increasing amounts of groundwater (right), with withdrawals during dry years exceeding replenishment during wet years.

A thirsty valley



Subtraction outraces addition





When drought empties reservoirs, such as Lake Cachuma near Santa Barbara, California, in 2015, groundwater can become an even more important source of water.

ied sediment to create 3D maps of geologic formations that are as much as 300 meters deep. After that, smaller devices can be towed through fields or orchards for higher resolution images. The maps can help managers identify areas where water will quickly soak in—avoiding ponding that can lead to crop diseases or undermine trees.

The maps also show where water is most likely to reach deep layers where pumping is causing subsidence. “The level of complexity that we’re capturing is amazing,” Knight says. California’s water resources agency recently committed \$12 million to using the helicopter-mounted system in groundwater basins throughout the state.

RESTORING GROUNDWATER could become even more important because of climate change. The state has long relied on abundant mountain snow to provide a reliable, year-round source of surface water. Its many reservoirs were designed to fill with snowmelt by July, and then release the water to satisfy the peak demand during the hot summer. But because of a warming trend, the annual snowpack is already becoming thinner and melting sooner. And climate scientists predict more and more precipitation in California will fall as rain, rather than as snow in the mountains. All that means reservoirs will fill sooner and water will have to be released earlier in the spring, before it’s needed. In the summer, farmers would likely have to rely even more heavily on groundwater.

To adapt to that future, officials are pondering a new arrangement in which dam operators would release water ahead of rainstorms. That would make room for the storm water, and the discharge would allow downstream sites to put more into the ground. The idea sounds simple, but involves significant changes in regulations, operations, and in some cases infrastructure, Fogg says. Still, several pilot projects are underway. In the American River watershed, a flood control agency wants to retrofit some upper reservoirs. If the strategy is implemented there and in an adjacent Sierra Nevada river basin, Fogg and colleagues estimate about one-third of a cubic kilometer of water could be stored underground each year. That’s 10% to 25% of the annual statewide deficit, Fogg says.

Recharge water that comes from mountain reservoirs often has high quality. But a different source, stormwater runoff from urban or managed landscapes, could pose a problem: preventing contaminants—including farm fertilizers—from seeping into groundwater. Fisher has been studying ways to remove certain contaminants by adding biomatter such as wood mulch and almond shells to the soil at recharge sites. His team has found that the materials can promote the growth of microbes that remove nitrate, a common pollutant. “If we’re going to be putting hundreds of thousands or millions of acre feet of water in the ground every year, we should be taking every opportunity to make that water cleaner on the way in,” Fisher says.

Recharge isn’t the whole solution. In the San Joaquin Valley, scientists estimate recharge alone can eliminate, at best, just 25% of the groundwater deficit—in part because there is so little surface water to begin with in the region. So, any additional savings will likely have to come from reduced pumping, with its political challenges, as well as shifting water to the most productive croplands while leaving others uncultivated. That will require new canals and other infrastructure, and a new level of coordination. Across the state, multiple government and private entities will need to work together on managing supply and demand at the scale of entire basins, in order to minimize the economic cost of using less water. “There has to be policy innovation or financial innovation to get people to move away from this myth that we still have an unlimited groundwater supply and that we’re just never going to hit bottom,” Famiglietti says.

Bridget Scanlon, a hydrologist at the University of Texas, Austin, is optimistic that innovation will occur. “California has opportunities to move towards more sustainable management, and I think they are,” she says. Fogg is hopeful, too, but adds a cautious note. “Civilization has never been very successful at controlling water demand,” he notes.

Luckily, California’s recent winters have provided enough precipitation to allow aquifers to recover a bit. The state may not find out whether it learned the lessons of the last drought until the next one. ■



ENGINEERING AN EMPIRE

Ingenious water management helped the ancient Wari state expand throughout the Andes. Why couldn't it survive a drought?

By Lizzie Wade

When Wari colonists arrived in the Moquegua Valley of southern Peru some 1400 years ago, people already living there were likely nervous. The Wari state, with its capital city of Huari high in the Andes near what is now Ayacucho, Peru, had been expanding its reach. The Wari takeover was violent in places; the invaders sacrificed local people and displayed their heads as trophies.

But this time the Wari colonists did something unexpected. Rather than trying to seize the fertile valley floor, where people already lived, the newcomers occupied high, dry land that no one else had figured out how to use. They constructed their government and religious buildings on top of a high mesa, now called Cerro Baúl, and erected canals and aqueducts that carried water much farther than any previously attempted in the valley. They carved mountain slopes into agricultural terraces, which efficiently trapped and distributed water from rain and snowmelt to plots of maize, quinoa, and peppery berries called molle. People from several other regions moved to the new farms and towns, forming a powerful labor force that helped maintain the sprawling water infrastructure.

Remote Cerro Baúl is home to some of the best preserved Wari canals and terraces, but the remains of their sophisticated water infrastructure have been found in both the Wari heartland and in several of the state's many colonies, including around the Wari center of

Pikillacta near present-day Cuzco and in the Huamachuco region, more than 700 kilometers to the north of Huari. Such innovative hydraulic engineering enabled Wari—which some scholars argue was South America's first empire—to expand and thrive for some 400 years despite an often dry, drought-prone climate, recent studies suggest. (Archaeologists refer to this state as “Wari,” not “the Wari,” similar to the names of modern nations like Peru or France.) Wari

ancient civilizations, including the Classic Maya and the Old Kingdom of Egypt, appear to have collapsed in a time of drought. But how could drought have doomed Wari, a society that had been built on learning to take maximum advantage of limited water, and had seemingly even expanded through previous dry spells? To find an answer, researchers are trying to reconstruct two intricate, fragmented narratives—the human and the environmental—and weave them together. The history of climate “in the Andes is extremely complicated,” says Benjamin Vining, an environmental archaeologist at the University of Arkansas, Fayetteville. “And the only thing more complicated is human behavior.”

THE WARI HOMELAND around today's city of Ayacucho is dry, like much of Peru. It sits just 200 kilometers from the Pacific Ocean but nearly 3000 meters above sea level, nestled in the Andes, and the vast majority of precipitation in South America falls far to the east, over the Amazon rainforest. As a result, Peru's mountains and coast depend on rivers fed by mountaintop glaciers, plus what little precipitation falls. “That means water is one of the most valuable commodities,” Williams says.

Conditions in the Andes were at least as harsh around 600 C.E., when Wari was expanding beyond the Ayacucho region, recent and ongoing research suggests. Broxton Bird, a paleoclimatologist at Indiana University–Purdue University Indianapolis, is now analyzing a sediment core—drilled from Lake Pumacocha about 250 kilometers north of Ayacucho—that shows cool and relatively dry conditions between 475 and 725 C.E. Those data support evidence of aridity from another high-resolution re-



colonists and those who joined their community were able to “settle empty zones and make them productive,” says Donna Nash, an archaeologist at the University of North Carolina, Greensboro. Archaeologist Patrick Ryan Williams of the Field Museum calls the Wari strategy “conquest by hydraulic superiority.”

Those studying the Wari state's rise and fall, however, confront a puzzle. Its end, about 1000 years ago, appears to have coincided with a severe drought. Across history, the pattern might seem familiar; other



cord preserved in a mineral deposit (called a speleothem) from Huagapo Cave, also in the central Peruvian Andes, he says.

Such dry periods certainly stressed prehistoric communities—sometimes intensely, if they tipped into regional droughts. But for Wari, they also appear to have led to innovation, including new and better ways of storing, moving, and using precious water. Their canals were far longer and sturdier than any that came before, and although some other cultures had used agricultural terraces, Wari massively scaled up the technology and brought it to new regions. “In a moment of crisis, they came with the solution,” says Francesca Fernandini, an archaeologist at the Pontifical Catholic University of Peru (PUCP). Those technologies likely gave Wari colonists a strategic advantage—and a way to expand into new territories.

Wari’s expansion was not always peaceful, however. Wari art often depicts warriors, notes archaeologist Tiffany Tung of Vanderbilt University. And strontium isotopes preserved in trophy heads uncovered in the Wari heartland site of Conchopata show the victims grew up elsewhere, evidence that Wari warriors captured and sacrificed people from faraway lands, she says. People buried at Conchopata also show more head trauma than people buried in communities controlled by other Andean cultures that existed before and at the same time as Wari.

At first, the Moquegua valley seemed likely to yield signs of a violent Wari takeover. Cerro Baúl was essentially a border outpost, butting up against territory occupied by colonists

from Tiwanaku, another expansive Andean state that had its capital near Lake Titicaca in what is now northern Bolivia. But when researchers examined bodies from Tiwanaku cemeteries in the Moquegua area, they found that those buried after Wari colonists arrived showed no signs of increased violence. Instead, the valley’s peoples—Wari, Tiwanaku, and local Moquegua communities—appear to have coexisted for 400 years, from about 600 to 1000 C.E., each preserving its own style of pottery, architecture, temples, and burials.

Meanwhile, the Wari community, which Williams estimates numbered about 3000 people, pursued far more ambitious water projects than its neighbors. Whereas people living close to the valley floor typically dug 1- to 3-kilometer-long irrigation canals from the river to their low-lying fields, the Wari community built a 20-kilometer-long canal that snaked high up the mountain slopes and brought water to several settlements built along its path. The earth and gravel terraces on which the Wari farmed—an agricultural innovation independently developed in many hilly, water-stressed ecosystems—retained moisture around crop roots while allowing excess water to drain to the terraces below. Wari leaders living on and ruling from Cerro Baúl were “able to sculpt the landscape and put water where they wanted it,” Nash says.

That hydraulic infrastructure required an incredible amount of labor to build and maintain, Nash says. She has excavated in the agricultural settlement of Cerro Mejía, just 2 kilometers away from Cerro Baúl’s

elite civic and religious center. Based on the variety of domestic pottery and other material, she thinks people from four separate cultures came together under the Wari umbrella in Cerro Mejía, including some Moquegua locals and people from the coast. “I envision this as a multiethnic, pioneering frontier colony,” she says. Wari leaders appeared to be able to marshal them all “to perform huge amounts of labor,” Williams says.

Formal diplomacy, likely with Tiwanaku representatives, was probably conducted in the form of elite feasts in the palace atop Cerro Baúl, which also housed a brewery. The site is now littered with thousands of molle berries, used for making the typical Wari beer called *chicha de molle*. Tiwanaku-style jewelry found in the Wari palace, as well as a small Tiwanaku shrine tucked into Cerro Baúl’s Wari palace, suggest other ties, perhaps formed as elite Tiwanaku women married into the Wari power structure, Nash says.

For many centuries, the system appeared to sustain peace and social cohesion, even during hard times. Between 850 and 950 C.E., for example, excavations show that part of the Wari colony at Cerro Baúl suffered a devastating landslide that buried people, houses, and large swaths of farmland. “It was a massive disaster,” Nash says. “But when the Wari government was going strong, they could [cope with] things like this.” The terraces were soon rebuilt.

STILL, THE RECONSTRUCTION was flimsy, perhaps reflecting a rush to prevent starva-





tion immediately after the landslide. And in what may be an early sign that support for the Wari government had begun to crack, no one mobilized additional efforts to improve the new terraces. The community appears to have fractured even further by the time a new natural disaster hit: an extreme drought. Paleoclimate records like the core from Lake Pumacocha and the speleothem from Huagapo Cave show this drought was much more severe than the dry period at the beginning of Wari's expansion, Bird says.

By the time the drought reached the Moquegua valley in the 11th century, archaeological evidence suggests the Wari colony at Cerro Baúl was already weakened, Williams says. Around 900 C.E., after centuries of relatively separate coexistence, more Tiwanaku villagers started to move into Wari territory, as shown by the remains of Tiwanaku-style houses, ceramics, and cemeteries. Small Tiwanaku temples appeared on top of abandoned Wari agricultural fields, suggesting parts of the canal system were no longer functioning, which would have weakened the community's ability to cope when the drought arrived. Increasing factionalism and decreasing cooperation to maintain infrastructure "might mean this society is more vulnerable to even the beginnings of a changing climate," Williams says.

Around 1050 C.E., the administrative and religious Wari buildings on top of Cerro Baúl were abandoned, after what Williams calls an "end of times party." The revelers intentionally burned particular

rooms, including parts of the *chicha de molle* brewery, then scattered smashed drinking vessels on top, a common offering in Andean societies. Archaeologists can't be sure whether the elite Wari leaders of Cerro Baúl left the region entirely or blended into the new, smaller communities that sprang up in Wari's wake. The more middle-class residents of Cerro Mejía likely retreated into smaller towns located higher on mountain slopes, Nash says; these were easier to defend against attacks and nearer to short segments of the Wari canal that were still functioning.

Cerro Baúl wasn't the only Wari community in trouble around 1050 C.E. Across the Wari state, people appear to have abruptly abandoned settlements they had worked hard to build and maintain. Even the capital of Huari emptied out, with its residents likely moving closer to the coast, Tung says. It remains a mystery, however, whether the collapse of the Wari capital rippled out to weaken colonies like Cerro Baúl, or the colonies gave up first and ceased to send tribute and supplies back to the heartland, eroding the state from the outside in. In any case, Williams says, "The Cerro Baúl colony couldn't sustain itself without being part of the larger whole."

CERRO BAÚL'S STORY is adding to the increasingly nuanced view that scholars have of drought's role in the collapse of ancient societies around the world. Once, it was conventional wisdom that drought had toppled ancient civilizations such as the Maya. Now, scholars rarely see a lack of

Elite Wari colonists lived on top of high, dry Cerro Baúl (right). Their administrative center included a brewery for making *chicha de molle*, a beer drunk from decorative ceramic vessels (left).

water as the sole cause. Rather, they say, there is often a complex interplay between the social and natural environments. Sometimes, droughts simply drive wedges deep into existing cracks in political and economic systems.

In Cerro Baúl, for instance, it appears that Wari hydraulic expertise should have enabled the colony to cope with that final drought, Nash says. "But if the politics were bad, if their institutions were unraveling," then the community was vulnerable. "So, you don't blame the drought," she says. "You blame the government."

"The critical moment," says Luis Jaime Castillo, an archaeologist at PUCP, is not necessarily when canals run dry. It "is the moment when people lose confidence in the system."

Ironically, Wari engineering long outlasted the state itself. Beginning in the 1300s, the expanding Inca Empire repurposed Wari canals, roads, and agricultural terraces to feed and connect their far-flung territories. Some of the ancient terraces, with their Incan and Wari roots, are still in use today, Williams says. Indeed, he notes, terracing is being revived as a sustainable and hydraulically efficient way to farm in the Andes, as today's communities confront the ancient problem of drought, but now with a new face: human-caused climate change. ■

INSIGHTS

PERSPECTIVES

1573

1574

1575

1576

1577

CLIMATE

Anthropogenic megadrought

Human-driven climate warming worsens an otherwise moderate drought

By **David W. Stahle**

Historical documents from the Spanish Entrada on the northern frontier of New Spain (now the U.S. Southwest) include anecdotal evidence for unusual aridity in the late 16th century (1). However, a quantitative record of the 16th-century megadrought has only recently been obtained from hundreds of exactly dated and moisture-sensitive tree-ring chronologies developed across Canada, the United States, and Mexico. On page 314 of this issue, Williams *et al.* (2) provide a new assessment of proxy climate data from the U.S. Southwest. They determine that the 16th-century megadrought was the worst multi-decadal drought episode in the Southwest over the past 1200 years, and that the second-worst event occurred from 2000 to 2018 over southwestern North America (SWNA) and may be ongoing. The study also pinpoints substantial anthropogenic (human) contribution to the severity of the current drought.

The 16th-century megadrought affected much of North America but was most severe and sustained over the southwestern United States and northern Mexico. Williams *et al.* define megadrought precisely,

but in simpler terms, megadroughts are dry spells more severe and sustained than any witnessed during the 20th-century period of instrumental observations. The instrumental record for the United States shows that the droughts of the 1930s and 1950s were the most severe, widespread, and long-lasting soil-moisture droughts of the 20th century (3). The episode of dryness over the Southwest that commenced during the early 2000s has now eclipsed even the Dust Bowl (1930s) and southern Great Plains (1950s) droughts in duration and intensity (2).

The southwestern megadroughts of the medieval era caused fierce wildfires, ecosystem changes, and subsistence crises among ancient societies (4–6). Indeed, the disruption of agriculture and social order by intense drought appears to have dictated the cultural time horizons of southwestern prehistory (6). For example, the 16th-century megadrought is implicated in the abandonment of the Salinas Pueblos (New Mexico) and likely aggravated the indigenous hemorrhagic fevers that killed half of the native population of Mexico that remained after the Spanish conquest (7).

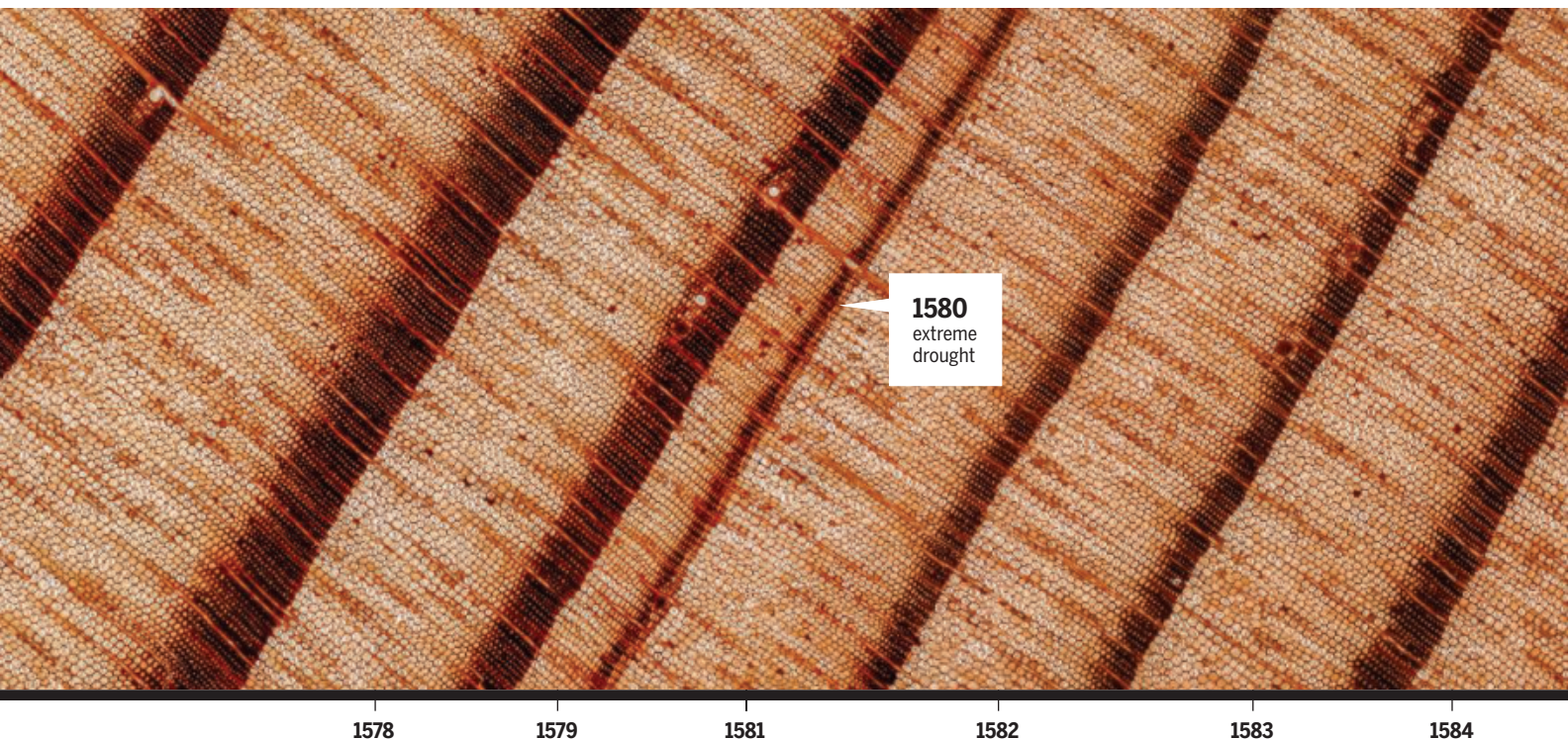
Scientists have not yet deciphered the climate boundary conditions or low-frequency

ocean-atmospheric dynamics capable of producing megadroughts. Nor do they understand why the frequent droughts of the medieval period abated over North America after 1600 CE, at least until very recently. Because megadroughts are rare events not represented in the modern instrumental record, proxy paleoclimate data and model simulations often are used to investigate these prolonged and widespread droughts.

Climate modeling experiments have revealed that stochastic atmospheric variability and land-surface feedbacks (the flux of energy and moisture from the surface) are sufficient to produce megadroughts in long simulations (8). These drought drivers must surely have played a role in some of the real-world decadal droughts of the past. Paleoclimate investigations also have identified forcing of southwestern megadroughts by persistent anomalies in tropical Pacific sea surface temperature (SST) and changes in radiation balance caused by increased solar activity, reduced volcanic activity, or both (9, 10).

In a noteworthy example of global-scale climate coherence, the 16th-century mega-

Department of Geosciences, University of Arkansas, Fayetteville, AR 72701, USA. Email: dstahle@uark.edu



drought over North America occurred simultaneously with a multidecadal pluvial in paleolake levels and gridded soil-moisture reconstructions for Australia and New Zealand. Such widely separated and opposing long-term moisture conditions are consistent with cold La Niña-like conditions in the El Niño–Southern Oscillation (ENSO): climate-altering, quasi-periodic variations in tropical Pacific SSTs (11).

The simultaneous co-occurrence of medieval megadroughts in the mid-latitudes of North and South America also has been reported (12) and is based on the Paleo Hydrodynamics Data Assimilation (PHYDA) reconstruction. This co-occurrence of decadal droughts over southwestern North America and Patagonia is statistically significant and is linked with prolonged La Niña-like SST anomalies across the tropical Pacific in the PHYDA reconstructions (12). Multidecadal modulation has been observed in instrumental measurements, proxies, and some models of the intensity, frequency, and large-scale teleconnection patterns of ENSO (13). The low-frequency activity of ENSO remains a leading candidate for the forcing of megadroughts over the Americas.

Williams *et al.* add anthropogenic forcing to the list of factors capable of transforming a garden-variety dry spell into a full-blown multiyear megadrought. The study combines hydrological modeling, new 1200-year tree-ring reconstructions of summer soil moisture, and a careful statistical evaluation of the issues that influence the uncertainty of comparison between modern and prehis-

toric droughts. The data demonstrate that the 2000–2018 SWNA drought was the second driest 19-year period since 800 CE. The derived reconstruction represents a nearly seamless evaluation of anthropogenic influence on soil moisture in the U.S. Southwest during the early 21st century, placed in the context of the past 1200 years. The sobering conclusion is that 47% of the severity in the current megadrought can be attributed to anthropogenic climate warming. In the absence of this anthropogenic contribution to warmer regional temperatures, the 2000–2018 interval would have been just another episode of reduced precipitation, low soil moisture, and poor tree growth in the U.S. Southwest during the past millennium. Instead, the artificially increased temperature, lower relative humidity, and rising vapor-pressure deficits have killed millions of western trees (14) and helped to make the early 21st century the second most severe and sustained period of megadrought in 1200 years.

Megadroughts cause sufficient environmental and socioeconomic hardship without the unwanted anthropogenic amplification documented by Williams and colleagues. Climate models predict that conditions might worsen by the mid-21st century, when average vapor-pressure deficits over the Southwest could be comparable to the most severe drought episodes of the past millennium (15). Meanwhile, declines in wildlife populations and the overappropriation of water resources might have made nature and society less resilient to heat waves, water shortages, and wildfires. Fortunately, reason-

This annual tree-ring sequence reveals reduced growth of a Douglas fir in California during the late 16th-century megadrought.

able policy options exist to begin muting anthropogenic climate change. These include a number of “no-regrets strategies” to promote energy efficiency and innovation, create jobs, grow investments, and help solve the energy and climate crises. ■

REFERENCES AND NOTES

1. S. White, *Clim. Past* **15**, 1809 (2019).
2. A. P. Williams *et al.*, *Science* **368**, 314 (2020).
3. K. M. Andreadis, E. A. Clark, A. W. Wood, A. F. Hamlet, D. P. Lettenmaier, *J. Hydrometeorol.* **6**, 985 (2005).
4. W. J. Calder, D. Parker, C. J. Stopka, G. Jiménez-Moreno, B. N. Shuman, *Proc. Natl. Acad. Sci. U.S.A.* **112**, 13261 (2015).
5. J. M. Vose, J. S. Clark, C. H. Luce, T. Patel-Weynand, *Effects of Drought on Forests and Rangelands in the United States: A Comprehensive Science Synthesis* (Forest Service Gen. Tech. Rep. WO-93b, U.S. Department of Agriculture, 2016).
6. R. K. Bocinsky, J. Rush, K. W. Kintigh, T. A. Kohler, *Sci. Adv.* **2**, e1501532 (2016).
7. R. Acuna-Soto, D. W. Stahle, M. D. Therrell, R. D. Griffin, M. K. Cleaveland, *FEMS Microbiol. Lett.* **240**, 1 (2004).
8. S. Stevenson, A. Timmermann, Y. Chikamoto, S. Langford, P. DiNezio, *J. Clim.* **28**, 1865 (2015).
9. B. I. Cook *et al.*, *Wiley Interdiscip. Rev. Clim. Change* **7**, 411 (2016).
10. N. J. Steiger *et al.*, *Sci. Adv.* **5**, eaax0087 (2019).
11. B. I. Cook *et al.*, *J. Geophys. Res. Atmos.* **123**, 11307 (2018).
12. N. J. Steiger, J. E. Smerdon, P. Williams, American Geophysical Union Fall Meeting, Abstract GC51A-07 (2019).
13. A. V. Fedorov, S. G. Philander, *Science* **288**, 1997 (2000).
14. M. L. Goulden, R. C. Bales, *Nat. Geosci.* **12**, 632 (2019).
15. A. P. Williams *et al.*, *Nat. Clim. Chang.* **3**, 292 (2013).

ACKNOWLEDGMENTS

I thank M. C. A. Torbenson, R. D. Griffin, S. Feng, and I. M. Howard. D.W.S.'s drought research is supported by NSF grants AGS-1266014, AGS-1501321, and AGS-1702894.

10.1126/science.abb6902

CANCER

Burning bridges in cancer genomes

Cytoskeletal forces break chromosomal fusions and trigger mutational avalanches

By **Jacob Paiano** and **André Nussenzweig**

Cancer is driven by mutations. A large fraction of mutations arise from unavoidable errors of DNA replication, which accumulate gradually over generations (1). Recent studies indicate that cancer genomes frequently harbor mutation signatures that result from chromothripsis. This is a sudden form of localized and massive chromosomal rearrangement, usually involving one or a few chromosomes. Chromothripsis is thought to arise through a single shattering event, after which tens to hundreds of chromosomal segments are joined in a random order and orientation. This one-off catastrophic event is common in cancer, with frequencies reaching 65% in certain cancer types (2). Until now, the mechanisms that explain this burst of mutagenesis remained largely unclear. On page 282 of this issue, Umbreit *et al.* (3) provide a unifying account of how extreme genome complexity is an outcome of a mutagenesis mechanism that involves aberrant DNA replication in human cells.

DNA replication and mitosis normally occur sequentially and in a mutually exclusive manner. However, when replicating cells are exposed to a mitotic cellular environment, this leads to “pulverization” of DNA, in which chromosomes are fragmented into many small shards (4). If only a limited number of chromosomal regions are incompletely replicated when cells enter mitosis, mitotic chromosome breakage can be beneficial. Underreplicated structures are sensed by a DNA repair salvage pathway in mitotic prophase that allows cells to complete their replicative cycle, minimizing chromosome missegregation (see the figure) (5). By contrast, concurrent breakage of many replication forks during chromothripsis is likely to be catastrophic unless checkpoints that survey DNA damage are impaired.

Previous studies have focused on aberrant nuclear structures that are seemingly not afforded the same checkpoint protections as the rest of the genome, such as micronuclei and chromosome bridges. These structures form after cells fail to properly segregate their chromosomes during mitosis. End-to-end fused chromosomes or failure-to-decatenate (unentwine) sister chromatids result in stretched DNA bridges that connect two primary nuclei, whereas missegregated DNA can be excluded from the daughter nucleus and form an adjacent micronucleus.

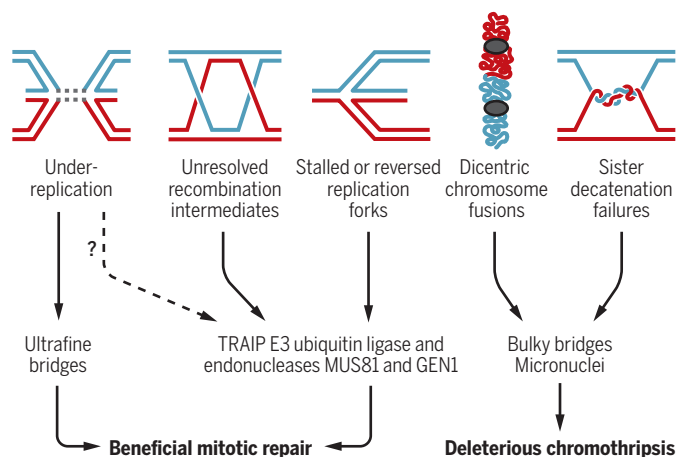
tion of chromosome bridges. Beginning with a single chromosome fusion event in cancer or immortalized human cell lines, they use an innovative approach of live-cell imaging and single-cell whole-genome sequencing to track both the cellular and genetic repercussions after generation of chromatin bridges that connect daughter cells. The authors find compelling evidence for bridge breakage driven largely by localized actomyosin cytoskeletal forces on the bridge rather than through TREX1-mediated cleavage. As the daughter cells progress through the cell cycle,

replication appears to be defective on the remaining broken-bridge DNA remnants or “stubs.” This is reminiscent of replication defects observed in micronuclei and is the first account of aberrant replication in bridges (6, 8). Moreover, the stub of the broken bridge acquires severe damage after progression into mitosis. Eventually, the DNA associated with the stub can be missegregated into a micronucleus and again accumulates DNA damage, as previously described (6, 9). Thus, the authors show, through long-term evolution experiments, that a single dicentric chromosome fusion event can trigger a cascade of mutations in the subsequent daughter cell divisions that foment genome instability and subclonal mutational heterogeneity.

The parallel pathways initiated within chromatin bridges and micronuclei that precipitate cancer-associated rearrangements provide insight into the mechanisms of replication-associated genome instability. Although further work is necessary to understand the causes of replication defects in bridges and micronuclei, the authors suggest that micronuclei and chromosome bridges share a common nuclear envelope defect (3, 8). This may impair import of numerous proteins, including those necessary for DNA replication. In addition to defective nuclear architecture, an altered chromatin state or histone composition within bridges and micronuclei may contribute to faulty replication and repair. Umbreit *et al.* find that a relatively small amount of DNA damage produced by focal

Resolving DNA damage in mitosis

To properly segregate sister chromatids, several pathways act early in mitosis to resolve structures and complete replication. Attempts to resolve chromosome fusions that yield dicentric chromosomes or failures in decatenation can generate bulky bridges and micronuclei, which trigger chromothripsis.



Defective and asynchronous replication has been observed in micronuclei, and incompletely replicated chromosomes from micronuclei are subject to chromosome fragmentation upon entry into mitosis (3, 6). However, whether bridges and micronuclei cause chromothripsis by similar or different mechanisms is unclear. An interesting model for how chromosome bridges are fragmented to generate chromothripsis was recently proposed. In this study, TREX1 (three-prime repair exonuclease 1) cytoplasmic exonuclease-mediated digestion of bridges after rupture of the primary nucleus was found to be the primary source of breakage that initiates chromothripsis (7).

Umbreit *et al.* provide additional insight into chromothripsis induced during resolu-

Laboratory of Genome Integrity, National Cancer Institute, National Institutes of Health, Bethesda, MD, USA.
Email: andre_nussenzweig@nih.gov

actomyosin forces on a bridge will result in localized mutational signatures. However, a second extensive wave of damage involving large stretches of DNA and massive fragmentation requires entry into mitosis.

Although the association between mitotic errors and tumorigenesis are strong, a detailed understanding of the events that promote genomic instability is still lacking. During the early stages of tumorigenesis, activated oncogenes produce replication stress that yields unprocessed replication structures and underreplicated regions that persist into mitosis. The structure-specific endonuclease SLX, crossover junction endonuclease MUS81, and flap endonuclease GEN1 complexes have been shown in a variety of contexts to cleave remaining replication structures in mitosis and have been linked to chromosome pulverization during premature mitotic activation (10). The E3 ubiquitin ligase TRAP1 has been recently shown in *Xenopus* egg extracts to facilitate the disassembly of replication forks to provide substrates for mitotic breakage and repair (11). Whether the mechanism of damage and repair during chromothripsis is similar to what has been observed in mitotic resolution during replication stress remains unclear, but the study of Umbreit *et al.* suggests that the role of mechanical forces should be considered when determining the modes of breakage. Further, their study raises the issue of what determines when mitotic pathways of resolution are helpful versus harmful for genome integrity (see the figure). Although this study models different routes that can lead to chromothripsis, these experiments were done in adherent tissue culture cells. Future experiments that study micronuclei, chromatin bridges, and cell migration in a densely packed tumor environment in vivo will undoubtedly provide further insights into the etiology of cancer. Ultimately, a better understanding of this complex problem may suggest ways to prevent mutations associated with chromothripsis. ■

REFERENCES AND NOTES

1. C. Tomasetti, B. Vogelstein, *Science* **347**, 78 (2015).
2. ICGC/TCGA Pan-Cancer Analysis of Whole Genomes Consortium, *Nature* **578**, 82 (2020).
3. N. T. Umbreit *et al.*, *Science* **368**, eaba0712 (2020).
4. R. T. Johnson, P. N. Rao, *Nature* **226**, 717 (1970).
5. S. Minocherhomji *et al.*, *Nature* **528**, 286 (2015).
6. K. Crasta *et al.*, *Nature* **482**, 53 (2012).
7. J. Maciejowski, Y. Li, N. Bosco, P. J. Campbell, T. de Lange, *Cell* **163**, 1641 (2015).
8. S. Liu *et al.*, *Nature* **561**, 551 (2018).
9. C.-Z. Zhang *et al.*, *Nature* **522**, 179 (2015).
10. S. C. West *et al.*, *Cold Spring Harb. Symp. Quant. Biol.* **80**, 103 (2015).
11. L. Deng *et al.*, *Mol. Cell* **73**, 915 (2019).

ACKNOWLEDGMENTS

The authors are supported by the Intramural Research Program of the National Cancer Institute.

10.1126/science.abb4899

METABOLISM

Probing metabolism in time and space

Mass spectrometry imaging detects hotspots of metabolite production within cells

By Theodore Alexandrov

The “metabolon” was proposed in 1985 to be a complex of metabolite-catalyzing enzymes that channel metabolites from one enzyme to the next, thus limiting their diffusion (1). Although the spatial collaboration of enzymes is an intuitive and appealing idea, the detection of metabolons within cells has been challenging. Most of the evidence has been indirectly obtained—for example, by using structural biology to model the interactions between enzymes or by using fluorescence microscopy to reveal the colocalization of metabolic enzymes within cells (2). However, the demonstration of a metabolon in action requires detection of the metabolites. On page 283 of this issue, Pareek *et al.* (3) fill this gap by demonstrating increased metabolic fluxes and by detecting hotspots of metabolites produced by the purinosome, a metabolon involved in the biosynthesis of purines. This provides direct experimental evidence of metabolons, as well as an approach to characterize their activity.

The metabolon concept gives metabolism a spatial construct, providing an additional

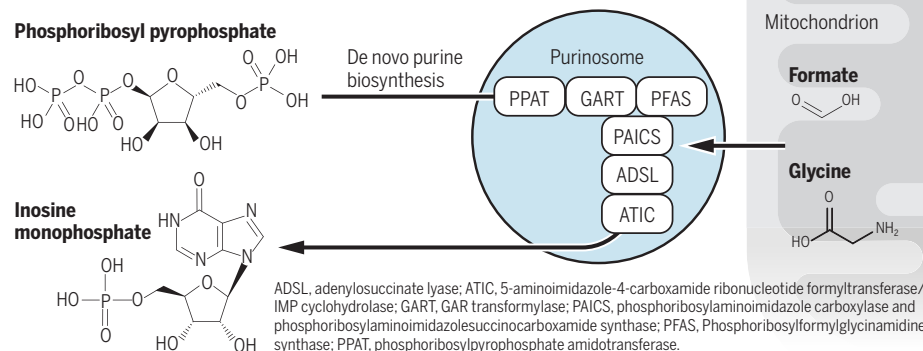
layer of spatial compartmentalization. Since the 1980s, despite multifaceted and long-standing interest, the metabolon has remained elusive because of its dynamic nature and weak interactions between the enzymes. Despite early successes of in vitro analyses, purification of multienzyme complexes from cells rendered unusable x-ray crystallography, the state-of-the-art approach to determine structures of proteins (2). In parallel, fluorescence microscopy provided an alternative approach to colocalize individual sequential enzymes within cells, particularly in response to a perturbation that stimulated the activity of the metabolon of interest (4). However, evidence for intracellular metabolite production by metabolons was missing.

Pareek *et al.* investigated the purinosome, a metabolon consisting of six enzymes, which, given the metabolite phosphoribosyl pyrophosphate, converts it into inosine monophosphate in sequential steps (see the figure). Inosine monophosphate is a key representative of purines, a class of small molecules with a broad range of critical functions, in particular serving as building blocks for DNA and RNA. The authors cultured human cells in purine-depleted media to stimulate the cells to increase de novo purine biosynthesis. They used flux analysis, a mass spectrometry method for temporal interrogation of known metabolic pathways that can be used to trace how isotopically labeled

Structural and Computational Biology Unit, European Molecular Biology Laboratory, Heidelberg, Germany, and Skaggs School of Pharmacy and Pharmaceutical Sciences, University of California, San Diego, La Jolla, CA, USA. Email: theodore.alexandrov@embl.de

The purinosome metabolon

The purinosome comprises six enzymes that channel metabolites to produce purines. Using the metabolite phosphoribosyl pyrophosphate, as well as formate and glycine from mitochondria, the purinosome synthesizes the purine inosine monophosphate.



substrates are transformed in the sequence of metabolic reactions (5). By quantifying metabolite fluxes, the authors showed that purine biosynthesis happens in a channeled (purinosome-assisted) manner. By tracing the metabolites formate and glycine provided by mitochondria and consumed by the purinosome, they confirmed that mitochondria-proximal purinosomes are actively involved in purine synthesis. In addition, Pareek *et al.* used mass spectrometry imaging, a method that is able to detect metabolites in tissues and cells at subcellular resolution (6). They detected, in single cells, multiple micrometer-size hotspots of high concentrations of key intermediates and products of purine biosynthesis. Overall, their results provide important insight into the activity of purinosomes and the proximity of active purinosomes with mitochondria, as well as demonstrate the activity and “metabolic output” of individual purinosomes.

The study of Pareek *et al.* also represents a milestone in mass spectrometry imaging-based spatial metabolomics. As a result of vast experimental and computational developments over the past two decades (7), this technology has matured and promises to reveal spatial aspects of metabolism in biology and medicine. Applications include the characterization of metabolic roles of individual cells, treatment response prediction, and support of intraoperative diagnostics. However, only recently was submicrometer resolution demonstrated for the detection of small molecules with this technology (8–10). In this context, the work of Pareek *et al.* stands out as a cutting-edge example of how mass spectrometry imaging can help to address long-standing biological questions by providing a previously inconceivable capacity for detecting metabolites and activity of metabolic pathways with subcellular resolution.

Much remains to be discovered about purinosomes and other metabolons, their function, and their link to other cellular compartments and programs. In particular, the spatially resolved detection of metabolites, protein complexes, and organelles in the same field of view is out of reach. Correlative fluorescence microscopy and subcellular mass spectrometry imaging will be essential to achieve this. By demonstrating the activity of purinosomes in situ, the work of Pareek *et al.* raises further questions. What makes the metabolic enzymes in a metabolon come together? The enzymes of the dhurrin metabolon in plants, for example, were shown to be assembled by incorporating them into the endoplasmic reticulum membrane (11). However, it is still not clear what regulates the formation of metabolons in the cytoplasm (such as purinosomes), their observed assembly around molecular scaffolds, and

localization at the periphery of cellular membranes. One hypothesis suggests that liquid-liquid demixing (phase separation) processes may be involved (12). Given that mitochondria are highly dynamic organelles that constantly fuse and divide, it will be interesting to understand how the proximity of active purinosomes to mitochondria is achieved.

It may now also be possible to assess how many different metabolons exist. Besides the known metabolic pathways (2), perhaps metabolons for unknown or poorly characterized metabolic pathways will be found. Mass spectrometry, cryo-electron microscopy (cryo-EM), and computational methods can drive discovery, as recently illustrated by the observation of a metabolon containing fatty acid synthase and carboxylase in the fungus *Chaetomium thermophilum* (13). Once there is a better understanding of metabolons in homeostasis, the development of metabolon therapies that target remodeled metabolism in diseases such as cancer and diabetes, as well as in inflammation and autoimmunity, may be feasible.

There is an increasing role for cutting-edge technologies in the discovery and characterization of metabolons in cells and, eventually, in tissues. Such emerging technologies will need to be integrated with fluorescence microscopy to colocalize enzymes in real time and to assess their proximity to relevant organelles. Cryo-EM and in situ structural biology will enable visualization of complexes in cells, thus avoiding detrimental purification. Computational modeling will help researchers to investigate the potential of enzymes for metabolite channeling (14). And, following the path paved by Pareek *et al.*, metabolomics, flux analysis, and mass spectrometry imaging will likely continue to play key roles in characterizing the activity of metabolons (15), especially given the rapid development of these technologies and their ongoing use to probe metabolism in time and space. ■

REFERENCES AND NOTES

1. P. A. Srere, *Trends Biochem. Sci.* **10**, 109 (1985).
2. D. L. Schmitt, S. An, *Biochemistry* **56**, 3184 (2017).
3. V. Pareek *et al.*, *Science* **368**, 283 (2020).
4. A. M. Pedley, S. J. Benkovic, *Trends Biochem. Sci.* **42**, 141 (2017).
5. C. Jang *et al.*, *Cell* **173**, 822 (2018).
6. I. S. Gilmore *et al.*, *Annu. Rev. Anal. Chem.* **12**, 201 (2019).
7. T. Alexandrov, *Annu. Rev. Biomed. Data Sci.* **3**, 10.1146/annurev-biomedata-011420-031537 (2020).
8. N. Winograd, *Annu. Rev. Anal. Chem.* **11**, 29 (2018).
9. J. Decelle *et al.*, *Trends Cell Biol.* **30**, 173 (2020).
10. M. Niehaus *et al.*, *Nat. Methods* **16**, 925 (2019).
11. T. Laursen *et al.*, *Science* **354**, 890 (2016).
12. P. L. Kastiris, A. C. Gavin, *Essays Biochem.* **62**, 501 (2018).
13. P. L. Kastiris *et al.*, *Mol. Syst. Biol.* **13**, 936 (2017).
14. F. Wu, S. Minter, *Angew. Chem. Int. Ed.* **54**, 1851 (2015).
15. T. Obata, *Curr. Opin. Biotechnol.* **64**, 55 (2020).

ACKNOWLEDGMENTS

The author is funded by European Research Council grant 773089.

CATALYSIS

Light expands a catalyst's repertoire

Visible light helps a Pd carbonylation catalyst both break and make carbon-halogen bonds

By Prasad Kathe and Ivana Fleischer

Carbonyl groups are present in many synthetic targets, which necessitates the development of robust and efficient methods for their synthesis. One of the most elegant and atom-economic approaches is carbonylation, the transformation of organohalides RX (where X is halide and R an organic chain) with carbon monoxide (CO) in the presence of a nucleophile (1). This reaction generates a carbon-carbon and a carbon-

“This approach enabled the reaction of two challenging substrates at room temperature.”

heteroatom bond from readily available precursors in a single step by using metal complexes as catalysts. Despite its tremendous success, even at industrial scales, the substrate scope of classical carbonylation is severely limited—a problem that cannot be addressed by conventional manipulation of the catalyst. On page 318 of this issue, Torres *et al.* (2) report a solution by activating the palladium-based catalyst with visible light, thus changing the course of the catalytic cycle, which allows challenging substrates to be converted under mild reaction conditions.

The elemental catalytic steps of a typical carbonylation are reaction of the metal with the electrophile (oxidative addition); insertion of CO; coordination of the nucleophile; and finally, reductive elimina-

tion, which furnishes the product and the catalyst. The limitations of carbonylation chemistry for some substrates are connected to these steps, especially the first one, when the substrate bond is cleaved, and the last one, in which the product is formed. The reactivity of the metal center can be typically modulated by the choice of spectator ligands by varying their electronic and steric properties. For example, in oxidative addition, the metal provides two electrons to the substrate and is oxidized. Therefore, electron-donating ligands can enable this process (3). The reductive elimination is the opposite reaction, as the metal is being reduced by accepting electrons. Given these opposing effects, it is difficult to design a catalyst that would facilitate both steps. Indeed, all attempts to develop catalysts for challenging carbonylations have focused on just one of the catalytic steps.

Oxidative addition is favored for substrates with weak C-X bonds (for example, aryl iodides). The more challenging compounds, such as alkyl halides, do not undergo this step easily and they exhibit an increased tendency for the occurrence of unwanted side reactions. Alkyl halides have been successfully used in carbonylations by employing electron-rich catalysts (4) or ultraviolet light activation (5), but only with strong nucleophiles, such as alcohols.

Reductive elimination is problematic for weakly coordinating nucleophilic reaction partners, such as sterically hindered nucleophiles or chlorides. The use of chlorides is of particular interest, because carbonylation affords acyl chlorides, which can be easily converted to a broad range of carboxylic acid derivatives. It was shown that sterically hindered catalysts are needed to promote this reaction, but only in connection with high-temperature reaction conditions and electrophilic substrates that readily undergo oxidative addition (6).

To date, there have been no reported approaches addressing both challenging steps and thus both substrates at the same time, which has tremendously restricted the possible carbonylation targets. The elegant solution offered by the approach of Torres *et al.* is based on the application of visible-light irradiation as an external tool to modify catalyst properties (see the figure). Irradiation can excite the complex if light is absorbed in the corresponding wavelength region or in the presence of the photocata-

Lighting up catalytic carbonylation

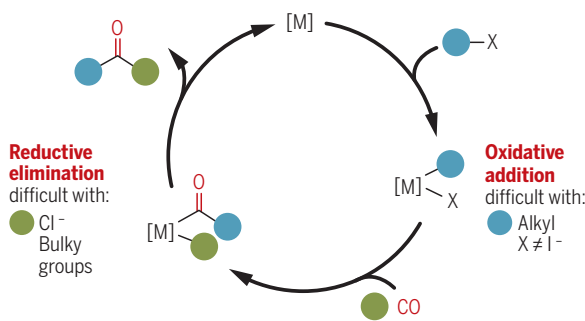
Developing better catalysts for adding carbon monoxide to challenging substrates is difficult because oxidative addition and reductive elimination oppose each other. Torres *et al.* show that light-driven catalysts can activate difficult substrates through radical intermediates.

Classical carbonylation

For alkyl halides (alkyl, blue; halide, X), the initial oxidative addition step with catalyst [M] is difficult, as is the reductive elimination step if the nucleophile (green) is sterically hindered or a chloride.

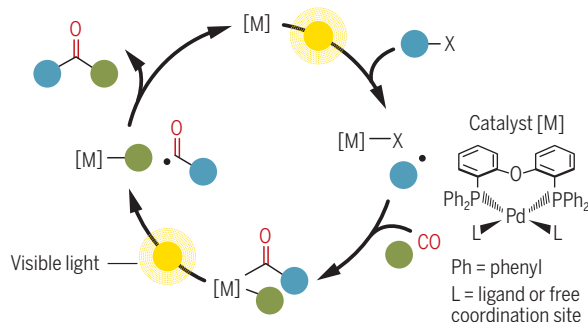
Valuable carbonyl functionality

- target in natural compounds
- synthetic intermediates



Light-driven carbonylation

Visible-light irradiation of catalytic species in a carbonylation reaction drives two difficult elemental steps as single-electron transfers to give radical intermediates and thus expands the substrate scope.



lyst. Although metal catalysts have been irradiated before, the influence on only a single catalytic step was observed (7, 8).

In the present study, an unprecedented effect on catalysis was observed. The visible light was able to excite both catalytic intermediates responsible for the decisive steps of oxidative addition and reductive elimination. In this process, the mechanistic course of these steps is changed from two-electron redox events to single-electron transfer (SET) steps that produce radical species (9). This approach enabled the reaction of two challenging substrates at room temperature.

The catalyst design is relatively simple: a combination of a palladium (II) precursor and the commercially available bidentate DPEphos ligand, bis[(2-diphenylphosphino)phenyl]ether (10). By applying a low pressure of CO (4 atm) and in the presence of a base and a chloride source, a range of aryl and alkyl bromides and iodides were successfully

converted to acyl chlorides. It was also shown that either in the presence of a second nucleophile or by adding the nucleophile in a second step in the same vessel, various esters, amides, and thioesters could be accessed. Torres *et al.* were able to use nucleophiles that could not be employed in classic carbonylation chemistry, which opened up interesting applications.

The study was accompanied by detailed mechanistic investigations that provided strong evidence that both steps occur through one-electron chemistry. The authors suggest that when the catalyst resting state (DPEphos)Pd(CO)₂ is irradiated in the presence of the electrophile, a SET occurs, generating a Pd(I) species and the corresponding aryl or alkyl radical. These species undergo a coupling that features the insertion of CO to complete the oxidative addition induced by the low-barrier radical (7). After a ligand exchange against chloride, the catalytic intermediate is irradiated again, and an unprecedented radical-induced reductive elimination occurs, possibly through acyl radicals.

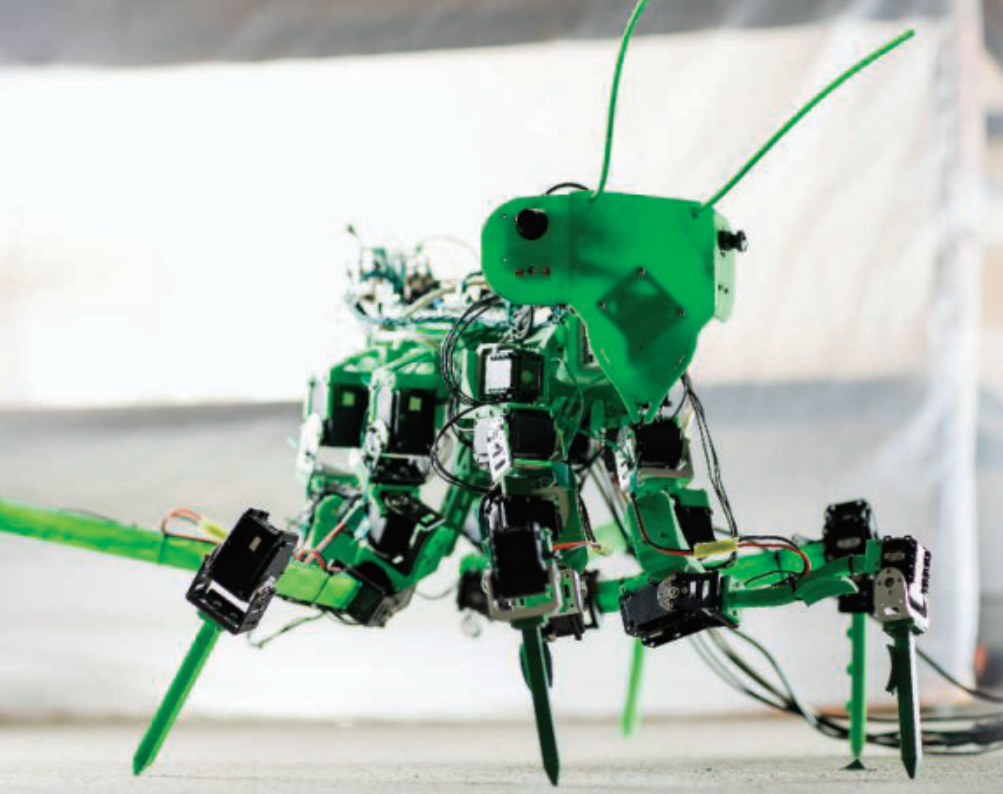
The simple and inspired synthetic tool provided by Torres *et al.* holds great potential for broader use in homogeneous catalysis. Especially given that it is possible to change the course of the oxidative addition and reductive elimination within the same catalytic cycle, this approach may lead to

many applications and even to discovery of new reactions. Studies on structure-activity relations of the catalyst could unravel finer details about the underlying mechanism and also provide possibilities to tune the catalysts for other applications. ■

REFERENCES AND NOTES

1. M. Beller, X. F. Wu, *Transition Metal Catalyzed Carbonylation Reactions: Carbonylative Activation of C-X Bonds*, (2014), pp. 1-228.
2. G. M. Torres, Y. Liu, B. A. Arndtsen, *Science* **368**, 318 (2020).
3. J. A. Labinger, *Organometallics* **34**, 4784 (2015).
4. B. T. Sargent, E. J. Alexanian, *J. Am. Chem. Soc.* **138**, 7520 (2016).
5. T. Fukuyama, S. Nishitani, T. Inouye, K. Morimoto, I. Ryu, *Org. Lett.* **8**, 1383 (2006).
6. J. S. Quesnel, B. A. Arndtsen, *J. Am. Chem. Soc.* **135**, 16841 (2013).
7. S. Roslin, L. R. Odell, *Chem. Commun.* **53**, 6895 (2017).
8. P. Chuentragool *et al.*, *Angew. Chem. Int. Ed.* **58**, 1794 (2019).
9. S. Zhao, N. P. Mankad, *Catal. Sci. Technol.* **9**, 3603 (2019).
10. M. Kranenburg *et al.*, *Organometallics* **14**, 3081 (1995).

10.1126/science.abb2104



Mantisbot (6) models the neural circuits of the praying mantis for target tracking.

NEUROSCIENCE

Robots with insect brains

A literal approach to mechanistic explanation provides insight in neuroscience

By **Barbara Webb**

It is an engineer's dream to build a robot as competent as an insect at locomotion, directed action, navigation, and survival in complex conditions. But as well as studying insects to improve robotics, in parallel, robot implementations have played a useful role in evaluating mechanistic explanations of insect behavior, testing hypotheses by embedding them in real-world machines. The wealth and depth of data coming from insect neuroscience hold the tantalizing possibility of building complete insect brain models. Robotics has a role to play in maintaining a focus on functional understanding—what do the neural circuits need to compute to support successful behavior?

Insect brains have been described as “minute structures controlling complex behaviors” (1): Compare the number of neurons in the fruit fly brain (~135,000) to that in the mouse (70 million) or human (86 billion). Insect brain structures and circuits evolved independently to solve many of the same problems faced by vertebrate brains (or a

robot's control program). Despite the vast range of insect body types, behaviors, habitats, and lifestyles, there are many surprising consistencies across species in brain organization, suggesting that these might be effective, efficient, and general-purpose solutions.

Unraveling these circuits combines many disciplines, including painstaking neuroanatomical and neurophysiological analysis of the components and their connectivity. An important recent advance is the development of neurogenetic methods that provide precise control over the activity of individual neurons in freely behaving animals. However, the ultimate test of mechanistic understanding is the ability to build a machine that replicates the function. Computer models let researchers copy the brain's processes, and robots allow these models to be tested in real bodies interacting with real environments (2). The following examples illustrate how this approach is being used to explore increasingly sophisticated control problems, including predictive tracking, body coordination, navigation, and learning.

The visual target tracking of dragonflies has been replicated on a (wheeled) robot platform performing active pursuit (3), giving new insight into the neural mecha-

nisms. The starting point was neurophysiological characterization of the responses of small target motion detector (STMD) neurons in the dragonfly brain. These show a distinctive facilitation profile, that is, a slow buildup of activity to targets that move on consistent trajectories in the visual field. A computational neural model incorporating such facilitation properties was shown to improve tracking performance in the presence of clutter and distractors, even outperforming state-of-the-art computer vision algorithms (4). The implementation on the robot involved insect-like early visual processing, including resolution, spectral sensitivity, and temporal and spatial high-pass filtering such that the receptors respond most to rapid changes in the stimulus. The passage of fast-moving small objects against the background can be detected from a local rise followed by a fall (or vice versa) in intensity of receptor activation. In a retinotopic array of STMDs (as a neural map), center-surround inhibition and a winner-take-all process (suppressing all but the strongest signal) select a single target position, and its direction and rate of motion are used to facilitate the activation of model STMDs in the predicted future location. The facilitation enhances pursuit and may explain selective attention responses observed in downstream neurons (5).

When the robot makes a quick movement (a saccade) to visually pursue the target, this will change the relative position of the target in the visual field (e.g., to keep it centered). Hence the position in the neural map to which the facilitation should be propagated depends not only on the target's motion but on the robot's (or dragonfly's) own motion. This means that the target pursuit system must receive some information about the motor command. In addition, the implementation on a robot demonstrated the robustness of the model to challenges such as changing illumination and unexpected motor disturbance (bumps). It also confirmed that the optimal time constant for facilitation depends on the specific circumstances (target velocity and background clutter), suggesting that STMD neurons should exhibit dynamic modulation of facilitation. The neural model on the robot thus allowed neural data that had been collected from an immobilized insect to be understood in the context of continuous behavioral control in natural conditions, predicting that further experiments should reveal inputs from motor systems and dynamic modulation of the STMD response.

School of Informatics, University of Edinburgh, Edinburgh, UK. Email: b.webb@ed.ac.uk

Insect target tracking behavior has also been examined in the praying-mantis-inspired “mantisbot” (6). Here the focus is on how the detected position of a visual target can be translated into the complex coordination of head, body, and leg joints in a hexapod to make a successful orienting movement. The solution implemented on the robot exploits a detailed, distributed leg control network based on local reflexes [also used to model walking control for the stick insect (7)] that can be modulated by relatively simple high-level signals to alter the stepping motion toward a given target direction. The same network can also, through a simple switch, be used to control posture changes instead of walking, corresponding to the animal tracking the target with its head and body only. The tuning of the network in the mantisbot was based on (robotic) methods of inverse kinematics, in which the geometric relation of joint angles to the end-of-limb position is used to derive, inversely, for a desired end-of-limb position, the required values for joint angles. This method allowed a deterministic setting of the synaptic values in the model that would have been set by evolution in the animal.

The mantisbot controller demonstrated that descending information from the insect brain to motor circuits can be in the simple form of a desired vector of motion. Additionally, it showed that it is crucial even for simple saccades that the brain maintains a short-term memory of the position of the prey. Other insect behaviors require more sophisticated directional memory, such as the ability of ants, bees, and wasps to maintain an estimate of their home location during long and convoluted foraging excursions, by continuous integration of their velocity (path integration). The underlying neural circuitry for this advanced spatial capacity has been unraveled (8). The insect central complex (CX) receives celestial compass inputs (9) and encodes heading direction relative to visual targets and self-motion (10). Identified neurons that have the required connectivity to combine this information with the speed (estimated from the motion of the visual surrounding) could form the basis of a distributed vector memory, constantly updated to reflect the geocentric location of the animal relative to its starting point (8). Moreover, the precise and highly regular connectivity pattern between these neurons and specific output neurons of the CX provides a mechanism for steering the animal home, essentially by evaluating (before acting) whether turning left or right would most improve alignment to the target. A neural model that copies CX neuroanatomy at the single-neuron level can thus explain the path integration capability of insects (8).

This model has recently been extended with a proposal for how insects could return to a discovered food source and take efficient routes between multiple sources (11). This would require that a snapshot of the state of the vector memory could be stored for salient locations in the world and then reactivated—to interact with the same steering circuitry—when the animal wants to revisit the location. As yet, the neural basis for such a memory is unknown.

The CX model has been demonstrated to work for path integration on both wheeled and flying robots. However, the key “robotic” contribution to understanding this circuit was mostly conceptual. Taking a robotic perspective meant that, rather than focusing on how the CX neurons “represent” external stimuli, the question became, how do the neurons transform the stimuli into the control of action? For example, accumulating speed in eight directions, following the eightfold columnar structure in each half of the CX, is a redundant Cartesian encoding (using more axes than required) of the home vector. However, it greatly simplifies the subsequent calculation of the desired turning direction, allowing a simple column shift to the right or left to “rotate” the vector by 90°.

Where next? Another prominent subcircuit, found in the brains of all insects, that is coming under increasing scrutiny is the mushroom body (MB). This region is known to be involved in associative learning of the value of olfactory stimuli. Its distinctive architecture, which has been compared to that of the vertebrate cerebellum (12), has been shown in multiple modeling studies, and some robot applications (13), to support pattern learning by encoding inputs as sparse activation of a small subset of a larger neural population and correlating with a reward signal. A recent study directly evaluated the effectiveness of an augmented MB model on robot benchmark datasets for real-world place recognition (14). This work suggests that a key function of the MB is to produce an efficient and compact reencoding of stimuli (in this case, outdoor images from a moving platform over a long route) that can be exploited for recognition, even in changing conditions. The results show that the insect-inspired network produces performance comparable to that of state-of-the-art deep-learning approaches for autonomous navigation, with a much smaller and faster computational footprint (13).

However, currently modelers have not converged in their accounts of the key MB learning mechanisms. Most (but not all) focus on a change in synaptic weight between the parallel fibers of the Kenyon cells (KCs), encoding the stimulus, and the output neurons. The output neurons are sometimes interpreted

as encoding the response, and sometimes the predicted stimulus value. In some models, the synaptic change depends on coincident firing of KCs and output neurons, in other models on delivery of a reward signal (or alternatively, a prediction error signal) by dopaminergic neurons that target the synapse, and some models combine both mechanisms. Moreover, there is a cornucopia of new information emerging about the precise anatomy and individual neural function of the MB, particularly for neurogenetic model systems such as the fruit fly (*Drosophila melanogaster*), which has yet to be incorporated in computational or robot models. For example, the MB is divided into multiple compartments in which specific reward inputs target specific output neurons, and the KCs, output, and dopaminergic neurons form distinct tripartite synapses, suggesting a more complex flow of information between them.

What about modeling the whole insect brain? Several groups, inspired by detailed *D. melanogaster* brain wiring diagrams, are now pursuing this target (15). But just including more detail in brain models for its own sake is unlikely to lead to insights unless it is grounded in understanding behavior. For example, the MB seems overengineered for forming simple odor-value associations—indeed, it evolved to deal with the dynamic complexity of actively responding to fluctuating stimuli streams in real environments. Posing such a problem for a robot should be an effective way to illuminate the key computations involved and to rigorously evaluate new models. It could also result in smarter robots. ■

REFERENCES AND NOTES

1. M. Kinoshita, U. Homberg, in *Brain Evolution by Design: From Neural Origin to Cognitive Architecture*, S. Shigeno et al., Eds. (Springer, 2017), pp. 123–151.
2. B. Webb, *Nature* **417**, 359 (2002).
3. Z. M. Bagheri, B. S. Cazzolato, S. Grainger, D. C. O’Carroll, S. D. Wiederman, *J. Neural Eng.* **14**, 046030 (2017).
4. Z. M. Bagheri, S. D. Wiederman, B. S. Cazzolato, S. Grainger, D. C. O’Carroll, *Bioinspir. Biomim.* **12**, 025006 (2017).
5. B. H. Lancer, B. J. E. Evans, J. M. Fabian, D. C. O’Carroll, S. D. Wiederman, *J. Neurosci.* **39**, 8497 (2019).
6. N. S. Szczecinski, A. P. Getsy, J. P. Martin, R. E. Ritzmann, R. D. Quinn, *Arthropod Struct. Dev.* **46**, 736 (2017).
7. T. I. Tóth, S. Daun, *Physiol. Rep.* **7**, e14080 (2019).
8. T. Stone et al., *Curr. Biol.* **27**, 3069 (2017).
9. U. Homberg, S. Heinze, K. Pfeiffer, M. Kinoshita, B. el Jundi, *Philos. Trans. R. Soc. London B Biol. Sci.* **366**, 680 (2011).
10. J. D. Seelig, V. Jayaraman, *Nature* **521**, 186 (2015).
11. F. Le Moë, T. Stone, M. Lihoreau, A. Wystrach, B. Webb, *Front. Psychol.* **10**, 690 (2019).
12. S. M. Farris, *Arthropod Struct. Dev.* **40**, 368 (2011).
13. L. I. Helgadottir, J. Haenicke, T. Landgraf, R. Rojas, M. P. Nawrot, in 2013 Sixth International IEEE/EMBS Conference on Neural Engineering (NER) (2013), pp. 891–894.
14. M. Chancan, L. Hernandez-Nunez, A. Narendra, A. B. Barron, M. Milford, *IEEE Robot. Autom. Lett.* **5**, 993 (2020).
15. L. T. Collins, *Biol. Cybern.* **113**, 465 (2019).

10.1126/science.aaz6869

RETROSPECTIVE

Daniel S. Greenberg (1931–2020)

Incisive science journalist and commentator

By **Colin Norman**

Daniel S. Greenberg, pioneering journalist, author, and a founding editor of *Science's* news section, died on 9 March at his home in Washington, D.C. He was 88. Dan was among the first reporters to write about the productive but sometimes troubled relationship between basic research and the U.S. government, and for more than five decades he was an influential, often acerbic, observer of research policy and the research community itself.

Dan's career as a science journalist began in 1961 when he was hired by *Science* with the vague remit to write about issues involving science and scientists. He was not an obvious choice: He had no formal scientific training—he graduated from Columbia University in 1953 with a degree in English—and later admitted that he had not even heard of *Science* at the time. But he did have 6 years of reporting experience at an evening newspaper in Wilmington, Delaware, and *The Washington Post*, as well as an intimate knowledge of Washington politics, having spent a year working as a congressional fellow. Soon after Dan joined *Science*, the editor who had hired him left; he was on his own.

With the support of Philip Abelson, who was appointed *Science's* editor-in-chief in 1962, Dan built up the news section, then called News and Comment, into an authoritative and insightful source of information and analysis of government policies for basic research and the U.S. research enterprise. Dan led a small, talented team of reporters in covering a wide range of issues, including the space program; the growth of the National Institutes of Health; the channeling of scientific advice into the government; and the expensive project-turned-fiasco called Mohole, which aimed at drilling through Earth's crust.

At the time, the idea of a journalist-written section in a publication devoted to publishing research papers was highly unusual, and so was the approach that Dan and his team took. They covered basic research policy in much the same way a business reporter would cover development of economic pol-

icy: as a set of competing interests. Federal funding of basic research had ballooned in the postwar years, and scientists had become advisers to the expanding science bureaucracy. The fierce competition for government dollars led some scientists to become lobbyists for particular projects and disciplines, in stark contrast to the image of the scientist as a dispassionate seeker of the truth.

Dan laid out this viewpoint in his 1967 book, *The Politics of Pure Science*, which drew heavily on his reporting for *Science*. It became a widely acclaimed and discussed work. (I first came across it in 1968 as a student at the University of Manchester in the United Kingdom, where it was recommended reading for a course on science policy.) However,



it was not greeted with universal enthusiasm. In a preface to the second edition, Dan noted that it sparked “reactions that flowed from the belief that the scientific community should be exempt from the types of journalistic inquiries that are commonplace to other segments of our society.” He called that attitude “nonsense.”

Dan left *Science* in 1970 and launched the biweekly newsletter *Science and Government Report (SGR)*, through which he continued to chronicle developments in the basic research enterprise, many of which he found troubling, such as paid lobbying of Congress for projects that had not been peer reviewed and growing corporate influence on academic research. Dan wrote *SGR* himself, with the help of multiple sources

within the government and academia. His wife, Wanda Reif, a lawyer and former congressional aide, provided management and business support.

Although its circulation never exceeded 2000 readers, *SGR* flourished in the pre-internet days when expensive newsletters were a critical source of insider information. It was a must read for anybody interested in science policy. Dan sold *SGR* in 1997 and distilled much of his reporting into two books, *Science, Money, and Politics* (published in 2001) and *Science for Sale* (published in 2007). *The Politics of Pure Science*, long out of print, was republished in 1999.

Dan's writing style was unmistakable: direct, often critical, and sometimes bemused. It could also be funny: He satirized the endless thirst for research grants through the exploits of a character he called Dr. Grant Swinger, Director of the Center for the Absorption of Federal Funds. And he loved to skewer pompous scientists and officials by printing extracts from speeches under the headline “High Vacuum Oratory.”

His legacy goes beyond a vast collection of published writing. Dan influenced other publications' coverage of basic research and was a role model and mentor to many young science writers, myself included. I first met him in the early 1970s when I was a correspondent for *Nature* based in Washington, D.C. Like *Science*, *Nature* had launched a news section written by journalists. Dan's advice to a rather green young reporter finding his way through the complexities of the U.S. research system proved invaluable, as did Dan and Wanda's friendship over subsequent decades.

We would meet over dinner in Washington, D.C., and Dan would offer amused, sometimes outraged, and always insightful comments about people and the background to decisions in science policy. Our discussions over the years usually involved events we had already covered—we were writing for similar audiences, and Dan, a competitive journalist, was not about to give away his upcoming stories; nor was I.

Warm and unpretentious, Dan had an infectious sense of humor. He was a proud father and grandfather, with four daughters from his previous marriage, a stepdaughter, and 18 grandchildren. He was also devoted to his Labrador dogs, Walter and Ben, named after the journalist Walter Lippmann and Benjamin Franklin.

Dan died before the coronavirus pandemic hit the United States. Wanda says she misses the discussions they would have had about the pandemic and the government's response. Dan would have had plenty of interesting things to say. ■

Former News Editor, *Science*, Washington, DC, USA.
Email: norman.colin@gmail.com

10.1126/science.abb9194



POLICY FORUM

The John E. Amos coal-fired power plant in West Virginia was retrofitted in response to Mercury and Air Toxics Standards.

ENVIRONMENTAL ECONOMICS

Deep flaws in a mercury regulatory analysis

The U.S. EPA ignores scientific evidence, economic best practice, and its own guidance

By Joseph Aldy¹, Matthew Kotchen², Mary Evans³, Meredith Fowle⁴, Arik Levinson⁵, Karen Palmer⁶

The U.S. Environmental Protection Agency (EPA) has proposed to roll back the legal basis of its Mercury and Air Toxics Standards (MATS), in part on the basis of a benefit-cost analysis (BCA) that is seriously flawed in three ways (1, 2). The analysis disregards economically important but indirect public health benefits, or “co-benefits,” in a manner inconsistent with economic fundamentals. It fails to account for recent science that identifies important sources of direct health benefits from the reduction of mercury emissions. And it ignores transformative changes in the structure and operations of the electricity sector over the past decade. These analytical shortcomings run counter to long-standing guidance for economic analysis from the U.S. Office of Management and Budget (OMB) and from the EPA itself. If finalized, the new rule will undermine continued implementation of MATS and set a concerning precedent for use of similarly inappropriate analyses in the evaluation of other regulations.

In 2012, the EPA issued MATS as the first federal regulatory limits on hazardous air pollution from coal-burning power plants. Now, as part of its new proposal, the EPA has produced a flawed analysis to argue that the benefits of reducing power plant emissions of mercury and other hazardous air pollutants (HAPs) do not justify the costs. It concludes that the original MATS rule was not “appropriate and necessary,” a legal requirement under the Clean Air Act. The proposal is not to revoke MATS itself, with which power plants have complied since 2016, but instead to remove the statutory basis of MATS. In effect, the new rule would reverse the EPA’s previously held findings in 2012 and 2016 and, as a consequence, invite legal challenges to MATS (3). The ultimate result is likely to be weaker regulations on mercury and other HAPs.

Beyond the specific implications for MATS, the supporting BCA marks a fundamental shift in how the EPA compares the costs and benefits of its actions. If finalized, it will set a precedent that undermines the EPA’s ability to appropriately compare the full set of costs and benefits of other regulations, both existing and new. The likely result will be weaker and inefficient regulations on many pollutants, not just mercury and other HAPs.

THE ELIMINATION OF CO-BENEFITS

The EPA’s proposal to reverse its “appropriate and necessary” finding relies on a specious economic analysis that does not count co-benefits. Co-benefits arise when compliance with a regulation leads to reductions in some other pollutant that is not the regulation’s intended target. In the case of MATS, the activities that power plants undertake to reduce mercury and HAPs emissions (for example, switching to cleaner fuels or installing pollution control equipment) also reduce emissions and eventual pollution concentrations of harmful particulate matter. The vast majority of the economic benefits of MATS that the EPA quantified in its 2011 BCA were from reductions in particulate matter due to such expected compliance actions by power plants. Lower fine particulate matter concentrations produce health benefits such as reduced premature mortality and morbidity. The expected benefits ranged from \$33 billion to \$90 billion per year, easily exceeding the expected costs of \$9.6 billion (4).

The EPA’s move to disregard public health co-benefits—and reverse the conclusion of its 2011 BCA—is inconsistent with standard practice for economic analyses. BCAs should seek to account for all economic consequences of a regulation, relative to a baseline without the regulation. These include benefits and costs associated with changes in a directly targeted pollutant, as well as co-benefits or co-costs of changes in other pollutants. It is only through consistent and full recognition of all benefits and costs, including co-benefits and co-costs, that a BCA provides a comprehensive and transparent analysis to inform decision-making.

In cases in which a portion of the direct benefits are not (or cannot be) quantified, showing that even just the quantified co-benefits exceed the costs is sufficient to conclude that the regulation’s overall benefits exceed the costs. That is how the EPA approached its original analysis in 2011, and we find no basis for the agency’s reinterpretation of the same numbers now.

The EPA’s disregard of co-benefits conflicts with long-standing guidance from OMB on the conduct of BCAs and from the EPA’s own guidelines for economic analysis (5, 6). Both agencies have recognized the importance of including co-benefits in economic analyses of regulatory actions. Regarding MATS in particular, the OMB stated as recently as 2017 that particulate matter co-benefits “make up the majority of the monetized benefits, even though the

¹John F. Kennedy School of Government, Harvard University, Cambridge, MA, USA. ²School of Forestry and Environmental Studies, Yale University, New Haven, CT, USA. ³Robert Day School of Economics and Finance, Claremont McKenna College, Claremont, CA, USA. ⁴Department of Agricultural and Resource Economics, University of California, Berkeley, Berkeley, CA, USA. ⁵Department of Economics, Georgetown University, Washington, DC, USA. ⁶Resources for the Future, Washington, DC, USA. Email: matthew.kotchen@yale.edu

regulation is designed to limit emissions of mercury and other hazardous air pollutants. The consideration of co-benefits, including the co-benefits associated with reduction of particulate matter, is consistent with standard accounting practices and has long been required" under OMB guidance (7).

WHAT ABOUT DIRECT BENEFITS?

In its original, 2011 analysis, the EPA woefully undercounted direct health benefits of reducing mercury emissions, and recent research suggests that even by focusing exclusively on the direct impacts, the benefits of MATS could still exceed the costs. The entirety of the direct health benefits, \$0.5 million to \$6 million per year, were estimated through a single, narrowly defined impact and exposure pathway: changes to the IQs of children born to mothers who, when pregnant, ate freshwater fish caught by recreational fishers. To be fair to the EPA in 2011, the estimated co-benefits easily swamped the \$9.6 billion costs, so the agency might have thought it less critical to further quantify all of the difficult-to-measure direct benefits, and less was known about how to do so at the time.

Today, however, research has revealed more about the wider effects of how power-plant mercury emissions disperse and bioaccumulate in seafood that is consumed by a far greater portion of the population (8). This means that the EPA's most recent comparison of costs and benefits could have readily accounted for the additional and far more substantial exposure through freshwater and coastal commercial fisheries. But the agency chose not to quantify those direct benefits.

The EPA also fails to consider mercury's harmful effects on the human cardiovascular system, such as a greater likelihood of heart attacks. One recent study accounts for these impacts, along with a broader assessment of how consumers are exposed to mercury through food consumption. Although the estimates are not expressed on an annual basis to allow for direct comparison, the authors find that MATS will produce \$150 billion in cumulative health benefits through 2050, more than 90% of which comes from fewer heart attacks (9).

This evidence notwithstanding, the EPA today continues to rely exclusively on the narrow set of direct benefits monetized in 2011. By failing to quantify other direct benefits of mercury reductions, or even discuss research published since 2011, the EPA leaves open the question of whether it draws the right conclusion, even based on its own, inappropriately narrow criterion that excludes co-benefits.

A LOT HAS CHANGED SINCE 2011

The EPA's continued reliance on outdated estimates made in 2011 about future U.S. electricity generation provides a misleading picture today about MATS costs and benefits. Although forecasting errors were to be expected when the EPA conducted its prospective analysis before MATS implementation, the EPA's new analysis ignores considerable and well-known evidence of major changes in the electricity sector that have occurred since then.

In 2011, the EPA predicted that roughly half of electricity generation in 2015 would come from coal and one-fifth from natural gas (4). The actual shares today are around one-third from coal and one-third from natural gas (3). This means that less of our electricity comes from mercury-emitting sources. Additionally, one-fifth of coal-fired capacity has been retired, and the plants still operating generate 30% less power than the EPA projected, primarily because of inexpensive natural gas and lower-than-expected power demand (10, 11). Fewer plants have incurred the costs to install pollution control equipment than expected, and those that did are incurring lower-than-expected costs for operations and maintenance. Indeed, the pollution control investments that have been made to comply with MATS are about half of what EPA projected in 2011.

The substantial shift away from coal-fired generation in the United States has also changed the baseline against which the benefits of MATS were estimated in 2011. Mercury emissions have fallen more than 80%, and sulfur dioxide emissions, a precursor to ambient particulate matter, have fallen more than 60% (3). The vast majority of these reductions have been due to market factors independent of MATS (10, 11), which means that the baseline scenarios used in 2011 to estimate MATS benefits were off by a wide margin.

Another big change since 2011, ignored in the EPA's most recent analysis, is that power plants began complying with the MATS rule in 2016. This means that the EPA now has access to 3 years of real-world data, rather than forecasts, with which to estimate the rule's costs and benefits. Nevertheless, the EPA has ignored these data, missing an opportunity to conduct a retrospective analysis—or to draw from related peer-reviewed retrospective analyses in the academic literature (10, 11)—that would more accurately inform policy-makers and the public. Instead, the EPA is continuing to rely on outdated forecasts that most likely overestimate both the costs and benefits, with ambiguous implications for the net result.

EPA CAN AND SHOULD DO BETTER

The EPA's proposed MATS rule reverses its twice-held "appropriate and necessary" finding. Given the agency's U-turn on a finding of such importance, it should have provided supporting evidence that follows best practices and takes advantage of the best available science and most recent data. Yet, the EPA contravenes its own and OMB's guidance and ignores co-benefits, overlooks new research about the health consequences of mercury exposure, and relies on outdated 2011 projections of coal use and compliance costs.

The EPA can and should do better. No BCA is perfect because some impacts are difficult to quantify, and even the best forecasts are generally not completely accurate. But the EPA's original 2011 BCA in support of MATS represented a genuine and credible effort to quantify the expected costs and benefits, according to current data and science at the time. This stands in marked contrast to the EPA approach now. Until the time when a comparable effort is completed and the results can be reviewed, we find no defensible, economic basis for EPA's reversal of the "appropriate and necessary" finding. ■

REFERENCES AND NOTES

1. EPA, Compliance Cost, HAP Benefits, and Ancillary Co-Pollutant Benefits for "National Emission Standards for Hazardous Air Pollutants: Coal- and Oil-Fired Electric Utility Steam Generating Units – Reconsideration of Supplemental Finding and Residual Risk and Technology Review" (EPA, 2018); www.epa.gov/sites/production/files/2018-12/documents/mats-an-cost-benefit_memo12-2018.pdf.
2. EPA, *Fed. Regist.* **84**, 24 (2019); www.govinfo.gov/content/pkg/FR-2019-02-07/pdf/2019-00936.pdf.
3. J. Aldy et al., Report on the Proposed Changes to the Federal Mercury and Air Toxics Standards. Report of the External Environmental Economics Advisory Committee (E-EEAC, 2019); www.e-eeac.org/mats-report.
4. EPA, Regulatory Impact Analysis for the Final Mercury and Air Toxics Standards, EPA-452/R-11-011 (December 2011); www3.epa.gov/ttnecas1/regdata/RIAs/matsriafinal.pdf.
5. OMB, Circular A-4: Regulatory Analysis (Executive Office of the President, 17 September 17, 2003); www.whitehouse.gov/sites/whitehouse.gov/files/omb/circulars/A4/a-4.pdf.
6. EPA, *Guidelines for Preparing Economic Analyses, May 2014 Update* (EPA/National Center for Environmental Economics, 2014); www.epa.gov/sites/production/files/2017-08/documents/ee-0568-50.pdf.
7. OMB, *2017 Draft Report to Congress on the Benefits and Costs of Federal Regulations and Agency Compliance with the Unfunded Mandates Reform Act* (Executive Office of the President, 2017); www.whitehouse.gov/wp-content/uploads/2017/12/draft_2017_cost_benefit_report.pdf.
8. E. M. Sunderland, M. Li, K. Bullard, *Environ. Health Perspect.* **126**, 017006 (2018).
9. A. Giang, N. E. Selin, *Proc. Natl. Acad. Sci. U.S.A.* **113**, 286 (2016).
10. J. Coglianese, T. D. Gerarden, J. H. Stock, *Energy J.* **41**, 55 (2019).
11. J. Linn, K. McCormack, *RAND J. Econ.* **50**, 733 (2019).

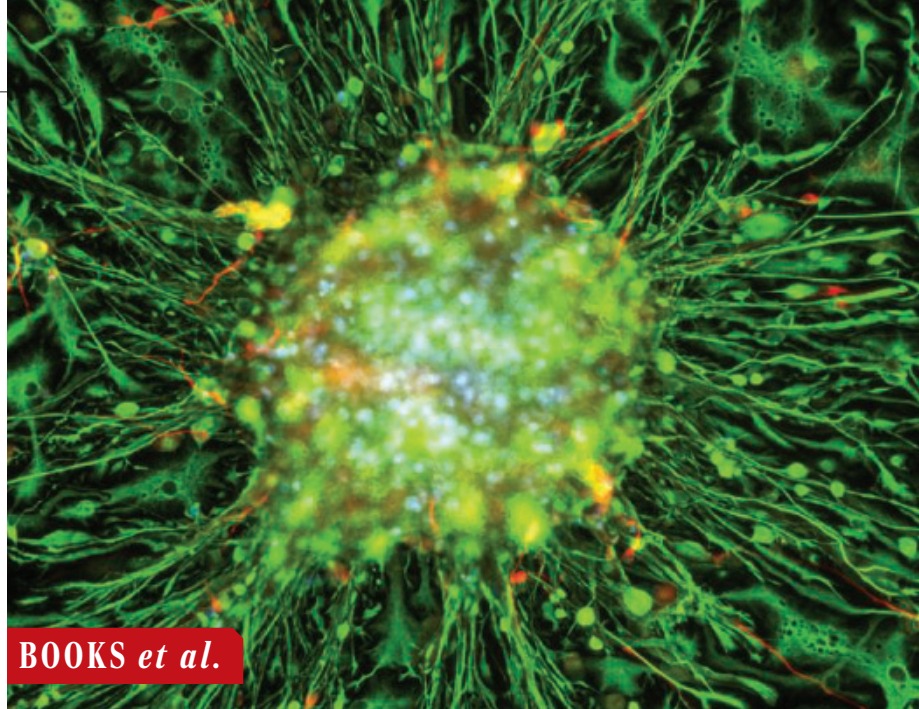
ACKNOWLEDGMENTS

All authors contributed to this paper through their engagement with the External Environmental Economics Advisory Committee (E-EEAC) (3), an independent organization established after the dissolution in June 2018 of the original EEAC that had operated for more than 25 years within the EPA's science advisory board structure.

Published online 9 April 2020

10.1126/science.aba7932

sciencemag.org **SCIENCE**



BOOKS *et al.*

NEUROSCIENCE

Repairing damaged brains

Stem cell therapies slowly gain traction as viable treatments for brain disorders

By **Adrian Woolfson**

In the late 19th century, the Spanish neuroanatomist Santiago Ramón y Cajal documented, in exquisite detail, the fantastical, uncharted landscapes of the human brain. The ornate cellular structures he drew were, according to Cajal, fragile and irreplaceable. Brain cells, he stated, “may die” and cannot “be regenerated.” Cajal then threw down the gauntlet, asserting that it was the job of the “science of the future to change, if possible, this harsh decree.”

Jack Price’s engaging book *The Future of Brain Repair* details past, present, and future attempts to address Cajal’s formidable challenge. In so doing, it provides a vibrant and compelling guide to the important and rapidly evolving fields of stem cell-based therapies and brain repair, which together, he believes, are poised to deliver unprecedented changes to the management of brain diseases.

Unlike the diverse blood cells generated throughout life by specialized stem cells in

bone marrow, the two known brain stem cell types—“tucked into the underside of the dentate gyrus” of the hippocampus and surrounding the ventricles of the forebrain in the subependymal zone—differentiate into a much more restricted set of cells. This intrinsic lack of versatility, coupled with the fact that brain cells are postmitotic and consequently unable to divide, underlies the brain’s inability to efficiently repair itself.



The Future of Brain Repair
Jack Price
MIT Press, 2020. 288 pp.

Two broad strategies for repair are suggested. The first would be to bypass endogenous neural stem cells by introducing non-native brain cells. The second would be to coax native cells into a different set of behaviors.

Parkinson’s disease, a progressive movement disorder caused by the incremental destruction of dopaminergic neurons, has provided a fertile testing ground for the first strategy. The first human neural transplantation experiments conducted during the 1980s, which used dopamine-producing cells from human fetal brain cells or from patients’ own adrenal medullas, failed to meet expectations. It appeared as if not any old cells would do. Although a proof of concept for the feasibility of such approaches was provided, a more precisely defined and renewable source of donor cells was lacking, as

The therapeutic promise of neurosphere stem cells (shown here) has not yet been realized.

was an accompanying robust and affordable commercial-scale manufacturing process.

In the 1990s, researchers showed that neural progenitor cells could be cultured as “neurospheres”—balls of cells that maintain self-replication and multipotency over protracted durations. This discovery led, in 2006, to the first human neural stem cell transplant in a group of children with Batten disease, a rare neurodegenerative disorder. The results, again, were disappointing: The overall survival of treated patients showed no discernible improvement over that of untreated patients. Similar studies in patients with ischemic stroke have proved more promising, but researchers suspect improvements in these cases resulted from the graft’s secretion of neuroprotective proteins rather than from cell replacement.

Two other innovations, however, have the potential to address Cajal’s regenerative vision. The first is our ability to culture embryonic stem cells (ES cells) to produce billions of pluripotent stem cells, which are, in turn, capable of producing every cell type in the human body. Therapies derived from ES cells have been shown to be highly effective in animal models of Parkinson’s disease, with evidence suggesting that the transplanted neurons exert their effect by synthesizing dopamine.

The second innovation issues from the work of Shinya Yamanaka, who demonstrated in 2006 that terminally differentiated cells of any type can be reprogrammed into induced pluripotent stem cells (iPSCs) through the administration of just four transcription factors. iPSCs may then be converted into select cell types using different transcription factor cocktails.

Although not without complications—extended culture of iPSCs has been shown, for example, to result in mutations in P53 and other oncogenes—ES cells and iPSCs have the potential to transform the science of brain repair and regenerative medicine by enabling the generation and therapeutic deployment of relevant neuronal subtypes in a scalable and low-cost manner. These cells have the additional advantage of retaining the capacity to build new tissues from scratch.

Perhaps most interesting, however, is the recent convergence of pluripotent stem cells with gene editing. Together, these technologies offer the possibility of augmenting natural neural stem cell behavior. ■

ACKNOWLEDGMENTS

The reviewer is a shareholder of Sangamo Therapeutics.

The reviewer is the executive vice president of research and development at Sangamo Therapeutics, Brisbane, CA, USA. Email: adrianwoolfson@yahoo.com

10.1126/science.abb1642

DENDROCHRONOLOGY

What tree rings can tell us

From ancient timbers to mountaintop forests, trees hold important climate clues

By **Lori Daniels**

Many of us have counted the rings of a tree to reveal its age. But did you know that evidence of epic fires, volcanoes, hurricanes, floods, drought, famine, and the rise and fall of ancient empires is also embedded in a tree's circumference? Valerie Trouet's *Tree Story* is an informative introduction to the science of tree rings. An accomplished and globally recognized dendroclimatologist, Trouet is knowledgeable across diverse fields of science and is a talented writer and engaging storyteller.

Long chronologies are formed by cross-dating the rings of living trees with those of dead trees. The oldest living dendrochronologically dated tree is a bristlecone pine in California that is ~5000 years old. The longest tree-ring chronology is composed of living and archaeological oak-pines from Germany and spans an astounding 12,650 years.

The quest for long-lived trees leads dendrochronologists deep into the wilderness

and to the tops of mountains. Here, they extract increment cores using hand-operated borers, a nondestructive way to collect rings from living trees. Dendrochronologists can also be found analyzing archaeological ruins and shipwrecks at the bottom of the ocean, where tree rings of past centuries are preserved in ancient timbers. Trouet entertains readers with adventurous tales of accessing remote field sites and the inevitable mishaps that occur when one is navigating an unfamiliar culture using a foreign language.

Climate history is often embedded in long tree-ring chronologies. In some cases, the relations are intuitive—wide rings in trees growing on mountaintops indicate warm years, whereas narrow rings in trees of semiarid climates indicate hot, dry summers. Other relations are more challenging to decipher and require multiple proxies and other climate-sensitive biotic and abiotic time series. Drawing from a diversity of tree-ring research and interdisciplinary collaborations, Trouet chronicles fascinating examples of how dendrochronology helps to answer questions about past environments and human history.

Drought-sensitive tree rings from the Mediterranean cross-referenced with the annual

Tree Story: The History of the World Written in Rings

Valerie Trouet
Johns Hopkins University
Press, 2020. 256 pp.

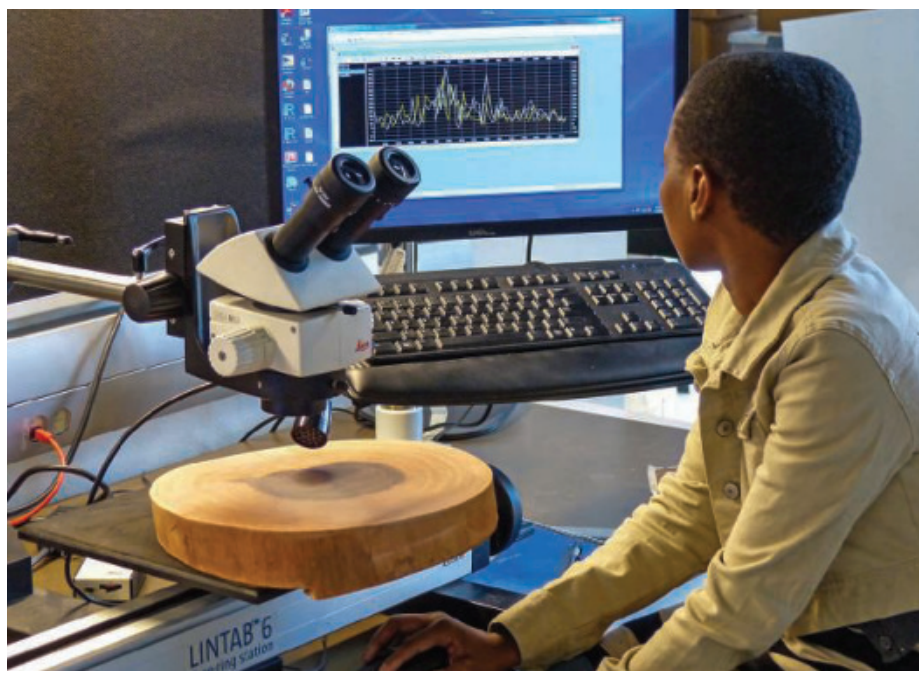


increments of a stalagmite deep in a Scottish cave, for example, have revealed the seesaw climate of the North Atlantic Ocean, a driver of contemporary global climate and the key to understanding the onset of the Little Ice Age. Meanwhile, the tree rings of blue oaks in the Central Valley reflect regional drought and snow accumulation in the nearby Sierra Nevada, showing California's recent megadrought to be a 500-year record.

Cross-referencing tree rings with marine records from corals, fish otoliths, and bivalve shells has enriched our understanding of the relationship between the ocean and the atmosphere, shedding light on, for example, the El Niño–Southern Oscillation and other variations in the Pacific climate system. Cross-referencing tree rings with ice cores from the remote ice sheets of Greenland and Antarctica, meanwhile, has allowed us to chronicle volcanic eruptions that had global effects on temperature, and river flows that drove agricultural collapse and famines in countries ranging from Ireland to Egypt. Trouet even demonstrates how tree rings helped decipher the environmental context of the bubonic plague, revealing how climate change amplified past epidemics.

In *Tree Story*, Trouet tackles some of the pressing environmental challenges of this millennium. She clearly explains the science underpinning the now-famous “hockey-stick” curve and deftly debunks the arguments of climate-change deniers. She shows how tree-ring science provides distinctive context to the record-breaking droughts, hurricanes, and wildfires that have plagued the world in the past decade. In the case of wildfires, using crossdated fire-scar records and tree-ring climate proxies, she shows how the combination of displacement of indigenous peoples by Europeans, ongoing land-use change, and fire suppression has transformed landscapes, making them more flammable, especially as the climate warms.

Using tree rings to disentangle complex interactions, Trouet shows how past societies have dealt with unexpected climatic changes. She concludes with a challenge to scientists and our society: For the first time in human history, thanks to centuries of scientific discoveries and research, we have foresight into the changes that lie ahead. “We have our work cut out for us,” she warns. ■



Dendrochronologist Zakia Hassan Khamisi measures tree-ring widths in a Tanzanian *Brachystegia spiciformis*.

LETTERS

QQ group: 970508760

Edited by Jennifer Sills

Protect Indigenous peoples from COVID-19

As coronavirus disease 2019 (COVID-19) spreads through Brazil, President Jair Bolsonaro has repeatedly denied the severity of the pandemic and broadcasted misleading information and mixed messages about how to respond, advocating for hydroxychloroquine use and the end of the country's quarantine (1). Current scientific evidence contradicts these recommendations (2, 3), and the president's speech puts the population of Brazil at risk. The public health system in Brazil's state of Amazonas has already "collapsed," according to a statement by the mayor of the state's capital city (4). The Bolsonaro administration must immediately reverse its current posture of minimizing the threat of COVID-19 and take steps to protect Brazil's vulnerable populations, including its Indigenous and traditional peoples.

The standard risk groups for COVID-19 are elderly people and those with comorbidities (3), but in Brazil it makes sense to expand the risk group designation to include Indigenous peoples. Pathogens have historically been one of the most powerful factors in decimating Indigenous peoples in South America (5, 6). COVID-19 poses a particular threat to these communities given that Brazil's federal government has marginalized and neglected Indigenous peoples even when their rights are guaranteed by law or by international agreements (7, 8).

Indigenous and traditional peoples can be expected to be especially vulnerable to severe acute respiratory

syndrome-coronavirus 2 (SARS-CoV-2), the virus that causes COVID-19. In addition to their history of susceptibility to epidemics (6), many of these isolated communities lack medical posts, doctors, and basic medications, to say nothing of the ventilators that would be needed to treat a COVID-19 outbreak. Bolsonaro's administration recently dismissed 8000 Cuban doctors who served small communities in the country's interior (9), which has been especially harmful to Indigenous and traditional communities in the Amazon region.

Brazil's government must take action in the Amazon to protect these people. Instead of allowing evangelical missionaries to enter into contact with isolated Indigenous groups (10), all means of transport to these areas should be restricted. The first Indigenous case of the disease was confirmed on 1 April (11). In line with international guidelines (12), Brazil's government should ensure isolation and monitoring in Indigenous areas as well as for all those who have contact with them. The government must act quickly to provide doctors, personal protective equipment, and testing capabilities in these areas. On the national scale, Brazil must maintain a nationwide quarantine to mitigate the disease's impact. Measures favored by Brazil's president, such as "vertical isolation" or a partial breach of isolation (1), conflict with World Health Organization recommendations and scientific studies (3, 12), thereby putting Brazil's entire population at risk. The effectiveness of hydroxychloroquine has not been confirmed, although its risks have been (2). Protecting Indigenous and traditional peoples from COVID-19 by acknowledging their increased risk and acting accordingly will protect public health for all Brazilians

Indigenous peoples in Brazil's Amazon region are at increased risk in a COVID-19 outbreak.

as well as safeguard the sustainability of the Amazon.

Lucas Ferrante^{1*} and Philip M. Fearnside²

¹Ecology Graduate Program, National Institute for Research in Amazonia (INPA), Manaus, Amazonas, Brazil. ²Department of Environmental Dynamics, National Institute for Research in Amazonia (INPA), Manaus, Amazonas, Brazil.

*Corresponding author.

E-mail: lucasferrante@hotmail.com

REFERENCES AND NOTES

1. T. Fernandes, F. Fabiani, "Em pronunciamento, Bolsonaro defende cloroquina e retoma embate com governadores e prefeitos" *Folha de São Paulo* (2020) [in Portuguese].
2. D. Lowe, "Hydroxychloroquine update for April 6" *Science Translational Medicine* (2020).
3. J. Bedford *et al.*, *Lancet* **395**, 1015 (2020).
4. "Prefeito de Manaus afirma que saúde do AM entrou em colapso," *Veja* (2020).
5. J. Diamond, *Guns, Germs, and Steel: The Fates of Human Societies* (W.W. Norton, 1997).
6. H. Pringle, *Science*, 10.1126/science.aac6784 (2015).
7. L. Ferrante, P. M. Fearnside, *Environ. Conserv.* **46**, 261 (2019).
8. L. Ferrante, M. Gomes, P. M. Fearnside, *Land Use Pol.* **94**, 104598 (2020).
9. "Bolsonaro diz que médicos cubanos queriam implantar guerrilha no Brasil," *O Estado de Minas* (2019) [in Portuguese].
10. S. Branford, "Bringing Christ and coronavirus: Evangelicals to contact Amazon indigenous," *Mongabay* (2020).
11. T. Borges, S. Branford, "First COVID-19 case among indigenous people confirmed in Brazilian Amazon," *Mongabay* (2020).
12. World Health Organization, "Critical preparedness, readiness and response actions for COVID-19" (2020).

10.1126/science.abc0073

Ecosystem aridity and atmospheric CO₂

In their Report "Global ecosystem thresholds driven by aridity" (14 February, p. 787), M. Berdugo *et al.* found that more than 20% of the land surface is projected to cross an aridity threshold by 2100, which could lead to widespread desertification ("Crossing thresholds on the way to ecosystem shifts," M. Hirota and R. Oliveira, *Perspectives*, 14 February, p. 739). Efforts to identify robust thresholds are essential to guide effective policy (1). Such efforts, however, commonly overlook two important aspects of vegetation-water relations: the effect of CO₂ on the efficiency with which plants use water and the effect of CO₂ on potential evapotranspiration, and thus aridity.

Under elevated CO₂, plants increase the efficiency with which they use water (2). In water-limited regions, this has an outsized impact, leading to dryland ecosystems becoming less water-limited, with an increased number of leaves and/or increased photosynthesis per leaf (3). Aridity thresholds are thus projected to shift as a function of CO₂ (4, 5). In addition, although large future increases in aridity are commonly projected

using drought indices (6), these projections do not account for the direct effect of CO₂ on vegetation. When the effect of CO₂ on plant water use is included, projected increases in aridity are greatly decreased (7–10).

Observed dynamics of natural dryland vegetation (4, 11) and experimental evidence (12) support these conclusions and suggest that elevated CO₂ improves the resilience of semi-arid ecosystems, which is often accompanied by substantial greening (4, 11). Rising CO₂ has thus already led to a shift in the relationship between ecosystem function and water resources. Understanding the extent to which this direct effect of CO₂ offsets the indirect effect of increased potential evapotranspiration driven by atmospheric warming remains an important area of research. By omitting the direct influence of CO₂, however, projections of future aridity and the cascading effects on ecosystems overestimate the degree to which ecosystems will cross aridity thresholds this century.

Information on ecological thresholds is essential for understanding the limiting factors of future ecosystem function but requires a full consideration of ecophysiology. We agree with Berdugo *et al.* that immediate action is necessary to avoid the negative impacts of climate change and potential desertification, but such action will be most effective when informed by more comprehensive scientific projections.

Trevor F. Keenan^{1,2*}, Xiangzhong Luo^{1,2},

Yao Zhang^{1,2}, Sha Zhou^{1,2,3,4}

¹Department of Environmental Science, Policy, and Management, University of California, Berkeley, Berkeley, CA 94720, USA. ²Climate and Ecosystem Sciences Division, Lawrence Berkeley National Laboratory, Berkeley, CA 94720, USA. ³Lamont-Doherty Earth Observatory of Columbia University, Palisades, NY 10964, USA. ⁴Earth Institute, Columbia University, New York, NY 10025, USA.

*Corresponding author.

Email: trevorkeen@lbl.gov

REFERENCES AND NOTES

1. W. Steffen *et al.*, *Science* **347**, 1259855 (2015).
2. A. Lavergne *et al.*, *Glob. Chang. Biol.* **25**, 2242 (2019).
3. S. Fatichi *et al.*, *Proc. Natl. Acad. Sci. U.S.A.* **113**, 12757 (2016).
4. R. J. Donohue *et al.*, *Geophys. Res. Lett.* **40**, 3031 (2013).
5. A. L. S. Swann, F. M. Hoffman, C. D. Koven, J. T. Randerson, *Proc. Natl. Acad. Sci. U.S.A.* **113**, 10019 (2016).
6. J. Huang *et al.*, *Nat. Clim. Chang.* **6**, 166 (2016).
7. Y. Yang *et al.*, *Nat. Clim. Chang.* **9**, 44 (2019).
8. P. C. D. Milly, K. A. Dunne, *J. Am. Water Resour. Assoc.* **53**, 822 (2017).
9. L. Lemondant, P. Gentile, A. S. Swann, B. I. Cook, J. Scheff, *Proc. Natl. Acad. Sci. U.S.A.* **115**, 4093 (2018).
10. M. L. Roderick *et al.*, *Water Resour. Res.* **51**, 5450 (2015).
11. A. M. Ukkola *et al.*, *Nat. Clim. Chang.* **6**, 75 (2015).
12. T. J. Zelikova *et al.*, *Proc. Natl. Acad. Sci. U.S.A.* **111**, 15456 (2014).

10.1126/science.abb5449

Response

We reported that increases in aridity observed across global drylands indicate that more than 20% of the Earth's surface

will cross one or several of the aridity thresholds identified by 2100. Keenan *et al.* suggest that this proportion will be lower because a CO₂-enriched atmosphere will promote higher water-use efficiency of vegetation and affect potential evapotranspiration (1). However, Keenan *et al.* do not quantify how these CO₂-driven adjustments affect the nonlinear responses we reported (which are robust and constitute the core findings of our study), the aridity levels at which they occur, or the proportion of Earth's surface that will be affected.

Keenan *et al.* argue that plant water use will decrease estimated increases in aridity. Of course, the proportion of terrestrial surface affected by the thresholds identified would vary if aridity projections change. We used (but did not produce) one of the most accepted aridity projections available (2). However, we acknowledge that aridity projections are currently under debate. Once there is a global consensus on projections, the agreed-upon numbers could be used to refine the estimates provided in our study, which focused on identifying aridity thresholds, not questioning projections.

As we acknowledged in our Report's Methods section, there are limitations to our space-by-time substitution approach. In addition to water use efficiency changes described by Keenan *et al.*, factors such as species turnover, adaptation to the new climatic conditions, increasing albedo, topography (3), and potential legacy effects of current climatic and management conditions (4) could affect ecosystem responses to increases in aridity. The lack of global and consistent estimations of the effect of these processes on aridity projections, however, prevented us from considering them in our quantitative estimations.

Keenan *et al.*'s assumptions also have limits: Increases in soil temperature projected with climate change, and thus associated soil moisture losses, may be higher than previously reported (5), and increases in water use efficiency may not be compensated by enhanced dryness driven by ongoing warming (6). This, together with an increased frequency of extreme climatic events, could dampen or even reverse the positive effect of CO₂ fertilization on vegetation growth and evapotranspiration in the future (7), particularly in drylands (8). In addition, vegetation greening is not always related to increasing productivity (9–11). Thus, we cannot assume that the influence of CO₂ fertilization on vegetation observed in recent decades will be maintained in the future, which will likely be characterized by the rise of temperature-driven impacts of climate change, such as increases in aridity,

on ecosystems (12). However, we agree with Keenan *et al.* on the importance of investigating the opposite effects of elevated CO₂ and increased atmospheric dryness on vegetation. We look forward to future research that will help elucidate these complex interactions and further hone aridity projections.

Miguel Berdugo^{1*}, Santiago Soliveres², Manuel Delgado-Baquerizo³, Fernando T. Maestre^{2,4}

¹Institut de Biologia Evolutiva (UPF-CSIC), 08003 Barcelona, Spain. ²Departamento de Ecología, Universidad de Alicante, 03690 San Vicente del Raspeig, Alicante, Spain. ³Departamento de Sistemas Físicos, Químicos y Naturales Universidad Pablo Olavide, 41704 Sevilla, Spain. ⁴Instituto Multidisciplinar para el Estudio del Medio "Ramón Margalef," Universidad de Alicante, 03690 San Vicente del Raspeig, Alicante, Spain.

*Corresponding author.

Email: mglberdugo@gmail.com

REFERENCES AND NOTES

1. X. Lu, L. Wang, M. F. McCabe, *Sci. Rep.* **6**, 20716 (2016).
2. J. Huang, H. Yu, X. Guan, G. Wang, R. Guo, *Nat. Clim. Chang.* **6**, 166 (2016).
3. P. Kutiel, H. Lavee, *Isr. J. Plant Sci.* **47**, 169 (1999).
4. C. Monger *et al.*, *Front. Ecol. Environ.* **13**, 13 (2015).
5. J. L. Soong, C. L. Phillips, C. Ledna, C. D. Koven, M. S. Torn, *J. Geophys. Res. Biogeosci.* **10.1029/2019JG005266** (2020).
6. E. N. J. Brookshire, T. Weaver, *Nat. Commun.* **6**, 7148 (2015).
7. L. A. Gherardi, O. E. Sala, *Ecol. Lett.* **18**, 1293 (2015).
8. A. Ahlström *et al.*, *Science* **348**, 895 (2015).
9. S. Walther *et al.*, *Glob. Chang. Biol.* **22**, 2979 (2016).
10. D. Yan, R. L. Scott, D. J. P. Moore, J. A. Biederman, W. K. Smith, *Remote Sens. Environ.* **223**, 50 (2019).
11. C. Giguère-Croteau *et al.*, *Proc. Natl. Acad. Sci. U.S.A.*, **10.1073/pnas.1816686116** (2019).
12. J. Peñuelas *et al.*, *Nat. Ecol. Evol.* **1**, 1438 (2017).

10.1126/science.abb5840

TECHNICAL COMMENT ABSTRACTS

Comment on "Light-induced lattice expansion leads to high-efficiency perovskite solar cells"

Nicholas Rolston, Ross Bennett-Kennett, Laura T. Schelhas, Joseph M. Luther, Jeffrey A. Christians, Joseph J. Berry, Reinhold H. Dauskardt

Tsai *et al.* (Reports, 6 April 2018, p. 67) report a uniform light-induced lattice expansion of metal halide perovskite films under 1-sun illumination and claim to exclude heat-induced lattice expansion. We show that by controlling the temperature of the perovskite film under both dark and illuminated conditions, the mechanism for lattice expansion is in fact fully consistent with heat-induced thermal expansion during illumination.

Full text: dx.doi.org/10.1126/science.aay8691

Response to Comment on "Light-induced lattice expansion leads to high-efficiency perovskite solar cells"

Hsinhan Tsai, Wanyi Nie, Aditya D. Mohite

Rolston *et al.* suggest through a convective heating scheme that the mechanism of light-induced lattice expansion is from light-induced thermal heating. We bring out key differences in the physical observables that are not discussed and different from what is observed in the original paper by Tsai *et al.*

Full text: dx.doi.org/10.1126/science.aba6295

“YOU SHOULD AIM TO CONVEY WHAT IS INNOVATIVE ABOUT YOUR RESEARCH”

Longzhi Tan, Stanford University, USA
Grand Prize Winner 2019

GENOMICS, PROTEOMICS, AND SYSTEMS BIOLOGY APPROACHES

Honoring research in genomics, proteomics, integrative omics and systems biology approaches, including computational, to facilitate comprehensive understanding of living cells, organisms and species.

The *Science* & SciLifeLab Prize for Young Scientists is an annual prize awarded to early-career scientists. The prize is presented in four categories: Cell and Molecular Biology; Genomics, Proteomics, and Systems Biology Approaches; Ecology and Environment; and Molecular Medicine.

As a winner, you will have your essay published by *Science*, win up to USD 30,000 and be invited to Sweden where you will receive your award, present your research and meet with leading scientists in your field.

Get ready for a life-changing moment in your scientific career – apply now, deadline is July 15!

[SCIENCEPRIZE.SCILIFELAB.SE](https://scienceprize.scilifelab.se)



*Knut och Alice
Wallenbergs
Stiftelse*

Science
AAAS

SciLifeLab



DRY TIMES

By David Malakoff and Andrew Sugden

Drought “is the death of the earth,” wrote the poet T. S. Eliot. A lack of water withers crops, kills trees, and dries up streams and lakes. Humans have long tried to cope by migrating to wetter regions or inventing new ways of moving water to where it is needed, including by pumping it out of the ground. But as human populations grow, climate change takes hold, and groundwater supplies shrink, droughts pose an increasingly complex challenge to people and the environment.

This special issue examines the science and social impacts of droughts—past, present, and future. Review articles assess our current knowledge of the causes of drought and consequences for forests and soils, how drought relates to political conditions, and options for improving drought resistance in crops.

Additionally, three News Features highlight drought’s influence on the rise and fall of an ancient South American empire, California’s efforts to restore its depleted groundwater, and researchers’ methods for predicting the famines that droughts sometimes bring.

Drought is defined by the absence of life-giving water. Some scholars believe that the forbidding presence of a drought that struck the United Kingdom in 1921 helped inspire Eliot’s repeated allusions to water and drought in his poetry. That year, less than 260 millimeters of precipitation—one of the lowest levels ever recorded—fell in parts of England, prompting the writer to reflect on a natural force that has long shaped our planet.

Caroline Ash, Pamela Hines, Tage Rai, and Jesse Smith also edited this special section.



NEWS

The hunger forecast p. 226

Deep deficit p. 230

Engineering an empire p. 234

REVIEWS

On the essentials of drought in a changing climate p. 256

Hanging by a thread? Forests and drought p. 261

The physiology of plant responses to drought p. 266

Harnessing rhizosphere microbiomes for drought-resilient crop production p. 270

The effects of drinking water service fragmentation on drought-related water security p. 274

RELATED ITEMS

PERSPECTIVE p. 238

BOOKS *ET AL.* p. 250

LETTERS pp. 251 & 252

REPORT p. 314

VIDEO

PODCAST

An outback field near Deniliquin in New South Wales, stricken by the devastating 2006–2007 Australian summer drought, after hot northerly winds blew away the soils of the farming landscape



REVIEW

On the essentials of drought in a changing climate

Toby R. Ault

Droughts of the future are likely to be more frequent, severe, and longer lasting than they have been in recent decades, but drought risks will be lower if greenhouse gas emissions are cut aggressively. This review presents a synopsis of the tools required for understanding the statistics, physics, and dynamics of drought and its causes in a historical context. Although these tools have been applied most extensively in the United States, Europe, and the Amazon region, they have not been as widely used in other drought-prone regions throughout the rest of the world, presenting opportunities for future research. Water resource managers, early career scientists, and veteran drought researchers will likely see opportunities to improve our understanding of drought.

Unlike most natural disasters, but like a disease, a drought begins before it presents any symptoms (1). To understand this, imagine that it is May of 2013 and that you are a farmer in the Caribbean. It has been a little dry recently but otherwise all seems well ahead of the summer rains. The weather is warm, the skies are clear, and the horizon has a yellowish hue from dust carried across the Atlantic from the far-off Sahel (2). Although you do not know it yet, the worst drought in at least half a century has already begun (2). Before it is over, it will persist for 3 years, push 2 million people into food insecurity, and affect nearly every island in the Caribbean (2).

In the United States, drought cost \$250 billion in damages and killed nearly 3000 people between 1980 and 2020, making it the costliest natural disaster and the second most deadly one (3). Over the last 12 centuries of human civilization, multidecadal megadroughts contributed to the demise of some of the most complex societies of the preindustrial era, including the Khmer and Mayan Empires, the Puebloan cliff dwellers of the southwestern United States, and the Yuan Dynasty of China (4). The Old Testament vividly describes drought as a punishment from God that left “Judah wailing, her cities languishing, the land cracked, and wild donkeys standing on barren heights, panting like jackals.” Adding, “Even the doe in the field deserts her newborn fawn because there is no grass” (Jeremiah 14).

Droughts of the future may eclipse those of past centuries in their duration, severity, and frequency (5, 6). Although aggressively cutting greenhouse gas emissions reduces these risks, even low levels of warming could amplify drought hazards across much of the world, including the Caribbean, Central America, Brazil, western Europe, central Africa, Southeast Asia, and Australia (6, 7).

Defining drought

Although the crisis of drought is easily recognized, there is no universally accepted criterion for what constitutes one (4, 8–10). Instead, multiple definitions, indices, and metrics exist to meet the particular needs of different research communities or applications (10). What they have in common was adroitly articulated by the late Kelly Redmond: They are intervals of time when “the supply of moisture fails to meet its demand” (9). Whereas the atmosphere delivers the supply of moisture, the demand for it arises from countless sources—a hot, dry atmosphere demands water vapor from the surface; plants demand water for transpiration; and our infrastructure demands water resources for irrigation, municipal water supply, and hydroelectric power generation, among many other uses.

Droughts are classified according to their impact (8, 10), which imposes an approximate time scale for each type. A meteorological drought stems from rainfall shortages over a period of weeks, whereas an agricultural drought exacts crop losses and may linger for months. A hydrological drought develops on seasonal to interannual time horizons by depleting streamflow or reservoir levels.

Socioeconomic droughts, which affect water resources required for human applications (e.g., municipal drinking water), arise from either a shortage of supply or an excess of demand (10). Although the rest of this review will focus on the physics of meteorological and agricultural drought in a changing climate, the basic ideas are broadly relevant to other types of droughts.

An analytical arsenal for drought research

A simple “bucket” model (Eq. 1) builds on the concept of drought as a phenomenon that arises from either a shortage of precipitation supply (P) or an excess of evapotranspiration demand (E) [e.g., (11) and references therein]:

$$P - E = \frac{dS}{dt} + R_o + G_w \quad (1)$$

where the terms on the right are changes in soil moisture storage (dS/dt), runoff (R_o), and groundwater flow (G_w) (11).

In principle, if we had observations of precipitation minus evapotranspiration ($P - E$), dS/dt , and R_o going back at least a century, then we could readily characterize drought variability on intraseasonal to multidecadal time horizons. In practice, only precipitation measurements are available from the past few decades, and those records are subject to large uncertainties that affect our understanding of drought (12). Measuring E and dS/dt accurately and consistently across space and through time has vexed drought scientists for generations (8, 13).

Drought indices

As an alternative to measuring soil moisture directly, drought indices track relative departures from normal conditions (14, 15). The full palette of drought indices available for researchers and water resource managers is described in other reviews (8, 10), and new indices are routinely added to this collection (16). Broadly, they fall into two categories: indices that track the supply of moisture from precipitation alone (17) and those that approximate the balance of moisture arising from the combined effects of precipitation, evapotranspiration, and, sometimes, storage (14, 15).

The Standardized Precipitation Index (SPI) (17) is designed to track precipitation deficits and surpluses across multiple time scales (e.g., 1, 3, or 12 months), making it ideal for differentiating between different types of drought (e.g., meteorological versus agricultural). However, the SPI's exclusion of evapotranspiration limits its usefulness for some applications and research questions (15). The Standardized Precipitation Evapotranspiration Index (SPEI) (15) was developed to address this limitation while preserving the robust statistical features of the SPI.

Both the SPI and the SPEI emerged to fill a need for drought indices that was imperfectly carved out by the Palmer Drought Severity Index (PDSI) several decades earlier (14). Like the SPEI, PDSI approximates evapotranspiration demand, but it also accounts for moisture storage by different types of soils (14). The “self-calibrating” PDSI (18) is most appropriate for large-scale studies of drought variability and long-term change (12, 19–21). Even so, the magnitude of future change expected from the PDSI depends strongly on its formulation and the historical data used to calibrate it (21).

The SPEI and PDSI depend on simplified estimates of potential evapotranspiration (PET) that must be parameterized, and doing so accurately requires meteorological variables beyond precipitation (12, 21). Consider the widely used, physically based Penman-Monteith equation, which approximates PET as a function of net surface radiation (R_n), soil heat flux (G), water vapor pressure deficit ($e_s - e_a$), slope of the temperature-saturation vapor

Department of Earth and Atmospheric Science, Cornell University, Ithaca, NY, USA.
E-mail: toby.ault@cornell.edu

pressure relationship (Δ), psychrometric constant (γ), and two resistance terms (r_s , for surface resistance, and r_a for atmospheric resistance) (22):

$$ET = \frac{\Delta(R_n - G) + \rho_a c_p \frac{e_s - e_a}{r_a}}{\Delta + \gamma(1 + \frac{r_s}{r_a})} \quad (2)$$

where ρ_a is the density of air and c_p is the heat capacity of dry air.

Use of Eq. 2 requires temperature, humidity, surface pressure, net radiation, and wind speed data (22). Of these, only temperature is widely available across large spatial scales and going back more than a few decades (12). Using the Penman-Montieth equation (Eq. 2) to study drought at continental scales therefore usually entails merging gridded observational datasets with reanalysis products (12); errors in these observational fields will introduce uncertainties into drought indices computed from them (12).

Nevertheless, PDSI and SPEI (as well as others) can be computed from observational and model output alike, which, ostensibly, allows projections of the future to be compared against historical conditions using the same indices for both data products (5, 12, 20, 21).

piration, including lateral flow and subsoil storage of moisture in the rock layer (23, 24).

More sophisticated land surface models (LSMs) assimilate data from multiple sources to estimate historical variations in land surface hydrology (25). However, as with drought indices, observational uncertainties affect the quality of soil moisture data in LSMs (26), and appropriate observational boundary conditions only span 1979 to the present (25). Consequently, LSM output covers a short and heavily forced period of the recent past, which presents a challenge for detecting and attributing the imprint of climate change in soil moisture (27).

An advantage of LSMs, however, is that they simulate the moisture, energy, and biogeochemical fluxes between the atmosphere and the land surface, just as the land surface components of general circulation models (GCMs) do. LSMs therefore also serve as an important bridge between observational data and climate model simulations of the past, present, and future.

Finally, over the past decade, observations of soil moisture from either in situ measurements (28) or remote sensing (29) have emerged as invaluable tools for validating LSMs and monitoring drought. However, these products cover

$$P - E = -\frac{1}{g} \left(\frac{\partial \phi}{\partial t} + \nabla \cdot \int_0^{p_s} q \vec{V} dp \right) \quad (3)$$

with total precipitable water, ϕ , defined as the vertical integral of water vapor:

$$\phi = \int_0^{p_s} q dp \quad (4)$$

Changes to the $P - E$ balance of Eq. 3 must originate from one of two sources: (i) localized fluxes of precipitation or evaporation (i.e., the first term inside the parentheses on the right) or (ii) the convergence or divergence of vertically integrated moisture flux (i.e., the second term inside the parentheses). This second term can be further decomposed into separate changes originating from the mean flow, transport by transient eddies, divergence of the high-level winds, and advection of moisture gradients by the lower atmosphere (30).

In addition to atmospheric moisture budgets, idealized numerical modeling experiments serve as invaluable tools for investigating the origins of drought (31). These experiments typically force a free-running atmosphere with prescribed sea surface temperature (SST) anomalies that are hypothesized to cause drought (31). Running multiple atmospheric simulations, all of which are forced with the same SST field, and then averaging these simulations together disentangles the SST “signal” in droughts from the atmospheric “noise.”

Causes of drought

The general circulation of the atmosphere delivers moisture from the world’s oceans to its continents. Some of that moisture becomes trapped in glaciers, aquifers, and lakes; the rest flows through soils, plants, and rivers. Drought occurs from aberrations to the flow of moisture through these terrestrial systems.

The largest disruptions to the global hydrological cycle occur during the El Niño and La Niña events (Fig. 1) (31–33). For example, El Niño displaces tropical rainfall in northeast Brazil, Central America, and the Caribbean, causing drought in those regions (32). Meanwhile, the areas that normally see strong convection, such as Indonesia and northern Australia, also experience rainfall shortages, crop losses, and wildfires (34, 35).

Although the El Niño–Southern Oscillation’s (ENSO’s) impacts on the global climate were recognized decades ago, moisture budgets and idealized SST-forcing experiments have now revealed key details of the dynamical processes responsible for those teleconnections (31, 33). Winter storms shift equatorward during El Niño years (36) because deep convection modifies the structure and flow of the storm tracks and hence the transport of moisture (36). This in turn can trigger drought in the Pacific Northwest and the

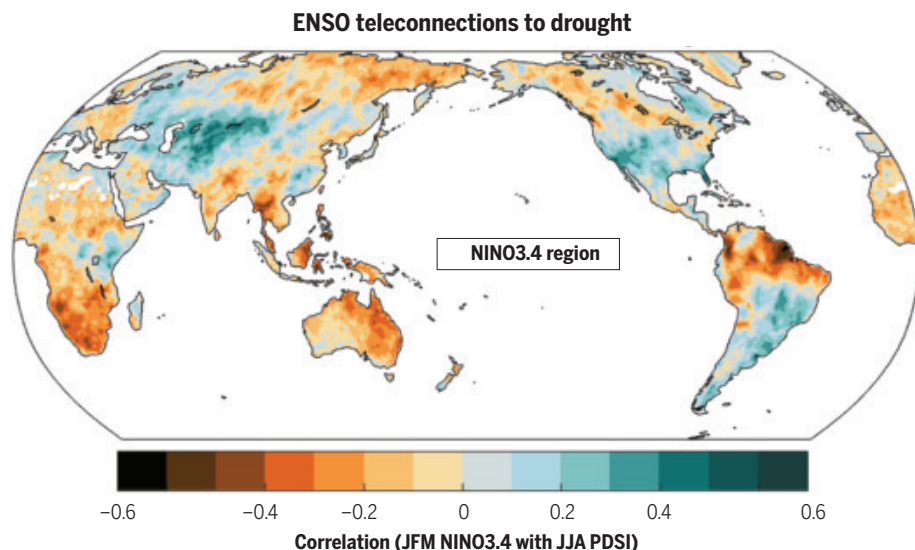


Fig. 1. Correlation coefficients between NINO3.4 SST (ERSSTv3b) and self-calibrating PDSI (30). All correlations are computed between boreal winter [January–February–March (JFM)] SSTs with PDSI during the following boreal summer [June–July–August (JJA)].

Modeling soil moisture

Given the apparent simplicity of Eq. 1, one might be tempted to model soil moisture directly using meteorological variables as boundary conditions, thus circumventing the need for drought indices (11). For example, the simplified bucket model extends global soil moisture estimates back to 1948 (11), but it lacks a number of critical processes that affect evapotrans-

a relatively short time period; they do not provide much information about interannual, let alone decadal, variations during the historical period.

Diagnosing drought dynamics

Atmospheric moisture budgets express the local balance of $P - E$ as a function of specific humidity (q) and horizontal winds (\vec{V}) (30):

southeastern United States owing to additional downstream effects (36).

On shorter time scales, seasonal modes of variability such as the North Atlantic Oscillation (NAO) can modify storm tracks crossing the Atlantic (37). During the positive phase of the NAO, winter storms crossing the Atlantic

tend to make landfall at higher latitudes (e.g., the United Kingdom and Scandinavia), which in turn favors drier conditions across France, Spain, Italy, and the Mediterranean region in general (37, 38).

Over longer time scales, decadal SST variability appears to be connected to drought (31),

although it can be difficult to disentangle such long-term effects from anthropogenic forcing (which may also affect decadal SST variations) (31).

Atmospheric moisture budgets also serve as invaluable tools for evaluating the realism of GCMs and for diagnosing their predictions of future aridity (39), although this remains a relatively underexplored area for future research.

Back to the future

If you are a water resource manager and you remember just one thing from this review, it should be this: Cutting CO₂ emissions reduces drought risk (6, 7). In many regions, including Central America, the Caribbean, the Amazon, Western Europe, and southern Africa, avoiding even just half a degree of warming makes a difference: Regional drying is more severe if global warming reaches 2.0°C than if it is curtailed at 1.5°C (6, 7).

Climate change alters the balance of moisture throughout the world by disrupting its supply through changes in the general circulation (39, 40). Meanwhile, higher temperatures can increase moisture demand from the land surface (12, 41) for the same reason that a sauna will dry out a towel faster than a steam room (see Eq. 2). Accordingly, regions seeing both a decrease in supply and an increase in demand are very sensitive to even low levels of warming (6).

Plants, however, may use water more efficiently as CO₂ concentrations increase in the atmosphere (42), and this “CO₂ fertilization effect” might partially offset a portion of future drying predicted for some regions (42–44). Nevertheless, there are several examples of models that predict reductions in soil moisture despite increases in overall precipitation and an increase in water use efficiency by plants (5, 42, 44). That is, the improvements in efficiency from higher CO₂ concentrations reduce the total amount of drying, which is substantial, but they do not reverse it (Fig. 2).

Finally, ENSO will likely continue to disrupt hydroclimate across vast spatial scales (32). When it does, the impacts of El Niño on drought could be even more severe than they are today for two reasons: (i) We expect climate change to strengthen ENSO events (45, 46), and (ii) a hotter atmosphere demands more moisture from the land surface when droughts occur (41, 47). Even now, higher temperatures may already be worsening aridity beyond anything seen in the past few centuries (27).

The future of drought research

Legions of studies have used the analytical arsenal described earlier to confront fundamental questions about the physics, dynamics, and risks of drought in a changing climate. For example, they have asked:

1) How do future droughts and long-term changes in aridity compare with modern-day

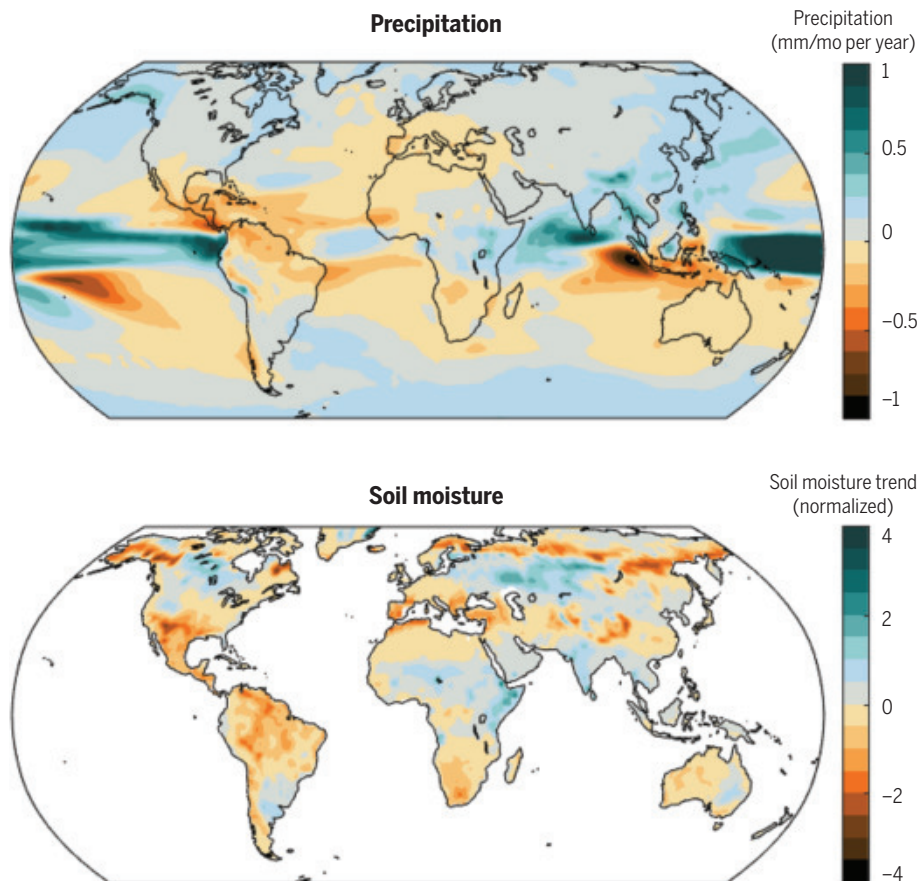


Fig. 2. Annual precipitation totals (blue) and JJA volumetric soil moisture averages (brown) from the CESM large ensemble (50).

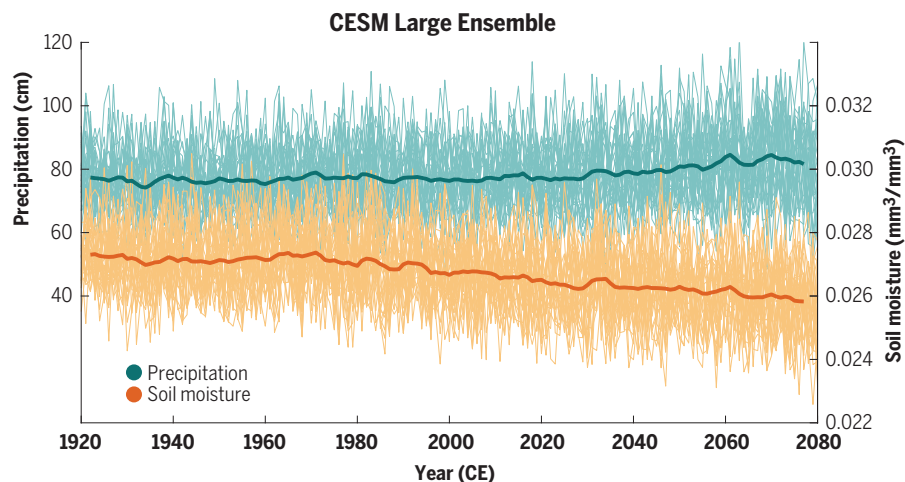


Fig. 3. Ensemble-averaged 21st-century Climate Model Intercomparison Project V (CMIP5) trends computed from annual precipitation (top) and column-integrated soil moisture (bottom).

Tropical decadal variability in CMIP5

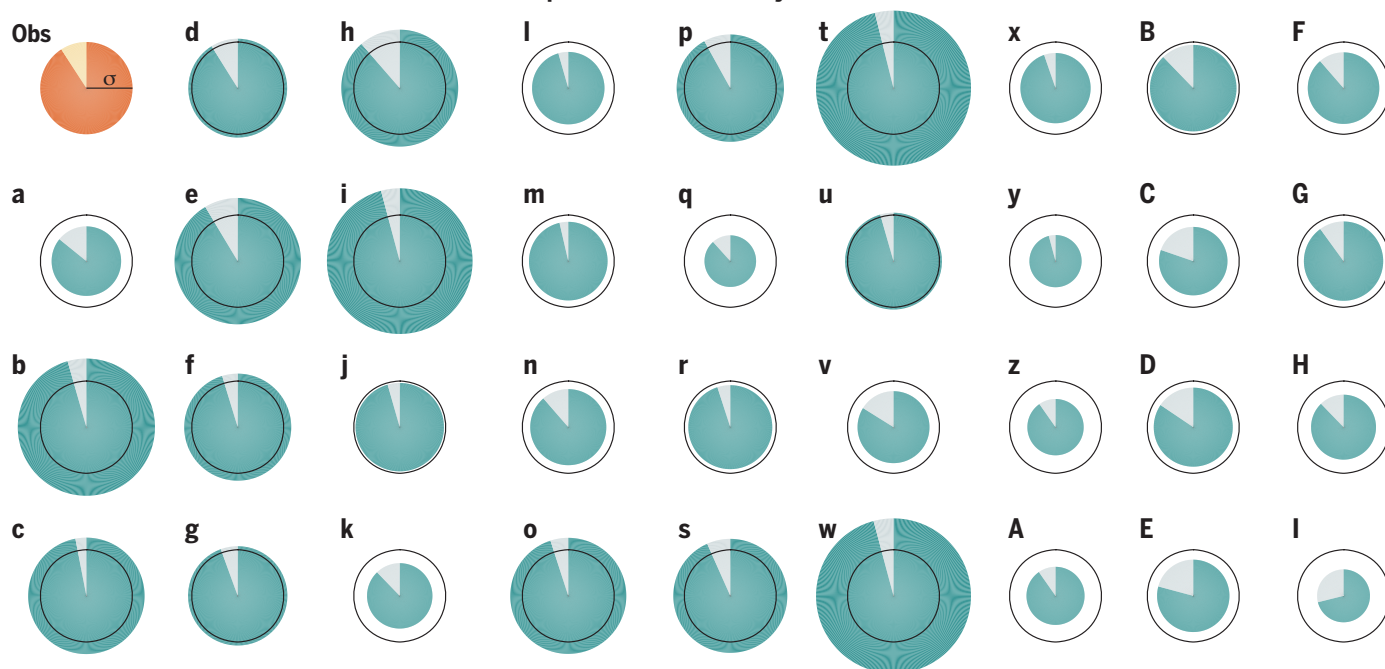


Fig. 4. Summary of tropical Pacific variability in observations and models.

The circle in the topmost left is derived from observational data, with the radius being proportional to the standard deviation ($\pm 1.5^{\circ}\text{C}$) of NINO3.4 and the lighter color representing the fraction of the total variance that occurs on decadal time scales in the NINO3.4 region ($\sim 8.5\%$). The remaining charts summarize this same information for individual members of the CMIP5. Again, the radii of each circle are proportional to the standard deviation of a given model, and the lighter color represents the fraction of total variance occurring on decadal time horizons. For reference, the outline of the observational NINO3.4 chart is included on each model diagram. Variability in circle size emphasizes the now well-known differences in El Niño and Southern Oscillation amplitudes across the CMIP5 archive. Differences in the fraction of variance occurring

on decadal time scales, in conjunction with differences in ENSO amplitudes, have received less attention. The models are identified by a single letter as follows: (a) ACCESS1.3; (b) BNU-ESM; (c) CCSM4; (d) CESM1-BGC; (e) CESM1(CAM5-FV2); (f) CESM1(CAM5); (g) CESM1(FASTCHEM); (h) CESM1(WACCM); (i) CMCC-CESM; (j) CMCC-CMS; (k) CMCC-CM; (l) CNRM-CM5-2; (m) CNRM-CM5; (n) CSIRO-Mk3.6.0; (o) CanCM4; (p) CanESM2; (q) EC-EARTH; (r) FGOALS-g2; (s) FIO-ESM; (t) GFDL-CM2.1; (u) GFDL-CM3; (v) GFDL-ESM2G; (w) GFDL-ESM2M; (x) GISS-E2-H-CC; (y) GISS-E2-H; (z) GISS-E2-R-CC; (A) GISS-E2-R; (B) HadCM3; (C) HadGEM2-AO; (D) HadGEM2-CC; (E) HadGEM2-ES; (F) IPSL-CM5A-LR; (G) IPSL-CM5A-MR; (H) IPSL-CM5B-LR; and (I) MIROC-ESM-CHEM. When multiple realizations were available, only the first simulation was used.

conditions (19–21, 41)? Which indices and models should be used to characterize future droughts (21, 42, 43)? Is there already a *detectable* imprint of anthropogenic climate change on global drought (19, 20, 27)?

2) How will regional changes in temperature affect moisture demand from the atmosphere through evapotranspiration (42, 43)? What role does vegetation play in coupling the land surface to the atmosphere (42–44)?

3) How will the supply of moisture to land evolve in response to large-scale changes in the general circulation (39)? How will ENSO and other seasonal variations influence drought in the future (46, 48)?

In addressing these questions, researchers have begun assembling the puzzle of drought risks in a changing climate. Many regions may face events that are more severe, frequent, and long-lasting than those of the recent past (13, 21, 26) or even the last millennium (4, 5, 27). However, not all of the pieces fit together.

Wet, hot American summer drought

Perhaps the most contentious debate among drought researchers stems from differences

between drought indices (as described above) computed from GCMs and soil moisture simulated by those same models. Drought indices depict unprecedented drying throughout much of the United States (5, 20, 21), but these indices do not account for biological processes (such as CO_2 uptake) that may alter the surface moisture balance in the future (42, 43). They are also sensitive to the length and quality of historical data used to calibrate them (12, 21) and may distort the magnitude of future changes if they are not calibrated appropriately (12, 19–21). Finally, their reliance on the Penman-Montieth equation might overestimate future PET rates (43).

Soil moisture projections from LSMs help to characterize some limitations of drought indices, although they have their own pitfalls. For example, soil moisture data are not widely available in most regions, making it difficult to directly compare LSM output against the historical record (26). LSMs typically overestimate evapotranspiration rates (49), which in turn makes them too strongly coupled to the atmosphere, and artificially enhance precipitation in some regions (49). Although they can simulate CO_2 “fertilization” in plants, their mod-

ules for representing ecological interactions among plants, soil moisture, and runoff all introduce new uncertainties that propagate into their projections of the future (26, 44).

Although GCM-based drought indices and soil moisture variables do not paint an entirely consistent picture of future drying, their differences may be superficial (44) (Fig. 2). In the case of the Community Earth System Model (CESM) “large ensemble” (50), the apparent paradox of increased drought risk in a wetter climate is easy to reconcile from the perspective of soil moisture balance: The increase in demand for evaporation from higher temperatures exceeds the increase in supply from precipitation. Future research could elaborate on these details in other models and other parts of the world.

Expanding outward

Quantifying how uncertainties in the large-scale circulation of GCMs are manifest in regional predictions of drought presents a harder problem for researchers (51). For example, GCM simulations of the 21st century depict a scenario in which the subtropics become drier

but wet equatorial regions become rainier (40) (Fig. 3). In a general sense, this subtropical drying is a robust thermodynamic response to higher temperatures: A warmer atmosphere can “hold” more water vapor, yet the rate at which water vapor increases in the atmosphere outpaces the rate of precipitation increase (39, 40). Accordingly, less moisture evaporates from the ocean to meet the demand for precipitation, which slows tropical circulation (40).

Most of the slowdown in tropical circulation occurs in the meridional Hadley cells, causing them to widen (40), which dries the subtropics. GCMs predict a similar outcome over the tropical Pacific Ocean because the east-west Walker circulation should also slow in conjunction with the Hadley cells (52). However, this is not happening (53)—or if it is happening, recent trends in the historical record are being dominated by other processes. One possible cause for this discrepancy is that the Walker circulation is responding differently in reality than it does in models to greenhouse gas forcings (48). That is, the recent observed changes are a forced dynamical adjustment in the coupled ocean-atmosphere system that the GCMs do not capture (48).

Alternatively, substantial internal *decadal* variability in the equatorial Pacific Ocean may be overshadowing the forced response of the Walker circulation (54). On this point, models do not agree with each other, let alone with the observations, on the relative importance of decadal variability in the tropical Pacific (Fig. 4).

For the time being, the issue must be regarded as unresolved. However, its resolution is vital to our portrait of 21st-century drought risk because the structure of the Walker circulation affects rainfall throughout the world (39).

The issues described above will manifest in the mean moisture balance of the tropics and subtropics, but droughts of the future will be caused by both the long-term changes in the general circulation and short-term deviations during El Niño and La Niña events (in addition to other modes of climate variability). Again, GCMs do not agree with one another, nor the historical record, on the amplitude of ENSO fluctuations and the relative importance of decadal variability (Fig. 4) (55, 56). Because the tropical Pacific exerts a major influence on global precipitation patterns (32) (Fig. 1), frequency biases in this region likely affect the statistics of precipitation in regions with strong ENSO teleconnections. Quantifying the relationship between ENSO frequency biases in GCMs (as well as potential changes in ENSO frequency) and drought presents an important area for future research.

New additions to the analytical arsenal

During the past 30 years, intellectual and technological breakthroughs accelerated the pace of drought research. In the 1990s, personal com-

puters enabled scientists to develop, analyze, and deploy our current generation of drought indices. In the early 2000s, investments in high-performance computing and land surface models helped lay the foundation for the sophisticated LSMs used today. In the 2010s, satellites began making unprecedented global measurements of surface soil moisture (29). Although all these technologies brought powerful tools into our analytical arsenal, they are not very egalitarian. Most farmers living in the Majority World must confront the hazards of drought in a changing climate with little, if any, access to the technological advancements of recent decades.

Encouragingly, the late 2010s also introduced very low-cost soil moisture sensors, which are already being deployed through public partnerships with local communities (57). These sensors transmit information about the state of the land surface continuously and nearly instantaneously, and researchers can use this data to validate satellite retrievals, initialize near-term predictions, or study the flow of moisture through the land surface with an unprecedented density of in situ measurements. At the same time, local communities are able to use data from those devices to gain insight into current conditions. During the 2020s, this emerging “Internet-of-things” technology could become the new frontier of drought monitoring and modeling.

Imagine, again, that you are a farmer in the Caribbean during a drought, but this time, the year is 2035. It is exceptionally hot (7), aquifers are depleted (58), and there are frequent blackouts because reservoir levels are so low at the hydroelectric power plant (59). What would you ask us—the people alive today—to do now to ensure that you are resilient in the face of drought in a changing climate?

REFERENCES AND NOTES

1. I. R. Tannehill, *Drought: Its Causes and Consequences* (Princeton Univ. Press, 1947).
2. D. A. Herrera et al., *Geophys. Res. Lett.* **45**, 10619–10626 (2018).
3. A. B. Smith, J. L. Matthews, *Nat. Hazards* **77**, 1829–1851 (2015).
4. B. I. Cook et al., *Wiley Interdiscip. Rev. Clim. Chang.* **7**, 411–432 (2016).
5. B. I. Cook, T. R. Ault, J. E. Smerdon, *Sci. Adv.* **1**, e1400082 (2015).
6. F. Lehner et al., *Geophys. Res. Lett.* **44**, 7419–7428 (2017).
7. M. A. Taylor et al., *J. Clim.* **31**, 2907–2926 (2018).
8. D. A. Wilhite, *Drought as a Natural Hazard: Concepts and Definitions* (Drought Mitigation Center Faculty Publications, 2000).
9. K. T. Redmond, *Bull. Am. Meteorol. Soc.* **83**, 1143–1148 (2002).
10. A. K. Mishra, V. P. Singh, *J. Hydrol. (Amst.)* **391**, 202–216 (2010).
11. Y. Fan, H. van den Dool, *J. Geophys. Res. D Atmospheres* **109**, D10102 (2004).
12. A. Dai, T. Zhao, *Clim. Change* **144**, 519–533 (2017).
13. A. Dai, T. Zhao, J. Chen, *Curr. Clim. Change Rep.* **4**, 301–312 (2018).
14. W. M. Alley, *J. Clim. Appl. Meteorol.* **23**, 1100–1109 (1984).
15. S. M. Vicente-Serrano, S. Beguería, J. I. López-Moreno, *J. Clim.* **23**, 1696–1718 (2010).
16. Z. Hao, A. Agha Kouchak, *Adv. Water Resour.* **57**, 12–18 (2013).
17. N. K. Guttman, *J. Am. Water Resour. Assoc.* **35**, 311–322 (1999).
18. N. Wells, S. Goddard, M. J. Hayes, *J. Clim.* **17**, 2335–2351 (2004).
19. J. Sheffield, E. F. Wood, M. L. Roderick, *Nature* **491**, 435–438 (2012).
20. A. Dai, *Nat. Clim. Chang.* **3**, 52–58 (2013).
21. K. E. Trenberth et al., *Nat. Clim. Chang.* **4**, 17–22 (2014).
22. R. G. Allen, L. S. Pereira, D. Raes, M. Smith, *Crop Evapotranspiration: Guidelines for Computing Crop Water*

- Requirements. FAO Irrigation and Drainage Paper 56 (FAO, 1998).
23. R. M. Maxwell, L. E. Condon, *Science* **353**, 377–380 (2016).
24. D. M. Remppe, W. E. Dietrich, *Proc. Natl. Acad. Sci. U.S.A.* **115**, 2664–2669 (2018).
25. M. Rodell et al., *Bull. Am. Meteorol. Soc.* **85**, 381–394 (2004).
26. A. Berg, J. Sheffield, *Curr. Clim. Change Rep.* **4**, 180–191 (2018).
27. K. Marvel et al., *Nature* **569**, 59–65 (2019).
28. W. A. Dorigo et al., *Hydrol. Earth Syst. Sci.* **15**, 1675–1698 (2011).
29. D. Entekhabi et al., *Proc. IEEE* **98**, 704–716 (2010).
30. K. E. Trenberth, C. J. Guillemot, *J. Clim.* **8**, 2255–2272 (1995).
31. S. D. Schubert et al., *J. Clim.* **29**, 3989–4019 (2016).
32. A. Dai, T. M. L. Wigley, *Geophys. Res. Lett.* **27**, 1283–1286 (2000).
33. K. E. Trenberth, J. Fasullo, L. Smith, *Clim. Dyn.* **24**, 741–758 (2005).
34. J.-H. Qian, A. W. Robertson, V. Moron, *J. Atmos. Sci.* **67**, 3509–3524 (2010).
35. N. Zeng, A. Mariotti, P. Wetzel, *Global Biogeochem. Cycles* **19**, GB1016 (2005).
36. R. Seager et al., *Q. J. R. Meteorol. Soc.* **136**, 277–296 (2010).
37. J. W. Hurrell, *Science* **269**, 676–679 (1995).
38. J. I. López-Moreno, S. M. Vicente-Serrano, *J. Clim.* **21**, 1220–1243 (2008).
39. R. Seager, N. Naik, G. A. Vecchi, *J. Clim.* **23**, 4651–4668 (2010).
40. I. M. Held, B. J. Soden, *J. Clim.* **19**, 5686–5699 (2006).
41. B. I. Cook, J. E. Smerdon, R. Seager, S. Coats, *Clim. Dyn.* **43**, 2607–2627 (2014).
42. A. L. S. Swann, F. M. Hoffman, C. D. Koven, J. T. Randerson, *Proc. Natl. Acad. Sci. U.S.A.* **113**, 10019–10024 (2016).
43. P. C. Milly, K. A. Dunne, *Nat. Clim. Chang.* **6**, 946–949 (2016).
44. J. S. Kankin, J. E. Smerdon, B. I. Cook, A. P. Williams, R. Seager, *J. Clim.* **30**, 8689–8710 (2017).
45. W. Cai et al., *Nat. Clim. Chang.* **5**, 132–137 (2015).
46. J. T. Fasullo, B. L. Otto-Bliesner, S. Stevenson, *Geophys. Res. Lett.* **45**, 9216–9225 (2018).
47. J. E. Herrera-Estrada, J. Sheffield, *J. Clim.* **30**, 6225–6246 (2017).
48. R. Seager et al., *Nat. Clim. Chang.* **9**, 517–522 (2019).
49. B. Mueller, S. I. Seneviratne, *Geophys. Res. Lett.* **41**, 128–134 (2014).
50. J. E. Kay et al., *Bull. Am. Meteorol. Soc.* **96**, 1333–1349 (2014).
51. C. Wang, L. Zhang, S. K. Lee, L. Wu, C. R. Mechoso, *Nat. Clim. Chang.* **4**, 201–205 (2014).
52. G. A. Vecchi et al., *Nature* **441**, 73–76 (2006).
53. M. L. L'Heureux, S. Lee, B. Lyon, *Nat. Clim. Chang.* **3**, 571–576 (2013).
54. E. S. Chung et al., *Nat. Clim. Chang.* **9**, 405–412 (2019).
55. T. R. Ault, J. E. Cole, S. St. George, *Geophys. Res. Lett.* **39**, L21705 (2012).
56. L. Parsons et al., *J. Clim.* **30**, 8885–8912 (2017).
57. M. Karamouz, A. Ghomlaghi, R. S. Alipour, M. Nazari, M. Fereshtehpour, in *World Environmental and Water Resources Congress 2019: Emerging and Innovative Technologies and International Perspectives*, G. F. Scott, W. Hamilton, Eds. (American Society of Civil Engineers, 2019), pp. 85–95.
58. S. Holding et al., *Nat. Clim. Chang.* **6**, 1100–1103 (2016).
59. Food and Agriculture Organization of the United Nations, *Drought Characteristics and Management in the Caribbean: Technical Report* (FAO, 2016).

ACKNOWLEDGMENTS

I thank D. H. Herrera, C. P. Evans, M. J. Alessi, C. R. Ault, P. C. Ault, and R. Moore for their helpful comments and feedback on the content covered by this review. **Funding:** This effort was partially supported by a National Science Foundation (NSF) grant (1602564) and an NSF CAREER award (1751535). **Competing interests:** None. **Data and materials availability:** Data used for the figures in this review originate from public archives as follows: Fig. 1: Global gridded PDSI data from (19) were obtained from Princeton University's Terrestrial Hydrology Research Group's public data repository (<https://hydrology.princeton.edu/data.pdsi.php>), and NINO3.4 SST data were downloaded from the ESRL PSD Climate Indices page (<https://www.esrl.noaa.gov/psd/data/climateindices/list/>). Fig. 2: All CMIP5 soil moisture data were downloaded from the Earth System Grid Federation node operated by the Lawrence Livermore National Lab (<https://esgf-node.llnl.gov/projects/cmip5/>). Fig. 3: Soil moisture data from the CESM large ensemble are available from NCAR's ESG node (https://www.earthsystemgrid.org/dataset/ucar.cgd.cesm4.CESM_CAM5_BGC_1E_Ind.proc.monthly_ave.html). Fig. 4: NINO3.4 time series used for this figure were also derived from the CMIP5 archive but were downloaded from NCAR's public repository of Climate Variability Diagnostic Package output (http://webext.cgd.ucar.edu/Multi-Case/CVDP_ex/CMIP5-Historical/).

10.1126/science.aaz5492



A carcass of an elephant that succumbed to drought is seen under a tree in Hwange National Park, in Zimbabwe, on 12 November 2019.

REVIEW

Hanging by a thread? Forests and drought

Timothy J. Brodribb^{1*}, Jennifer Powers², Hervé Cochard³, Brendan Choat⁴

Trees are the living foundations on which most terrestrial biodiversity is built. Central to the success of trees are their woody bodies, which connect their elevated photosynthetic canopies with the essential belowground activities of water and nutrient acquisition. The slow construction of these carbon-dense, woody skeletons leads to a slow generation time, leaving trees and forests highly susceptible to rapid changes in climate. Other long-lived, sessile organisms such as corals appear to be poorly equipped to survive rapid changes, which raises questions about the vulnerability of contemporary forests to future climate change. The emerging view that, similar to corals, tree species have rather inflexible damage thresholds, particularly in terms of water stress, is especially concerning. This Review examines recent progress in our understanding of how the future looks for forests growing in a hotter and drier atmosphere.

No tree species can survive acute desiccation. Despite this unambiguous constraint, predicting the death of trees during drought is complicated by the process of evolution, whereby the fitness of tree species may benefit equally from traits that either increase growth or enhance drought resilience. Complexity arises because improving either of these two beneficial states often requires the same key traits to move in opposite directions, which leads to important trade-offs in adaptation to water availability. This conflict promotes strategic diversity in different species' adaptations to water availability, even within ecosystems. Understanding how the diversity of tree species will be affected by future droughts requires a detailed knowledge of how the functions of different species interact with their environment. Temperature and atmospheric CO₂ concentration are fundamental elements that affect the water relations of all tree species, and the rapid rise in both of these potent environmental drivers has the poten-

tial to markedly change the way trees behave during drought. The future of many forest systems will be dictated by how these atmospheric changes interact with tree function.

Is rising CO₂ good for trees?

A primary example of conflicting selection pressures on trees can be seen in the basic operation of photosynthesis. Achieving a higher photosynthetic rate requires higher leaf porosity to CO₂, but a higher leaf porosity causes a parallel increase in water loss, which is detrimental during an environmental water shortage. This trade-off plays a fundamental role in structuring terrestrial plant evolution and ecology (1), emphasizing the potential for rising CO₂ levels and temperatures to affect forests during drought conditions. There has been a change in perspective over the past 10 years, from expectations of enhanced forest growth under enriched atmospheric CO₂ to the more sobering prospect of damage or decimation of standing forest caused by an increase in the drying rates of leaves and soil in a hotter climate (2).

Early discussions of plant responses to rising atmospheric CO₂ (3) focused largely on CO₂ fertilization, a concept that refers to the potentially beneficial effects of atmospheric CO₂ enrichment on plant growth. Under controlled conditions, elevated CO₂ can theoretically in-

crease plant growth by stimulating photosynthesis or by increasing the water use efficiency (WUE) of plants (the ratio of carbon intake to water lost by leaves). Both of these behaviors depend on the active response of stomata (microscopic valves on the leaf surface that regulate gas exchange) to CO₂ (4). Long-term studies of tree growth under artificially enhanced atmospheric CO₂ suggest that improved photosynthetic performance at elevated CO₂ can translate into increased growth (5, 6), but there is little evidence of any CO₂-associated growth enhancement in natural forest conditions (7, 8). This is thought to be either because of colimiting resources for plant growth, such as water and nitrogen (9–11), or because stomatal closure in response to rising CO₂ increases WUE (12, 13) at the cost of enhanced assimilation and growth. Controversially, it has been suggested that the impacts of future drought stress may be ameliorated by higher atmospheric CO₂ if WUE is sufficiently enhanced (14, 15). The validity of this concept depends largely on the effects of rising temperature on WUE and plant survival during extended rainfall deficits.

Rising temperature and drought

Ultimately, the impact of elevated CO₂ on forest trees is likely to come down to the intensity of the CO₂-associated temperature rise and its effect on trees' water use. This is because the distributions of tree species, in terms of water availability, broadly reflect their intrinsic tolerance of water stress (16–18). In other words, species from rainforests to arid woodlands face similar exposure to stress or damage during periods of drought (19). Hence, any increase in the rate of soil drying caused by elevated temperatures is likely to lead to increasing damage to standing forests during drought. Improved tree WUE could ameliorate the temperature effect, but this argument remains highly debatable because most reports of improvements in tree WUE with rising atmospheric CO₂ refer to intrinsic WUE, a value that converts to real plant water use only with a knowledge of leaf temperature and atmospheric humidity (20). Thus, rising atmospheric temperature and the associated increase in evaporative demand is likely to reverse the improvements in tree WUE that are proposed to result from higher CO₂. Recent evidence suggests that this is the case, with observations of reduced global tree growth and vegetation health associated with enhanced evaporative gradients and warming temperatures (21, 22).

In combination with the size and allometry of trees, the dynamic behavior of stomata and

¹School of Biological Sciences, University of Tasmania, Hobart, TAS 7001, Australia. ²Departments of Ecology, Evolution and Behavior and Plant and Microbial Biology, University of Minnesota, 140 Gortner Laboratory, Saint Paul, MN 55108, USA.

³Université Clermont Auvergne, INRAE, PIAF, 63000 Clermont-Ferrand, France. ⁴Hawkesbury Institute for the Environment, Western Sydney University, Penrith, NSW 2751, Australia.

*Corresponding author. Email: timothyb@utas.edu.au

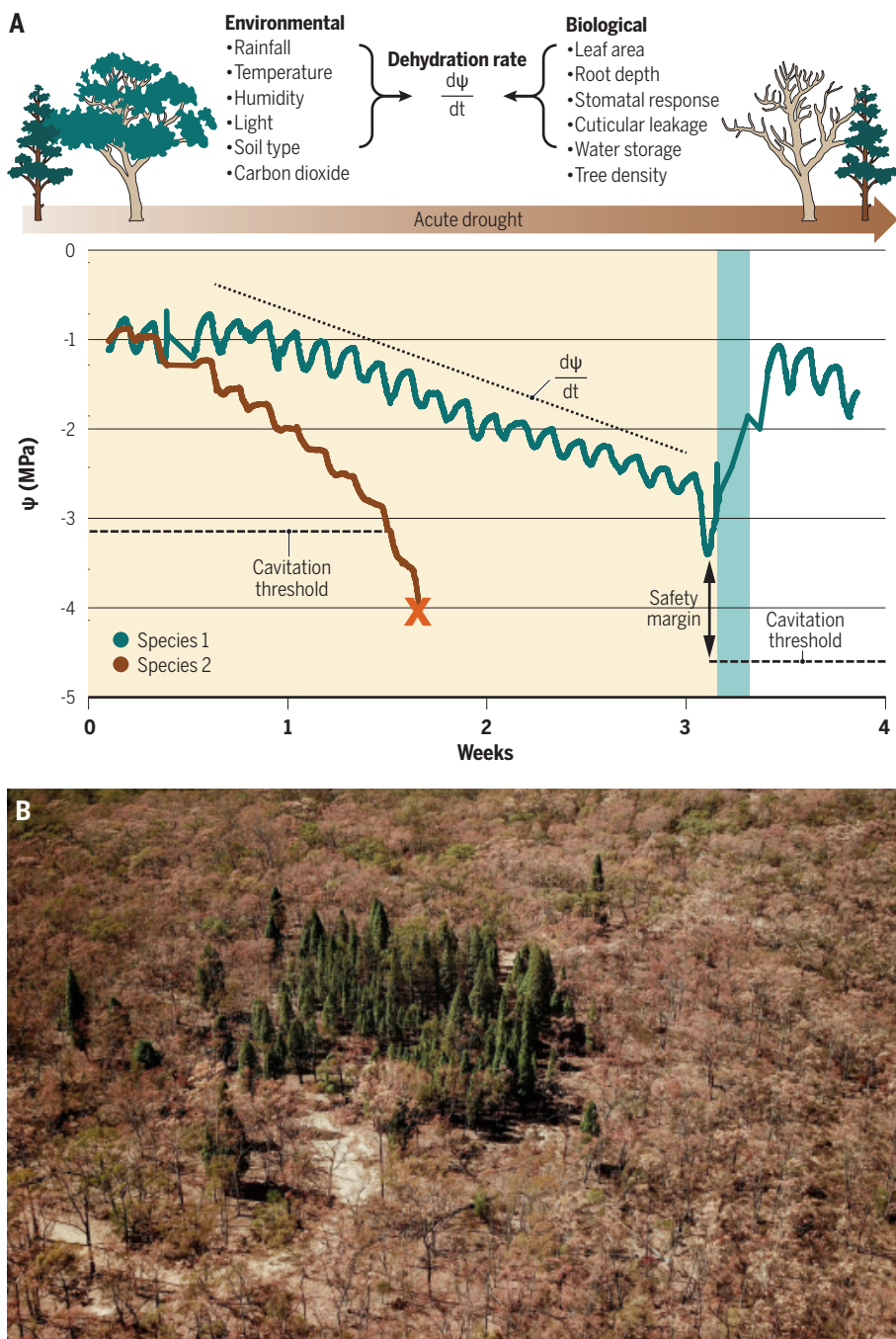


Fig. 1. Theoretical and observed impacts of drought on co-occurring tree species. (A) A representation of the impact of drought on two tree species with different thresholds for drought-induced vascular damage. Different xylem cavitation thresholds determine the water potential (Ψ : water stress intensifies as water potential becomes more negative) causing tree mortality. Two lines indicate the oscillating water stress between day and night as the two species (indicated by small tree icons) dehydrate after the cessation of rainfall (data are from two trees from a dry forest site in Tasmania, Australia). The cavitation threshold and the rate of drying ($d\Psi/dt$) both determine how many days into an acute drought each species will die. The taller species, which is more vulnerable to cavitation and faster drying, dies (indicated by an orange X) in week 2, whereas the shorter species survives until rainfall (indicated by the blue rectangle in week 3), enabling the tree to recover hydration. The proximity between the cavitation threshold and the lowest water potential during drought is known as the hydraulic safety margin. The dehydration rate is a product of a set of environmental and biological factors, many of which interact. Increasing temperature increases the rate of drying both directly and by interaction with biological factors, whereas CO_2 has the potential to reduce dehydration by its biological interaction with stomata and the photosynthetic rate. (B) Recent (2019) drought-induced mortality of native forest in eastern Australia. Large-scale mortality of *Eucalyptus* trees (seen as recently killed dry canopies) contrast with the more cavitation-resistant conifer species (*Callitris*). The observed pattern of mortality can be explained by the processes described in (A).

their regulation of water loss from tree canopies largely dictates the course of plant and soil dehydration. During atmospheric or soil water deficit, stomatal closure limits transpiration, preserving water content in the soil and tree (23). However, this well-characterized behavior becomes unpredictable when leaf temperatures are substantially elevated, with stomata permitting greater water loss than expected during both day (24, 25) and night (26–28). Additionally, plants continue to lose some residual water after the stomatal valves are closed, and this residual leakiness also appears to increase with elevated temperatures (29–31). Herein lies perhaps the greatest threat for forests subjected to warming atmospheric temperature, because warmer plants not only consume water faster when soils are hydrated, but they also have a diminished capacity to restrict water loss during drought, thereby exhausting soil water reserves.

Tree mortality is most commonly observed when drought and high temperature are combined (32–34), likely owing to the compounding effects of the increased evaporative gradient and the increased porosity of leaves at high temperature. The inevitable rise in the intensity and/or frequency of such events as global temperatures climb (35) has already been associated with an increase in tree mortality globally (36), especially in larger trees (37), which raises a grave concern about the capacity of existing forests to persist into the future. Establishing the magnitude of this threat is an important challenge that requires a fundamental understanding of how water deficit leads to tree mortality.

Much research has focused on the possible mechanisms behind tree death during drought. Possible mechanisms primarily include vascular damage, carbon starvation, and enhanced herbivory (38–42). These studies reveal the complex nature of tree death, where the moment of death is difficult to pinpoint or even define (43). Although it remains difficult to connect cause and effect at the point where drought injury becomes lethal, strong and consistent correlational data from trees suffering mortality or growth inhibition across the globe point unequivocally to the plant water transport system as a fundamental axis dictating the long-term survival of trees (44–47).

Forests on a thread

The massive woody structure of trees provides mechanical support for their photosynthetic crowns; however, the matrix of microscopic threads of water that is housed within the porous woody cells of the xylem is even more fundamental to tree survival. These liquid threads provide a highly efficient mechanism to transport large quantities of water over long distances under tension, from the roots to the leaves. Relying on this passive pathway to

replace the water transpired by leaves has the major drawback that the internal water column in trees becomes increasingly unstable during times of water stress, as the tension required to draw water from the soil increases. Rising xylem water tension (conventionally described as an increasingly negative water potential) during intensifying soil water deficit exposes a universal vulnerability in trees to xylem cavitation during drought (48). This occurs when the water potential in the xylem becomes sufficiently negative to draw minute bubbles through the cell wall into the lumen of the xylem cells, at which point the small bubbles trigger a very rapid formation of voids (in a process termed xylem cavitation), which subsequently become air bubbles or embolisms that block water flow. The vulnerability of a species to cavitation is conventionally quantified as a P50, which is the water potential that causes 50% of the xylem to cavitate. The most extreme form of xylem damage occurs when a feedback develops, as increasing xylem water tension caused by soil water deficit leads to xylem cavitation and blockage, further exacerbating the tension in the xylem, and ultimately killing the plant by completely severing the connection between soil and leaves. This process is likely to occur under acute water shortage (49, 50), killing plants (51) before the return of rainfall. Although this type of acute drought-induced mortality may not describe all instances of tree death during water shortage, the existence of quantifiable biophysical thresholds defining specific survival limits for different tree species has greatly enabled our capacity to understand tree mortality and distribution (42) and provides a robust basis for modeling future effects of drought (52, 53). Many aspects of the xylem cavitation process remain uncertain because of difficulties associated with measuring water flow in a system that operates under high tension (54); however, new methods are providing more clarity and confidence to our understanding of the critical sensitivity of plant vascular systems to damage under water stress (55, 56).

The water transport system in plants lies at the center of interactions between rainfall, soil water, carbon uptake, and canopy dehydration, which makes xylem hydraulics an obvious focus for understanding and predicting the thresholds between tree death or survival during exposure to drought and heat stress. Xylem vulnerability to cavitation varies markedly among species (19), not only indicating sensitivity to water deficit but also enabling the quantification of functional impairment if trees are not immediately killed by drought (43, 50). Although a knowledge of cavitation thresholds informs the triggering of tree damage, the rate of tree dehydration indicates how quickly that damage threshold is approached during drought. The characteristics

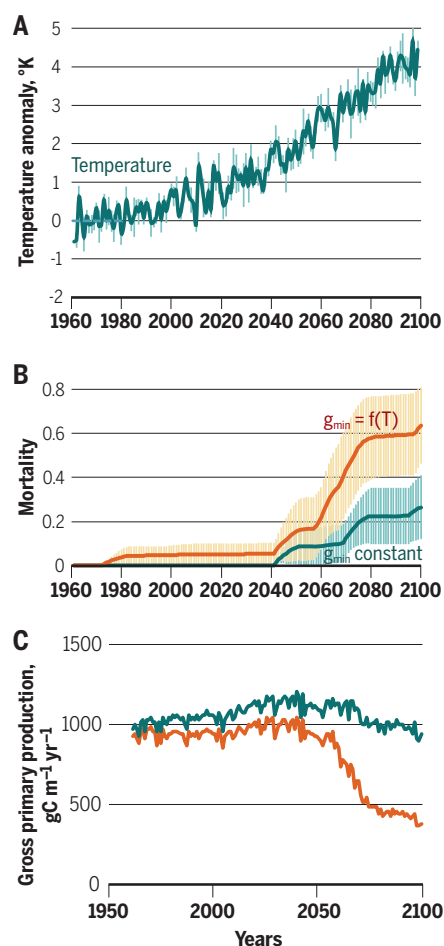


Fig. 2. A mechanistic hydraulic model of future drought-induced tree mortality. (A to C) Sensitivity of a process-based hydraulic model to predict tree mortality and gross primary production (GPP) under the representative concentration pathway (RCP) 8.5 climatic scenario. The model was parametrized with data for a population of a typical temperate coniferous tree, displaying a Gaussian distribution of cavitation resistance (mean xylem vulnerability of P50 = −3.5 MPa, variance = 0.3). Daily climatic data from five Eurocode climate models were used to simulate tree transpiration, soil water content, xylem water tension, and xylem cavitation. The lethal threshold of cavitation was set to 88%. The model forecasts an increase in tree mortality with the rise of temperature caused by predicted climate change. The predicted collapse of the tree population and forest GPP was more drastic when a more realistic temperature-dependent increase in the cuticular leakage (g_{min}) (108) was implemented in the model [$g_{min} = f(T)$; orange line] compared with a static cuticular leakage [g_{min} constant (gC); green line]

of tree species that are classically associated with adaptation to water availability—such as rooting depth, water storage, stomatal behavior, root and canopy area, and leaf phenology—can be predictably integrated to determine how plant water content will respond to environmental conditions. The combination of environ-

mental conditions with biological attributes results in a highly tractable framework (Fig. 1) for understanding the dynamics of mortality or survival during slow dehydration (57).

Despite the existence of sharp xylem cavitation thresholds, post-drought legacies of damage and mortality of trees are often protracted over months or years after peak drought intensity (58), which implies that more-complex interactions between plant water and carbon status are also important in the recovery process. Post-drought rainfall enables trees that have not suffered catastrophic xylem failure to replace drought-damaged xylem by woody regrowth (50), but this is highly costly and can lead to rapid depletion of tree carbon reserves (59), leaving them vulnerable to insect attack [although insect interactions remain unpredictable (60)] unless conditions remain favorable. Recovering, drought-damaged trees may invest disproportionately in new leaves rather than xylem growth (61), potentially making them more sensitive to subsequent water shortage because of reduced xylem water delivery. Although much remains to be learned about the physiology of plant hydraulics, the principles of hydraulic failure provide a solid framework for understanding and predicting mortality, damage, and recovery under a diversity of drought scenarios.

Modeling forest mortality in the future

Diverse approaches have been employed to predict how forests are likely to respond to hotter and potentially drier and more-variable conditions in the future. Progress toward understanding the mechanisms that lead to tree mortality has seen a movement away from traditional correlative niche models (62) in favor of more process-based modeling. Incorporation of theoretically derived mortality modules into dynamic vegetation models has the potential to capture drought mortality, but these models are currently rather unsophisticated and unreliable, particularly when applied outside the domain of calibration (63, 64). At the more functional end of the modeling spectrum are recent attempts to explicitly model drought mortality triggered by hydraulic failure (or associated carbon starvation) (52). In particular, the combination of tree hydraulics with the principles of stomatal optimization (assuming that stomatal behavior regulates assimilation and transpiration to achieve a maximum difference between photosynthetic gain and the risk of hydraulic damage) is emerging as a promising structure for models of land surface gas exchange (65–67). Although the mathematical rendering of physiological processes to predict forest productivity and tree survival provides a powerful approach for modeling the performances of species or genotypes in a range of future climates, a limitation in using these mechanistic formulations is that relatively small

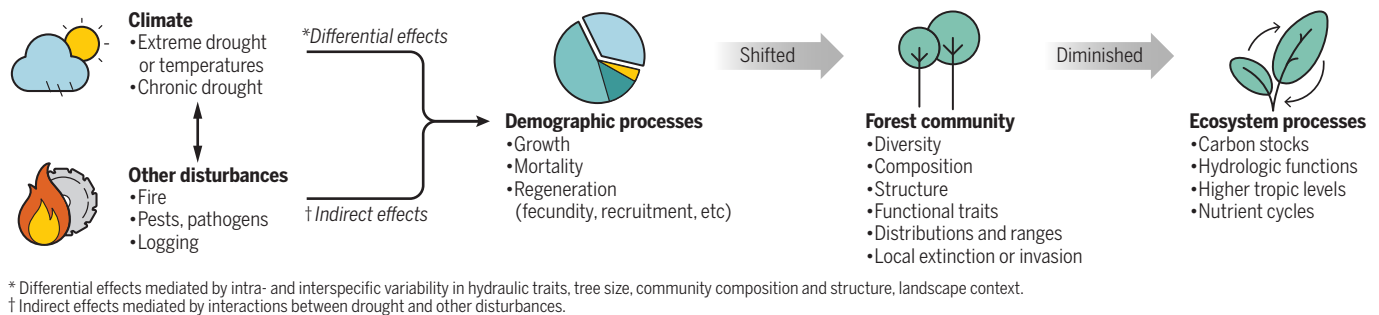


Fig. 3. Interactions between climate and forest community. Schematic of how climatic variability interacts with disturbance to affect tree demographic processes, which may result in shifted community diversity and species distributions as well as ecosystem processes.

changes in parameterization or biological assumption can substantially change predictions (Fig. 2). To capture this uncertainty, recent studies have spanned a range of assumptions, particularly with regard to how trees might acclimate to drought, in order to reveal a range of possible scenarios (15, 68).

Modeling provides the most credible view of how forests may cope with different intensities of future global warming, with most models suggesting large-scale mortality, range contraction, and productivity loss through this century under the current warming trajectories (Fig. 2). Greater precision as to the nature and pace of forest change is urgently needed, requiring dedicated work on key knowledge gaps (69) that limit model precision accuracy. These gaps are apparent in even the basic physiological processes of trees, such as stomatal behavior, tree water acquisition (70), and interactions between water and carbon stores in trees (67). Critical components such as the dynamic connection between trees and the soil are highly simplified in models owing to a lack of knowledge about water transfer and storage in the roots under conditions of water stress. The triggering of mortality is also highly oversimplified because the negative feedbacks likely to operate during acute tree stress are difficult to capture in a model. Avoiding this complexity, a commonly used proxy for lethal water stress is the point of 50% xylem cavitation in stems (Fig. 2). Although this threshold is not strictly correct (because trees can survive with a 50% impairment of water transport capacity), it does provide a readily measurable indication of rapid vascular decline incipient to complete failure of the vascular connection between roots and leaves. More-precise understanding of the post-drought transition to recovery or tree death is needed to accurately represent the legacy effects of drought in large-scale models.

Acclimation of forest in situ

The long generation time and slow growth of trees present a formidable challenge to survival in the face of rapid environmental change, particularly increases in aridity and the frequency of extreme-drought events. Avoidance of local extinction (extirpation) in tree species

is possible by two non-mutually exclusive mechanisms: (i) migration tracking the ecological niches to which they are adapted or (ii) adaptation and acclimation to novel climate conditions and persistence within their current range. Species distribution models based on climatic envelopes have predicted pronounced range shifts in tree populations over the next century; however, this mechanism of survival is contingent on the capacity of species to achieve rapid migration (71), and few tree species are likely to disperse rapidly enough to keep pace with the current rate of climate warming (72). The persistence of tree populations exposed to increased aridity in their current range will depend on adaptation and acclimation to higher intensities of plant water stress. Given the rapid pace of climate change, adaptation of organisms with such long generation times appears unlikely to enable persistence in most species.

The potential for rates of adaptation to keep pace with environmental change depends on a number of factors, including the levels of genetic diversity present in critical traits, differentiation between leading and trailing edge populations, and gene flow between populations. Very few studies have examined the genetic diversity present in important plant hydraulic traits, with the most-comprehensive studies focused on temperate deciduous and conifer species (73–75). The results of these studies suggest that genetic diversity of traits, such as cavitation resistance, is low in pine species (74) but may be higher in temperate angiosperms such as beech (73, 76). Overall, genetic diversity in hydraulic traits appears to be limited relative to the changes in intensity of water stress that are expected over the coming decades. This lack of genetic diversity across populations may limit the capacity for adaptation to increasing aridity in current distributions.

Acclimation by means of phenotypic plasticity presents another mechanism by which trees may adjust to novel climate regimes (77). Acclimation is dependent on trait plasticity in individuals and may occur over much shorter time scales than evolutionary processes such as adaptation. The acclimation of some physiological and morphological traits in response to changes in temperature and drought stress

is well documented. This includes the acclimation of photosynthesis, respiration, and leaf thermal tolerance to temperature (24, 71) and changes in resource allocation, such as sapwood-to-leaf ratio (78). For example, leaf shedding allows trees to rapidly reduce the leaf surface area available for transpiration and is a primary mechanism limiting water loss during drought. Studies examining intraspecific variation across precipitation gradients have shown that populations adjust to greater aridity through increasing sapwood-to-leaf ratios (79–81), increasing hydraulic capacity relative to leaf area deployed.

Acclimation in physiological traits related to drought tolerance is less well studied. However, the available data suggest that there is limited plasticity in key mechanistic traits. This is borne out in common-garden and reciprocal transplant experiments as well as throughfall exclusion experiments and studies of natural populations growing across aridity gradients (80, 82, 83). Low plasticity in hydraulic safety has also been observed with tree size (84), although the behavior of seedlings remains unknown. Pine species exhibit particularly low variation in cavitation resistance, with available evidence suggesting canalization of hydraulic traits, which constrains the capacity of pines to acclimate or adapt to drier conditions (74). Common-garden studies suggest that traits associated with hydraulic safety (Fig. 1) appear to be under strong genetic control (16, 81). This may be one reason why partial leaf shedding is a commonly observed response to drought, because higher plasticity in leaf area may assist trees in maintaining levels of water stress within the functional limits set by inflexible hydraulic failure thresholds. However, reducing leaf area comes at the cost of lowered productivity and growth rates, and it may adversely affect survival in trailing edge populations exposed to intense interspecific competition.

Communities and consequences

Although hydraulic failure may be sudden and pronounced, predicting the consequences of drought for tree populations and communities is more challenging than simply extrapolating from models of hydraulic processes. This is because drought may also affect demographic

processes beyond tree mortality and may interact with other disturbances. Stand-level interactions among individuals and species may attenuate or exacerbate drought impacts, and landscape-scale variations in topography, edaphic conditions, or forest-patch characteristics can modulate drought effects (Fig. 3). Moreover, current forest communities are responding to both extreme events, such as El Niño–Southern Oscillation (ENSO)–related droughts (85), and to directional changes in rainfall, such as decadal-long decreases in rainfall (86). What does seem certain is that these changes in forest composition and tree species distributions will have important consequences for the diversity and structure (69), hydrologic function (87), and carbon-storage potential (88) of future forests.

Interspecific variation in hydraulic and other traits is clearly linked to differential damage and mortality rates during extreme drought (47, 89, 90). However, other demographic processes or life history stages—such as fecundity, seedling recruitment, and tree growth—may also be affected, and species- or functional group-specific responses to drought may change community composition and functional traits over decadal time scales or even result in shifts among biomes, such as forests being replaced by shrublands (91). Regeneration dynamics are especially critical in mediating shifts between vegetation types or biomes (91), but, at this point, the data are too limited to generalize about how the likelihood of such shifts differs among forest types. For example, an extreme drought during the 2015 ENSO reduced seed rain of drought-deciduous tree species relative to evergreen trees and lianas in a seasonally dry tropical forest in Costa Rica (92). By contrast, in a semimoiest tropical forest in Panama, a 30-year record of leaf and fruit production showed elevated seed production during ENSO years that mirrors seasonal patterns, suggesting that the sunnier conditions that accompany ENSO favor fruit over leaf production (93).

Predicting or modeling the impacts of drought on forest communities is also complicated by interactions between changes in climate and interactions with other disturbance agents, such as fire (94), insects and pathogens (95), or logging (96). The catastrophic wildfires that have affected Australia in 2019 and 2020, after years of extreme drought, is just one such example of drought-fire interactions. Such interactions are also affecting forests in North America (97), Amazonia (94), and elsewhere (98). Increases in vapor-pressure deficit and temperature during drought dry out fuel, thereby increasing fire activity and the area that is burned (97). Drought-fire interactions may also cause tipping points and shifts among vegetation types in areas such as the southwestern Amazon (94). There, tree mortality is elevated during intense fires experienced in drought years (94), resulting in altered microclimatic conditions and grass

invasion into the understories, which further increases flammability and fire risk (94).

The identification of which trees and species within stands are most vulnerable to drought (37, 99) and of the factors that render certain stands within landscapes more susceptible to changing climates (100, 101) may inform both basic science and management strategies (69). Meta-analysis and theoretical models suggest that large trees are more likely than smaller trees to die during and after drought (37, 59). However, simple predictions of which size classes of trees die during drought may not hold in mixed-species forests, where different sizes of drought-weakened trees experience different levels of attack by host-specific bark beetles in idiosyncratic ways (102). Additional knowledge of community composition beyond tree size—i.e., size-species distributions—may help bridge predictions from the individual to the stand scale (69). Forest density may be an indication of competition for water, and trees growing at low densities may experience lower mortality rates (101) and less-pronounced reductions in growth during drought compared with those in higher density stands (103).

Advances in the remote sensing of proxies of plant stress, like canopy water content, may help us to monitor and map patterns at coarse geographic scales (104). These findings may guide silvicultural actions, such as selective thinning to reduce vulnerability to drought in managed forests (103). Finally, the diversity of hydraulic traits in forests has emerged as a property that helps explain ecosystem responses to climatic variability (105). Ecosystem fluxes inferred from eddy covariance measurements of forests with higher trait diversity of hydraulic traits appear more buffered against changes in soil water and vapor-pressure deficit compared with forests with low trait diversity (105), presumably because catastrophic failures of canopy dominants (Fig. 1B) are reduced. This underscores the idea that building large databases of hydraulic traits, rather than morphological traits such as specific leaf area and wood density, is a high priority to advance our understanding of forest vulnerability to drought (106).

Outlook

Drought is a natural phenomenon that plays a major role in limiting the distributions of species. However, the extremely rapid pace of climate change appears to be introducing enormous instability into the mortality rates of global forests (107). Instability and unpredictability are intrinsic aspects of the physiological processes that are linked to the drought-induced mortality process, whereby vascular damage is prone to failure and positive feedback, leading to tree death. Most models predict major damage to forests in the next century if current climate trajectories are not ameliorated. Debate still remains as to the magnitude of stabilizing

forces, such as tree acclimation and positive CO₂-associated effects on water use, but most observational data suggest that forest decline is well under way. Future improvements in physiological understanding and dynamic monitoring are needed to improve the clarity of future predictions; however, changes in community structure and ecology are certain, as are extinctions of tree species by the direct or indirect action of drought and high temperatures.

REFERENCES AND NOTES

1. T. J. Brodribb, M. Carriqui, S. Delzon, S. A. M. McAdam, N. M. Holbrook, *Nat. Plants* **6**, 273–279 (2020).
2. J. Peñuelas et al., *Nat. Ecol. Evol.* **1**, 1438–1445 (2017).
3. R. J. Norby et al., *Proc. Natl. Acad. Sci. U.S.A.* **102**, 18052–18056 (2005).
4. E. A. Ainsworth, A. Rogers, *Plant Cell Environ.* **30**, 258–270 (2007).
5. E. A. Ainsworth, S. P. Long, *New Phytol.* **165**, 351–371 (2005).
6. A. P. Walker et al., *Nat. Commun.* **10**, 454 (2019).
7. J. Peñuelas, J. G. Canadell, R. Ogaya, *Glob. Ecol. Biogeogr.* **20**, 597–608 (2011).
8. P. van der Sleen et al., *Nat. Geosci.* **8**, 24–28 (2015).
9. M. Levesque, L. Andreu-Hayles, N. Pederson, *Sci. Rep.* **7**, 46158 (2017).
10. C. Potter, S. Li, C. Hiatt, *Nat. Resources* **3**, 184–190 (2012).
11. Z. e. Gedalof, A. A. Berg, *Global Biogeochem. Cycles* **24**, GB3027 (2010).
12. W. K. Soh et al., *Sci. Adv.* **5**, eaax7906 (2019).
13. D. Frank et al., *Nat. Clim. Chang.* **5**, 579–583 (2015).
14. A. L. Swann, F. M. Hoffman, C. D. Koven, J. T. Randerson, *Proc. Natl. Acad. Sci. U.S.A.* **113**, 10019–10024 (2016).
15. J. S. Sperry et al., *Proc. Natl. Acad. Sci. U.S.A.* **116**, 25734–25744 (2019).
16. X. Li et al., *Plant Cell Environ.* **41**, 646–660 (2018).
17. M. Larter et al., *New Phytol.* **215**, 97–112 (2017).
18. S. Trueba et al., *Plant Cell Environ.* **40**, 277–289 (2017).
19. B. Choat et al., *Nature* **491**, 752–755 (2012).
20. J. R. Ehleringer, in *Stable Isotopes and Plant Carbon-Water Relations*, J. R. Ehleringer, A. E. Hall, G. D. Farquhar, Eds. (Elsevier, 1993), pp. 155–172.
21. W. Yuan et al., *Sci. Adv.* **5**, eaax1396 (2019).
22. P. Sanguinés de Cárcer et al., *Glob. Change Biol.* **24**, 1108–1122 (2018).
23. T. N. Buckley, *New Phytol.* **224**, 21–36 (2019).
24. J. E. Drake et al., *Glob. Change Biol.* **24**, 2390–2402 (2018).
25. J. Urban, M. W. Ingwers, M. A. McGuire, R. O. Teskey, *J. Exp. Bot.* **68**, 1757–1767 (2017).
26. B. H. Rosado, R. S. Oliveira, C. A. Joly, M. P. Aïdar, S. S. Burgess, *Agric. For. Meteorol.* **158–159**, 13–20 (2012).
27. M. J. Zeppel et al., *New Phytol.* **193**, 929–938 (2012).
28. T. E. Dawson et al., *Tree Physiol.* **27**, 561–575 (2007).
29. A. Bueno et al., *J. Exp. Bot.* **70**, 1613–1625 (2019).
30. A.-C. Schuster et al., *AoB Plants* **8**, plw027 (2016).
31. H. Cochard, A new mechanism for tree mortality due to drought and heatwaves. *bioRxiv* 531632 [Preprint]. 3 February 2019. <https://doi.org/10.1101/531632>.
32. P. J. Mitchell, A. P. O'Grady, K. R. Hayes, E. A. Pinkard, *Ecol. Evol.* **4**, 1088–1101 (2014).
33. C. D. Allen, D. D. Breshears, N. G. McDowell, *Ecosphere* **6**, 129 (2015).
34. S. Greenwood et al., *Ecol. Lett.* **20**, 539–553 (2017).
35. K. E. Trenberth et al., *Nat. Clim. Chang.* **4**, 17–22 (2014).
36. C. D. Allen et al., *For. Ecol. Manage.* **259**, 660–684 (2010).
37. A. C. Bennett, N. G. McDowell, C. D. Allen, K. J. Anderson-Teixeira, *Nat. Plants* **1**, 15139 (2015).
38. H. Hartmann et al., *New Phytol.* **218**, 15–28 (2018).
39. N. McDowell et al., *New Phytol.* **178**, 719–739 (2008).
40. W. R. Anderegg et al., *New Phytol.* **208**, 674–683 (2015).
41. N. McDowell et al., *New Phytol.* **219**, 851–869 (2018).
42. B. Choat et al., *Nature* **558**, 531–539 (2018).
43. W. M. Hammond et al., *New Phytol.* **223**, 1834–1843 (2019).
44. L. Rowland et al., *Nature* **528**, 119–122 (2015).
45. H. D. Adams et al., *Nat. Ecol. Evol.* **1**, 1285–1291 (2017).
46. W. R. Anderegg et al., *Proc. Natl. Acad. Sci. U.S.A.* **113**, 5024–5029 (2016).
47. R. P. Skellton, T. J. Brodribb, S. A. M. McAdam, P. J. Mitchell, *New Phytol.* **215**, 1399–1412 (2017).
48. M. T. Tyree, J. S. Sperry, *Annu. Rev. Plant Biol.* **40**, 19–36 (1989).
49. H. Cochard, S. Delzon, *Ann. For. Sci.* **70**, 659–661 (2013).
50. T. J. Brodribb, D. J. M. S. Bowman, S. Nichols, S. Delzon, R. Burlett, *New Phytol.* **188**, 533–542 (2010).
51. T. J. Brodribb, H. Cochard, *Plant Physiol.* **149**, 575–584 (2009).
52. W. R. Anderegg et al., *Nat. Geosci.* **8**, 367–371 (2015).
53. N. G. McDowell et al., *Nat. Clim. Chang.* **6**, 295–300 (2016).
54. H. Cochard et al., *J. Exp. Bot.* **64**, 4779–4791 (2013).
55. T. J. Brodribb et al., *New Phytol.* **209**, 1403–1409 (2016).

56. C. R. Brodersen, A. B. Roddy, J. W. Wason, A. J. McElrone, *Annu. Rev. Plant Biol.* **70**, 407–433 (2019).
57. N. Martin-StPaul, S. Delzon, H. Cochard, *Ecol. Lett.* **20**, 1437–1447 (2017).
58. X. Wu et al., *Glob. Change Biol.* **24**, 504–516 (2018).
59. A. T. Trugman et al., *Ecol. Lett.* **21**, 1552–1560 (2018).
60. H. Jactel, J. Koricheva, B. Castagnereyrol, *Curr. Opin. Insect Sci.* **35**, 103–108 (2019).
61. S. A. Kannenberg et al., *Glob. Change Biol.* **25**, 2978–2992 (2019).
62. V. Journé, J. Y. Barnagaud, C. Bernard, P. A. Crochet, X. Morin, *Ecology* **101**, e02912 (2020).
63. H. Bugmann et al., *Ecosphere* **10**, e02616 (2019).
64. L. Hülsmann, H. Bugmann, M. Cailleret, P. Brang, *Ecol. Appl.* **28**, 522–540 (2018).
65. C. B. Eller et al., *New Phytol.* **10.1111/nph.16419** (2020).
66. A. Wolf, W. R. Anderegg, S. W. Pacala, *Proc. Natl. Acad. Sci. U.S.A.* **113**, E7222–E7230 (2016).
67. J. S. Sperry et al., *Plant Cell Environ.* **40**, 816–830 (2017).
68. Y. Liu et al., *Proc. Natl. Acad. Sci. U.S.A.* **114**, 9918–9923 (2017).
69. J. S. Clark et al., *Glob. Change Biol.* **22**, 2329–2352 (2016).
70. C. M. Rodríguez-Domínguez, T. J. Brodribb, *New Phytol.* **225**, 126–134 (2020).
71. S. N. Aitken, S. Yeaman, J. A. Holliday, T. Wang, S. Curtis-McLane, *Evol. Appl.* **1**, 95–111 (2008).
72. Y. Liang, M. J. Duveneck, E. J. Gustafson, J. M. Serra-Diaz, J. R. Thompson, *Glob. Change Biol.* **24**, e335–e351 (2018).
73. R. Wortemann et al., *Tree Physiol.* **31**, 1175–1182 (2011).
74. J.-B. Lamy et al., *New Phytol.* **201**, 874–886 (2014).
75. A. Lobo et al., *For. Ecol. Manage.* **424**, 53–61 (2018).
76. B. Schultdt et al., *New Phytol.* **210**, 443–458 (2016).
77. A. B. Nicotra et al., *Trends Plant Sci.* **15**, 684–692 (2010).
78. M. Mencuccini, L. Bonosi, *Can. J. For. Res.* **31**, 442–456 (2001).
79. J. Martínez-Vilalta et al., *New Phytol.* **184**, 353–364 (2009).
80. T. Rosas et al., *New Phytol.* **223**, 632–646 (2019).
81. C. Pritzkow, V. Williamson, C. Szota, R. Trouvé, S. K. Arndt, *Tree Physiol.* **40**, 215–229 (2020).
82. R. López, F. J. Cano, B. Choat, H. Cochard, L. Gil, *Front. Plant Sci.* **7**, 769 (2016).
83. M. Tomasella et al., *Tree Physiol.* **38**, 198–211 (2018).
84. P. R. L. Bittencourt et al., *Glob. Change Biol.* **10.1111/gcb.15040** (2020).
85. K. J. Feeley, S. J. Davies, R. Perez, S. P. Hubbell, R. B. Foster, *Ecology* **92**, 871–882 (2011).
86. S. Fauset et al., *Ecol. Lett.* **15**, 1120–1129 (2012).
87. J. M. Vose et al., *For. Ecol. Manage.* **380**, 335–345 (2016).
88. Y. Yang et al., *Nat. Commun.* **9**, 3172 (2018).
89. I. Aleixo et al., *Nat. Clim. Chang.* **9**, 384–388 (2019).
90. J. S. Powers et al., *Glob. Change Biol.* **10.1111/gcb.15037** (2020).
91. J. Martínez-Vilalta, F. Lloret, *Global Planet. Change* **144**, 94–108 (2016).
92. M. J. O'Brien, D. Pérez-Aviles, J. S. Powers, *Glob. Change Biol.* **24**, 5270–5280 (2018).
93. M. Detto, S. J. Wright, O. Calderón, H. C. Muller-Landau, *Nat. Commun.* **9**, 913 (2018).
94. P. M. Brando et al., *Proc. Natl. Acad. Sci. U.S.A.* **111**, 6347–6352 (2014).
95. T. E. Kolb et al., *For. Ecol. Manage.* **380**, 321–334 (2016).
96. L. Qie et al., *Environ. Res. Lett.* **14**, 045012 (2019).
97. J. T. Abatzoglou, A. P. Williams, *Proc. Natl. Acad. Sci. U.S.A.* **113**, 11770–11775 (2016).
98. P. M. Brando et al., *Annu. Rev. Earth Planet. Sci.* **47**, 555–581 (2019).
99. V. Meakem et al., *New Phytol.* **219**, 947–958 (2018).
100. N. B. Schwartz, A. M. Budsock, M. Uriarte, *Ecology* **100**, e02677 (2019).
101. D. J. N. Young et al., *Ecol. Lett.* **20**, 78–86 (2017).
102. N. L. Stephenson, A. J. Das, N. J. Ampersee, B. M. Bulaon, J. L. Yee, *J. Ecol.* **107**, 2383–2401 (2019).
103. A. Bottero et al., *J. Appl. Ecol.* **54**, 1605–1614 (2017).
104. P. Brodribb, L. Anderegg, G. Asner, *Geophys. Res. Lett.* **46**, 2752–2760 (2019).
105. W. R. L. Anderegg et al., *Nature* **561**, 538–541 (2018).
106. R. J. Griffin-Nolan et al., *Funct. Ecol.* **32**, 1746–1756 (2018).
107. A. S. Jump et al., *Glob. Change Biol.* **23**, 3742–3757 (2017).
108. M. Riederer, C. Müller, Eds., *Annual Plant Reviews Volume 23: Biology of the Plant Cuticle* (Wiley, 2008).

ACKNOWLEDGMENTS

Funding: T.J.B. acknowledges support from Australian Research Council grant DP190101552. J.P. acknowledges support from the U.S. Department of Energy, Office of Science, Office of Biological and Environmental Research, Terrestrial Ecosystem Science (TES) Program (award no. DESC0014363). H.C. was financed by the ANR projects 16-IDEX-0001 and 18-CE20-0005. B.C. received funding from the Australia & Pacific Science Foundation APSF17/3 and an Australian Research Council grant ARC DP170100761. **Competing interests:** None declared.

10.1126/science.aat7631

REVIEW

The physiology of plant responses to drought

Aditi Gupta, Andrés Rico-Medina, Ana I. Caño-Delgado*

Drought alone causes more annual loss in crop yield than all pathogens combined. To adapt to moisture gradients in soil, plants alter their physiology, modify root growth and architecture, and close stomata on their aboveground segments. These tissue-specific responses modify the flux of cellular signals, resulting in early flowering or stunted growth and, often, reduced yield. Physiological and molecular analyses of the model plant *Arabidopsis thaliana* have identified phytohormone signaling as key for regulating the response to drought or water insufficiency. Here we discuss how engineering hormone signaling in specific cells and cellular domains can facilitate improved plant responses to drought. We explore current knowledge and future questions central to the quest to produce high-yield, drought-resistant crops.

Drought is a misfortune for agriculture, humanity, and livestock alike (1). Climate change is leading us toward a hotter, more parched world (2). There is an urgent need to produce high-yielding plants that use water more efficiently than their present-day counterparts (Fig. 1A). In the past decade, global losses in crop production due to drought totaled ~\$30 billion. Global population rose from 5 billion inhabitants in 1990 to more than 7.5 billion presently and is predicted to rise to 9.7 billion to 10 billion by 2050 (3), at which time 5 billion people are projected to be living in water-scarce regions (Fig. 1B) (4). Despite the moderate increase in global arable land, an additional 1 million ha will be needed

to ensure food security (Fig. 1C) (5). In addition, water demand for agriculture could double by 2050, whereas the availability of fresh water is predicted to drop by 50%, owing to climate change (Fig. 1D) (6). Certainly, plant biotechnology holds one of the promises to meet the societal demand for increased global crop production.

Water is crucial for plant survival, and water deficits limit plant growth. However, plants have strategies to prevent water loss, balance optimal water supply to vital organs, maintain cellular water content, and persevere through periods of drought. The ability of a plant to sense the water-deficiency signal and initiate coping strategies in response is defined as drought resistance. Drought resistance is a complex trait that proceeds through several mechanisms: (i) escape (acceleration of plant reproductive phase before stress that could

Department of Molecular Genetics, Centre for Research in Agricultural Genomics (CRAG), CSIC-IRTA-UAB-UB, Campus UAB (Cerdanyola del Vallès), 08193 Barcelona, Spain.
*Corresponding author. Email: ana.cano@cragenomica.es

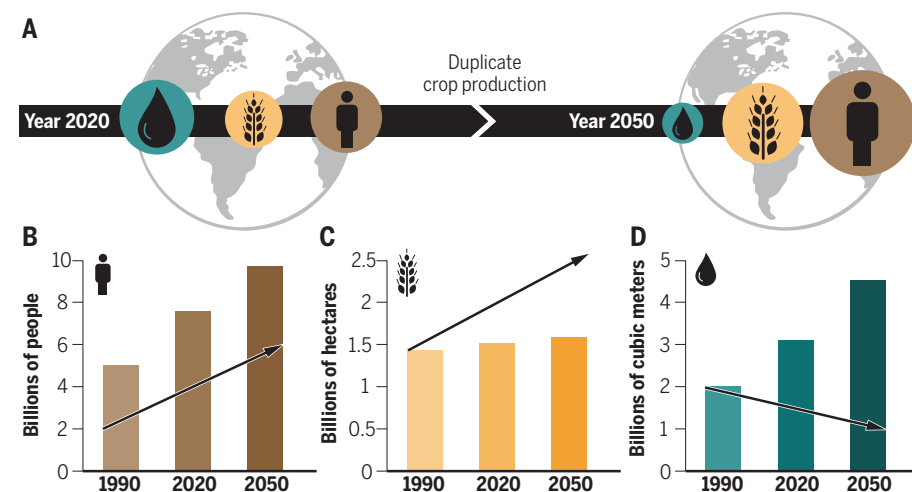


Fig. 1. Past, present, and future of global climate, agriculture, and food security. (A) Most scenarios predict that water scarcity will increase in the coming years. With the world's population continuously growing, crop production must also increase to fulfill civilization's basic needs. For this purpose, plants must become more water efficient. (B) Estimated world population for the 1990–2050 time period. The arrow indicates the estimated number of people living in water-scarce areas. (C) Global arable land for agriculture for the 1990–2050 time period. The arrow indicates the predicted demand for arable land to ensure food security, given the current rates of crop production per hectare. (D) Global freshwater demand for agriculture for the 1990–2050 time period. The arrow indicates the predicted decline in freshwater availability for agriculture, given the current trends for climate change and precipitation.

hinder its survival), (ii) avoidance (endurance with increased internal water content and prevention of tissue damage), and (iii) tolerance (endurance with low internal water content while sustaining growth over the drought period) (7). After a period of drought, the percentage of viable plants upon rewatering is referred to as the drought survival rate. From the perspective of molecular biology, cellular water loss marks the first event of drought stress. At the cellular level, drought signals promote production of stress-protectant metabolites such as proline and trehalose, trigger the antioxidant system to maintain redox homeostasis, and deploy peroxidase enzymes to prevent acute cellular damage and membrane integrity. Factors such as the extent of water stress and the plant organ in which the stress is sensed also trigger specific signaling responses, including but not limited to abscisic acid, brassinosteroids, and ethylene phytohormone pathways (8–11).

Drought's impact on agriculture depends on the degree and duration of the reduced precipitation and soil water gradients, as well as on plant species and developmental stages (8). In most instances, crops experience moderate droughts caused by prolonged precipitation deficits, reduced groundwater levels, and/or limited access to water supplies, leading to substantial losses in overall yield. Therefore, investigating the mechanisms of how a plant sustains its growth during moderate drought and devising strategies to improve plant health during such periods can provide solutions for future food security. Understanding the response of cellular signaling to water shortage is key for shedding light on these modern agricultural problems (12). Here we explore how water availability cues cell and tissue growth patterns and how these patterns are coordinated in the whole plant to improve drought resistance without loss of yield. Overexpression of drought-responsive genes often results in growth deficits and yield loss. Tissue- or time-specific expression of drought-response traits may improve drought response without depressing yield. A combination of strategies may boost agricultural yields despite increased water insecurity.

Traits for improving drought resistance

During drought spells, plant systems actively maintain physiological water balance by (i) increasing root water uptake from the soil, (ii) reducing water loss by closing stomata, and (iii) adjusting osmotic processes within tissues (13). Activated stress response pathways include phytohormone signaling as well as antioxidant and metabolite production and mobilization (11).

Roots respond to changes in soil moisture at the cellular scale and with the entire root system architecture. The root stem cell niche, meristem, and vasculature each coordinate responses to drought (Fig. 2, A and B). During

periods of water scarcity, the root system architecture undergoes morphological changes to enhance its ability to absorb water and nutrients (9, 10). These modifications can be traced to coordinated cell division, elongation, and differentiation events in the root apex. In the pursuit of moisture, root systems grow differentially and adapt their architecture to be either deep or shallow (Fig. 2C). Longer and deeper roots with reduced branching angles can efficiently capture water from soil that is dry at the surface but retains moisture in deep layers. By contrast, shallower root architectures are more beneficial for maximizing water capture from the soil surface in regions of low

moisture. The turgor-driven shape changes of guard cells are affected by the cell wall structure, plasma membrane, tonoplast properties, and cytoskeletal dynamics (16). Plant vascular tissues, the xylem and phloem, transmit water availability signals from roots to shoots and transmit photoassimilates from shoots to roots, respectively (17). Development of these inner vasculature tissues also affects drought resistance. Crop yield becomes most vulnerable if the drought occurs during a plant's reproductive phase. In *Arabidopsis thaliana*, early flowering associated with drought escape is linked to phloem loading and transport of the

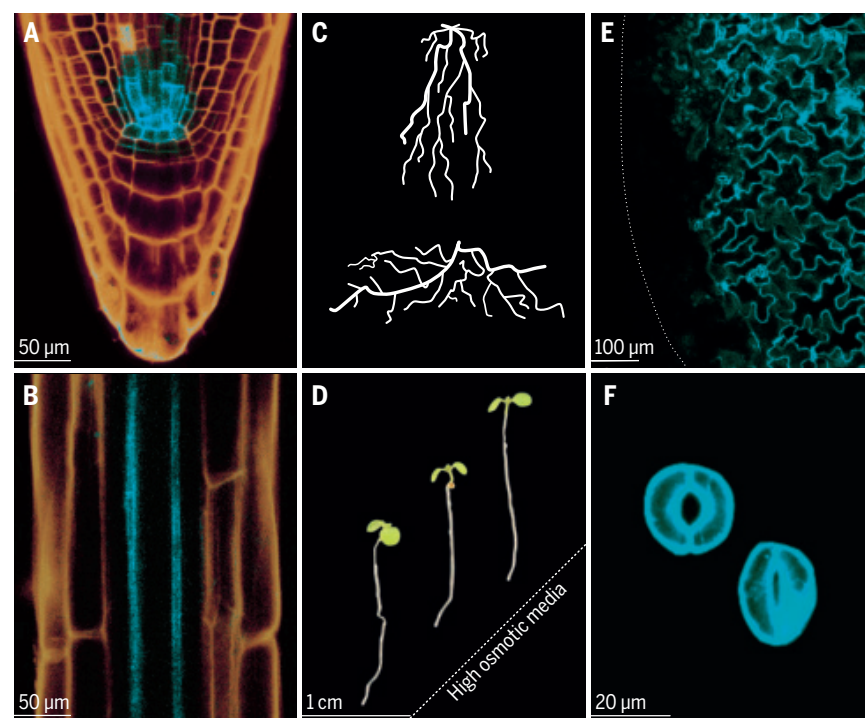


Fig. 2. Root and shoot traits that account for drought resistance. (A and B) Plants initially sense drought through their roots, where particular cell types (shown in blue)—such as stem cells, cortical cells, and vascular cells—mediate adaptive responses toward water limitations. Roots can modulate their system architecture to (C) maximize access to superficial humidity or delve into deep humid soil layers, as well as to (D) bend toward more humid soil zones (hydrotropism). (E and F) In aboveground plant organs such as leaves and stems, stomata work actively against dehydration. In water-limiting conditions, stomata remain closed to reduce water loss.

precipitation (9). Roots that encounter a soil environment with nonhomogeneous water distribution display hydropatterning by favoring lateral root emergence toward soil patches with higher water content, a process that is also mediated by auxin signaling (9, 14). Another adaptive response to nonhomogeneous distribution of moisture through soil is hydrotropism (Fig. 2D), in which root tips grow toward zones with higher water content to optimize the root system architecture for water acquisition (15).

Stomatal closure is a more rapid defense against dehydration (Fig. 2, D and E). Stomatal pores on leaf surfaces open or close accord-

ing to the turgidity of the surrounding guard cells. The turgor-driven shape changes of guard cells are affected by the cell wall structure, plasma membrane, tonoplast properties, and cytoskeletal dynamics (16). Plant vascular tissues, the xylem and phloem, transmit water availability signals from roots to shoots and transmit photoassimilates from shoots to roots, respectively (17). Development of these inner vasculature tissues also affects drought resistance. Crop yield becomes most vulnerable if the drought occurs during a plant's reproductive phase. In *Arabidopsis thaliana*, early flowering associated with drought escape is linked to phloem loading and transport of the

Phytohormones to combat drought

The hormone abscisic acid (ABA) regulates plant responses to dehydration and optimizes water use. Dehydration signals stimulate local production of ABA in different plant organs. However, ABA production is more efficient in the leaf mesophyll cells than in the root tissues (19). The accumulated ABA then activates downstream signaling components (20). ABA executes its function during stress

by mediating signal cross-talk with other pathways (Fig. 3) (21). Many existing schemes to improve water use efficiency and drought resistance engage the ABA pathway.

Genetic engineering to improve the function of PYR/PYL/RCAR (Pyrabactin Resistance 1/ PYR1-Like/Regulatory Component of ABA Receptors) and SnRK2 (SNF1-related protein kinase 2) and repress the negative regulator PP2C (clade A type 2C protein phosphatase) has resulted in improved water use efficiency in plants such as *A. thaliana* and wheat under controlled laboratory growth conditions and greenhouses (22–25). A regulatory network of ABA pathway genes, a hierarchy of ABA-related transcription factors, and signaling feedback were identified among ABA-mediated stress responses to drought (26). Engineering the ABA receptor PYR1 for heightened sensitivity toward the preexisting agrochemical mandipropamid resulted in improved drought resistance in *A. thaliana* and tomato (22). Virtual screening for ABA receptor agonists led to the identification of a bioactive ABA mimic called opabactin. This small molecule can enhance ABA receptor activation and downstream signaling to improve water use efficiency and drought resistance in *A. thaliana*, tomato, and wheat (27). Thus, computational design combined with experimental biology led to identification of a small molecule that can mitigate the effects of drought on crop yields.

Brassinosteroid hormones also regulate drought response through signaling components linked to the ABA response pathway (Fig. 3) (28, 29). Brassinosteroid signaling negative regulator BRASSINOSTEROID-INSENSITIVE 2 (BIN2) is dephosphorylated by ABA INSENSITIVE1 (ABI1) and ABI2. ABA activates BIN2 by inhibiting the activity of ABI1 and ABI2 (30). BIN2 phosphorylates SnRK2s and activates the downstream pathway (31). ABA signals can also converge with the brassinosteroid pathway at the level of downstream transcription factors (Fig. 3). BRI1-EMS-SUPPRESSOR 1 (BES1) inhibited ABA induction of a drought-related transcription factor RESPONSIVE TO DESICCATION 26 (RD26) (32). RD26 shows reciprocal antagonism with brassinosteroid by modulating BES1-regulated transcription and inhibiting brassinosteroid-regulated growth (33). WRKY46, -54, and -70 belong to another class of transcription factors that interact with BES1 to promote plant growth while repressing drought responses (34). BIN2 can

phosphorylate and destabilize WRKY54 to negatively regulate its effect on the BES1-mediated brassinosteroid response (35). BIN2 phosphorylates and activates the ubiquitin receptor protein DSK2, which leads to BES1 degradation via autophagy and coordinates plant growth and survival under drought conditions. (36). An AP2/ERF transcription factor called TINY is another candidate that

balances brassinosteroid-mediated stress adaptation with growth. TINY interacts with BES1 and antagonizes brassinosteroid-regulated growth. BIN2, on the other hand, phosphorylates and stabilizes TINY to promote ABA-induced stomatal closure and drought resistance (37). Thus, brassinosteroids as well as ABA aid drought resistance.

Tissue-specific responses for drought resistance

Stomatal closure preserves water in the plant. ABA content in leaves regulates stomatal movement in response to water availability (25) (Fig. 3). Because stomatal movements control CO₂ influx and transpiration, efforts to reduce water loss via stomatal closure occur at the cost of photosynthesis, growth, and yield (13). Therefore, most strategies to improve water efficiency and drought resistance in plants focus on fine-tuning stomatal conductance and manipulating ABA signaling via stomata-specific promoters (38). With optogenetics, scientists have improved the responsiveness of the stomata and overcome the coupling of CO₂ uptake with water vapor loss. Upon introducing BLINK1 (a light-activated synthetic K⁺ ion channel) into guard cells, stomata became more synchronized with fluctuating light conditions (39). This manipulation improved the performance of the stomata and, consequently, growth and productivity of the plant. Thus, water use efficiency was improved by engineering the stomata to maximize the amount of carbon fixed per unit of water lost.

Improving water acquisition by roots can also improve plant performance upon drought. In *A. thaliana*, the auxin pathway modulator EXOCYST SUBUNIT EXO70 FAMILY PROTEIN A3 (EXO70A3), which regulates root system depth, was identified through genome-wide association mapping (40). EXO70A3, a component of the exocytosis system, is expressed in root tips. EXO70A3 regulates local auxin transport by affecting the homeostasis of the auxin efflux carrier PIN-FORMED 4 in root columella cells (Fig. 3). Natural variation in EXO70A3 was correlated with seasonal precipitation and conferred different adaptive root system architecture configurations under different rainfall patterns. In areas with high temperatures and irrigated soils, deeper root architectures proved better for drought adaptation. In rice, the auxin-inducible gene *DEEPER ROOTING1* provides drought resistance by promoting a more vertical and deeper

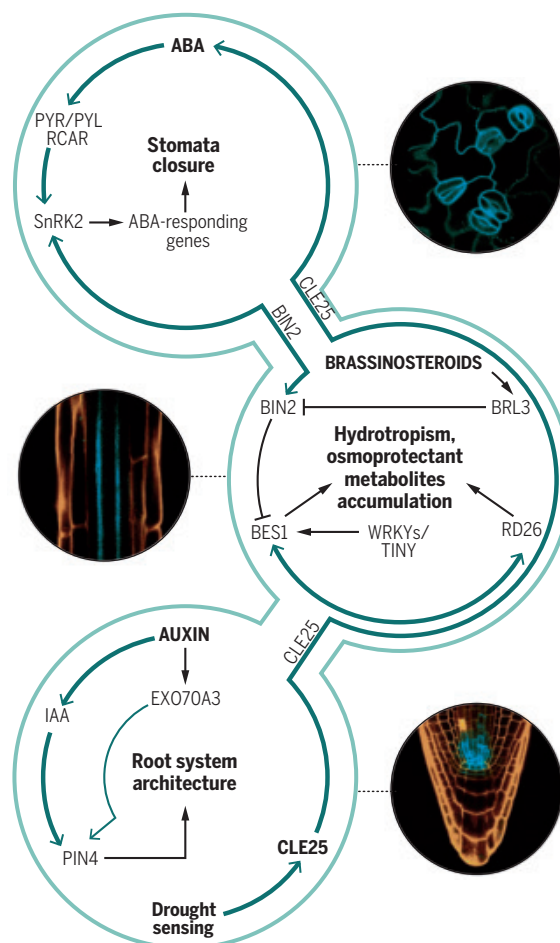


Fig. 3. Hormone signaling events underpinning drought. Schematic representation of hormone signaling modules that control drought adaptation. Plants work against dehydration in organs such as leaves, vasculature, and roots. ABA, through SnRK2, activates a variety of genes that trigger stomata closure and improve water balance. When roots sense drought, the CLE25 peptide moves through the vasculature to the leaves, where it locally controls ABA biosynthesis and stomata closure. Brassinosteroids also play roles in regulating plant drought response. Brassinosteroid pathways converge with ABA by activating SnRK2 through downstream pathway component BIN2 and vice versa. Independently of ABA, brassinosteroid receptors (BRI1, BRL1, and BRL3) modulate hydrotropic responses in the roots. The vascular BRL3 receptor coordinates plant growth and survival under drought stress by promoting the accumulation of osmoprotectant metabolites in the root tissues. Furthermore, noncanonical auxin responses via EXO70A3 and PIN4 can modulate root architecture patterning and depth to boost water absorption from the soil, thereby improving drought tolerance.

root system architecture (41). Although auxin modulates root architecture under stress (40, 41), hydrotropic root responses function relatively independent of auxin and involve ABA signaling in root elongation zones. Coordinated activity of ABA-inducible MIZU-KUSSEI1 (MIZ1) and SNF1-RELATED KINASE 2 (SnRK2.2) in root elongation zone cortical cells interprets water potential gradients in soil environments (15, 42).

Brassinosteroid receptors regulate root hydrotropic responses (Fig. 3). Overexpression of the vascular-enriched brassinosteroid receptor BRI1-Like3 (BRL3) promotes root hydrotropic bending. The *brl1brl3bak1* triple mutant of the BRL3 signalosome shows a reduced hydrotropic response, suggesting a role for the vascular BRL3 receptor complex in regulating hydrotropic responses (43) (Fig. 3). Activation of the BRL3 pathway in vasculature triggers accumulation of osmoprotectant metabolites such as proline, trehalose, and raffinose family oligosaccharides in plant roots in response to water withdrawal, which improves drought resistance without penalizing growth (43) (Fig. 3). Phloem-specific localization of BRL3 is likely to be the determining factor for promoting drought resistance without impairing yield (29, 43).

In drought conditions, roots sense water scarcity from soil. The aboveground segments of plants respond by closing stomata in leaves, implicating a systemic communication system. In times of drought, the CLE25 peptide is produced in the roots and moves through the vasculature to plant leaves to drive ABA production by activating the biosynthetic enzyme NCED3.

This burst of ABA synthesis leads to stomatal closure and improved water balance, thereby promoting drought survival (44) (Fig. 3). This insight into small-peptide signaling in *A. thaliana* may help with identification of similar mechanisms in crop plants for root-to-shoot mobilization of stress signals.

A view to the future

Genetic traits that sustain crop plant growth under moderate drought may come from multiple sources, including natural genetic variation in wild relatives or bioengineering. Traditional breeding has been the main strategy for exploiting the genetic diversity of adaptive traits in natural alleles. The advent of genomic technologies and gene mapping tools such as genome-wide association study (GWAS) and precision genome editing with the CRISPR-Cas9 system has been instrumental for the generation of alleles that can improve plant yield and performance under various stresses. Molecular studies that use tissue- or cell-specific promoters coupled with live microscopy techniques for real-time visualization of cellular processes are paving the way for analysis of drought response networks that can be targeted by various approaches (Fig. 4). Small molecules such as peptides or hormone agonists may be useful for fine-tuning drought response pathways while preserving yield in agriculture. Together, research efforts aimed at uncovering the physiology of plant responses to drought in model systems and translating these findings to crops will deliver new strategies to combat water scarcity. Discovering ways to ame-

liorate agriculture's "thirst" will ease competition for freshwater resources, even as the world's population grows.

REFERENCES AND NOTES

- Food and Agriculture Organization of the United Nations (FAO), "The impact of disasters and crises on agriculture and food security" (FAO, 2018).
- FAO, "Proactive approaches to drought preparedness – Where are we now and where do we go from here?" (FAO, 2019).
- United Nations, Department of Economic and Social Affairs, Population Division, "World population prospects: the 2010 revision, volume I: comprehensive tables" (ST/ESA/SER.A/313, United Nations, 2011); www.un.org/en/development/desa/population/publications/pdf/trends/WPP2010/WPP2010_Volume_I_Comprehensive-Tables.pdf.
- E. Koncagül, M. Tran, R. Connor, S. Uhlenbrook, "World water development report 2020 – Water and climate change" (SC-2018/WS/5, UNESCO WWAP, 2018).
- FAO, FAOSTAT Land Use Module, Arable land data, updated 4 December 2019; www.fao.org/faostat/en/#data/EL.
- P. H. Gleick, Ed., in *The World's Water 2000-2001: The Biennial Report on Freshwater Resources* (Island Press, 2000), p. 53.
- S. Basu, V. Ramegowda, A. Kumar, A. Pereira, *FI000Research* **5**, 1554 (2016).
- F. Tardieu, T. Simonneau, B. Muller, *Annu. Rev. Plant Biol.* **69**, 733–759 (2018).
- J. R. Dinneny, *Annu. Rev. Cell Dev. Biol.* **35**, 239–257 (2019).
- R. Reilán-Alvarez, G. Lobet, J. R. Dinneny, *Annu. Rev. Plant Biol.* **67**, 619–642 (2016).
- J. Bailey-Serres, J. E. Parker, E. A. Ainsworth, G. E. D. Oldroyd, J. I. Schroeder, *Nature* **575**, 109–118 (2019).
- Y. Eshed, Z. B. Lippman, *Science* **366**, eaax0025 (2019).
- J. Rodrigues, D. Inzé, H. Nelissen, N. J. M. Saibo, *Trends Plant Sci.* **24**, 652–663 (2019).
- N. E. Robbins 2nd, J. R. Dinneny, *Proc. Natl. Acad. Sci. U.S.A.* **115**, E822–E831 (2018).
- D. Dietrich et al., *Nat. Plants* **3**, 17057 (2017).
- T. N. Buckley, *New Phytol.* **224**, 21–36 (2019).
- J. D. Scharwies, J. R. Dinneny, *J. Plant Res.* **132**, 311–324 (2019).
- F. Andrés, G. Coupland, *Nat. Rev. Genet.* **13**, 627–639 (2012).
- S. A. M. McAdam, T. J. Brodribb, *Plant Physiol.* **177**, 911–917 (2018).
- R. Kalland et al., *Proc. Natl. Acad. Sci. U.S.A.* **114**, 11536–11541 (2017).
- T. Kuromori, M. Seo, K. Shinozaki, *Trends Plant Sci.* **23**, 513–522 (2018).
- S. Y. Park et al., *Nature* **520**, 545–548 (2015).
- P. Wang et al., *Mol. Cell* **69**, 100–112.e6 (2018).
- R. Mega et al., *Nat. Plants* **5**, 153–159 (2019).
- M. Okamoto et al., *Proc. Natl. Acad. Sci. U.S.A.* **110**, 12132–12137 (2013).
- L. Song et al., *Science* **354**, aag1550 (2016).
- A. S. Vaidya et al., *Science* **366**, eaaw8848 (2019).
- T. M. Nolan, N. Vukašinović, D. Liu, E. Russinova, Y. Yin, *Plant Cell* **32**, 295–318 (2020).
- A. Planas-Riverola et al., *Development* **146**, dev151894 (2019).
- H. Wang et al., *Mol. Plant* **11**, 315–325 (2018).
- Z. Cai et al., *Proc. Natl. Acad. Sci. U.S.A.* **111**, 9651–9656 (2014).
- Y. Chung, S. I. Kwon, S. Choe, *Mol. Cells* **37**, 795–803 (2014).
- H. Ye et al., *Nat. Commun.* **8**, 14573 (2017).
- J. Chen, Y. Yin, *Plant Signal. Behav.* **12**, e1365212 (2017).
- J. Chen et al., *Plant Cell* **29**, 1425–1439 (2017).
- T. M. Nolan et al., *Dev. Cell* **41**, 33–46.e7 (2017).
- Z. Xie et al., *Plant Cell* **31**, 1788–1806 (2019).
- F. Rusconi et al., *J. Exp. Bot.* **64**, 3361–3371 (2013).
- M. Papanatsiou et al., *Science* **363**, 1456–1459 (2019).
- T. Ogura et al., *Cell* **178**, 400–412.e16 (2019).
- Y. Uga et al., *Nat. Genet.* **45**, 1097–1102 (2013).
- D. Shkolnik, R. Nuriel, M. C. Bonza, A. Costa, H. Fromm, *Proc. Natl. Acad. Sci. U.S.A.* **115**, 8031–8036 (2018).
- N. Fabregas et al., *Nat. Commun.* **9**, 4680 (2018).
- F. Takahashi et al., *Nature* **556**, 235–238 (2018).

ACKNOWLEDGMENTS

Funding: A.I.C.-D. has received funding from the European Research Council (ERC) under the European Union's Horizon 2020 research and innovation programme (grant agreement 683163). A.I.C.-D. is a recipient of a BIO2016-78150-P grant funded by the Spanish Ministry of Economy and Competitiveness and Agencia Estatal de Investigación (MINECO/AEI) and Fondo Europeo de Desarrollo Regional (FEDER). A.G. has received funding by a postdoctoral fellowship from the "Severo Ochoa Programme for Centers of Excellence in R&D" 2016–2019 from the Ministerio de Ciencia e Innovación (SEV-2015-0533). A.G. and A.R.-M. have received funding from ERC-2015-CoG-683163 granted to the A.I.C.-D. laboratory. A.R.-M. is a predoctoral fellow from Fundación Tatiana Pérez de Guzmán el Bueno. This work was supported by the CERCA Programme/Generalitat de Catalunya. **Competing interests:** The authors declare no competing or financial interests.

10.1126/science.aaz7614

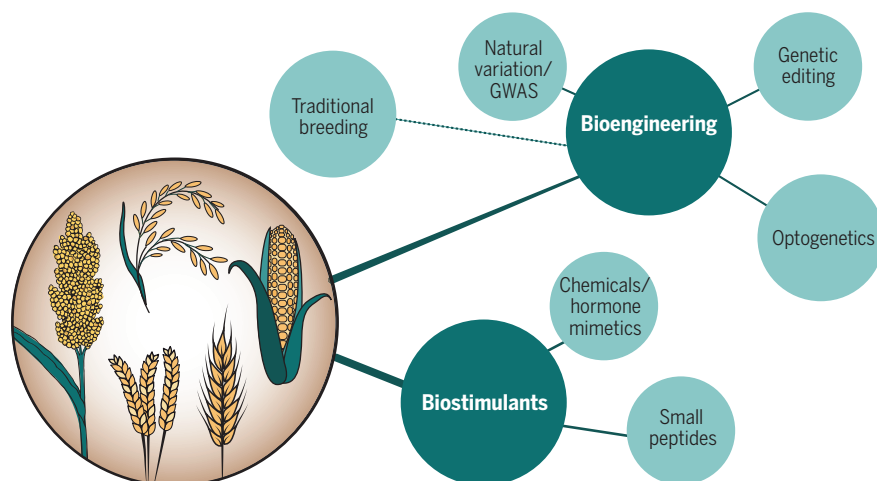


Fig. 4. The promise of overcoming drought in agriculture. Genetic strategies provide solutions to counteract drought and can be used to develop drought-smart crops. Natural allelic variations in plants can be selected to improve drought resistance and yield. Traditional breeding approaches have selected drought characteristics to obtain more-resistant crops. Advancements in gene mapping tools such as GWAS can explore the genetic diversity of drought resistance traits in natural alleles with nucleotide-level precision. Genetic engineering of drought response markers at the spatiotemporal scale and precise genome editing with tools such as CRISPR-Cas9 have opened new horizons for developing crops with improved drought resistance, without sacrificing yield. Emerging techniques such as optogenetics allow fine manipulation of cell- and tissue-specific responses to signaling and therefore increase growth and plant resistance to drought. Small peptides, hormone mimics, and receptor agonists can be used to design better agrochemicals and fine-tune drought resistance while preserving yield.

REVIEW

Harnessing rhizosphere microbiomes for drought-resilient crop production

Franciska T. de Vries^{1,2,*}, Rob I. Griffiths³, Christopher G. Knight¹, Oceane Nicolitch¹, Alex Williams¹

Root-associated microbes can improve plant growth, and they offer the potential to increase crop resilience to future drought. Although our understanding of the complex feedbacks between plant and microbial responses to drought is advancing, most of our knowledge comes from non-crop plants in controlled experiments. We propose that future research efforts should attempt to quantify relationships between plant and microbial traits, explicitly focus on food crops, and include longer-term experiments under field conditions. Overall, we highlight the need for improved mechanistic understanding of the complex feedbacks between plants and microbes during, and particularly after, drought. This requires integrating ecology with plant, microbiome, and molecular approaches and is central to making crop production more resilient to our future climate.

Interactions between plants and soil organisms are crucial for the functioning of terrestrial ecosystems and their response to a changing climate (1, 2). Plants and soil organisms interact by several distinct mechanisms. Plants fuel the soil food web through their belowground carbon (C) inputs—in the form of leaf and root litter—and root exudates. Although soil microbes are the primary decomposers of these C inputs, their biomass supports the existence of higher trophic levels; in turn, organisms from these higher trophic levels, such as Collembola and nematodes, stimulate the activity of soil microbes. Together, the activities of these organisms release nutrients for plant growth and determine the balance between C respiration and stabilization in the soil. But these organisms also interact directly with plants in the rhizosphere by feeding on (or infecting) roots, by forming symbiotic relationships such as mycorrhizae, or by promoting plant growth through phytohormone production or reducing plant stress signaling. It is well known that different plant species or genotypes can select for different soil communities (3). These selective pressures are especially strong in the rhizosphere, the area around the roots that is directly influenced by root processes and is the home of the rhizosphere microbiome. Recent studies suggest that root exudates have a pivotal role in selecting the rhizosphere microbiome, and that selecting a favorable rhizosphere microbiome via altering root exudation patterns might open up new opportunities to increase plant performance, with particular benefits for crop production (4).

In many regions of the world, the frequency and duration of drought spells is predicted to increase, leading to substantial threats to

global crop yields (5). Much recent research effort is focused on harnessing rhizosphere microbial communities to make food production more sustainable (6–8), and emerging evidence shows that plant microbiomes might also alleviate plant drought stress (9–11). However, despite an increased understanding of the mechanisms through which plants select their rhizosphere microbiome, and the subsequent feedbacks of the microbiome to plant growth and fitness, our understanding of these mechanisms under drought is still limited. More-

over, our understanding of the response of soil microbial communities to drought, and of the implications for crop response to drought, is hampered by the fact that very little of our knowledge comes from studying how soil microbes modify plant response to drought; of those studies that do concern this topic, only a modest proportion focus on crop plants. Here, we argue that an increased understanding of the complex feedbacks between plants and microbes during and after drought will pave the way for harnessing the rhizosphere microbiome to increase the resilience of crop production to drought.

Drought response traits

Drought is probably the abiotic stress that has the strongest effect on soil biota (12). In addition to osmotic stress, drought increases soil heterogeneity, limits nutrient mobility and access, and increases soil oxygen, often inducing a strong decrease in microbial biomass (13, 14). On short time scales, the resistance of microorganisms to this drastic alteration in environmental conditions is determined by specific “response traits” that protect against desiccation, such as a thick peptidoglycan cell wall in monoderm (Gram-positive) taxa, osmolyte production, sporulation, and dormancy (Fig. 1) (15–18). Similar traits have coevolved convergently in diverse organisms, notably in

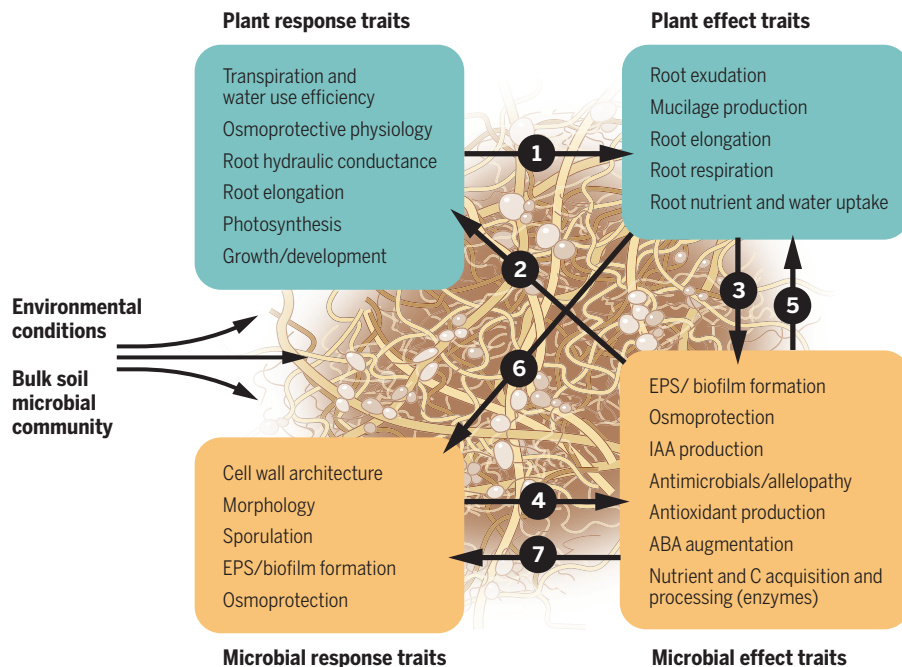


Fig. 1. Relationships among plant and microbial drought response and effect traits. Drought response traits determine the direct response of plants and microbes to drought, and these traits have a hypothesized link with drought effect traits (arrows 1 and 4), which determine the effect of drought on the plant. Plant and microbial effect traits can feed back to each other (arrows 3 and 5) and determine plant and microbial response to drought (arrows 2 and 6). Microbial effect traits can also feed back to influence microbial response to drought (arrow 7). All traits are affected by environmental conditions and bulk soil microbial communities. Morphology refers to filamentous hyphal growth of fungi. EPS, exopolysaccharide; ABA, abscisic acid; IAA, indole acetic acid. Tables 1 and 2 provide references for the traits included here.

¹Department of Earth and Environmental Sciences, University of Manchester, Manchester M13 9PT, UK. ²Institute for Biodiversity and Ecosystem Dynamics, University of Amsterdam, 1090 GE Amsterdam, Netherlands. ³CEH Bangor, Environment Centre Wales, Bangor LL57 2UW, UK. *Corresponding author. Email: ft.devries@uva.nl

fungi and the Gram-positive bacteria Actinomycetes (19). These organisms are described as stress-tolerant strategists according to the recently proposed high yield–resource acquisition–stress tolerance (Y-A-S) theory (20). This and other frameworks suggest a connection between drought response and effect traits [generally defined as determining the effect on ecosystem functioning of the microbial drought response, although here we focus on the effect of microbes on plant performance under drought (Fig. 1)]. However, to date there is little evidence of coupling between microbial drought tolerance mechanisms and those functional traits that affect plant performance under drought.

Plant signals

Although much research has focused on elucidating the microbial traits responsible for drought tolerance, accumulating evidence suggests that the indirect effects via plants can outweigh the direct effects of drought on microbial communities (21, 22). Root exudates are an important pathway of plant-microbial communication: They provide photosynthate C for microbial growth, but also facilitate direct communication between plants and microbes via signaling molecules and phytohormones. Drought can affect the quantity and quality of root exudates (21). A recent study showed that the drought history of root exudates was a

stronger driver of microbial respiration than the drought history of the soil and its microbial communities (22). On longer time scales, drought-induced shifts in plant growth and abundance seem to be more important than the direct effects of drought for altering soil microbial community composition mediated by root exudation (4). Such indirect effects of drought can modify the effect traits in microbial communities that are involved in basic metabolic processes. Altered rates and composition of root exudation can trigger increased microbial mineralization of nutrients, thus affecting plant recovery from drought (4), but longer-term changes in microbial communities have also been shown to affect the fitness of subsequent plant generations under drought (9). Thus, these changes in microbial communities have the potential to affect ecosystem carbon and nitrogen cycling (22). Indeed, drought has been shown to increase the frequency of effect traits related to carbon and nitrogen acquisition in fungi, as well as in bacteria (23, 24), which can feed back to plant performance under drought and during recovery after drought. On longer time scales, compositional changes in microbial communities, together with eco-evolutionary feedbacks between plants and microbes, horizontal gene transfer, and adaptation, can determine future drought responses of the plant-microbe holobiont (25) (Fig. 1 and Tables 1 and 2).

Microbial mechanisms

Despite their hypothesized link, the correlation between microbial drought response traits and microbial effect traits that confer an increased drought tolerance or faster recovery to plants (Fig. 1, arrow 4, and Table 1) has rarely been verified. One exception is arbuscular mycorrhizal fungi (AMF, specifically *Glomeromycota*), which can increase in abundance under drought [(26, 27), but see (28)] and confer drought tolerance to their host plant by enhancing antioxidant enzyme activity, thereby reducing oxidative stress and promoting better water use efficiency and greater biomass (8, 27). Similarly, the enrichment of *Streptomyces* under drought has been shown to play a subsequent role in the drought tolerance of plants (18, 29). Still, many of the microbial effect traits proposed as beneficial are common and shared across many microbial taxa, raising questions about their specific mode of action (30). Moreover, despite widespread claims of efficacy of inoculation with plant growth–promoting rhizobacteria (PGPRs) under laboratory conditions, we were unable to find studies demonstrating attribution of the beneficial effect to the specific selected trait, and there is limited evidence of inoculation success and subsequent benefits for plant growth under drought in field settings. Thus, understanding the mechanisms through which soil microbes affect plant drought

Table 1. Microbial community response and effect traits during drought. EPS, exopolysaccharide; IAA, indole acetic acid; ABA, abscisic acid; PGPR, plant growth–promoting rhizobacteria; ROS, reactive oxygen species; CE, controlled environment.

Response or effect	Trait	Description	Experimental system in which trait was measured	Reference
Response	Cell wall architecture	Monoderm (Gram-positive) bacteria increase relative to diderms; thicker cell walls mean increased resistance to water stress.	Field	(17)
Response	Morphology, filamentous hyphae	In certain fungi, spatially separated sources of water during drought are accessed through production of filamentous structures. This may aid the host plant or increase pathogenic fungi.	Field	(57)
Response	Sporulation	Protective spore production can promote persistence in the soil in certain species during extreme drought. Drought itself reduces the ability to sporulate.	Field, observational	(58)
Response and effect	EPS/biofilm	Production of an EPS matrix in mixed microbial communities generates an environment that is more osmotically stable during drought.	CE	(59)
Response and effect	Osmoprotection	Production of osmolytes by microbes and stimulation of osmolyte production in the roots via microbially derived signals impart a more stable osmotic environment during drought stress.	CE, field	(60)
Effect	Root elongation via IAA	During drought, bacteria produce auxins (IAA) and gibberellins, which act as growth stimulators, altering root morphology for greater water acquisition.	CE	(61)
Effect	Antimicrobial/allelopathy	Certain PGPR promote their own survival and potentially limit the growth of pathogens by producing allelopathic and antimicrobial molecules.	Field, observational	(23)
Effect	Antioxidant production	Drought leads to oxidative stress and internal cell damage. This can be directly mitigated by certain PGPR that produce antioxidants, such as glutamic and aspartic acids, and ROS-degrading enzymes such as superoxide dismutase.	Field, observational	(62)
Effect	ABA augmentation	Direct production and stimulation of the phytohormone ABA allows a greater drought stress response through holistic reorchestration of water use (Table 2).	CE	(60)
Effect	Nutrient acquisition via enzymes	Greater C and N scavenging enzyme production during drought can provide access to limited resources that are less available during drought.	Field	(23)

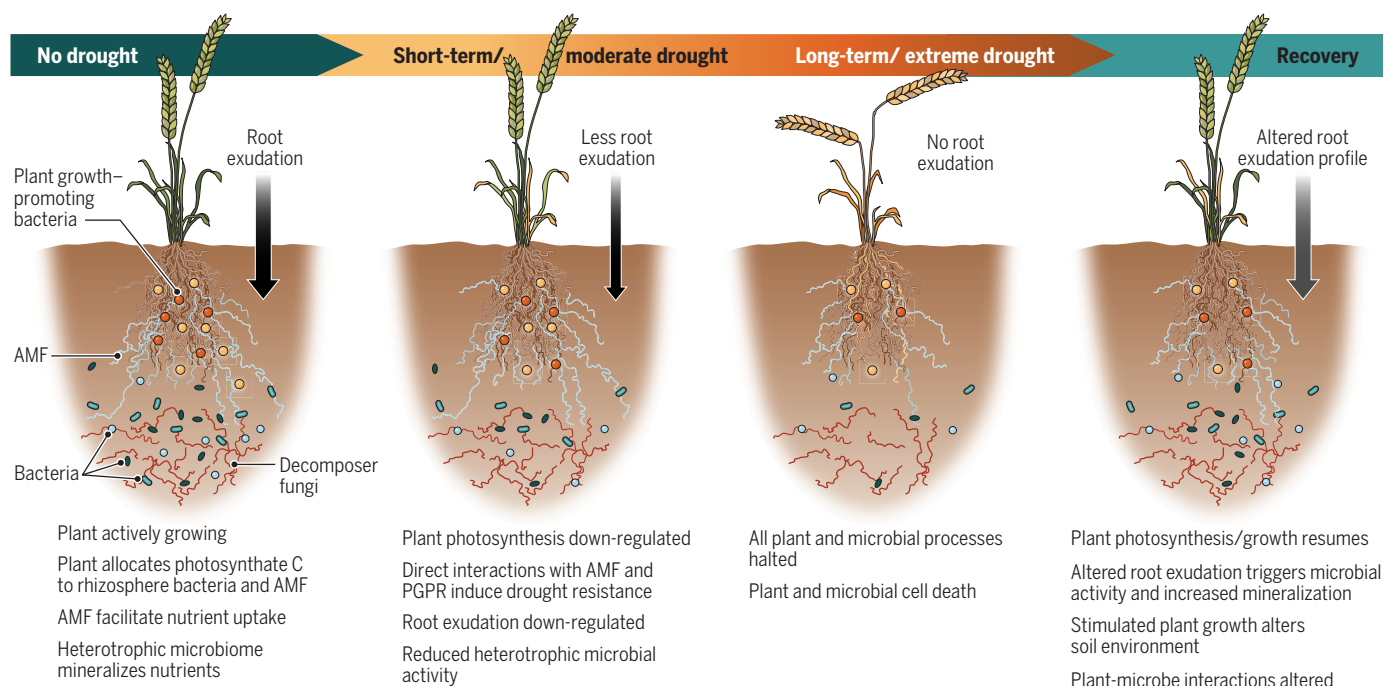


Fig. 2. Hypothesized alterations in plant-microbial interactions during and after drought. During drought, direct interactions with plant growth-promoting rhizobacteria (PGPR) and arbuscular mycorrhizal fungi (AMF) induce plant drought tolerance, but these interactions break down under severe or continuing drought. After drought, different plant-microbial interactions are assembled, with the potential of affecting future plant and soil response to drought.

tolerance and recovery, and their relevance and applicability under realistic field conditions, offers much potential for making crop production systems more resilient to drought.

Probiotics

There is increasing interest in manipulating host-microbiome interactions through adding bacteria (probiotics) in a range of systems, including gut-microbe systems. Guts have strong mechanistic parallels to the rhizosphere environment (31), and studies in humans provide proof of concept that manipulation of specific feedbacks is possible with probiotics. For example, trials in babies have shown colonization by a probiotic without major disruption of the resident microbiome, resulting in very specific activation of glycerol-3-phosphate (G3P) uptake genes by that community (32). Microbiome expression of G3P uptake genes has also been shown to be a critical response to drought in soy (17); in sorghum, it is thought to allow uptake and metabolism of G3P secreted by the host plant, enabling preferential root colonization by monoderm bacteria, which then aid in drought tolerance (18). Although the identification of such a specific pathway indicates that probiotic manipulation may be effective (32), crops, unlike human systems, are open to host engineering for adjusting that pathway (33). In humans, applying key small molecules (prebiotics) has been shown to have a host effect via the microbiome (34). For example, butyrate, a short-chain fatty acid, is an im-

portant molecule for interactions within the gut microbiome, as well as in anaerobic soil systems (35). Although there is little existing evidence of the efficacy of such small-molecule treatments in agricultural systems (36), the fundamental parallels between gut-microbiome and plant-microbiome interactions might inform targeted research into manipulating rhizosphere microbiome drought effect traits.

Primary and secondary plant metabolites

Plants themselves produce diverse small molecules in the rhizosphere. These primary and secondary metabolites, including volatiles, can be critical during stress (37, 38). For instance, in the early stages of drought, oak tree secondary metabolites play an important role in signaling to the rhizosphere; primary metabolites may serve a greater purpose during recovery (39). Interestingly, many of the drought-responsive microbial metabolites described in (39) act as precursors of immune phytohormones [such as phenylalanine, which is a precursor to salicylic acid (SA) biosynthesis and other stress-responsive secondary metabolites (40)]. The phytohormone abscisic acid (ABA) was also shown to be strongly induced during drought, although it decreased during recovery (39). ABA plays a central role in drought tolerance in crops (41) and has long been understood to be present in the rhizosphere (42), where it is actively metabolized by rhizosphere bacteria and may be involved in helping plants tailor their rhizosphere microbial communities (43). The fact that ABA-induced

sugar accumulation is the primary mechanism of drought tolerance in liverworts, ancestors to land plants (44), also indicates that this is a highly conserved drought response pathway. Thus, engineering its activity to generate more drought-resistant crops is promising (41). Furthermore, genes responsive to the immune hormones SA and jasmonic acid (JA) are down-regulated in sorghum during drought (28). Because SA-related exudation signals are instrumental in allowing both systemic resistance and the plant-mediated development of a rhizosphere-specific microbiome (45, 46), this is another potentially malleable pathway for establishing a drought-protective rhizosphere microbiome. However, manipulating the central plant metabolism, especially with respect to immune phytohormones such as ABA, could result in undesirable outcomes, such as altered disease resistance [as is the case with ABA overexpressing mutants of *Arabidopsis*, which experience increased susceptibility to the biotrophic pathogen *Dickeya dadantii* (47)].

Novel metagenomic approaches and high-resolution measurements in controlled experiments will improve our understanding of the production and role of drought-responsive metabolites. These methods need to be used not just during drought, where ultimately plant-microbial communication breaks down as the drought continues (3), but also after drought, when a fast sequence of physiological changes in both plants and microbes creates rapid feedback between plants and their microbiome (Fig. 2) (4). Moreover, many of these interactions

Table 2. Plant response and effect traits during drought. CE, controlled environment.

Response or effect	Trait	Description	Experimental system in which trait was measured	Reference
Response	Transpiration and water use decreased	Through changes in hormonal signaling, inducing stomatal closure, water loss is decreased. Increased cuticular wax deposition aids in foliar water retention.	Field	(63)
Response	Osmoprotective physiology favored	Changes in antioxidant physiology are induced to protect plants from oxidative stress.	Field	(64)
Response	Root hydraulic conductance increases	Aquaporin expression increases during drought. Dehydrin production promotes an osmotically stable environment.	Field	(65)
Response	Development limited	Photosynthetic activity decreases, foliar growth stops, root/shoot ratio increases.	Field	(66)
Effect	Changes in root exudation chemistry	This occurs as both quantity and composition of root exudates are responsive to drought. Different compositions are likely to influence a root microbiome that is more conducive to drought tolerance.	CE	(4, 22)
Effect	Increased mucilage production	More mucilage excretion around the roots helps to create a more osmotically positive environment.	CE	(67)
Effect	Altered soil C flux	Changes in soil C deposition occur, as well as its degradation and feedback into the atmosphere during drought.	CE	(68)

may be highly context-dependent. For example, investing in protective cell walls requires substantial allocation of resources to build these structures, which trades off with growth rates and competitiveness under resource-rich conditions; thus, this strategy might be selected against in agricultural soils (48). Similarly, plant cues via root exudation that stimulate microbial release of nutrients for plant regrowth after drought may not occur or may not play a role in nutrient-rich agricultural soils, where sufficient nutrients are available for plant (re)growth. Furthermore, nutrient-rich soils might increase the vulnerability of drought-stressed plants to pathogens that increase under drought (49), might select for inherently drought-sensitive plants and microbiomes (50, 51), and may reduce the benefits and root colonization of AMF (52). Much of our understanding of plant-microbial interactions under drought comes from non-crop species, whereas crop species are selected for traits that might inherently compromise drought resistance and beneficial interactions with rhizosphere microbiomes (53, 54). Therefore, manipulating the rhizosphere microbiome by introducing the selective traits into crops, or by inoculating soils with either probiotics or prebiotics, is likely to be more successful when paralleled by other measures to increase the sustainability of agro-ecosystems (6).

Translational possibilities

Understanding the full extent of interactions between plants and microbes, and how these

are affected over time under conditions of drought, will open many new research avenues to improve plant resilience to moisture stress. Efforts should focus on crop plants and be pursued in combination with management approaches, such as minimum tillage and maintenance of plant cover, to enhance soil organic matter and soil moisture retention. To promote plant drought resistance, given the uncertainties over bio-inoculant usefulness, we emphasize the importance of manipulating plant traits to both enhance the drought resistance of beneficial microbes and promote specific beneficial plant-microbe interactions. Such manipulations could include diversifying crops in time and space (intercropping), cultivar selection, or manipulation through breeding or new methodologies for localized gene editing [e.g., CRISPR (55)]. More generally, calls for more advanced noninvasive phenotyping of the plant root soil system (56) need to consider microbial phenotypes and interactions with plants, and the large body of knowledge on beneficial microbial traits identified in the bioinoculant literature needs to be extended, incorporating ecological and evolutionary studies, to identify in-field mechanisms by which rhizosphere microbes extend the plant phenotype under periods of drought and subsequent recovery (Fig. 2).

Conclusion

Increasing our mechanistic understanding, as well as our real-world understanding, of microbe-plant interactions under drought offers huge

potential for increasing the resilience of crop production to drought. We have outlined promising avenues to increase our understanding of the complex feedbacks between plant and microbial responses to drought; such research efforts will now need to focus on crop plants and be tested under realistic field conditions. Understanding the role of plant-microbe interactions during drought recovery, and in response to recurring droughts, is necessary if we are to harness these interactions not just for increasing crop resilience to drought, but also for maximizing crop yields, building soil carbon, and optimizing soil nutrient cycling.

REFERENCES AND NOTES

1. M. G. A. van der Heijden, R. D. Bardgett, N. M. van Straalen, *Ecol. Lett.* **11**, 296–310 (2008).
2. R. Caviglioli et al., *Nat. Rev. Microbiol.* **17**, 569–586 (2019).
3. R. L. Berendsen, C. M. J. Pieterse, P. A. H. M. Bakker, *Trends Plant Sci.* **17**, 478–486 (2012).
4. A. Williams, F. T. de Vries, *New Phytol.* **225**, 1899–1905 (2020).
5. Intergovernmental Panel on Climate Change (IPCC), *Global Warming of 1.5°C*, V. Masson-Delmotte et al., Eds. (Cambridge Univ. Press, 2018).
6. S. F. Bender, C. Wagg, M. G. A. van der Heijden, *Trends Ecol. Evol.* **31**, 440–452 (2016).
7. F. T. de Vries, M. D. Wallenstein, *J. Ecol.* **105**, 913–920 (2017).
8. T. J. Thirkell, M. D. Charters, A. J. Elliott, S. M. Sait, K. J. Field, *J. Ecol.* **105**, 921–929 (2017).
9. J. A. Lau, J. T. Lennon, *Proc. Natl. Acad. Sci. U.S.A.* **109**, 14058–14062 (2012).
10. X. Niu, L. Song, Y. Xiao, W. Ge, *Front. Microbiol.* **8**, 2580 (2018).
11. R. L. Rubin, K. J. van Groenigen, B. A. Hungate, *Plant Soil* **416**, 309–323 (2017).
12. G. Leng, J. Hall, *Sci. Total Environ.* **654**, 811–821 (2019).
13. D. Naylor, D. Coleman-Derr, *Front. Plant Sci.* **8**, 2223 (2018).
14. J. K. Jansson, K. S. Hofmockel, *Nat. Rev. Microbiol.* **18**, 35–46 (2020).
15. J. Schimel, T. C. Balser, M. Wallenstein, *Ecology* **88**, 1386–1394 (2007).
16. A. C. Martiny, K. Treseder, G. Pusch, *ISME J.* **7**, 830–838 (2013).

17. L. Xu et al., *Proc. Natl. Acad. Sci. U.S.A.* **115**, E4284–E4293 (2018).
18. L. Xu, D. Coleman-Derr, *Curr. Opin. Microbiol.* **49**, 1–6 (2019).
19. J. B. Martiny et al., *ISME J.* **11**, 490–499 (2017).
20. A. A. Malik et al., *ISME J.* **14**, 1–9 (2020).
21. C. Preece, J. Peñuelas, *Plant Soil* **409**, 1–17 (2016).
22. F. T. de Vries et al., *New Phytol.* **224**, 132–145 (2019).
23. N. J. Bouskill et al., *Front. Microbiol.* **7**, 323 (2016).
24. K. K. Treseder, R. Berlemont, S. D. Allison, A. C. Martiny, *PLOS ONE* **13**, e0206441 (2018).
25. C. V. Hawkes, B. G. Waring, J. D. Rocca, S. N. Kivlin, *Proc. Natl. Acad. Sci. U.S.A.* **114**, 6322–6327 (2017).
26. F. T. de Vries et al., *Nat. Commun.* **9**, 3033 (2018).
27. J. Li et al., *Front. Plant Sci.* **10**, 499 (2019).
28. N. Varoquaux et al., *Proc. Natl. Acad. Sci. U.S.A.* **116**, 27124–27132 (2019).
29. C. R. Fitzpatrick et al., *Proc. Natl. Acad. Sci. U.S.A.* **115**, E1157–E1165 (2018).
30. O. M. Finkel, G. Castrillo, S. Herrera Paredes, I. Salas González, J. L. Dangel, *Curr. Opin. Plant Biol.* **38**, 155–163 (2017).
31. S. T. Ramírez-Puebla et al., *Appl. Environ. Microbiol.* **79**, 2–9 (2013).
32. R. Murphy et al., *Benef. Microbes* **10**, 5–17 (2019).
33. M. Foo, I. Gherman, P. Zhang, D. G. Bates, K. J. Denby, *ACS Synth. Biol.* **7**, 1553–1564 (2018).
34. É. Szentirmai, N. S. Millican, A. R. Massie, L. Kapás, *Sci. Rep.* **9**, 7035 (2019).
35. P. Liu, Q. Qiu, Y. Lu, *Appl. Environ. Microbiol.* **77**, 3884–3887 (2011).
36. E. B. G. Feibert, C. C. Shock, L. D. Saunders, *Hortic. Sci.* **38**, 381–386 (2003).
37. M. A. Farag, H. Zhang, C.-M. Ryu, *J. Chem. Ecol.* **39**, 1007–1018 (2013).
38. P. Ahmad et al., *Plant Metabolites and Regulation Under Environmental Stress* (Academic Press, ed. 1, 2018).
39. A. Gargallo-Garriga et al., *Sci. Rep.* **8**, 12696 (2018).
40. T. Tohge, M. Watanabe, R. Hoefgen, A. R. Fernie, *Front. Plant Sci.* **4**, 62 (2013).
41. S. K. Sah, K. R. Reddy, J. Li, *Front. Plant Sci.* **7**, 571 (2016).
42. W. Hartung, A. Sauter, N. C. Turner, I. Fillery, H. Heilmeyer, *Plant Soil* **184**, 105–110 (1996).
43. A. A. Belimov et al., *Plant Physiol. Biochem.* **74**, 84–91 (2014).
44. A. Jahan et al., *Plant Physiol.* **179**, 317–328 (2019).
45. S. L. Lebeis et al., *Science* **349**, 860–864 (2015).
46. P. A. Bakker, R. F. Doornbos, C. Zamioudis, R. L. Berendsen, C. M. Pieterse, *Plant Pathol. J.* **29**, 136–143 (2013).
47. F. Van Gijsegem et al., *Front. Plant Sci.* **8**, 456 (2017).
48. M. D. Wallenstein, E. K. Hall, *Biogeochemistry* **109**, 35–47 (2012).
49. A. Meisner, W. de Boer, *Front. Microbiol.* **9**, 2279 (2018).
50. U. Friedrich et al., *Plant Soil* **353**, 59–71 (2012).
51. F. T. de Vries et al., *Nat. Clim. Chang.* **2**, 276–280 (2012).
52. N. C. Johnson, *Ecol. Appl.* **3**, 749–757 (1993).
53. S. Matesanz, R. Milla, *Environ. Exp. Bot.* **145**, 54–63 (2018).
54. Z. Wen et al., *New Phytol.* **223**, 882–895 (2019).
55. Z. Qiu, E. Egidio, H. Liu, S. Kaur, B. K. Singh, *Biotechnol. Adv.* **37**, 107371 (2019).
56. S. R. Tracy et al., *Trends Plant Sci.* **25**, 105–118 (2020).
57. C. S. Francisco, X. Ma, M. M. Zwyssig, B. A. McDonald, J. Palma-Guerrero, *Sci. Rep.* **9**, 9642 (2019).
58. D. Naylor, S. DeGraaf, E. Purdom, D. Coleman-Derr, *ISME J.* **11**, 2691–2704 (2017).
59. N. Khan, A. Bano, *PLOS ONE* **14**, e0222302 (2019).
60. S. S. K. P. Vurukonda, S. Vardharajula, M. Shrivastava, A. Skz, *Microbiol. Res.* **184**, 13–24 (2016).
61. M. D. Jochum et al., *Front. Microbiol.* **10**, 2106 (2019).
62. J. Chiappero, L. R. Cappellari, L. G. Sosa Alderete, T. B. Palermio, E. Banchio, *Ind. Crops Prod.* **139**, 111553 (2019).
63. M. Moshelion, O. Halperin, R. Wallach, R. Oren, D. A. Way, *Plant Cell Environ.* **38**, 1785–1793 (2015).
64. L. Szabados, A. Savouré, *Trends Plant Sci.* **15**, 89–97 (2010).
65. T. D. Eldhuset et al., *Plant Soil* **366**, 305–320 (2013).
66. J. Lipiec, C. Doussan, A. Nosalewicz, K. Kondracka, *Int. Agrophysics Lub.* **27**, 463–477 (2013).
67. M. A. Ahmed, E. Kroener, M. Holz, M. Zarebanadkouki, A. Carminati, *Funct. Plant Biol.* **41**, 1129–1137 (2014).
68. M. K. van der Molen et al., *Agric. For. Meteorol.* **151**, 765–773 (2011).
69. Data repository: doi:10.6084/m9.figshare.11962407.

ACKNOWLEDGMENTS

Funding: This work was funded by a NERC Discovery Grant (NE/P01206X/1) and a BBSRC David Phillips Fellowship to F.T.d.V. (BB/L02456X/1). **Author contributions:** All authors conceived the idea for the manuscript. F.T.d.V. led the writing of the manuscript with input from all authors. **Competing interests:** There are no competing interests. **Data and materials availability:** Bibliometric analysis is available in (69).

10.1126/science.aaz5192

REVIEW

The effects of drinking water service fragmentation on drought-related water security

Megan Mullin

Drought is a critical stressor that contributes to water insecurity. In the United States, an important pathway by which drought affects households' access to clean, reliable drinking water for basic needs is through the organization and activities of community water systems. Research on the local political economy of drinking water provision reveals the constraints on community water systems that affect their performance when confronting drought hazards. Fragmentation in responsibility for drinking water contributes to disparities in drought vulnerability, preparation, and response across households and across communities. The nature and extent of these disparities require further investigation to identify strategies for expanding water security in the face of drought and other water hazards.

By global standards, most Americans are water-secure with respect to drinking water, meaning that they have reliable access to affordable and safe drinking water in adequate supply for basic needs. Yet important gaps remain, especially in rural and impoverished communities, and overall risk to drinking water security is on the rise (1). Drought is a key contributor to the growth in water insecurity (2). Climatic and hydrologic conditions play a role in intensifying drought hazards for water consumers, as do social and political conditions, including water management regimes (3). In parts of the United States, especially the Southwest and interior West, droughts have become more frequent and severe over time, while changes in land use are producing increased water demand (4, 5). Warming temperatures reduce water storage in reservoirs and snowpack, and climate-induced pumping has contributed to widespread groundwater depletion (6). Deteriorating physical infrastructure for water storage, treatment, and delivery and inadequate technical, managerial, and financial capacity to adapt to changing conditions all heighten vulnerability to drought-related hazards.

Drought can push communities to the brink of their water supplies. U.S. states regularly declare drought emergencies and release funds for communities to drill new wells, repair existing facilities, or connect to a neighboring system. Loss of pressure in water distribution systems triggers boil-water advisories. Sometimes water systems completely run dry, making it necessary to turn to tanker trucks or even fire hoses to bring water into the community for weeks or months, until infrastructure can be improved or water supply augmented. Households whose private wells dry up or those receiving unreliable service from a water system purchase bottled or hauled water for drinking, cooking, and bathing. These events occur not just in the arid West but throughout the country,

because many water systems lack the capacity to withstand added stress from drought.

A growing body of research examines drinking water provision as it relates to drought, focusing on water managers' perceptions of scarcity (7–9), policy and management responses (10–15), and broader sociotechnical and socio-ecological relationships undergirding regional water resource governance (16–18). Other literature draws attention to the wide disparities in the quality and availability of drinking water service in the absence of drought (1, 19–21). An important link connecting drought hazards to household water security is the local political economy of drinking water provision. Nationwide, an estimated 87% of Americans receive their drinking water from a community water system (CWS) (22). Thus, for most households, the impact of drought on drinking water is mediated by the activities and responses of their CWS (Fig. 1). Understanding the political organization of drinking water delivery is critical for identifying strategies to expand water security in the face of drought and other water hazards.

Water security for drinking water systems during drought

Drought presents numerous challenges for drinking water management. Reduced water availability jeopardizes the ability to meet basic water needs in communities without surplus water supply. Drought also has negative impacts on water quality. Effects on water resources include microbial growth, increased organic load, saltwater intrusion, and leaching of natural and anthropogenic contaminants. Depending on local water management approaches and the condition of infrastructure, drought may further affect treated drinking water quality by way of pipe damage, increased water age in distribution systems, and changes in source mix (23).

The effects of drought on a CWS vary widely according to natural and physical features that determine exposure to drought hazard, local policies and management practices, and the CWS's position within a regional water

Nicholas School of the Environment, Department of Political Science, and Sanford School of Public Policy, Duke University, Durham, NC, USA. Email: megan.mullin@duke.edu

allocation system. Drinking water providers compete with other water users, including farms, power plants, and neighboring cities, for access to surface and groundwater resources, and environmental regulations limit overall water withdrawals. An institutional framework that includes water rights, contracts, allocation and purchase agreements, and collaborative management of water sources shapes a water system's ability to access adequate supply to meet its customers' basic needs when resources dwindle. These institutional constraints tend to be more long-standing and binding in regions with ongoing water stress because of feedbacks between water rights and infrastructure (24).

Even when a CWS is relatively unconstrained by the demands of other users, its ability to

times with great success. For example, in response to a statewide mandate in 2015, California water systems were able to reduce water use by an average of 25% (13). Instruments adopted as short-term drought response sometimes become part of a CWS's portfolio of strategies for managing demand in the long term (11), but they can be costly to implement. The two strongest instruments—pricing and mandatory use restrictions—are politically unpopular, harmful to water-intensive businesses and industry, and potentially deleterious to a community's growth goals (12, 15). Successful efforts to induce conservation can undermine a CWS's fiscal health by reducing the user fee revenue that funds water system operations. Drought response also requires a high degree of capac-

safe drinking water under normal conditions: They cannot take advantage of economies of scale in drinking water production and delivery; they have less access to private capital and other funding; and their technical, managerial, and operational capabilities are often inadequate to maintain regulatory compliance (34). Small systems also are less likely to engage in drought preparation and to respond quickly when drought conditions arise (10, 15, 35, 36). Institutional design makes a difference for drought response. Many water systems, especially small ones, are privately owned, often functioning as independent not-for-profit entities or ancillary to another business, such as a mobile home park (37). These systems, along with publicly owned special districts that lack broader authority beyond drinking water, have weak enforcement tools and operate outside the public view, which reduces their ability to influence water use behavior through education and outreach. Among the many data gaps on drinking water systems is a clear accounting of the distribution of ownership and governance structures across systems.

Small water systems are already at a disadvantage when it comes to protecting water security during drought, but the fragmentation of drinking water provision creates an additional problem: it differentiates between populations served by water systems along economic and racial lines. Several factors contribute to this differentiation. First, underlying residential segregation by race and income produces more homogeneity within geographic units as the number of units rises. Second, where water system service areas correspond with municipal boundaries, they replicate patterns of racial and economic segregation that exist across local jurisdictions (38). Third, where water service areas are not aligned with local government boundaries, service extension is the outcome of political decision-making and reflects power distributions in the community. In metropolitan areas, local policies guiding service provision historically have served to protect wealthy white residents from the spread of disease and to boost their property values (39, 40). In rural areas, the development of water institutions favored irrigation over provision of drinking water for domestic use (20, 41). The result in both cases is patterns of drinking water provision that systematically disadvantage communities of color and communities with low ability to pay (19, 21, 37, 42). These communities may be left without water service altogether or be made to depend on a small water system without an adequate revenue base to support its operation. Disparities in water and other local services subsequently undergird inequalities in growth, economic development, and political incorporation (43, 44). The nature and extent of demographic disparities between water systems is not well understood empirically, because few

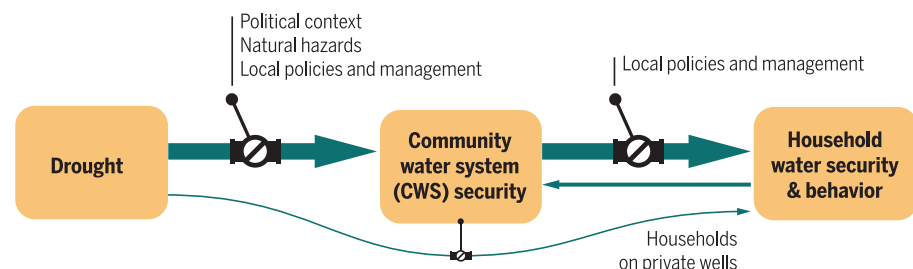


Fig. 1. Pathways for drought impacts on drinking water security. For most Americans, their local community water system mediates the impact of drought on drinking water security.

maintain water security during drought depends on historical policies and management practices that contribute to land-use and settlement patterns as well as the extent and condition of built infrastructure. Because neither drought nor drinking water are well integrated into local government land-use planning processes, communities miss opportunities to incorporate conservation and water resource protection into development decisions (25–27). Instead, water often gets used as a pretense in broader political conflict over growth management (28). Within the realm of water management, a CWS can improve its drought resilience through investments to diversify water sources, expand pumping capacity and storage, or build system interconnections. These types of investments require access to capital and the ability to generate stable and adequate revenue. Ongoing maintenance also can reduce drought vulnerability. Water loss through leaking distribution pipes exacerbates drought effects, and drought response can be delayed if unused intakes have been allowed to clog or emergency supply lines have been left to deteriorate. Rising drought frequency and rising drought severity may require distinct management responses.

Absent adequate long-term resilience planning and investment, short-term drought response can help protect water security within a CWS's service area. Water systems use a variety of instruments to encourage reductions in water use in order to stretch limited resources, some-

ity to monitor shortage conditions, implement appropriate policies, and then monitor and enforce those policies (29).

Some large CWSs are tackling the challenges of drought preparation and response and transitioning toward more-adaptive management to cope with changing climatic and hydrological conditions (8, 12, 16–18). However, apart from the very large systems, typically located in water-scarce regions, that most commonly receive research attention, there is limited evidence that CWSs more generally are expending effort to seek out information about their water supply or improve their drought preparedness (30, 31). Drought planning can challenge the dominant mindsets of decision-makers: CWS personnel, who prioritize avoidance of political conflict and the ability to meet customers' water demands, and elected politicians, who benefit more from disaster response than from disaster preparation (32, 33). The capacity to protect water quality and ensure adequate quantity during drought is not evenly distributed across CWSs. Some limitations are legacies of water allocation rules or infrastructure age, but many disparities are attributable to the political organization of CWSs and the demographic features of the communities they serve.

Water service is highly fragmented: of the 50,000-plus CWSs delivering drinking water year-round, more than 80% provide service to fewer than 3300 people (Fig. 2). Small water systems face myriad challenges in delivering

states have reliable, up-to-date maps of water system service areas that allow calculation of demographic attributes (45).

The effects of drinking water fragmentation have received attention in research and policy conversations with respect to water quality and affordability outcomes but less so for their impacts on drought resilience. Disparities in the size and composition of water service areas result in unequal vulnerability to drought hazards. CWSs with smaller, lower-income customer bases have less political influence in the state-, regional-, and watershed-level institutions that determine allocation priority, even when those institutions are designed to plan more proactively for drought contingency (46). Resource and information constraints can hinder participation in allocation processes, and decision-makers at these CWSs might perceive a stronger tension between sustainable management of the water resources and the imperatives of economic development. Because water service provision is funded overwhelmingly through user fees, small systems and those serving disadvantaged communities have less fiscal capacity to maintain robust infrastructure that minimizes leakage and protects water quality during periods of scarcity, especially if their customer base does not include major commercial users. These systems are also less able to make investments in response to detection of operational weaknesses (47). The challenges compound to put entire water systems at risk. During the 2011–2017 drought in California, nearly 150 CWSs serving an estimated 480,000 Californians experienced water shortages or requested emergency funding from the state in order to maintain water service. Most of these were small systems serving low-income populations, including many farmworker communities in the San Joaquin Valley (48).

Household water security during drought

Drought creates further disparities in drinking water security at the household level. Deteriorating infrastructure and low water pressure introduce variations in service within a CWS, with more-remote households and those in areas with older development more likely to experience problems with reliability and drinking water quality. Price increases intended to encourage conservation or those adopted to compensate for conservation-induced revenue shortfalls create an economic burden for low-income customers that could result in failure to pay and subsequent service shutoff. The difficulty associated with reducing water use depends on a variety of factors, including income, employment status, the proportion of typical water use that is dedicated to basic needs, and the extent to which one's livelihood is water-dependent. Commercial users that can help provide revenue stability for a CWS may end up competing for scarce resources with

CWSs by population served

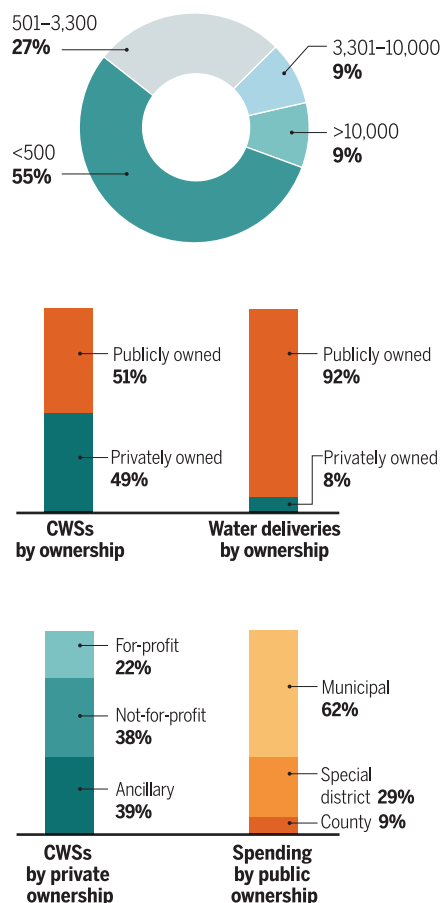


Fig. 2. Fragmentation in U.S. drinking water provision. A large majority of U.S. water systems serve fewer than 3300 people (64, 65). Ownership type affects a CWS's capacity for drought preparation and response.

households. The organizational form of a CWS—its boundaries, decision-making processes, and relationship to local government—influences the capacity of different users and groups to make claims and influence policy choices (24, 28, 41). Patterns of variation in water delivery that emerge within CWSs then feed back into overall CWS security by affecting the system's revenue base, its political influence in regional water allocations, and the salience and political framing of water issues in the media (17, 49).

For households that access drinking water from domestic wells, drought impacts are not directly mediated by a CWS but are indirectly affected by decisions of nearby CWSs about where to extend service. Those households that rely on domestic wells are particularly vulnerable to drought-induced groundwater depletion, especially in agricultural areas where drought induces additional pumping nearby (50). Service extension decisions may be influenced by a CWS's own vulnerability to drought hazards, but also they are the product of political conflict shaped

by existing power distributions. In South Texas, along the United States–Mexico border, irrigated agriculture dominates the institutional landscape for water decision-making, resulting in limited and inconsistent water service to the unincorporated *colonias* populated by low-income Mexican Americans (41). Residents' legal claims seeking greater participation in water-governing institutions have been unsuccessful, and patchy and precarious water service has left large communities with little drinking water security.

Tackling the challenge of drinking water fragmentation

Drought amplifies risks to drinking water security that are rooted in the local political organization of drinking water delivery. Two commonly cited solutions to fragmentation in water service are consolidation and collaboration. Full consolidation of water systems—integration of CWS management, operations, and facilities through merger or absorption—has long been viewed by regulators and policy analysts as an effective, and sometimes necessary, intervention for struggling water systems. For some water systems, consolidation can reduce risks associated with drought and other unpredictable events (51). However, this solution is, by nature, piecemeal and typically faces substantial political opposition stemming from community pride and concerns about local autonomy.

The second solution, collaboration, is a broader set of structures and processes for managing the problems of fragmented governance. Various forms of watershed, river basin, and groundwater basin authorities aim to coordinate the activities of multiple users to address common challenges, including drought. By bringing CWSs into conversation with other regional water users and one another, collaboration can promote information sharing, build social capital, and help CWSs reach agreements that balance short-term drought response with long-term supply planning (52). California has recently sought to promote collaboration among local water agencies to address problems related to water scarcity through programs for integrated regional water management and sustainable groundwater management. Participation in these efforts is costly, however, and representation in collaborative settings tends to reflect underlying power distributions (53, 54). Where collaborative processes are tied to funding, these uneven patterns of participation can have a meaningful impact on resource distributions (55). Collaboration could therefore aggravate rather than ameliorate disparities, and empirical evidence is lacking about trade-offs between collaboration and other dimensions of water resilience (56).

Water system governance beyond U.S. borders

The United States is not alone in facing challenges created by fragmentation in drinking water governance. In Canada and many European

nations, small water systems are prevalent and share many of the same financial and operational limitations that can put drinking water security at risk (34, 57). In the developing world, the consequences of fragmentation are more stark. Access to piped water from any type of provider is much less common—an estimated 31% of the population in the world's least-developed countries has piped water, compared with 96% of the population in Europe and North America (58). Lower rates of connection create more opportunities for selective extension of water service, often driven by wealth and electoral considerations. Emphasis on provision of new infrastructure to garner political support rather than maintenance of existing pipes contributes to widespread water loss and unreliable service. Informal water providers fill service gaps, playing an important role in providing water access for daily needs, but do so through a mechanism that becomes precarious in times of drought. Recent decades have seen widespread reform of water services in developing countries that favors local control and corporatization, or the separation of water finances and management from other government activities (59). Decentralization to small jurisdictions raises concerns about equity in water security, as the financial and management capacity of local water providers is a key factor in water delivery performance, especially under conditions of scarcity (60). The demands on water systems to self-finance their operations, typically through user fees, is a challenge in all settings, and substantial numbers of water systems in both developing and developed nations report that they are unable to cover basic operations and maintenance expenses (61).

Whereas large water systems in the United States have thus far avoided large-scale drought-induced water security crises, the same is not true internationally. In 2018, local officials in Cape Town, South Africa, warned of a looming “day zero,” when the city of four million people would run out of municipal water. By implementing severe restrictions, the water system managed to avoid turning off taps completely. The same was not true in surrounding Eastern Cape communities, where smaller water systems ran dry for months, requiring residents to spend hours in line waiting for periodic water deliveries and exposing them to grave public health risks. Those towns struggle to provide minimal levels of water to this day.

Pathways for policy and research

The challenges faced by U.S. CWSs demand a political analysis that extends beyond the boundaries of individual water systems. At the core of disparities in drinking water security is the reliance on local funding—in particular, user fees—to support drinking water provision. Rising threats to water security from drought and other stressors call for research into the

impacts of this governance and financial model. Not all political contributors to drinking water insecurity at the CWS or household level are funding-related: historic rights and allocations play a role, as well as ongoing power inequalities. But many drinking water system vulnerabilities relate to capacity. State-level policies for sharing revenue and resources across CWSs could enable more-vulnerable CWSs to invest in infrastructure repair, interconnectivity, supply adjustments, and demand management that reduce long-run vulnerabilities to drought. Reforms that reduce reliance on user fees may help buffer insecure CWSs from the fiscal costs associated with conservation. Designing appropriate policies requires that attention be paid to inequalities at multiple scales. Legal and fiscal analysis of policy options should consider lessons from school finance reform, where decades of efforts to equalize funding have been effective in reducing between-district, but not within-district, disparities in education outcomes (62).

As states increasingly take up the challenge of confronting climate change impacts, a high priority should be to enable local water systems to withstand drought. Many states support or require drought planning (11, 25), but these efforts do little to address the core vulnerabilities in water systems. A first step toward protecting water security during drought is to build a richer understanding of the distribution of vulnerabilities. Recent efforts in several states to develop maps of water system service areas should be replicated nationwide and integrated with data on drinking water finance, built infrastructure, and water supply and use. Systematic reporting on supply shortages, low-pressure events, and use of backup water supplies would help identify water systems at risk. Although states have expanded their collection and distribution of water data, many gaps remain, especially in relation to water use and the finances and performance of drinking water utilities (63). As drought hazards intensify, addressing weaknesses in drinking water management becomes all the more important to ensure universal water security.

REFERENCES AND NOTES

1. W. E. Jepson, A. Wutich, S. M. Collins, G. O. Boateng, S. L. Young, *WIREs Water* **4**, e1214 (2017).
2. D. Garrick, J. W. Hall, *Annu. Rev. Environ. Resour.* **39**, 611–639 (2014).
3. K. J. Bakker, *Econ. Geogr.* **76**, 4–27 (2000).
4. K. M. Andreadis, D. P. Lettenmaier, *Geophys. Res. Lett.* **33**, L10403 (2006).
5. T. S. Wilson, B. M. Sleeter, D. R. Cameron, *Environ. Res. Lett.* **11**, 054018 (2016).
6. T. A. Russo, U. Lall, *Nat. Geosci.* **10**, 105–108 (2017).
7. K. Dow, R. E. O'Connor, B. Yarnal, G. J. Carbone, C. L. Jocy, *Glob. Environ. Change* **17**, 228–237 (2007).
8. N. L. Engle, *Clim. Change* **118**, 291–306 (2013).
9. L. Dilling et al., *Clim. Risk Manage.* **23**, 32–42 (2019).
10. E. Maggioni, *Water Resour. Res.* **51**, 125–139 (2015).
11. A. Milman, C. Polsky, *J. Am. Water Resour. Assoc.* **52**, 605–619 (2016).
12. D. J. Hess et al., *Sociol. Forum* **31**, 807–827 (2016).
13. J. Palazzo et al., *Water Resour. Res.* **53**, 4459–4475 (2017).
14. M. P. Teodoro, Y. Zhang, D. Switzer, *Policy Stud. J.* **10.1111/psj.12287** (2018).
15. M. Mullin, M. E. Rubado, *Urban Aff. Rev.* **53**, 752–774 (2017).
16. S. Hughes, S. Pincetti, C. Boone, *Cities* **32**, 51–59 (2013).
17. M. Garcia, S. Islam, *Urban Water J.* **15**, 888–898 (2018).

18. G. Treuer et al., *Water Resour. Res.* **53**, 891–908 (2017).
19. C. L. Balazs, I. Ray, *Am. J. Public Health* **104**, 603–611 (2014).
20. C. Pannu, *Calif. Law Rev.* **100**, 223–268 (2012).
21. H. G. Leker, J. MacDonald Gibson, *PLOS ONE* **13**, e0193225 (2018).
22. C. A. Dieter, M. A. Maupin, *Public Supply and Domestic Water Use in the United States, 2015: U.S. Geological Survey Open-File Report 2017–1131* (U.S. Department of the Interior and U.S. Geological Survey, 2017).
23. S. J. Khan et al., *Water Res.* **85**, 124–136 (2015).
24. S. Pincetti, E. Porse, D. Cheng, *Environ. Manage.* **58**, 208–222 (2016).
25. D. A. Wilhite, M. J. Hayes, C. Knutson, K. H. Smith, *J. Am. Water Resour. Assoc.* **36**, 697–710 (2000).
26. X. Fu, Z. Tang, *Cities* **32**, 60–69 (2013).
27. G. Pierce, L. Lai, J. R. DeShazo, *J. Environ. Plann. Manage.* **62**, 2080–2100 (2019).
28. M. Mullin, *Governing the Tap: Special District Governance and the New Local Politics of Water* (MIT Press, 2009).
29. S. M. Olmstead, R. N. Stavins, *Water Resour. Res.* **45**, 1–10 (2009).
30. K. Cockerill, *Water Environ. J.* **28**, 242–251 (2014).
31. J. A. Ekstrom, L. Bedsworth, A. Fencel, *Clim. Change* **140**, 467–481 (2017).
32. D. Lach, H. Ingram, S. Rayner, *Tex. Law Rev.* **83**, 2027–2054 (2015).
33. A. Healy, N. Malhotra, *Am. Polit. Sci. Rev.* **103**, 387–406 (2009).
34. K. McFarlane, L. M. Harris, *Environ. Res.* **26**, 378–395 (2018).
35. S. Hughes, *Policy Stud. J.* **40**, 650–673 (2012).
36. C. J. Kirchhoff, M. C. Lemos, N. L. Engle, *Environ. Sci. Policy* **26**, 6–18 (2013).
37. G. Pierce, S. R. Gonzalez, *Environ. Justice* **10**, 168–173 (2017).
38. M. Mullin, in *Oxford Handbook of State and Local Government*, D. P. Haider-Markel, Ed. (Oxford Univ. Press, 2014).
39. W. Troesken, *Water, Race, and Disease* (MIT Press, 2004).
40. J. Trounstein, *Segregation by Design: Local Politics and Inequality in American Cities* (Cambridge Univ. Press, 2018).
41. W. Jepson, H. L. Brown, *Environ. Plann. A* **46**, 1032–1048 (2014).
42. S. M. Olmstead, *Land Econ.* **80**, 136–150 (2004).
43. M. W. Anderson, *UCLA Law Rev.* **55**, 1095–1160 (2008).
44. D. M. Puritoy, *Am. Behav. Sci.* **10.1177/0002764219859645** (2019).
45. J. VanDerslice, *Am. J. Public Health* **101** (suppl. 1), S109–S114 (2011).
46. R. L. Pirie, R. C. de Loë, R. Kreutzweiser, *J. Environ. Manage.* **73**, 25–38 (2004).
47. T. A. Scott, T. Moldogaziev, R. A. Greer, *Urban Stud.* **55**, 2821–2837 (2018).
48. L. Feinstein, R. Phurisamban, A. Ford, C. Tyler, A. Crawford, *Drought and Equity in California* (Pacific Institute, 2017).
49. K. J. Quesnel, N. K. Ajami, *Sci. Adv.* **3**, e1700784 (2017).
50. R. A. Pauloo et al., *Environ. Res. Lett.* **15**, 044010 (2020).
51. K. Hansen, M. Mullin, E. K. Riggs, *Perspect. Public Manag. Gov.* **10.1093/ppmgov/gvz017** (2019).
52. H. B. Zeff, J. D. Herman, P. M. Reed, G. W. Characklis, *Water Resour. Res.* **52**, 7327–7346 (2016).
53. M. Lubell, L. Lippert, *Int. Rev. Adm. Sci.* **77**, 76–100 (2011).
54. K. B. Dobbin, M. Lubell, *Policy Stud. J.* **10.1111/psj.12375** (2019).
55. I. Hui, N. Ulibarri, B. Cain, *Policy Stud. J.* **10.1111/psj.12266** (2018).
56. L. Rodina, *WIREs Water* **6**, e1334 (2019).
57. B. Rickert, M. Samwel, E. Shinee, F. Kožíšek, O. Schmoll, *Status of Small-Scale Water Supplies in the WHO European Region: Results of a Survey Conducted under the Protocol on Water and Health* (World Health Organization, 2016).
58. *Progress on Household Drinking Water, Sanitation and Hygiene 2000–2017: Special Focus on Inequalities* (United Nations Children's Fund and World Health Organization, 2019).
59. V. Herrera, A. E. Post, *World Dev.* **64**, 621–641 (2014).
60. J. Nelson-Núñez, J. P. Walters, D. Charpentier, *Water Policy* **21**, 1251–1265 (2019).
61. A. Danilenko, C. van den Berg, B. Macheve, L. J. Moffitt, *IBNET Water Supply and Sanitation Blue Book 2014: The International Benchmarking Network for Water and Sanitation Utilities Databook* (World Bank, 2014).
62. J. LaFortune, J. Rothstein, D. W. Schanzenbach, *Am. Econ. J. Appl. Econ.* **10**, 1–26 (2018).
63. L. Josset et al., *Earths Futur.* **7**, 433–449 (2019).
64. U.S. Environmental Protection Agency, “2006 Community Water System Survey, Volume II: Detailed Tables and Survey Methodology” (EPA Publication 815-R-09-002, 2009).
65. U.S. Census Bureau, 2012 Census of Governments: Finance—Surveys of State and Local Government Finances (2015); www.census.gov/data/datasets/2012/econ/local/public-use-datasets.html.

ACKNOWLEDGMENTS

The author thanks K. Hansen, E. V. Bell, A. Pickle, M. D. Smith, and referees for helpful comments and E. Monson for work on Fig. 1. **Funding:** Research contributing to this review was supported by a Collaboratory grant funded by Duke University. **Competing interests:** The author has no competing interests.

10.1126/science.aba7353

RESEARCH

IN SCIENCE JOURNALS

Edited by Michael Funk



SEX DETERMINATION

How egg temperature sets sex

In many reptiles, sex is determined by nest temperature during egg incubation. Temperature regulates the expression of an epigenetic modifier gene called *Kdm6b*, which is responsible for testis development. However, the molecular connection between temperature and sex-specific expression of this factor was previously unknown. Weber *et al.* have identified a link between temperature and the activation of a key regulator of *Kdm6b* called signal transducer and activator of transcription 3 (STAT3). After an influx of Ca^{2+} at the warmer, female-producing temperature, STAT3 is phosphorylated and silences *Kdm6b* transcription to repress testis development. —BAP *Science*, this issue p. 303

For reptiles such as the red-eared slider turtle, egg temperature determines an individual's sex.

TOPOLOGICAL OPTICS

A topological light funnel

Because most physical systems cannot be totally isolated from their environment, some degree of dissipation or loss is expected. The successful operation of such systems generally relies on mitigating

for that loss. Mathematically, such external interactions are described as non-Hermitian. Recent work has shown that controlling the gain and loss in these systems gives rise to a wide variety of exotic phenomena not expected for their isolated Hermitian counterparts. Using a time-dependent

photonic lattice in which the topological properties can be controlled, Weidemann *et al.* show that such a structure can efficiently funnel light to the interface irrespective of the point of incidence on the lattice. Such control of the topological properties could be useful for nanophotonic

applications in integrated optical chip platforms. —ISO

Science, this issue p. 311

GAS STORAGE

Delivering methane and hydrogen

The pressure for onboard storage of methane and hydrogen on vehicles is usually limited to 100 bar for the use of lightweight containers, but the amount stored can be increased with the use of absorbent materials. Efficient storage and delivery require a balance of volumetric and gravimetric storage. Chen *et al.* designed a metal-organic framework with trialuminum nodes and a large hexadentate aromatic linker that optimizes both parameters. This material surpassed the U.S. Department of Energy targets for methane and had a deliverable capacity of 14% by weight for hydrogen. —PDS

Science, this issue p. 297

TISSUE ENGINEERING

Elucidating the foreign body response

Synthetic materials are the building blocks for medical devices and implants but can induce a foreign body response after implantation, resulting in fibrous scar tissue encompassing the implant. Chung *et al.* define the role of interleukin-17 (IL-17) and cellular senescence in driving the foreign body response. The fibrous capsule from excised breast implants contained IL-17-producing T cells and senescent stromal cells. These findings were further validated in a murine model, and the authors found that blocking the IL-17 pathway or eliminating senescent cells mitigated local fibrosis around the implant. —OMS

Sci. Transl. Med. **12**, eaax3799 (2020).

BIOINSPIRED ROBOTICS

Origami takes flight

The wings of a ladybird beetle can sustain large aerodynamic forces during flight and are deployable

from a folded configuration within 100 milliseconds. The quick, springlike action and robustness of these wings stem from the geometry and deformation of a tape-spring-shaped vein in the beetle's wing frame. Baek *et al.* emulated the vein's structure to develop an origami design with elastic energy storage and self-locking capabilities that deploys within 116 milliseconds and can sustain loads of up to 210 grams (150 times its own weight). Kinetic and static behaviors were enhanced using the origami design in both a jumping robot and a jump-gliding robot. —MML
Sci. Robot. 5 eaaz6262 (2020).

CORAL REEFS

A complex landscape for reef management

Coral reefs are among the most biodiverse systems in the ocean, and they provide both food and ecological services. They are also highly threatened by climate change and human pressure. Cinner *et al.* looked at how best to maximize three key components of reef use and health: fish biomass, parrotfish grazing, and fish trait diversity. They found that when human pressure is low, all three traits can be maximized at high conservation levels. However, as human use and pressure increase, it becomes increasingly difficult to promote biodiversity conservation. At some levels of human impact, even the highest amount of protection is not able to maximize biodiversity conservation. —SNV

Science, this issue p. 307

GENE EDITING

A PAMless base editor

CRISPR-Cas DNA base editing typically requires a specific motif for targeting known as a protospacer-adjacent motif (PAM). This requirement limits the sequences within a genome that can be targeted. Walton *et al.* engineered specific variants of the *Streptococcus pyogenes* Cas9 enzyme named SpG and SpRY that could recognize and edit a wider array of PAMs. Using SpRY,

the authors were able to correct previously uneditable mutations associated with human disease. Although off-target effects were observed for these engineered Cas enzymes at levels similar to those of the wild-type enzyme, depending on the context, these engineered enzymes widen the potential applications of precision genome editing. —LMZ

Science, this issue p. 290

CATALYSIS

Lighting the way coming and going

Catalysts accelerate chemical reactions by breaking existing bonds and then forming new ones. Often, the factors that favor the first process can muddle the second one, constraining a catalyst's generality. Torres *et al.* found that visible light excitation of a palladium complex can facilitate both the breaking and making of carbon-halogen bonds (see the Perspective by Kathe and Fleischer). The reaction specifically forms acid chlorides by carbonylation of a wide variety of alkyl or aryl bromides and iodides. These products in turn can react further to form amides and esters. —JSY

Science, this issue p. 318;
see also p. 242

DROUGHT

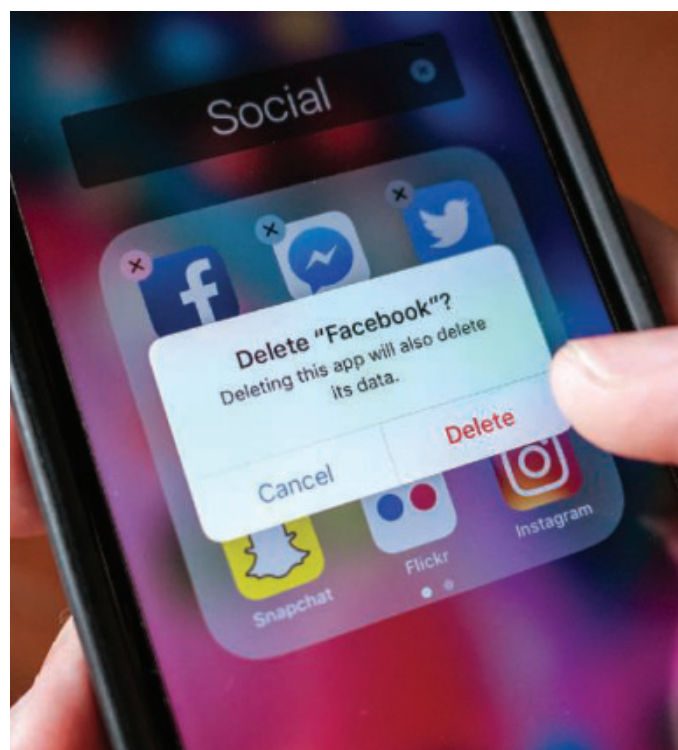
A trend of warming and drying

Global warming has pushed what would have been a moderate drought in southwestern North America into megadrought territory. Williams *et al.* used a combination of hydrological modeling and tree-ring reconstructions of summer soil moisture to show that the period from 2000 to 2018 was the driest 19-year span since the late 1500s and the second driest since 800 CE (see the Perspective by Stahle). This appears to be just the beginning of a more extreme trend toward megadrought as global warming continues. —HJS

Science, this issue p. 314;
see also p. 238

IN OTHER JOURNALS

Edited by **Caroline Ash**
and **Jesse Smith**



SOCIAL MEDIA

Connected, but at what cost?

Facebook users, randomized to deactivate their accounts for 4 weeks in exchange for \$102, freed up an average of 60 minutes a day, spent more time socializing offline, became less politically polarized, and reported improved subjective well-being relative to controls. However, the treatment group also became less knowledgeable about current events. Allcott *et al.* report that after the 4-week deactivation period ended, the treated subjects' Facebook use remained persistently lower than that of the controls, and treated subjects lowered the amount of compensation they would demand to deactivate their accounts for another 4 weeks. —BW
Am. Econ. Rev. 110, 629 (2020).

Disconnecting from Facebook led ex-users to socialize offline more, become less politically polarized, and improve their subjective well-being.

IMMUNOPSYCHIATRY

Depressing effects of microglia

Microglia act as the brain's resident cleanup squad by phagocytosing apoptotic cells, plaques, and pathogens. Because they can prune and reshape synapses, microglia

may also be influential in the pathogenesis of psychiatric illnesses. Lago *et al.* report that CD300f, a receptor found on microglia that recognizes the "eat me" signal phosphatidylserine, may be involved in major depressive disorder (MDD). A polymorphism of CD300f affects signaling and

is associated with protection against MDD in women but not men. A lack of CD300f impairs microglial metabolic fitness, and *Cd300f^{-/-}* female mice exhibited depressive-like behavior in models of MDD. Caveats about murine MDD models aside, this suggests that microglia and CD300f may be suitable future therapeutic targets for this disorder. —STS

Proc. Natl. Acad. Sci. U.S.A. **117**, 6651 (2020).

METABOLISM

Gut microbes and obesity

A plethora of studies have uncovered correlations between gut microbiome composition and common disorders such as metabolic disease. The hope is that these correlations can be translated into therapies using mechanism-based approaches. An alternative approach is fecal microbiota transplantation (FMT), a procedure in which gut microbiota from healthy donors are delivered to individuals who have, or are at risk of developing, a specific disorder. Yu *et al.* conducted a small, double-blind clinical trial to determine whether obese adults at risk of developing type 2 diabetes would benefit from oral FMT capsules derived from healthy, lean donors. After 3 months, they found durable microbial shifts in the recipients but no clinically meaningful changes in their metabolism or weight. —PAK

PLOS Med. **17**, e1003051 (2020).

CELL BIOLOGY

Lighting up endosomes

Endosomes are small, dynamic vesicles that sort and deliver signaling molecules to the correct location in the cell. Gupta *et al.* describe a new probe comprising a lipid-like small molecule that localizes to late endosomes, which they conjugated to a dye suitable for super-resolution imaging. These high-density, environmentally sensitive probes allowed them to visualize endolysosomes in primary cells for more than 7 minutes without affecting their structure



PSYCHOLOGY

Honesty “nudge” fails to replicate

Prior research has found that asking people to sign a tax form before rather than after filling it out increases honest reporting. This line of research has since been used as an example of the power of subtle behavioral “nudges” to influence positive behavior change compared with more-difficult-to-implement structural reforms. In a high-powered replication, Kristal *et al.* failed to reproduce this effect across several studies. Priming honesty by signing one’s name before providing information rather than afterward had no effect on subjects’ honesty. These findings have implications for current debates about the limitations of behavioral nudge-style interventions that favor subtle, easy-to-implement changes to the environment over more costly structural reform. —TSR

Proc. Natl. Acad. Sci. U.S.A. **117**, 7103 (2020).

Signing a tax form before filling it out does not produce more-honest reporting than signing after completing it.

or function. They were able to detect transient interactions between endosomes and identify endosome motility defects related to mutations associated with Niemann-Pick disease, a neurodegenerative endolysosomal storage disorder. These tools could be used to screen for small molecules that alter endosome dynamics. —VV

Nat. Chem. Biol. **16**, 408 (2020).

ECOLOGY

Extinctions and introductions

Introduced species have generally been considered a bad thing by ecologists because of the alterations that they can make to native ecosystems. In the case of introduced mammalian herbivores, however, there might sometimes be a silver lining. In a global survey

of introductions, Lundgren *et al.* show that biological traits of introduced herbivores can have the potential to match those of the large mammal herbivores that became extinct in the Late Pleistocene as a result of predation by humans. The loss of 35% of the world’s large mammal herbivores led to changes in biodiversity patterns and ecosystem structure and function, which may now be at least partly reversed as introduced species begin to fill the trait space once occupied by those that were lost to extinction. —AMS

Proc. Natl. Acad. Sci. U.S.A. **117**, 7871 (2020).

ORGANIC SYNTHESIS

Reacting at the most substituted center

Nucleophilic substitution is one of the key fundamental

mechanisms in organic synthesis that is generally used, except for a few isolated instances, to functionalize sterically unhindered primary and secondary carbon centers. Lanke and Marek report an efficient regio- and stereo-selective mechanism of intermolecular nucleophilic displacement at the quaternary carbon center of cyclopropyl carbinol derivatives. It proceeds with a complete inversion of configuration at the quaternary stereocenter and demonstrates high diastereo- and enantioselectivities. Because cyclopropyl carbinols can be easily formed from commercially available alkynes, the proposed mechanism could be used as a general synthetic method to produce various acyclic structures with stereodefined tertiary alkyl groups. —YS

J. Am. Chem. Soc. **142**, 5543 (2020).

RESEARCH ARTICLE SUMMARY

BIOCHEMISTRY

The Ccr4-Not complex monitors the translating ribosome for codon optimality

Robert Buschauer*, Yoshitaka Matsuo*, Takato Sugiyama, Ying-Hsin Chen, Najwa Alhusaini, Thomas Sweet, Ken Ikeuchi, Jingdong Cheng, Yasuko Matsuki, Risa Nobuta, Andrea Gilmozzi, Otto Berninghausen, Petr Tesina, Thomas Becker, Jeff Collier†, Toshifumi Inada†, Roland Beckmann†

INTRODUCTION: The tightly controlled process of gene expression requires messenger RNAs (mRNAs), which represent DNA-derived blueprints for polypeptides, to be translated by the protein-producing machinery of the cell, the ribosomes. Therefore, protein levels depend largely on cellular mRNA levels, and the control of mRNA decay is one of the most critical processes for setting the overall level of gene expression. Half-lives of mRNAs vary greatly between different transcripts, and regulation of the mRNA decay rate is intimately connected to the elongation phase of mRNA translation. To that end, codon optimality has been established as a key parameter for determining mRNA half-life in multiple eukaryotic organisms. It has also been established that the timely decay of short-lived mRNAs enriched with nonoptimal codons requires the Ccr4-Not complex. Ccr4-Not is an essential protein complex, with its best understood role in mRNA degradation, where it serves as the major cytoplasmic 3'-poly(A)-tail deadenylase that initiates decay of most mRNAs. By deadenylation and subsequent activation of the mRNA decapping machinery, the Ccr4-Not complex renders

mRNAs accessible to the major degrading exonucleases, such as Xrn1 on the 5' end and the exosome on the 3' end. The molecular mechanism underlying codon optimality monitoring and coordination with mRNA decay by the Ccr4-Not complex has remained elusive.

RATIONALE: Because nonoptimal codons affect decoding kinetics of the ribosome and mRNA degradation occurs largely cotranslationally, it is highly plausible that codon optimality is directly monitored on the ribosome. In addition, a direct physical link between the participating Ccr4-Not complex and the ribosome has been suggested previously, and the Not4 subunit of the complex, an E3 ligase, ubiquitinates the eS7 protein of the 40S ribosomal subunit in yeast. Therefore, we set out to gain insights into the connection between the Ccr4-Not complex and the translation machinery in the context of mRNA homeostasis by combining cryo-electron microscopy (cryo-EM), ribosome profiling, and biochemical analysis.

RESULTS: We used affinity-purified native Ccr4-Not-ribosome complexes from *Saccharomyces*

cerevisiae for analysis by cryo-EM and found that recruitment of Ccr4-Not to the ribosome occurs via the Not5 subunit. The N terminus of Not5—in particular, a three α -helix bundle—interacted specifically with the ribosomal E-site, and deletion of the Not5 N-terminus resulted in the loss of stable ribosome association of the Ccr4-Not complex. However, ubiquitination of the small ribosomal subunit protein eS7 through the Not4 subunit still occurred. The Not5 interaction involved

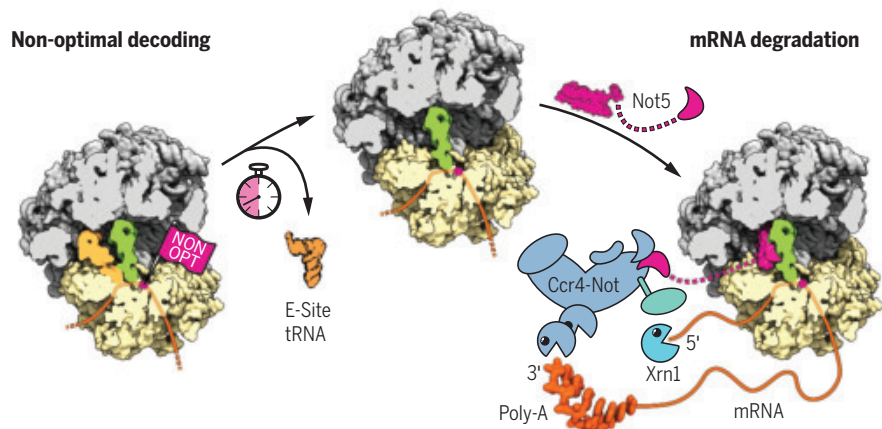
the ribosomal protein eS25 of the small subunit, in addition to transfer RNA (tRNA) and ribosomal RNAs (rRNAs). We found that Ccr4-Not interacts with both initiating and elongating ribosomes. In either case, Not5 engaged the E-site only when the ribosome adopted a distinct conformation lacking accommodated tRNA in the A-site, indicative of impaired decoding kinetics. Ribosome profiling revealed that low-optimality codons were enriched in the A-site in the Ccr4-Not-bound elongating ribosomes. This observation explained the low A-site tRNA occupancy observed with cryo-EM and suggested a link to codon optimality monitoring. Consistently, using mRNA stability assays, we found that loss of Not5 resulted in the inability of the mRNA degradation machinery to sense codon optimality. The observed dysregulation of mRNA half-life was detected upon Not5 deletion, Not5 N-terminal deletion, eS25 deletion, and loss of eS7 ubiquitination by Not4, which apparently serves as an upstream prerequisite for further Ccr4-Not activity on the ribosome. In addition, mRNA decapping was found to be impaired in these mutants, which confirmed that, in this pathway, Ccr4-Not triggers decapping downstream of optimality monitoring.

CONCLUSION: Our analysis elucidates a direct physical link between the mRNA decay-mediating Ccr4-Not complex and the ribosome. Dependent on preceding ubiquitination of eS7 by the Not4 subunit, the Ccr4-Not complex binds (via the Not5 subunit) specifically to the ribosomal E-site when the A-site lacks tRNA because of slow decoding kinetics. This state of the ribosome occurs in the presence of nonoptimal codons in the A-site, which explains the shorter half-lives of transcripts enriched in nonoptimal codons. Thus, our findings provide mechanistic insights into the coordination of translation efficiency with mRNA stability through the Ccr4-Not complex. ■

The list of author affiliations is available in the full article online.

*These authors contributed equally to this work.

†Corresponding author. Email: beckmann@genzentrumlm.de (R.B.); toshifumi.inada.a3@tohoku.ac.jp (T.I.); jmc71@case.edu (J.C.)
Cite this article as R. Buschauer et al., *Science* 368, eaay6912 (2020). DOI: 10.1126/science.aay6912



Ccr4-Not couples translation efficiency to mRNA degradation. When ribosomes encounter nonoptimal codons, low decoding efficiency leads to an increased likelihood of dissociation of the E-site tRNA before the cognate tRNA is accommodated in the A-site. As a result, the ribosomal E-site adopts a specific conformation, which is recognized by the Ccr4-Not complex through the N-terminus of its Not5 subunit, eventually triggering mRNA degradation by Xrn1.

RESEARCH ARTICLE SUMMARY

CANCER GENOMICS

Mechanisms generating cancer genome complexity from a single cell division error

Neil T. Umbreit^{*†}, Cheng-Zhong Zhang^{*†}, Luke D. Lynch[‡], Logan J. Blaine[‡], Anna M. Cheng, Richard Tourdot, Lili Sun, Hannah F. Almubarak, Kim Judge, Thomas J. Mitchell, Alexander Spektor, David Pellman[†]

INTRODUCTION: The chromosome breakage-fusion-bridge (BFB) cycle is a catastrophic mutational process, common during tumorigenesis, that results in gene amplification and drives rapid genome evolution. Major mechanisms underlying the BFB cycle are not understood, including its key feature of how chromosome bridges are broken. Furthermore, the simple pattern of DNA sequence rearrangement predicted by the canonical BFB model is not commonly observed in cancer genomes. Instead, the DNA sequence signature of BFB cycles is often accompanied by other genomic rearrangements, including chromothripsis, another catastrophic mutational pattern.

RATIONALE: We recreated essential steps of the BFB cycle in a defined system, enabling mechanistic studies and determination of the immediate and long-term genomic consequences of bridge formation. To identify the immediate outcomes of bridge breakage, we used live-cell imaging coupled with single-cell whole-genome sequencing (Look-Seq). Complex mutational mechanisms, some of which occurred over two generations, could be deconvolved by the comparison of haplotype copy number and structural variants in daughter or granddaughter cells. We then determined the long-term consequences of bridge breakage with genomic analysis of populations derived from single cells after

breakage of a bridge formed from an experimentally induced dicentric fusion of chromosome 4.

RESULTS: We showed that chromosome bridge breakage requires actomyosin-dependent mechanical force. Bridge formation and breakage is then coupled to a cascade of additional mutational events. For the initial step, we determined that direct mechanical bridge breakage can generate simple breaks and local DNA fragmentation, providing one explanation for a rearrangement pattern frequently observed in cancer genomes termed “local jumps.”

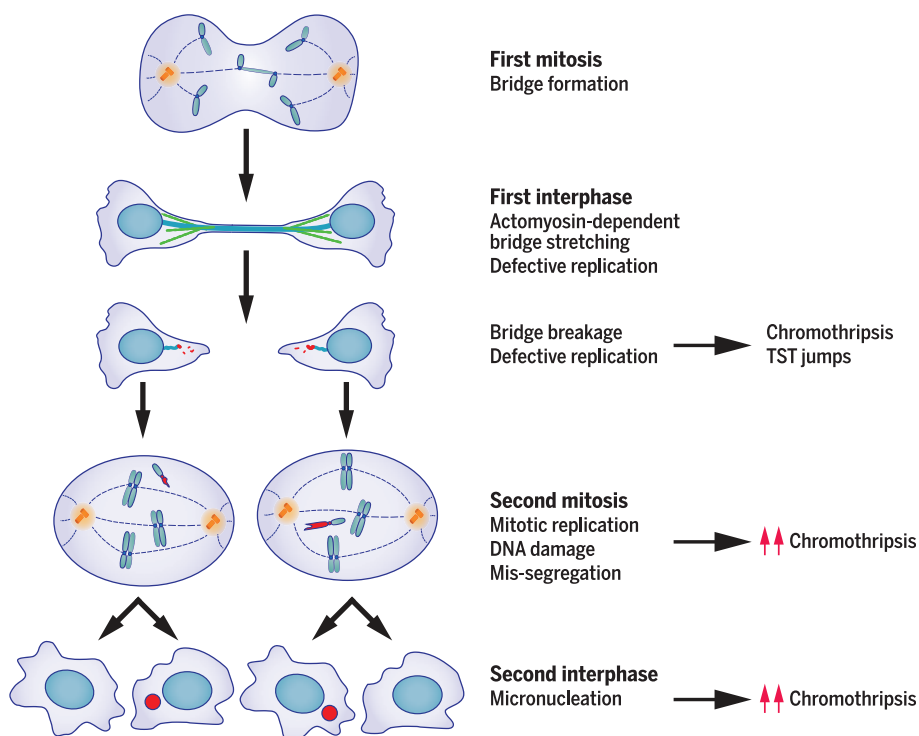
ON OUR WEBSITE

Read the full article at <http://dx.doi.org/10.1126/science.aba0712>

Concomitantly, there is defective DNA replication of bridge DNA, which our data suggest can generate complex rearrangements. Some of these rearrangements exhibit a distinct

sequence signature of tandem arrays of many short (~200 base pairs) insertions that we term “Tandem Short Template (TST) jumps.” We validated the presence of TST jumps in a human cancer by use of single-molecule long-read DNA sequencing. Next, a second wave of DNA damage and increased chromothripsis occurs during the mitosis after bridge formation, when chromosomes from broken bridges undergo an unexpected burst of aberrant DNA replication. Last, these damaged bridge chromosomes missegregate with high frequency and form micronuclei in the following cell cycle, which can generate additional cycles of bridging, micronucleation, and chromothripsis. Genome sequence analysis of clonal populations established that the breakage of chromosome bridges initiates iterative cycles of complex karyotype evolution. We observed an analogous series of events after the formation of micronuclei, suggesting a unifying model for how cancer-associated defects in nuclear architecture (“nuclear atypia”) promote genome instability.

CONCLUSION: We identified a cascade of events that explains how a single cell division error—chromosome bridge formation—can rapidly generate many hallmark features of cancer genomes, including ongoing genome evolution with subclonal heterogeneity. These results motivate a substantial revision of the chromosome BFB model, establishing that episodes of chromothripsis will be inherently interwoven with BFB cycles. These mutational events are common in cancer but likely also occur during development and across organismal evolution. ■



A storm of mutagenesis generates cancer genome complexity from a single cell division error.

The interphase actomyosin cytoskeleton (green fibers) stretches and breaks chromosome bridges, promoting local chromosome fragmentation (damaged DNA indicated in red). Defective DNA replication, first during interphase and later in the subsequent mitosis, generates additional DNA damage and chromothripsis, in some instances leaving behind a specific mutational signature (TST jumps). Bridge chromosomes frequently missegregate and form micronuclei, promoting additional chromothripsis.

The list of author affiliations is available in the full article online.

^{*}These authors contributed equally to this work.

[†]Corresponding authors. Email: neilt_umbreit@dfci.harvard.edu (N.T.U.); david_pellman@dfci.harvard.edu (D.P.); cheng-zhong.zhang@dfci.harvard.edu (C.-Z.Z.)

[‡]These authors contributed equally to this work.

Cite this article as N. T. Umbreit *et al.*, *Science* **368**, eaba0712 (2020). DOI: 10.1126/science.aba0712

RESEARCH ARTICLES

BIOSYNTHETIC ENZYMES

Metabolomics and mass spectrometry imaging reveal channeled de novo purine synthesis in cells

Vidhi Pareek^{1*}, Hua Tian^{1,2}, Nicholas Winograd^{1†}, Stephen J. Benkovic^{1†}

Metabolons, multiprotein complexes consisting of sequential enzymes of a metabolic pathway, are proposed to be biosynthetic “hotspots” within the cell. However, experimental demonstration of their presence and functions has remained challenging. We used metabolomics and in situ three-dimensional submicrometer chemical imaging of single cells by gas cluster ion beam secondary ion mass spectrometry (GCIB-SIMS) to directly visualize de novo purine biosynthesis by a multienzyme complex, the purinosome. We found that purinosomes comprise nine enzymes that act synergistically, channeling the pathway intermediates to synthesize purine nucleotides, increasing the pathway flux, and influencing the adenosine monophosphate/guanosine monophosphate ratio. Our work also highlights the application of high-resolution GCIB-SIMS for multiplexed biomolecular analysis at the level of single cells.

De novo purine biosynthesis (DNPB) is a highly conserved, energy-intensive pathway that coordinates with the purine nucleotide salvage process to maintain purine levels to support cellular proliferation, survival, and metabolic adaptation under varying nutritional supply and evolving environmental demands (Fig. 1A) (1). The de novo pathway is carried out by six enzymes in higher organisms, including humans, commencing with phosphoribosyl pyrophosphate (PRPP), which is converted to inosine monophosphate (IMP) in 10 sequential steps (fig. S1A). IMP is the branchpoint intermediate that is converted to either adenosine 5'-monophosphate (AMP) or guanosine 5'-monophosphate (GMP) by four enzymes. By contrast, the free purine bases hypoxanthine, adenine, and guanine can be combined with PRPP to regenerate their respective mononucleotides by the action of salvage enzymes—hypoxanthine guanine phosphoribosyltransferase (HGPRT) and adenine phosphoribosyltransferase (APRT)—in a single step (Fig. 1A) (2–5).

We previously reported the partial colocalization of multiple DNPB enzymes observed as cytosolic punctate structures, heterogeneous in their size, number, and composition, by fluorescence microscopy (2, 6–8). A substantial fraction of these dynamic structures, called purinosomes, show proximity to mitochondria (9), whereas others reside on microtubules and show directed movement toward mitochondria (10). The mitochondria-associated purinosomes

are proposed to constitute the active DNPB metabolon, but the dynamic and fragile nature of such multienzyme complexes (purinosomes and all metabolons in general) (11, 12) has impeded their in vitro reconstitution. Moreover, artifacts introduced by transient overexpression and limitations of fluorescence imaging-based methods have made it challenging to determine the complete enzymatic and ancillary protein composition, to elucidate their relative stoichiometry in the complex, and to ascertain the functional state of the enzymes in purinosomes.

With the purinosome as a potential precedent, we sought support for the hypothesis that cellular metabolic pathways might generally organize in space and time to confer different properties on the collective versus the individual enzymes. Although this study is restricted to HeLa cells, we envision the extension of this methodology to a variety of cells in normal and disease states, leading to insights into how the function of metabolic pathways might be altered to sustain cellular processes.

A model to probe the de novo purine biosynthesis pathway

The two alternative routes of purine synthesis, salvage and de novo, were probed by following the incorporation of labeled hypoxanthine or glycine (Gly), respectively, in the intermediates and end nucleotides of the two pathways (Fig. 1A). Upon purine depletion, where purinosome formation has previously been observed, HeLa cells showed significant de novo synthesis, indicated by higher abundance of the DNPB intermediate 5-aminoimidazole-4-carboxamide ribonucleotide (AICAR) (Fig. 1B) as well as [¹⁵N]Gly incorporation in the products, AMP and GMP (hereafter AMP/GMP) (Fig. 1C). When cultured in purine-rich (P+) media, the cells

instead seemed to only carry out salvage synthesis, quantified by [¹⁵N₄]hypoxanthine incorporation in AMP/GMP (Fig. 1C). Thus, we used the purine-depleted HeLa cells, which show high DNPB flux, as the model system to probe the metabolic consequence of purinosome formation.

We developed a model to mathematically predict the distribution of isotopic labels that would be expected in the absence of the DNPB metabolon, and then tested the predictions by performing an in vivo isotope incorporation experiment. When cells are grown in isotopically labeled [¹³C₃, ¹⁵N]Ser (label on backbone and side-chain carbons as well as the backbone amine), labeled carbon and nitrogen can enter into various metabolites within the pathway (Fig. 1D). Cells take up labeled Ser from the media, which is then internalized by mitochondria through the mitochondrial Ser transporter SFXN1 and is acted upon by a suite of enzymes [serine hydroxymethyltransferase 2 (SHMT2) and different isoforms of methylenetetrahydrofolate dehydrogenase/cyclohydrolase (MTHFD)] that constitute the mitochondrial one-carbon metabolism, producing Gly and formate (13, 14). These products exit the mitochondria and are incorporated in different cytosolic pathways, including the DNPB pathway, by the action of the enzymes GART (trifunctional phosphoribosylglycinamide formyltransferase) and ATIC (bifunctional 5-aminoimidazole-4-carboxamide nucleotide formyltransferase/IMP cyclohydroxylase) (Fig. 1D) (15).

We considered a null hypothesis model assuming each of the 10 steps of the pathway, starting with PRPP and leading up to the formation of IMP, to be independent of each other; all the intermediates to be completely equilibrated with their respective cytosolic pools; and a homogeneous distribution of all the enzymes (i.e., no purinosome formation and localization proximal to mitochondria), coenzymes, substrates, and cofactors in the cytosol. The model allows prediction of the isotopomer distribution in DNPB pathway intermediates and end products assuming uniform isotopically labeled Gly (1 – *x*) and formate (1 – *y*) incorporation across the pathway (Fig. 1E). If *x* and (1 – *x*) are the respective fractions of unlabeled and labeled Gly, and *y* and (1 – *y*) are the respective fractions of unlabeled and labeled formate generated from the mitochondrial metabolism of [¹³C₃, ¹⁵N]Ser, the incorporation of labeled Gly and formate into the DNPB pathway can be mathematically described (Fig. 1E). It follows that the observed isotopomer distribution in DNPB pathway intermediates that show one Gly and one formate incorporation [i.e., phosphoribosyl-*N*-formylglycinamide (FGAR), phosphoribosyl aminoimidazole succinocarboxamide (SAICAR), and AICAR] can be used to calculate the source Gly (1 – *x*) and formate (1 – *y*) isotope enrichment (Fig. 1F), as well as to predict the expected isotopomer distribution

¹Department of Chemistry, Pennsylvania State University, University Park, PA 16802, USA. ²Materials Research Institute, Pennsylvania State University, University Park, PA 16802, USA.

*Present address: Huck Institutes of the Life Sciences, Pennsylvania State University, University Park, PA 16802, USA.

†Corresponding author. Email: sjb1@psu.edu (S.J.B.); nxw@psu.edu (N.W.)

Fig. 1. A theoretical model to interrogate DNPB in HeLa cells upon pathway up-regulation. (A) Purine

nucleotides can be regenerated by salvage synthesis (conversion of free purine base back to the nucleotides) or a 10-step de novo purine biosynthesis (DNBP) starting with PRPP. [$^{15}\text{N}_4$]Hypoxanthine (Hypo) incorporation is used to monitor salvage; [^{15}N]Ser-derived Gly ([^{15}N]Gly) incorporation is used to monitor DNBP flux.

(B) Abundance of the DNPB pathway intermediate AICAR for purine-rich (P+) or purine-depleted (P-) media conditions. * $P < 0.02$ (two-tailed t test). **(C)** [^{15}N]Ser incorporation in the end products AMP and GMP. Data in (B) and (C) are means \pm SD of three independent experiments. **(D)** The metabolic interdependence of the cytosolic and mitochondrial metabolism to support DNPB and the flow of stable isotope-labeled Gly and formate, generated in mitochondria from labeled [$^{13}\text{C}_3$, ^{15}N]Ser, into the DNPB pathway intermediates and the end-product nucleotides. Pink circles denote ^{13}C and ^{15}N atoms of the labeled Ser backbone (produces [$^{13}\text{C}_2$, ^{15}N]Gly, +3 Da); blue circles represent the ^{13}C at its side-chain β position ([^{13}C]formate, +1 Da). Each pink and blue circle denotes incorporation of one labeled atom. Red diamond. SFXN1

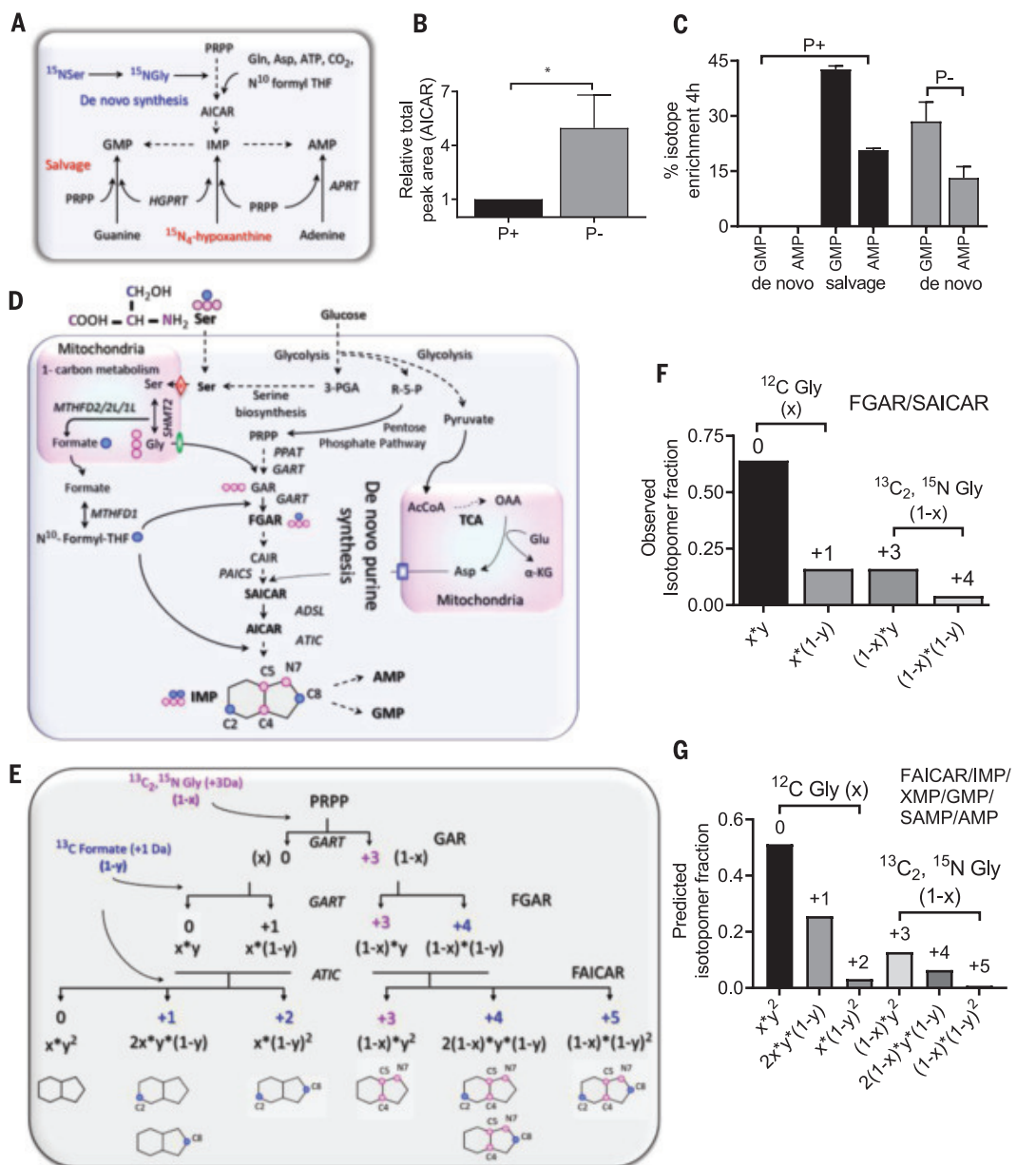
(mitochondrial Ser transporter); green oval, SLC25A38 (mitochondrial Gly transporter); blue rectangle, SLC25A12/SLC25A13 (mitochondrial glutamate/aspartate transporter). See fig. S1 caption for acronyms not defined in text. **(E)** The classical DNPB pathway model and the isotopomers of intermediates and end nucleotides, with the labeled positions indicated on the product purine ring. Labeled Gly [x , unlabeled fraction; $(1 - x)$, labeled fraction] and labeled formate [y , unlabeled fraction; $(1 - y)$, labeled fraction] generated from [$^{13}\text{C}_3, ^{15}\text{N}$]Ser enter the DNPB pathway at three different steps (curved arrows); the first two are catalyzed by the enzyme GART and the third is catalyzed by the enzyme ATIC.

in 5-formamidoimidazole-4-carboxamide ribonucleotide (FAICAR) and all the downstream nucleotides (Fig. 1G). [^{13}C , ^{15}N]Ser is particularly useful in generating unique isotopomer species arising from unlabeled and labeled Gly with no overlap between them and allowing for calculation of the newly generated pools of

each intermediate and end product (see supplementary materials).

Channeled de novo purine biosynthesis by purinosomes adjacent to mitochondria

Our model describes DNPB as a simple diffusive relay of reactions (Fig. 1E), and the follow-



Note that the +3, +4, and +5 isotopomer species in the end nucleotides show no interference from the preexisting or unlabeled nucleotide pools that are generated in parallel. **(F)** Example showing the use of the model to calculate $(1 - x)$ and $(1 - y)$ from the observed FGAR and SAICAR isotopomers. The values were calculated for each individual experiment. **(G)** The isotopomer distribution in FAICAR is predicted using the values of $(1 - x)$ and $(1 - y)$ and the observed SAICAR isotopomer distribution. All the end-product nucleotides (IMP, AMP, GMP) generated via DNPB in the time course of the experiment are expected to have the same isotopic distribution as FAICAR (fig. S1, A to C).

ing testable predictions arise from it: (i) IMP and all the downstream nucleotides must have the same isotopomer distribution of +3, +4, and +5 species, because there is no further isotope incorporation after FAICAR formation; and (ii) labeled Gly and formate enrichment in the DNPB intermediates and end nucleotides generated

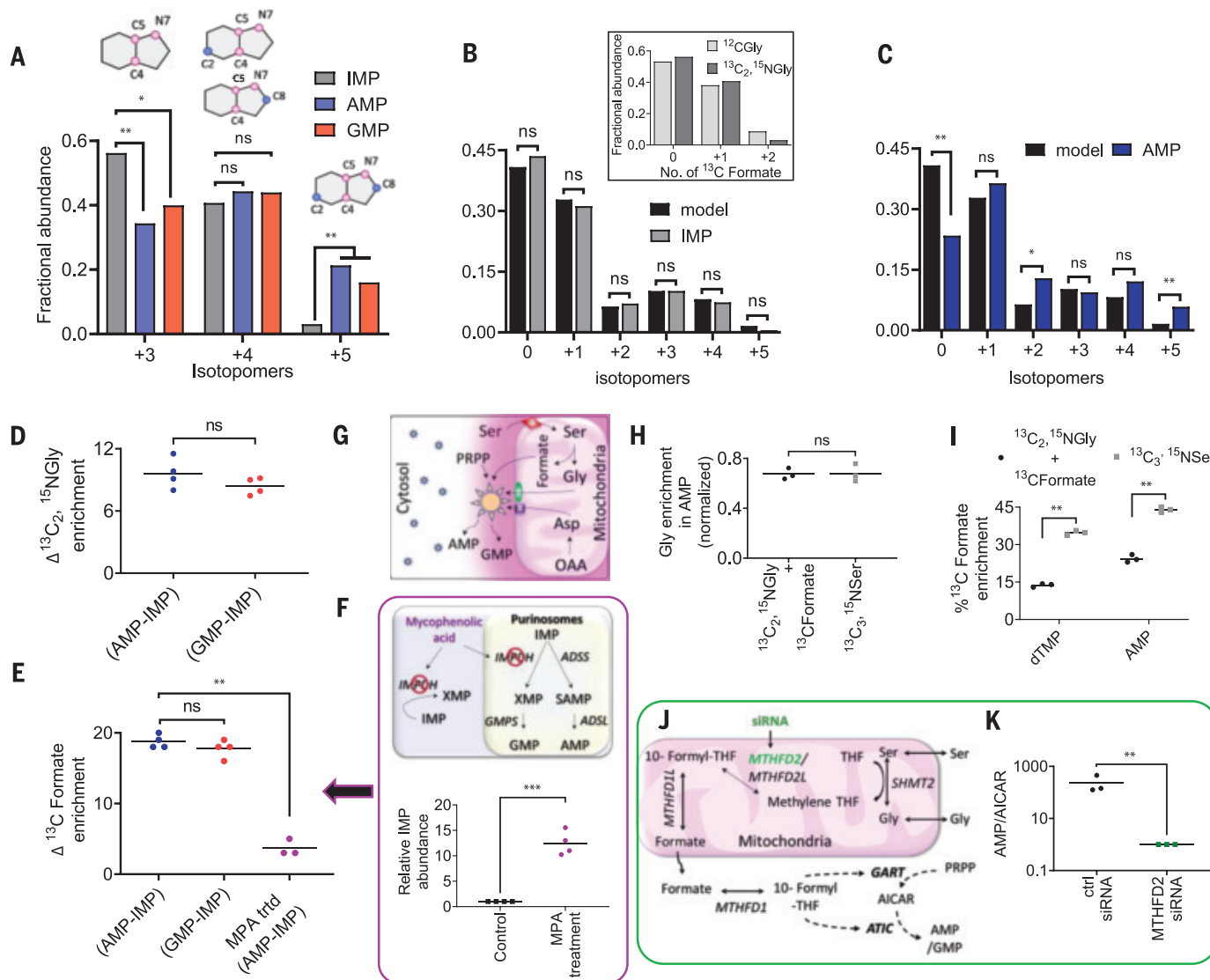


Fig. 2. HeLa cells show highly channeled DNPB by enzymes proximal to mitochondria. (A) Fractional distribution of de novo synthesized +3, +4, and +5 isotopomers in IMP, AMP, and GMP. The +3 isotopomer has a significantly lower fractional contribution in AMP and GMP relative to IMP, but that of the +5 isotopomer is significantly higher than IMP. A paired two-tailed *t* test was performed to analyze the ratio of isotopic abundance of each isotopomer. Data from four independent replicates were combined to assess the significance of the isotopomeric differences between IMP and AMP/GMP. **P* < 0.05, ***P* < 0.005; ns, not significant. (B and C) The isotopomer distribution calculated according to the model described in Fig. 1G matched the observed distribution in IMP (B) but not AMP (C) [or GMP (fig. S2F)]. Inset in (B) shows overlay of the observed fractional abundances of IMP isotopomers arising from 0, 1, or 2 ^{13}C incorporations (derived from formyl-THF) in purine ring containing either unlabeled Gly or $^{13}\text{C}_2, ^{15}\text{N}$ Gly for one representative experiment. The values were computed as described in fig. S1C. (D and E) There is a ~10% difference in $^{13}\text{C}_2, ^{15}\text{N}$ Gly (D) and a ~15 to 20% difference in ^{13}C formate enrichment (E) between newly synthesized AMP/GMP and IMP. (F) ^{13}C Formate enrichment difference between AMP and IMP is significantly lowered upon mycophenolic acid (MPA) treatment [magenta symbols in (E)]. (G) Localization of a "complete" functional purinosome (which shows channeling, shown as large sun symbol) near mitochondria, the site of production of isotopically labeled Gly and formate, leads to higher isotope enrichment in the purine nucleotides, AMP

and GMP, produced by metabolic channeling. Free enzymes and incomplete purinosomes residing away from the mitochondria (small sun symbols) show lower isotope enrichment because of their limited accessibility to labeled substrates. Other symbols and acronyms are the same as in Fig. 1A and fig. S1A. (H and I) Comparison of Gly and formate enrichment, respectively, in AMP [and GMP (fig. S2H)] when molar equivalents of $^{13}\text{C}_2, ^{15}\text{N}$ Gly + ^{13}C formate were added to the media instead of $^{13}\text{C}_3, ^{15}\text{N}$ Ser. As a result of the regeneration of labeled Ser from Gly and formate (fig. S2G) and further Ser metabolism in the mitochondria, channeled synthesis of AMP/GMP was still supported. (I) Consistent with the lower formate uptake, indicated by lower isotope enrichment in deoxythymidine monophosphate (dTMP), enrichment in AMP was lower with Gly + formate than with Ser. (J) DNPB enzymes GART and ATIC use 10-formyl-THF, and the cytosolic availability of this cofactor depends on the mitochondrial one-carbon metabolism that generates formate from Ser. (K) Knockdown of the mitochondrial one-carbon metabolism enzyme MTHFD2 by siRNA treatment led to a significant reduction in the de novo synthesized AMP and GMP flux but significant AICAR accumulation. For each experiment, three or four biological replicates were performed with one or two technical replicates; (A), (B), and (C) and fig. S2, D to F, correspond to the same representative experiment. In (B) and (C), data from four independent experiments were used for statistical analysis. **P* < 0.05, ***P* < 0.005. In (D), (E), (H), (I), and (K), the mean and individual data points are plotted. **P* < 0.05, ***P* < 0.005 (paired two-tailed *t* tests).

during the course of the experiment should be the same (fig. S1, B and C). To test these predictions, we performed isotopic incorporation experiments to probe the mitochondria-dependent generation of isotopically labeled Gly and formate and their incorporation in purines by supplying a limited concentration of [$^{13}\text{C}_3$, ^{15}N]Ser (30 μM) for 4 hours, followed by high-resolution quantitative liquid chromatography–mass spectrometry (LC/MS) of cellular metabolite extracts (fig. S2, A to C).

In contrast to the prediction, the fractional abundances of the two isotopomers (+3 and +5) in IMP were significantly different from those in AMP and GMP (Fig. 2A and fig. S2F), respectively, signifying that IMP and AMP/GMP have distinct isotopomeric distributions. To understand the source of this difference, using the observed FGAR and SAICAR isotopomer distribution in each independent experiment, we computed the complete isotopomer distribution in IMP as described by the model and compared it with the observed isotopomer distribution for IMP and all the nucleotides downstream of it, namely xanthosine monophosphate (XMP), succinyl-AMP (SAMP), AMP, and GMP (pathway steps shown in fig. S1A). Whereas the observed distribution for IMP and XMP matched the model-predicted isotopomer distribution (Fig. 2B and fig. S2D), AMP, SAMP, and GMP all showed a significantly different isotopomer distribution relative to the prediction (Fig. 2C and fig. S2, E and F). Consequently, IMP and its precursor substrates FGAR and SAICAR appear to have been synthesized from the same cytosolic pool of substrates (Gly and formate) and to have different isotopic enrichment relative to the substrate pool used for AMP and GMP synthesis. Moreover, no pathway intermediates with the isotopic enrichment seen in AMP/GMP were detected.

Next, using the observed isotopomer distribution in AMP and GMP, we computed the percentage isotopic enrichment in the source substrates of the channeled pathway. The newly generated channeled DNPB products, AMP/GMP, had higher isotope enrichment than IMP, synthesized by the unchanneled pathway, with respect to both Gly and formate. The newly synthesized AMP/GMP showed ~10% higher Gly enrichment (Fig. 2D) and 15 to 20% higher formate enrichment relative to IMP (Fig. 2E). We conclude that the synthesis of AMP and GMP is accomplished in a highly channeled manner, preventing pathway intermediates from equilibrating with their bulk cytosolic pools. The higher isotope enrichment in AMP/GMP relative to IMP indicates the physical proximity of an “active” DNPB metabolon or plausible direct association of the enzymes with the mitochondrial metabolite transporters.

To test this explanation, we poisoned cells with mycophenolic acid (MPA), a specific high-affinity inhibitor of IMP dehydrogenase

(IMPDH), an enzyme involved in the synthesis of guanine nucleotides (16). IMPDH inhibition is expected to cause accumulation and leakage of IMP from purinosomes, leading to intermixing of IMP produced from the two independent pathways. As expected, treatment of cells with the inhibitor resulted in significant accumulation of IMP (by a factor of ~12) (Fig. 2F) as a result of forced release of IMP synthesized by the channeled purinosomes. Consistent with our hypothesis, upon MPA treatment the observed labeled formate enrichment in AMP and IMP was similar (Fig. 2E and fig. S2I). Likewise, when the concentration of isotope-labeled Ser (120 μM) was increased by a factor of 4, it led to homogeneous spread of labeled formate across the cytosolic volume. Under these conditions, GMP and AMP (synthesized by channeled pathway) and the intermediates XMP and IMP (synthesized by unchanneled pathway) showed similar formate isotope enrichment (fig. S2, C and M).

These observations provide a rationale for the interpretation that the mitochondria-proximal purinosome must represent the “active” DNPB metabolon. This proximity results in the preferential capture of Ser-derived Gly and formate by “active” purinosomes for channeled DNPB, in which the equilibration of the purinosome-synthesized intermediates with their respective bulk cytosolic pools is limited. The detected IMP, on the other hand, must arise from a second diffusive substrate pathway or incomplete purinosomes. Consequently, the “active” DNPB metabolon represents the assembly of nine enzymes localized proximal to mitochondria, capable of catalyzing the conversion of PRPP to AMP and GMP in a sequence of 14 highly channeled steps (Fig. 2G). This may also rationalize the previously reported directed migration of purinosomes along the microtubule to facilitate the access of mitochondrially generated metabolites, Gly, Asp, and formate.

Instead of labeled Ser, when molar equivalents of labeled Gly and formate are supplemented in the media, action of the enzymes MTHFD1 and SHMT1 regenerated cytosolic labeled Ser (17) (fig. S2G). Under these conditions, we still observed channeled AMP/GMP synthesis, as reflected by the similar isotope incorporation in AMP and GMP (Fig. 2, H and I, and fig. S2H). The percentage of Gly incorporation in the end nucleotides AMP/GMP was normalized by the observed Gly enrichment in reduced glutathione to account for the differences in the uptake of Ser and Gly (Fig. 2H and fig. S2H).

Next, we examined whether the channeled DNPB exhibited an increase in the pathway efficiency, a hallmark of metabolons. We estimated the difference in the efficiencies of the DNPB channeled versus unchanneled pathways operating in parallel. The ratio of total newly synthesized AMP and GMP was higher

than that of the total IMP produced during our experiment by a factor of ~7, highlighting the effectiveness of the mitochondria-associated multienzyme assembly in achieving greater pathway flux (fig. S2J). The role of mitochondrial metabolism in supporting the channeled pathway was further tested by knocking down the mitochondrial formate production pathway, and consequently 10-formyltetrahydrofolate (10-formyl-THF) production, by targeting MTHFD2 (one of the enzymes involved in mitochondrial one-carbon metabolism) (18) (Fig. 2J). Upon small interfering RNA (siRNA)-mediated knockdown of MTHFD2 (fig. S2K), there was a disruption in the pathway efficiency by a factor of ~100, reflected in the accumulation of the intermediate AICAR and a decrease in the production of the end product (AMP) relative to the control (Fig. 2K).

IMP lies at a branchpoint step, and its partitioning into the two possible downstream nucleotides AMP or GMP presents an intriguing scenario. The kinetic parameters for the individual enzymes and their overall availability are expected to favor guanine nucleotide synthesis over the adenine nucleotide by at least a factor of ~25 (7). On the other hand, the abundance of adenine nucleotides is higher than that of guanine nucleotides by a factor of ~10, and the adenine nucleotide content in the human genome is higher (~30%) than the guanine nucleotide content (~20%) (19). The channeled pathway favors the synthesis of adenine nucleotides over guanine nucleotides (fig. S2L). We hypothesize that cells may achieve preference for adenine nucleotides by regulating the composition of purinosomes to favor the enzymes adenylosuccinate synthetase (ADSS) and bifunctional adenylosuccinate lyase over IMPDH and GMP synthetase, by modulating the orientation of the branchpoint enzymes in the purinosome, or by localizing purinosomes close to the mitochondrial site of Asp production, thus increasing the availability of Asp for ADSS.

Application of high-resolution GCIB-SIMS imaging to probe biochemistry at the single-cell level

Mass spectrometry imaging (MSI) has emerged as a powerful tool to spatially locate the endogenous and exogenous compounds in various biological systems (20–23). We used GCIB-SIMS, which permits high-mass ion detection with low chemical damage, to study the cytoplasmic distribution of intact molecular ions of purine biosynthetic pathway intermediates and end nucleotides in a frozen hydrated monolayer of HeLa cells (fig. S3) (24–28). Cryo-scanning electron microscopy (cryo-SEM) images of frozen hydrated HeLa cells demonstrated that the cell size and morphology remain unperturbed after sample preparation (fig. S5, A to C). For multilayer in situ chemical

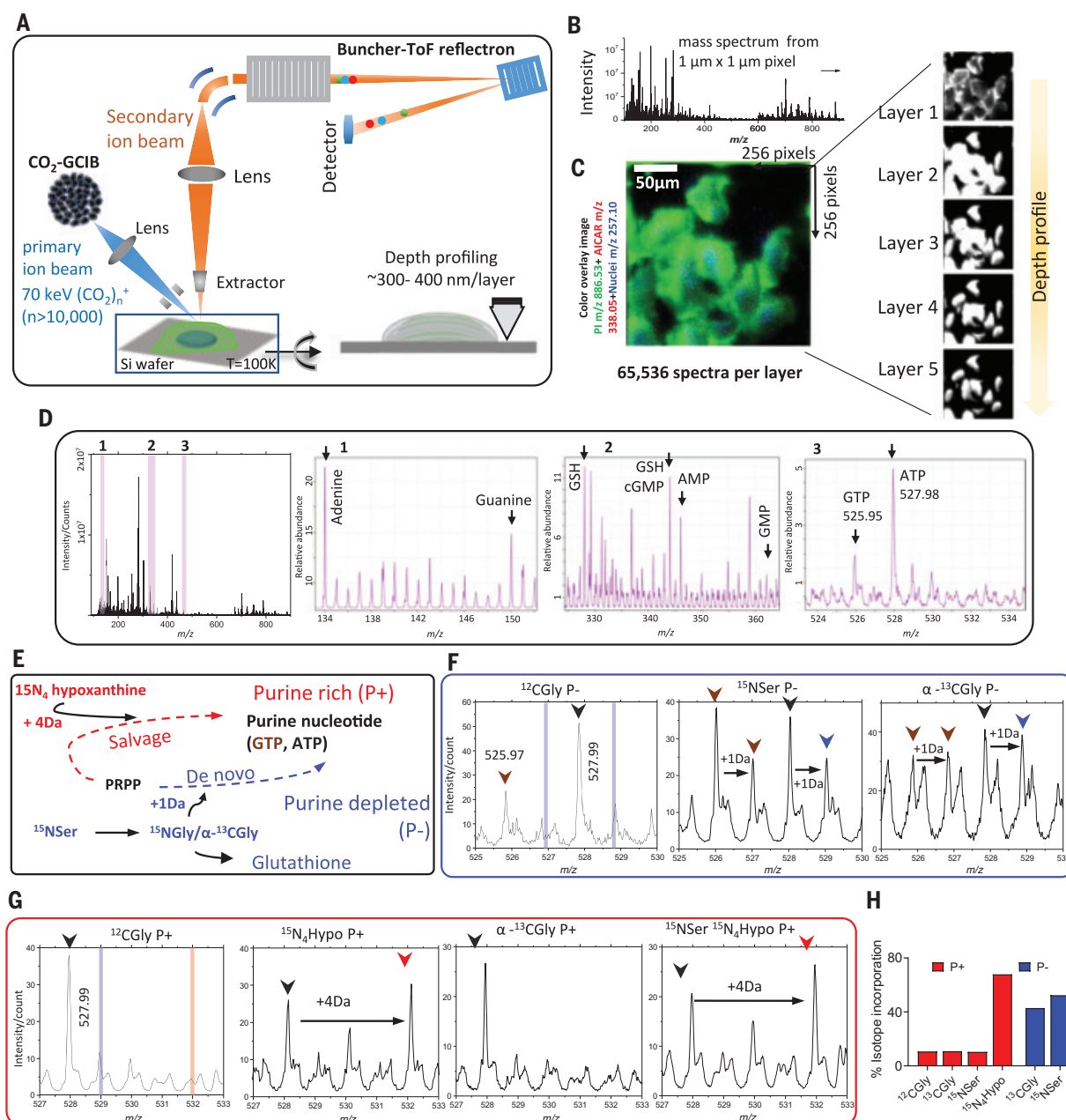


Fig. 3. Identification of unique molecular ions of purine nucleotides in the intracellular pool by in situ GCIB-SIMS. (A) Schematic of GCIB-SIMS imaging of HeLa cells. Imaging uses a finely focused 70-keV $(\text{CO}_2)_n^+$ ($n > 10,000$) cluster beam to interrogate frozen hydrated HeLa cells three-dimensionally at $1\text{-}\mu\text{m}$ spatial resolution. Coupled with a buncher-ToF and direct-current beam setup, maximum spatial resolution and mass resolution can be retained. A pixel-by-pixel analysis was performed across a lateral field of view of $256\text{ }\mu\text{m} \times 256\text{ }\mu\text{m}$. (B) Mass spectra in the m/z range 0 to 900 were recorded for each pixel. (C) A composite two-dimensional colored image was generated combining the signal across all the layers PI (38.4; green) at m/z 886.53, phosphate-sugar backbone at m/z 257.10 (blue) from nucleotides, and ^{15}N -enriched DNP intermediate AICAR (red). Combination of mass spectral analysis and the spatial distribution of specific cellular signals demonstrates the reliability of the method for in situ biochemical studies. (D) Complete negative ion spectra from frozen hydrated HeLa cells with the unique peak assignments for the metabolites relevant to the study. The ordinate axis represents absolute intensity for each ion. Zoom-in view of the m/z ranges marked as 1, 2, and 3

highlighted in pink bar are presented to show the peaks corresponding to (1) adenine and guanine base, (2) reduced glutathione (GSH), AMP, and (3) salt adducts of ATP and GTP (spectra of all the standard compounds can be found in fig. S3). The intensities are relative to the highest abundant molecular ion. (E) Stable isotope enrichment under purine-rich (P+) and purine-depleted (P-) conditions via salvage (red) or de novo (blue) pathways, respectively. Isotope tracer experiments were leveraged to specifically label the purine base ring using either $^{15}\text{N}_4$ hypoxanthine, imparting +4 Da mass increment, or ^{15}N Ser (metabolized to ^{15}N Gly) or ^{13}C Gly, imparting +1 Da mass increment. (F and G) Select SIMS ion spectra from P- (F) and P+ (G) HeLa cells for unlabeled (black arrowhead), $^{15}\text{N}_4$ -labeled (red arrowhead), or ^{13}C , ^{15}N ATP (blue arrowhead) and GTP (brown arrowhead) are shown along with the expected peak positions corresponding to +4 Da (vertical red bar) or +1 Da (vertical blue bar) mass increment, respectively. The intensities are relative to the highest abundant molecular ion. (H) The isotope enrichment profile was similar to that obtained from the high-resolution LC/MS spectrum of metabolite extracts of similarly grown cells.

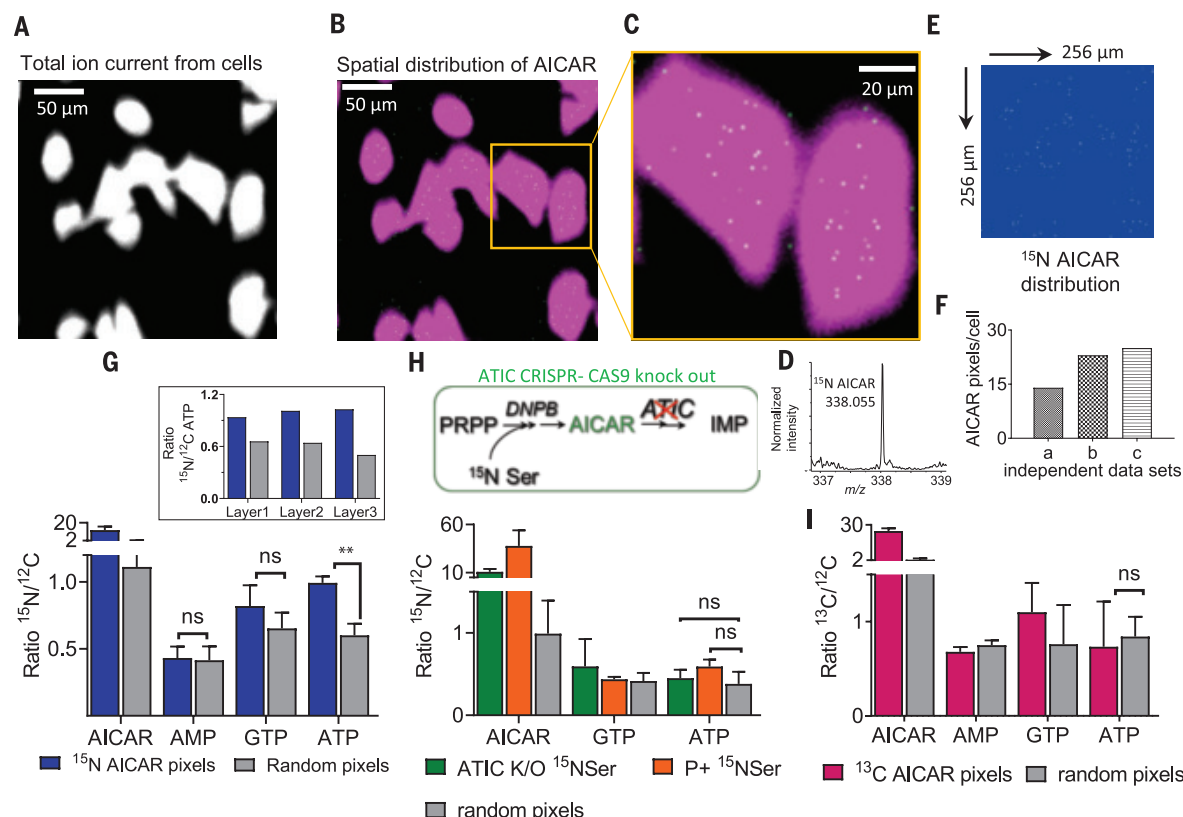


Fig. 4. Combining GCIB-SIMS and isotope label incorporation to identify the loci of channeled DNPB in single cells. (A) Representative GCIB-SIMS image of P- HeLa cells grown on a Si substrate, with a field of view of $256 \mu\text{m} \times 256 \mu\text{m}$, after allowing ^{15}N Ser enrichment for 14 hours. Image was generated using cumulative total ion current in negative ion mode. (B) Spatial distribution of ^{15}N AICAR pixels in each analyzed layer was generated using $\Delta m/z = 0.01$, centered at m/z 338.055. (C) Zoomed-in view of the area of interest [yellow box in (B)] shows an overlay of the pixels with high ^{15}N AICAR abundance (white) and cell image generated using total ion current (magenta). (D) Zoomed-in region of mass spectrum showing ^{15}N AICAR peak from the selected pixels within the cell boundary with AICAR signal/noise ratio above 30%. (E) Spatial distribution of the labeled AICAR pixels after applying the signal cutoff. (F) Total number of ^{15}N AICAR pixels per cell obtained from three independent biological replicates. (G) Comparison of level of ^{15}N enrichment in the DNPB intermediate AICAR and the end-product nucleotides AMP, GTP, and ATP for the ^{15}N AICAR pixels and equivalent numbers of random pixels selected from across

the cell. Error bar corresponds to the variation observed for each layer analyzed for a sample. The ratio of total signal intensity for the unique peak corresponding to the isotope-enriched (^{15}N -labeled) and the respective unlabeled (^{12}C) molecule of interest was determined for each layer using $\Delta m/z = 0.02$, centered at the expected exact mass corresponding to the molecular ions of interest. $**P < 0.005$. Inset: In each layer analyzed, the ratio of ^{15}N ATP/ ^{12}C ATP in the ^{15}N AICAR pixels was consistently found to be higher than that in the random pixels selected from the whole cell. (H) In the HeLa cells with ATIC CRISPR-Cas9 knock out (ATIC K/O; deficient in ATIC, one of the de novo pathway enzymes) and in cells grown in purine-rich media, selective ^{15}N enrichment in ATP in the pixels corresponding to ^{15}N AICAR was not observed upon ^{15}N Ser supplementation. (I) P- HeLa cells under high Gly concentration were used as a negative control where limited 10-formyl-THF results in diminished purinosome-mediated synthesis and thus leads to low ATP enrichment. ^{13}C AICAR pixels in the negative control showed no selective labeled ATP enrichment. MSI and statistical analysis were performed on at least three independent biological replicates.

profiling, we used high-voltage GCIB-SIMS with a $(\text{CO}_2)_n^+$ ($n > 10,000$) cluster size and a focus spot $1 \mu\text{m}$ in diameter, generating an array of mass spectra [mass/charge ratio (m/z) 90 to 900] corresponding to each $1 \mu\text{m} \times 1 \mu\text{m} \times \sim 300$ to 400 nm voxel and covering a total lateral field of view of $\sim 256 \mu\text{m} \times 256 \mu\text{m}$ in each layer (Fig. 3, A to D).

The validity of the GCIB-SIMS images was confirmed by monitoring the deprotonated molecular ion $[\text{M-H}]^-$ of phosphoinositol lipid [PI 38:4, m/z 885.53, known to localize in the cell membrane (29)] (fig. S5G). Next, we confirmed that the cellular metabolites were localized within the cellular boundary and that the

lateral and depth distribution of metabolites was also preserved (fig. S5D). The analysis confirmed that the spectrum obtained from each pixel of a lateral layer remained unaffected by the analysis performed on the adjacent pixels. Subsequently, a depth profile through the cell during a continuous layered scan showed that deeper layers remained undisturbed while the upper layers were being analyzed (Fig. 3C).

A GCIB-SIMS scan of cells produces a set of complex mass spectra because the ionizable metabolites yield several ionic species, including the pseudo-molecular ion, salt adducts, and fragment ions; hence, interpretation can

be challenging (20, 28) (Fig. 3D and fig. S3). Before further analysis of the purine biosynthetic pathway, unique peaks were identified that primarily constituted the metabolites of interest, with minimum interference from other compounds. The ionization of pure standard compounds, including all purine nucleotides and the intermediates SAICAR and AICAR, were studied to optimize SIMS measurement that would yield intact deprotonated ions as a characteristic ion (fig. S3). Isotope tracer experiments were leveraged to validate the peak assignments by following the incorporation of isotope-labeled hypoxanthine, Ser, and Gly in the cells grown under P+ or P-

conditions, respectively (Fig. 3, E to H). Before MSI, cells were supplemented with stable isotope-labeled [^{15}N]Ser/[^{13}C]Gly (+1 Da isotopomer generation via the DNPB pathway) (Fig. 3F) or [$^{15}\text{N}_4$]hypoxanthine (+3.988 Da isotopomer generation via purine salvage pathway) (Fig. 3G and fig. S5, H to L). Isotope label incorporation continued for 12 to 14 hours to ensure sufficient enrichment allowing detection of all isotopomers by GCIB-SIMS. The isotope incorporation percentage measured by SIMS was in agreement with that obtained in bulk analysis by high-resolution LC/MS of cell extracts after 12 hours of incorporation (Fig. 3H).

In situ GCIB-SIMS imaging captures the metabolon in action

As estimated from fluorescence imaging, purinosomes are roughly spheroid multiprotein assemblies with a diameter range of 0.2 to 0.9 μm (2), thus making 3D molecular scanning GCIB with a focal diameter of 1 μm particularly suitable to capture active functional purinosomes. The metabolic channeling observed for the DNPB pathway, if arising as a result of active DNPB by purinosomes, would lead to higher local concentration of the pathway intermediates and end nucleotides close to the enzyme complexes acting as biosynthetic hotspots. We exploited this feature to identify and characterize purinosomes. HeLa cells were grown in purine-depleted media and supplemented with [^{15}N]Ser (see supplementary materials for experimental details) for isotope enrichment for 12 to 14 hours before performing MSI. Because of the mitochondria compartment-specific conversion of Ser to Gly, we expected the mitochondria-associated DNPB metabolon to show spatially confined higher concentrations of isotopically labeled intermediates and end-product nucleotides. Bulk metabolomic estimations by LC/MS showed that AICAR is efficiently channeled and accumulates only under limited formyl-THF availability (figs. S5K and S6A). Therefore, the cytoplasmic loci with high concentrations of the [^{15}N]-labeled DNPB intermediate AICAR were used as the reporter of the active purinosomes in the flash-frozen HeLa cells.

The total ion spectrum image was used to define the cellular boundary in each layer (Fig. 4A). From the total ion spectrum of cells, the peak corresponding to labeled AICAR (m/z 338.05, $\Delta m/z$ 0.01) was selected to obtain its spatial distribution in each layer (Fig. 4, B to D). Each layer was analyzed independently, and pixels with less than 30% of the highest intensity per pixel and/or that appeared outside the defined cell boundary were discarded from the analysis. AICAR showed a nonhomogeneous distribution with distinct, isolated higher-concentration voxels (Fig. 4E and fig. S7, A and B), with ≥ 3 AICAR ions per voxel.

This result suggests a higher abundance of AICAR molecules per voxel by a factor of 300 to 1000 relative to the abundance expected for a homogeneous distribution throughout the cellular volume (fig. S6B). We observed an average density of 10 to 30 [^{15}N]-enriched AICAR pixels per cell (Fig. 4F), although we expect this to be an underestimation of the number of active purinosomes per cell because of technical limitations.

To analyze the chemical composition of the labeled AICAR pixels, we generated cumulative mass spectra of all such pixels in the top two or three layers from all the cells in a single field of view. Next, we analyzed the isotope enrichment of the downstream pathway metabolites AMP, ATP, and GTP. In each layer, [^{15}N]AICAR pixels showed an elevated [^{15}N]/[^{12}C] ratio for the downstream end-product nucleotide ATP relative to random cellular pixels (Fig. 4G and fig. S7, D and F). The higher [^{15}N]/[^{12}C] ratio of ATP in the labeled AICAR pixels was consistently seen in each layer analyzed and across all replicate experiments performed (Fig. 4G, inset, and fig. S7, E and G). This trend confirms that the enrichment observed in P- HeLa cells was a specific signal arising as a result of an active, channeled DNPB pathway.

We suspect that a similar correlation was not observed for the peak corresponding to the molecular ion from GTP because of the contribution of deoxy-GTP to the same peak in the cytosolic signal. Similarly, [^{15}N] label enrichment in AMP could not be observed because of low mass resolution, resulting in overlap of the AMP +1 peak with unlabeled IMP and thus interfering with the precise estimation of [^{15}N]AMP. Also, such correlation between labeled AICAR and ATP was not observed in any of the control experiments—namely, ATIC CRISPR knockout HeLa cells (lacking the enzyme to catalyze the conversion of DNPB intermediate AICAR to IMP) (30) (Fig. 4H and fig. S7H), P+ [^{15}N]Ser (cells with no observable DNPB flux) (Figs. 1C and 4H), and P- [^{13}C]Gly (with leaky and inefficient channeled DNPB) (Fig. 4I and fig. S5, H to L). Together, our results are consistent with the hypothesis that purine production is localized to biosynthetic “hotspots” congruent with the “active” purinosome metabolon within the cell. GCIB-SIMS allows selective identification and analysis of the mitochondria-associated active purinosomes and shows that the levels of the isotopically labeled metabolites AICAR and ATP are statistically above those of the purinosome's surroundings.

We have shown that the DNPB pathway is carried out by a metabolon that consists of at least nine enzymes that act synergistically to increase the pathway flux by a factor of ~ 7 and to preferentially partition a key intermediate, IMP, into AMP by a factor of 3 to 4 over GMP. On the basis of our findings, we propose a

functional definition of the purinosomes as the “active” DNPB metabolon, located proximal to the mitochondria (Fig. 2G). We envision that a better understanding of the importance of the purinosome metabolon for human health and its role in aggressive cancers with high purine demand may reveal therapeutically important metabolic vulnerabilities. Our work demonstrates the application of mass spectrometry-based techniques to investigate and quantify metabolic channeling in pathways where enzyme coclustering has been observed (31) and highlights the usefulness of high-energy GCIB-SIMS imaging to explore single-cell biochemistry.

REFERENCES AND NOTES

1. E. Villa, E. S. Ali, U. Sahu, I. Ben-Sahra, *Cancers* **11**, 688 (2019).
2. A. M. Pedley, S. J. Benkovic, *Trends Biochem. Sci.* **42**, 141–154 (2017).
3. J. M. Buchanan, S. C. Hartman, in *Advances in Enzymology and Related Areas of Molecular Biology*, Vol. 21, F. F. Nord, Ed. (Wiley, 1959), pp. 199–261.
4. S. C. Hartman, J. M. Buchanan, *Annu. Rev. Biochem.* **28**, 365–410 (1959).
5. G. R. Greenberg, L. Jaenicke, in *CIBA Foundation Symposium on the Chemistry and Biology Of Purines*, G. E. W. Wolstenholme, C. M. O'Connor, Eds. (Wiley, 1957), pp. 204–232.
6. S. An, R. Kumar, E. D. Sheets, S. J. Benkovic, *Science* **320**, 103–106 (2008).
7. H. Zhao et al., *J. Biol. Chem.* **290**, 6705–6713 (2015).
8. C. Y. Chan et al., *Proc. Natl. Acad. Sci. U.S.A.* **112**, 1368–1373 (2015).
9. J. B. French et al., *Science* **351**, 733–737 (2016).
10. C. Y. Chan et al., *Proc. Natl. Acad. Sci. U.S.A.* **115**, 13009–13014 (2018).
11. M. Kyoung, S. J. Russell, C. L. Kohnhorst, N. N. Esemoto, S. An, *Biochemistry* **54**, 870–880 (2015).
12. Y. Deng et al., *J. Biol. Chem.* **287**, 36201–36207 (2012).
13. M. Yang, K. H. Vousden, *Nat. Rev. Cancer* **16**, 650–662 (2016).
14. N. Kory et al., *Science* **362**, eaat9528 (2018).
15. G. S. Ducker, J. D. Rabinowitz, *Cell Metab.* **25**, 27–42 (2017).
16. M. D. Sintchak et al., *Cell* **85**, 921–930 (1996).
17. C. F. Labuschagne, N. J. van den Broek, G. M. Mackay, K. H. Vousden, O. D. Maddocks, *Cell Rep.* **7**, 1248–1258 (2014).
18. R. Nilsson et al., *Nat. Commun.* **5**, 3128 (2014).
19. J. C. Venter et al., *Science* **291**, 1304–1351 (2001).
20. N. Winograd, *Annu. Rev. Anal. Chem.* **11**, 29–48 (2018).
21. S. Fearn, *Mater. Sci. Technol.* **31**, 148–161 (2015).
22. S. G. Boxer, M. L. Kraft, P. K. Weber, *Annu. Rev. Biophys.* **38**, 53–74 (2009).
23. J. S. Fletcher, J. C. Vickerman, N. Winograd, *Curr. Opin. Chem. Biol.* **15**, 733–740 (2011).
24. H. Tian et al., *Angew. Chem. Int. Ed.* **58**, 3156–3161 (2019).
25. T. B. Angerer, P. Blenkinsopp, J. S. Fletcher, *Int. J. Mass Spectrom.* **377**, 591–598 (2015).
26. S. Rabbani, A. M. Barber, J. S. Fletcher, N. P. Lockyer, J. C. Vickerman, *Anal. Chem.* **83**, 3793–3800 (2011).
27. J. S. Fletcher et al., *Anal. Chem.* **80**, 9058–9064 (2008).
28. M. K. Passarelli, A. G. Ewing, *Curr. Opin. Chem. Biol.* **17**, 854–859 (2013).
29. H. Tian et al., *Anal. Chem.* **89**, 4611–4619 (2017).
30. V. Baresova et al., *Mol. Genet. Metab.* **119**, 270–277 (2016).
31. L. J. Sweetlove, A. R. Fernie, *Nat. Commun.* **9**, 2136 (2018).
32. V. Pareek et al., *Penn State ScholarSphere* (2020); <https://doi.org/10.26207/8rm3-g809>.

ACKNOWLEDGMENTS

HeLa ATIC CRISPR-CAS9 knockout cells were a gift from the Zikanova lab, Charles University and General University Hospital, Prague, Czech Republic. V.P. and S.J.B. thank A. Patterson and P. Smith (Huck Institutes of Life Sciences, Penn State) for running LC/MS. H.T. and V.P. acknowledge technical assistance from P. Blenkinsopp and E. Mengusoglu (Ionoptika, UK) for image processing and single-pixel analysis. V.P. thanks S.J.B.'s lab members A. M. Pedley and L.-N. Zou for very useful discussions and inputs. **Funding:** Supported by NIH grant GM024129 (S.J.B.), the Huck Institutes of Life Sciences (V.P.), and the Materials

Research Institute and the Institutes of Energy and the Environment at Penn State (H.T.). **Competing interests:** The authors declare no conflict of interest. **Author contributions:** V.P. and S.J.B. conceived and designed the experiments; all cell culture, isotope incorporation, and metabolomics experiments were performed and analyzed by V.P. and the results interpreted by V.P. and S.J.B.; V.P., H.T., N.W., and S.J.B. designed the MSI experiments; H.T. and V.P. performed and analyzed MSI experiments; and V.P., H.T., N.W., and S.J.B. interpreted and wrote the

manuscript. **Data and materials availability:** The extracted peak areas for the metabolites analyzed in this study can be found in the accessory files. The GCIB-SIMS imaging data are available from Penn State ScholarSphere (32).

SUPPLEMENTARY MATERIALS

science.sciencemag.org/content/368/6488/283/suppl/DC1
Materials and Methods

Tables S1 to S3
Figs. S1 to S7
Data S1 to S4
References (33–41)

26 September 2019; accepted 25 February 2020
10.1126/science.aaz6465

GENE EDITING

Unconstrained genome targeting with near-PAMless engineered CRISPR-Cas9 variants

Russell T. Walton^{1,2,*†}, Kathleen A. Christie^{1,2,3}, Madelynn N. Whittaker^{1,2}, Benjamin P. Kleinstiver^{1,2,3‡}

Manipulation of DNA by CRISPR-Cas enzymes requires the recognition of a protospacer-adjacent motif (PAM), limiting target site recognition to a subset of sequences. To remove this constraint, we engineered variants of *Streptococcus pyogenes* Cas9 (SpCas9) to eliminate the NGG PAM requirement. We developed a variant named SpG that is capable of targeting an expanded set of NGN PAMs, and we further optimized this enzyme to develop a near-PAMless SpCas9 variant named SpRY (NRN and to a lesser extent NYN PAMs). SpRY nuclease and base-editor variants can target almost all PAMs, exhibiting robust activities on a wide range of sites with NRN PAMs in human cells and lower but substantial activity on those with NYN PAMs. Using SpG and SpRY, we generated previously inaccessible disease-relevant genetic variants, supporting the utility of high-resolution targeting across genome editing applications.

The requirement for DNA-targeting CRISPR-Cas enzymes to recognize a short sequence motif adjacent to target sites in foreign DNA is a critical step for CRISPR systems to distinguish self from nonself (1, 2). For genome editing applications, however, the necessity of protospacer-adjacent motif (3–6) (PAM) recognition by Cas9 and Cas12a proteins constrains targeting and affects editing efficiency and flexibility. The prototypical Cas9 from *Streptococcus pyogenes* (SpCas9) naturally recognizes target sites with NGG PAMs (where N is A, C, G, or T) (5, 7, 8), making it one of the most targetable CRISPR enzymes characterized to date. Although other naturally occurring Cas orthologs can, in principle, expand targeting by recognizing divergent noncanonical PAMs, most Cas9 and Cas12a enzymes (9–12) require extended motifs that limit their utility for genome editing. Thus, the PAM requirement prevents the accurate positioning of CRISPR target sites and is a major barrier for genome editing applications that command high-resolution target site positioning [e.g., tar-

geting small genetic elements, base editing, generating efficient homology-directed repair-mediated alterations, performing tiling screens, etc. (13–19)].

One method to improve the targeting range of genome editing technologies is to purposefully engineer CRISPR enzymes that can target previously inaccessible PAMs. SpCas9 primarily recognizes its optimal NGG PAM by direct molecular readout of the guanine DNA bases via the amino acid side chains of R1333 and R1335 (20) (Fig. 1, A and B, and fig. S1A). Modification of either arginine alone ablates SpCas9 nuclease activity against sites with NGG, NAG, or NGA PAMs (8, 20), necessitating the use of molecular evolution to alter PAM preference by mutation of other amino acids in the PAM-interacting (PI) domain. Several protein engineering strategies have been pursued toward expanding targeting with SpCas9, including using directed evolution or structure-guided engineering to develop variants with altered PAM profiles (e.g., SpCas9-VQR, VRQR, and VRER) (8, 21) or relaxed PAM preferences (e.g., SpCas9-NG and xCas9) (22, 23). Although these variants expand the potential targeting space of SpCas9, target sites encoding most noncanonical PAMs still remain inaccessible for genome editing.

In this study, we used structure-guided engineering to nearly completely relax the PAM requirement of SpCas9. This approach enabled the generation of a highly enzymatically active NGN PAM variant (named SpG), and subsequent optimization of SpG led to a variant (named

SpRY) capable of editing nearly all PAMs. We demonstrate that SpG and SpRY improve editing resolution and offer previously unrealized genome editing capabilities. More broadly, the molecular strategy described herein should in principle be extensible to a wide diversity of Cas orthologs, paving a path toward the development of a suite of editing technologies no longer constrained by their inherent targeting limitations.

Structure-guided mutagenesis to relax SpCas9 PAM preference

In our attempt to eliminate the PAM requirement of SpCas9, we first developed a variant capable of recognizing a reduced NGN PAM relative to the canonical NGG sequence. Our previous efforts to alter SpCas9 PAM preference illuminated several PAM-proximal residues important for PAM recognition (8) (Fig. 1B), observations that are supported by structural studies (20, 24, 25) [fig. S1, A to E, and (26)]. Characterizations of SpCas9-VQR [harboring D1135V/R1335Q/T1337R substitutions (where D1135V indicates an Asp¹¹³⁵→Val substitution, etc.)] and the derivative SpCas9-VRQR variant (that additionally encodes G1218R) suggest that these enzymes target an expanded number of noncanonical PAMs, including those with variable bases in the third position of the PAM (NGAN>NGNG, where > symbol indicates relative activity) (8, 21). We therefore hypothesized that R1335Q-harboring variants with other PI domain substitutions could recognize an expanded number of PAMs (fig. S1, F to I). Thus, we used SpCas9-VRQR as a molecular scaffold to further relax SpCas9 PAM preference.

To more thoroughly investigate the impacts of amino acid substitutions in PI domain residues, we developed a high-throughput PAM determination assay (HT-PAMDA) to comprehensively profile the PAM preferences of a large number of SpCas9 variants [fig. S2, A to D, and (26)]. HT-PAMDA accurately replicated the PAM profiles of wild-type (WT) SpCas9 and other previously described variants (Fig. 1C and fig. S2D). To engineer an SpCas9 variant capable of more-relaxed targeting, we used HT-PAMDA to sequentially determine the contributions of substitutions at five PI-critical positions, D1135, S1136, G1218, E1219, and T1337, in the context of SpCas9-VRQR [fig. S2E and (26)]. We identified several variants bearing

¹Center for Genomic Medicine, Massachusetts General Hospital, Boston, MA 02114, USA. ²Department of Pathology, Massachusetts General Hospital, Boston, MA 02114, USA.

³Department of Pathology, Harvard Medical School, Boston, MA 02115, USA.

*Present address: Department of Biological Engineering, Massachusetts Institute of Technology, Cambridge,

MA 02142, USA. †Present address: Broad Institute of MIT and Harvard, Cambridge, MA 02142, USA.

‡Corresponding author. Email: bkinstiver@mgh.harvard.edu

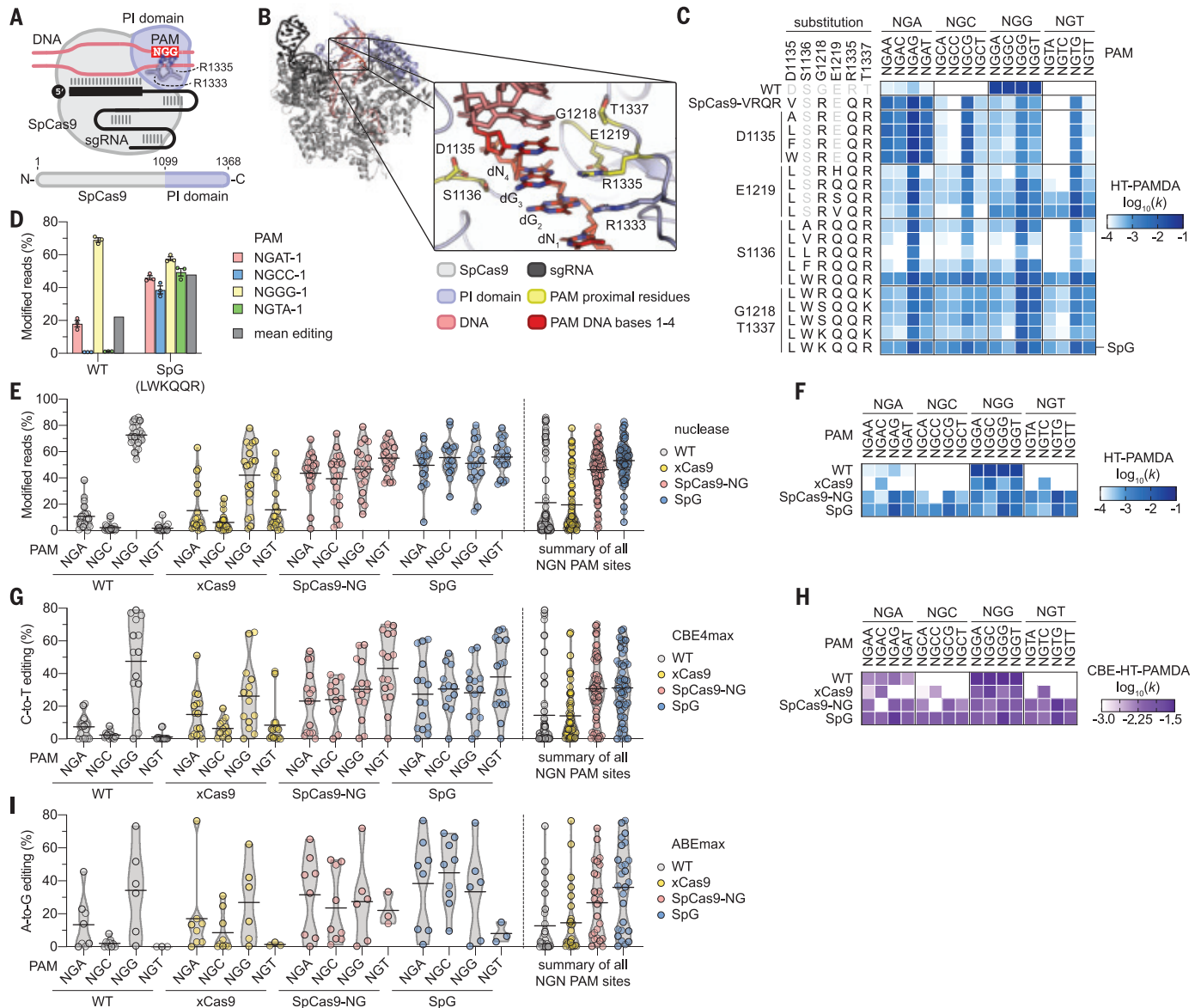


Fig. 1. Engineering and characterization of SpCas9 variants capable of targeting NGN PAMs. (A) Schematic of SpCas9, highlighting the PI domain along with R1333 and R1335 that make base-specific contacts to the guanines of the NGG PAM. Single-letter abbreviations for the amino acid residues are as follows: A, Ala; C, Cys; D, Asp; E, Glu; F, Phe; G, Gly; H, His; I, Ile; K, Lys; L, Leu; M, Met; N, Asn; P, Pro; Q, Gln; R, Arg; S, Ser; T, Thr; V, Val; W, Trp; and Y, Tyr. sgRNA, single-guide RNA; N, N terminus; C, C terminus. (B) Rendering of a crystal structure of SpCas9 with amino acid side chains proximal to the second guanine of the NGG PAM shown in yellow. In the zoomed image, the nontarget strand (NTS) is hidden for clarity. Image was generated from Protein Data Bank (PDB) ID 4UN3 (20). (C) HT-PAMDA characterization of WT SpCas9 and engineered variants to illustrate their NGNN PAM preferences. The \log_{10} rate constants (k) are the mean of at least two replicates against two distinct spacer sequences (see also fig. S2, A to C and E). (D) Modification of endogenous sites in human cells bearing canonical and noncanonical PAMs with WT SpCas9 and SpG. Editing assessed by targeted sequencing; mean, SEM, and individual data points shown for $n = 3$ biological replicates. (E) Mean nuclease activity plots for WT,

xCas9 (23), SpCas9-NG (22), and SpG on 78 sites with NGN PAMs in human cells. The horizontal black lines represent the mean of 19 to 20 sites for each PAM class (see also fig. S5A), and the gray outlines are violin plots. (F) HT-PAMDA characterization of WT, xCas9, SpCas9-NG, and SpG to illustrate their NGNN PAM preferences. The \log_{10} rate constants are the mean of at least two replicates against two distinct spacer sequences. (G) Mean C-to-T editing plots for WT, xCas9, SpCas9-NG, and SpG CBEs on 57 cytosines within the editing windows (positions three through nine) of 20 target sites harboring NGN PAMs in human cells. The horizontal black lines represent the mean of 12 to 16 cytosines for each PAM class (see also fig. S6A), and the gray outlines are violin plots. (H) CBE-HT-PAMDA data for WT, xCas9, SpCas9-NG, and SpG to illustrate their NGNN PAM preferences. The \log_{10} rate constants are single replicates against one spacer sequence (see also fig. S6, C and D). (I) Mean A-to-G editing plots for WT, xCas9, SpCas9-NG, and SpG ABEs on 24 adenines within the editing windows (positions five through seven) of 21 target sites harboring NGN PAMs in human cells. The horizontal black lines represent the mean of three to nine adenines for each PAM class (see also fig. S7A), and the gray outlines are violin plots.

combinations of rational substitutions at these five important residues that exhibited more-balanced tolerances for any nucleotide at the third and fourth PAM positions (Fig. 1C and fig. S2E). One variant bearing D1135L/S1136W/G1218K/E1219Q/R1335Q/T1337R substitutions, henceforth referred to as SpG, exhibited the most-even targeting of NGA, NGC, NGG, and NGT PAMs (Fig. 1C and fig. S2E).

We then compared the activities of WT SpCas9 with those of SpG and nearly all intermediate variants in human embryonic kidney (HEK) 293T cells to corroborate our HT-PAMDA findings. Using an optimal nuclear localization signal (27) (fig. S3) and nonsaturating nuclease expression conditions in HEK 293T cells, we examined the human cell editing activities of this large collection of variants on four sites with NGA, NGC, NGG, and NGT PAMs [fig. S4, A and B, and (26)]. These experiments revealed high-activity editing on the four NGN PAM sites with SpG (Fig. 1D and fig. S4B), results that were consistent with the PAM preference of SpG characterized using HT-PAMDA (Fig. 1C and fig. S2F). We then sought to bolster the activity of SpG through the addition of non-specific contacts mediated by L1111R and A1322R substitutions, mutations that are necessary for the NGN PAM tolerance of SpCas9-NG (22) (fig. S4, C and D). However, the L1111R and A1322R substitutions were detrimental to the human

cell editing activities of SpG, albeit without alteration of PAM preference [figs. S4, E and F, and S2, F and G, and see (26)].

SpG activities as a nuclease, CBE, and ABE

Given the broad compatibility of SpG with NGN PAMs as determined by HT-PAMDA but our limited testing on only 16 target sites in HEK 293T cells, we more thoroughly compared its nuclease activity in human cells against WT SpCas9, xCas9(3.7), and SpCas9-NG. We assessed the editing activities of SpG and these three nucleases on 78 sites bearing NGNN PAM sequences that encompassed an approximately even distribution of nucleotide identities in the third and fourth positions of the PAM (fig. S5A and table S1). Our assessment recapitulated the PAM preference of WT SpCas9 (7, 8), with a mean editing activity of 72.8% on sites with NGG PAMs and a reduced 4.7% mean editing across the remaining NGH sites (where H is A, C, or T) (Fig. 1E). SpG exhibited the highest mean editing activities across all NGN PAM sites, averaging 51.2% on sites with NGG PAMs and 53.7% on sites with NGH PAMs (Fig. 1E). Of the two variants reported to recognize sites with NGN PAMs, xCas9 displayed more-modest editing (42.2% on NGG and 12.5% across NGH), while SpCas9-NG editing activities were even across NGN PAM sites (46.9% on NGG and

46.0% across NGH) but lower compared with those of SpG (Fig. 1E).

To better understand the PAM requirements of each of the NGN PAM variants, we used HT-PAMDA to profile SpG, xCas9, and SpCas9-NG (Fig. 1F and fig. S2F). These experiments demonstrated that SpG exhibited the most even and robust targeting of all the NGN PAMs (targeting efficacy ranked as follows: SpG > SpCas9-NG > xCas9) (Fig. 1F), consistent with the results of our 78-site human cell experiment (Fig. 1E). Closer inspection of our HT-PAMDA and human cell data did not reveal substantial first PAM, fourth PAM, or first spacer position preferences for WT SpCas9, SpG, or SpCas9-NG [fig. S5, B to D, and (26)]. This analysis also attributed the decreased activities observed with xCas9 to a preference for a C in the fourth position of the PAM, which likely makes targeting of sites with NGND PAMs (where D is A, G, or T) less efficient [fig. S5E; for a more complete analysis of xCas9 PAM preference, see (26)]. For the four nucleases, HT-PAMDA values for each NGNN PAM class correlated with mean editing activities in HEK 293T cells (fig. S5F). Together, these results indicate that SpG is an efficient and broadly targeting nuclease across sites bearing NGN PAMs.

Given the ubiquitous use of base editor (BE) technologies to mediate single nucleotide substitutions in various organisms (17, 18, 28), we

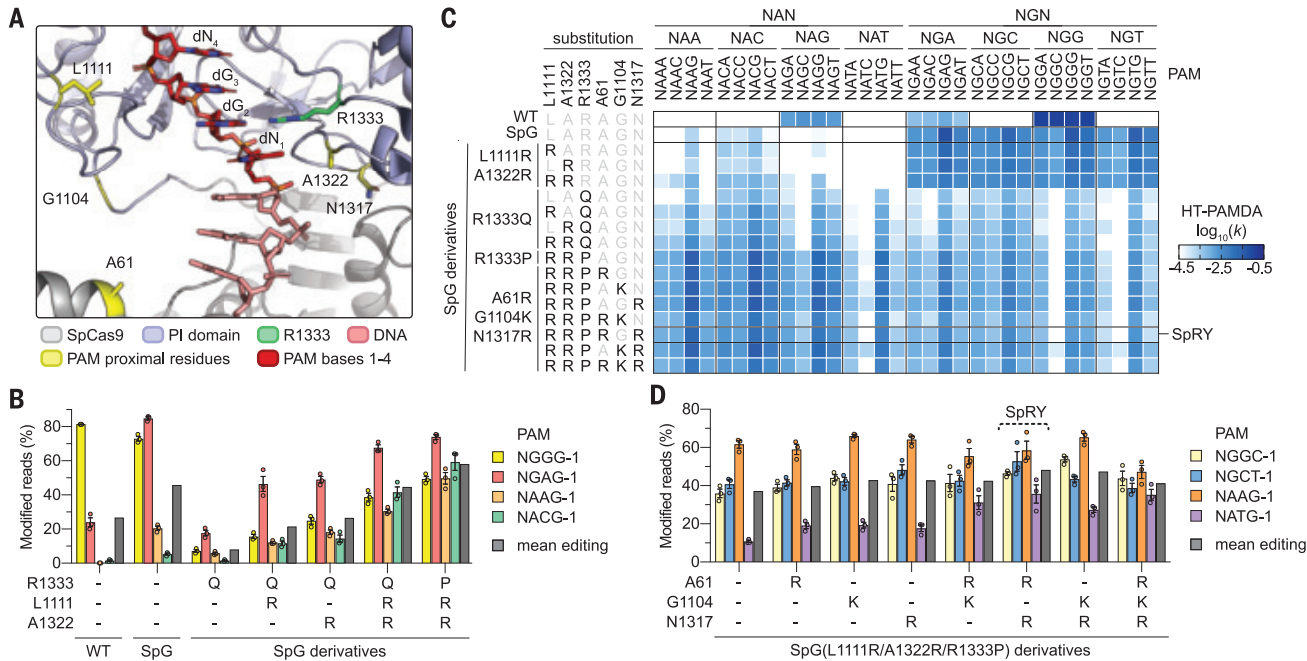


Fig. 2. Engineering and characterization of SpCas9 variants capable of targeting NRN PAMs. (A) Crystal structure of SpCas9 to illustrate amino acid side chains of R1333 and selected PAM-proximal residues. The NTS is hidden for clarity. Image generated from PDB ID 4UN3 (20). (B) Modification of endogenous sites in human cells bearing different NRN PAMs with WT SpCas9, SpG, and SpG derivatives. Editing assessed by targeted sequencing; mean, SEM, and individual data points shown for $n = 3$. (C) HT-PAMDA characterizations of WT

SpCas9, SpG, and SpG derivatives to illustrate their NRNN PAM preferences. The \log_{10} rate constants are the mean of at least two replicates against two distinct spacer sequences (see also fig. S2, A to C). (D) Modification of endogenous sites in human cells bearing different NRN PAMs by SpG(L1111R/A1322R/R1333P) and derivatives bearing additional substitutions. See fig. S8C for all variants tested. Editing assessed by targeted sequencing; mean, SEM, and individual data points shown for $n = 3$.

investigated whether the improved activities of SpG could enhance BE activities across sites with NGN PAMs. We compared C-to-T editing with WT SpCas9, xCas9, SpCas9-NG, and SpG BE4max cytosine base editor (29) (CBE) constructs across 22 endogenous sites in human cells bearing NGNN PAMs (fig. S6A). We observed that, whereas WT- and xCas9-CBE exhibited mean C-to-T editing efficiencies >15% only on sites with NGG PAMs, both SpG- and SpCas9-NG-CBE were capable of mean C-to-T editing >23% across NGN sites (Fig. 1G) and displayed typical CBE substrate preferences (fig. S6B). To ensure that the CBE versions of the PAM variants harbored the same PAM profiles as the nucleases, we developed a modified CBE high-throughput PAM determination assay (CBE-HT-PAMDA) [fig. S6C and (26)]. The PAM compatibilities of the CBEs were largely consistent with the preferences of the nucleases (compare Fig. 1, H and F, respectively, and see fig. S6, D and E).

Beyond C-to-T editing, adenine base editor (ABE) constructs have also been developed that mediate A-to-G edits (18). Thus, we also compared the A-to-G editing potencies of WT SpCas9, xCas9, SpCas9-NG, and SpG in the ABEmax architecture (29) across 21 endogenous sites harboring NGNN PAMs (fig. S7A). Similar to our observations for CBEs, WT- and xCas9-ABE could only efficiently perform A-to-G edits on target sites with NGG PAMs (Fig. 1I). However, both SpG- and SpCas9-NG-ABE efficiently edited target sites with NGNN PAMs, with SpG-ABE exhibiting the most-robust activity across all NGNN sites (Fig. 1I) with typical ABE substrate preferences (fig. S7B).

Collectively, these results demonstrate that SpCas9 PAM preference can be relaxed to a single NGN nucleotide motif by designing a more tolerant PI domain. The SpG variant developed through this strategy exhibits robust nuclease, CBE, and ABE activities across NGN PAMs.

Engineering SpCas9 variants capable of targeting NRN PAMs

Notwithstanding the efficient modification of sites with NGN PAMs using SpG, many genomic regions remain inaccessible to genome editing. Because we observed efficient modification of sites bearing NGN PAMs with SpG, we speculated that SpG could be used as a molecular scaffold upon which to further relax PAM specificity. To alter recognition of the second position of the PAM, we hypothesized that substitution of R1333 to glutamine might enable access to sites harboring NAN PAMs by forming a base-specific contact with the adenine base in the second position of the PAM (8, 20, 24) (Fig. 2A). However, our initial tests of SpG(R1333Q) nearly abolished activity in human cells against four sites bearing NRN PAMs (where R is A or G) (Fig. 2B), revealing

that the R1333Q alone was insufficient to enable highly active targeting of NAN PAMs [consistent with observations for WT SpCas9 (8, 20)]. Notably, contrary to our previous finding that L1111R and A1322R substitutions negatively affected SpG activity (fig. S4, E and F), we observed that these nonspecific DNA contacts were able to rescue some activity of SpG(R1333Q) across the four sites bearing NRN PAMs in human cells (Fig. 2B). Concurrent HT-PAMDA experiments to analyze the same variants corroborated a general relaxation of PAM specificity against NRN PAMs but with a lower overall activity (Fig. 2C).

Next, to determine whether the R1333Q substitution was the most permissive for recognition of an expanded number of PAMs, we used HT-PAMDA to investigate whether variants harboring other amino acid substitutions at residue 1333 might be more amenable to highly active and broad targeting of NRN PAMs. Systematic evaluation of SpG(L1111R/A1322R) variants harboring all 20 possible amino acids at residue 1333 revealed that the range of substitutions at this position cause different second PAM position preferences and overall levels of activity (fig. S8A). Unexpectedly, variants bearing R1333 substitutions to alanine, cysteine, or proline conferred the most-efficient collective targeting of NRN PAMs. Experiments in HEK 293T cells against the same four sites harboring NRN PAMs demonstrated that one SpG(L1111R/A1322R) variant that also harbored the R1333P substitution exhibited greater activity on NRN PAMs compared with the precursor R1333Q-containing variants (Fig. 2B). HT-PAMDA experiments confirmed these observations (Fig. 2C).

Given that the addition of L1111R and A1322R to SpG-R1333Q improved on-target activity, we sought to determine whether additional analogous substitutions could further enhance editing of sites with NRN PAMs. We used crystal structures of SpCas9 (20, 24, 25) to identify other positions in the PI domain where amino acid substitutions to positively charged residues might be expected to increase activity by forming novel nonspecific DNA contacts (Fig. 2A). We used HT-PAMDA to determine the single or combinatorial effects of three such substitutions—A61R, G1104K, and N1317R—in the context of SpG(L1111R/A1322R) variants also bearing R1333A, R1333C, or R1333P substitutions (Fig. 2C and fig. S8B). This analysis revealed that different combinations of the three nonspecific substitutions were well tolerated by nearly all variants and that the NRN PAM preferences of variants harboring R1333A, R1333C, or R1333P substitutions were similar, as demonstrated by HT-PAMDA.

To determine which variant exhibited the highest activities in human cells, we tested this large series of variants against four additional sites bearing NRN PAMs (fig. S8C).

We observed that the SpG(L1111R/A1322R) variant harboring the R1333P substitution and a combination of A61R/N1317R offered the greatest mean editing against NRN PAMs (Fig. 2D). Use of HT-PAMDA to examine the sequential effects of the substitutions encoded by this variant demonstrated a stepwise progression from NGN to NRN PAM preference and also revealed the unexpected finding that this variant may target some NYN PAMs (where Y is C or T) (fig. S8D). Together, our human cell and HT-PAMDA data suggest that the SpG(L1111R/A1322R) derivative containing A61R, N1317R, and R1333P substitutions (henceforth referred to as SpRY, for SpCas9 variant capable of targeting NRN>NYN PAMs) enables targeting of sites with NRN PAMs.

SpRY activities as a nuclease, CBE, and ABE in human cells

Having established the potential of SpRY to widely expand sequence targeting, we more thoroughly assessed its nuclease activities in HEK 293T cells. We compared the on-target editing of WT SpCas9 and SpRY across 64 sites, 32 harboring NANN PAMs and 32 harboring NGNN PAMs (fig. S9, A and B, respectively). We observed that, consistent with prior reports (7, 8), WT SpCas9 preferred NGG>NAG>NGA PAMs with negligible targeting of the remaining NRN PAMs (Fig. 3A). In comparison, SpRY was more effective than WT at targeting sites encoding NRN PAMs, except for those harboring canonical NGG PAMs (Fig. 3A). Across the 32 sites with NGN PAMs, SpRY often exhibited comparable activities to SpG, although SpG remained the most effective NGN PAM variant (figs. S9, B and C). Overall, SpRY was capable of efficiently editing most sites with NRN PAMs, where the range of activities could not necessarily be explained by PAM preference alone. These results demonstrate the ability to effectively target a range of sites with NAN PAMs using a Cas9 variant.

Combined with the observation of modest levels of NYN targeting with SpRY in HT-PAMDA (fig. S8D), structural analysis of the R1333P substitution in SpRY led us to speculate that R1333P-containing variants might also enable targeting of any base in the second PAM position (including thus far unexamined NYN PAMs) (fig. S9D). We examined the activities of WT SpCas9 and SpRY across 31 sites with NYN PAMs (15 NCNN and 16 NTNN sites) (fig. S9E). SpRY was able to edit 13 of 31 sites (42%) with NYN PAMs to levels of modification above 20%, compared with zero sites with WT SpCas9 (Fig. 3B). Although the mean editing activities on sites with NYN PAMs were about half of what we observed on sites with NRN PAMs, the activities were greater than the essentially negligible editing with WT SpCas9 (Fig. 3B). The PAM preference of SpRY as determined by HT-PAMDA was generally consistent with the mean

nuclease editing levels for each PAM class [fig. S9F and (26)], although additional experiments are needed to more thoroughly characterize the substrate requirements of SpRY (fig. S9, G to J). Collectively, these results demonstrate the ability to target sites with NRN PAMs and some NYN PAMs using an SpCas9 variant.

Because SpRY enables nuclease targeting of many sites with NNN PAMs in human cells, we examined its compatibility with base editors, which are dependent upon the availability of PAMs to appropriately position the CBE or ABE edit windows (28). Assessment of SpRY-CBE across 14 sites bearing NRN PAMs re-

vealed mean C-to-T editing of 38.0% across all substrate cytosines (fig. S10A), with SpRY-CBE achieving >20% modification of at least one cytosine per site for all but one site (Fig. 3C). Comparatively, WT-CBE most efficiently modified sites bearing NGG PAMs and was also capable of modifying sites bearing NAG

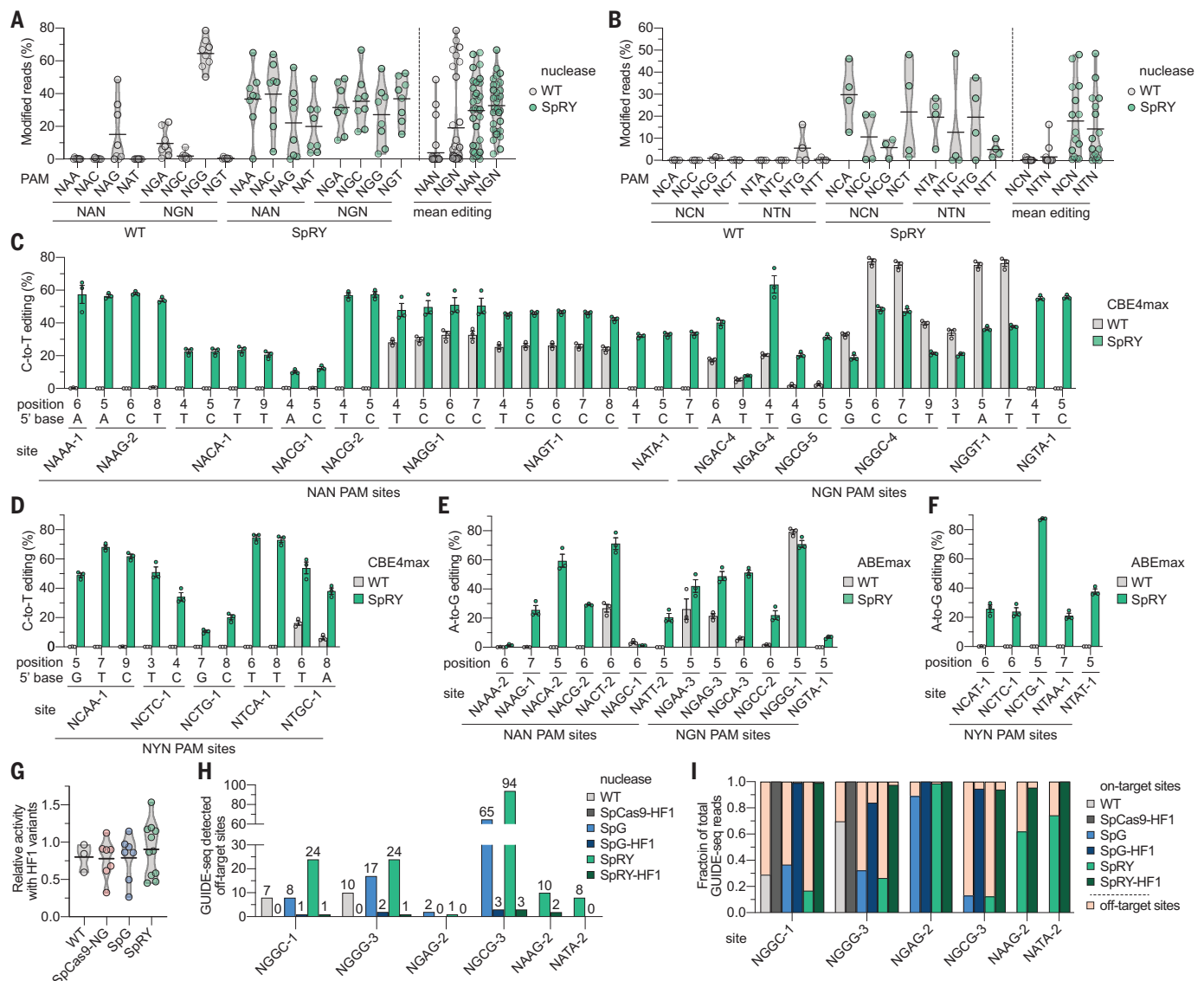


Fig. 3. Comparison of WT SpCas9 and SpRY nuclease and base editor activities across NNN PAM sites in human cells. (A and B) Mean nuclease activity plots for WT SpCas9 and SpRY on 64 sites with NRN PAMs (A) and 31 sites with NYN PAMs (B) in human cells. The horizontal black lines represent the mean of eight or three to four sites [(A) and (B), respectively] for each PAM of the indicated class (see also fig. S9, A to C), and the gray outlines are violin plots. (C and D) C-to-T base editing of endogenous sites in human cells bearing NRN and NYN PAMs [(C) and (D), respectively] with WT SpCas9 and SpRY-CBE4max constructs. Editing of cytosines in the edit window (positions three through nine) assessed by targeted sequencing; the five NYN PAM target sites were selected from high-activity sites in (B); mean, SEM, and individual data points shown for $n = 3$. (E and F) A-to-G base editing of endogenous sites in human cells bearing NRN and NYN PAMs [(E) and (F), respectively] with WT SpCas9 and SpRY-ABEmax constructs. Editing of adenines

in the edit window assessed by targeted sequencing; the five NYN PAM target sites were selected from high-activity sites in (B); mean, SEM, and individual data points shown for $n = 3$. For base editing data in (C) to (F), see also table S5. (G) Relative nuclease activity plots for SpCas9-HF1, SpCas9-NG-HF1, SpG-HF1, and SpRY-HF1 compared with their parental variants across 3 to 10 endogenous sites in HEK 293T cells. Mean modification from sites in fig. S11A shown as dots; horizontal black lines represent the mean of those sites, and the gray outlines are violin plots. The HF1 variants additionally encode N497A, R661A, Q695A, and Q926A substitutions (21). (H) Histogram of the number of GUIDE-seq-detected off-target sites for SpCas9 variants across sites with NGG, NGN, and NAN PAMs (see fig. S12, A to C, respectively). (I) Fraction of GUIDE-seq reads attributed to the on- and off-target sites for WT SpCas9, SpG, SpRY, and their respective HF1 variants across two to six targets (see also fig. S12, A to C, and table S6).

and NGA PAMs, albeit at lower efficiency than SpRY (Fig. 3C and fig. S10A). We also assessed the activities of SpRY-CBE on five high-activity NYN PAM sites from our nuclease datasets (see fig. S9E). For these preselected high-activity sites, we observed robust levels of editing compared with negligible editing with WT-CBE (Fig. 3D and fig. S10B). Similar to our observations for SpG-CBE, SpRY-CBE exhibited typical CBE substrate preferences (fig. S10C).

We then examined the A-to-G editing activities of SpRY-ABE across 13 sites with NRN PAMs and five high-activity sites with NYN PAMs (NYN sites selected from fig. S9E). For the NRN PAM sites, we observed mean A-to-G editing activities of 34.7% with SpRY-ABE on substrate adenines (fig. S10D) and achieved >20% modification on at least one adenine for 10 of 13 sites (Fig. 3E). With WT-ABE, the most efficient editing was observed on the NGG PAM site, and minor editing was detected on three sites with noncanonical PAMs (Fig. 3E). Across the five preselected high-activity sites harboring NYN PAMs, A-to-G editing activities were generally more modest with SpRY, but we did observe editing of one adenine to near 90%; no editing with WT ABE_{max} was observed on any of the five sites (Fig. 3F). Overall, SpRY-

ABE exhibited greater mean A-to-G editing compared with WT-ABE across sites containing NRN and NYN PAMs with typical ABE substrate requirements (fig. S10, D to F).

An important consideration for genome editing is the ability to mitigate potential off-target effects. To reduce off-target editing observed with WT SpCas9, we and others previously engineered high-fidelity (HF) variants of SpCas9 with improved genome-wide specificities (21, 30). Because the relaxed PAM tolerances of SpG and SpRY can, in principle, lead to recognition of additional off-target sites, we first tested whether our variants were compatible with the fidelity-enhancing substitutions of SpCas9-HF1 (21). Across several target sites bearing different PAMs, we observed that WT, SpCas9-NG, SpG, SpRY, and their HF1 derivatives exhibited comparable levels of on-target modification (Fig. 3G and fig. S11A).

We then performed genome-wide, unbiased identification of double-strand breaks enabled by sequencing (GUIDE-seq) experiments (31) to analyze the genome-wide specificity profiles of these variants. In transfections containing the GUIDE-seq double-stranded oligodeoxynucleotide tag, we also observed similar levels of on-target editing between WT, SpG, SpRY,

and their HF1 derivative variants (fig. S11, B to F). Analysis of GUIDE-seq experiments revealed that SpG and SpRY exhibited a somewhat increased propensity for off-target editing compared with WT SpCas9, albeit at similar absolute levels previously reported for WT SpCas9 (21, 37) (Fig. 3H). Nearly all novel off-targets for SpG and SpRY were attributable to the expanded PAM recognition by these variants (fig. S12, A to C). Importantly, the HF1 variants were able to eliminate nearly all off-target editing events (Fig. 3H) and substantially increased the fraction of total editing events observed at the on-target sites (Fig. 3I). These results demonstrate that SpG- and SpRY-HF1 offer improved fidelity for applications that necessitate high specificity.

Expanded targeting of SpG and SpRY enables the generation of protective genetic variants

The necessity of DNA-targeting CRISPR enzymes to recognize a PAM fundamentally limits precision targeting, a constraint that is exacerbated when using base editors whose activities are restricted to short “editing windows” (17, 18, 28) (Fig. 4A). In a proof-of-concept application, we leveraged the expanded targeting of SpG and the near-PAMless qualities of SpRY to generate biologically relevant

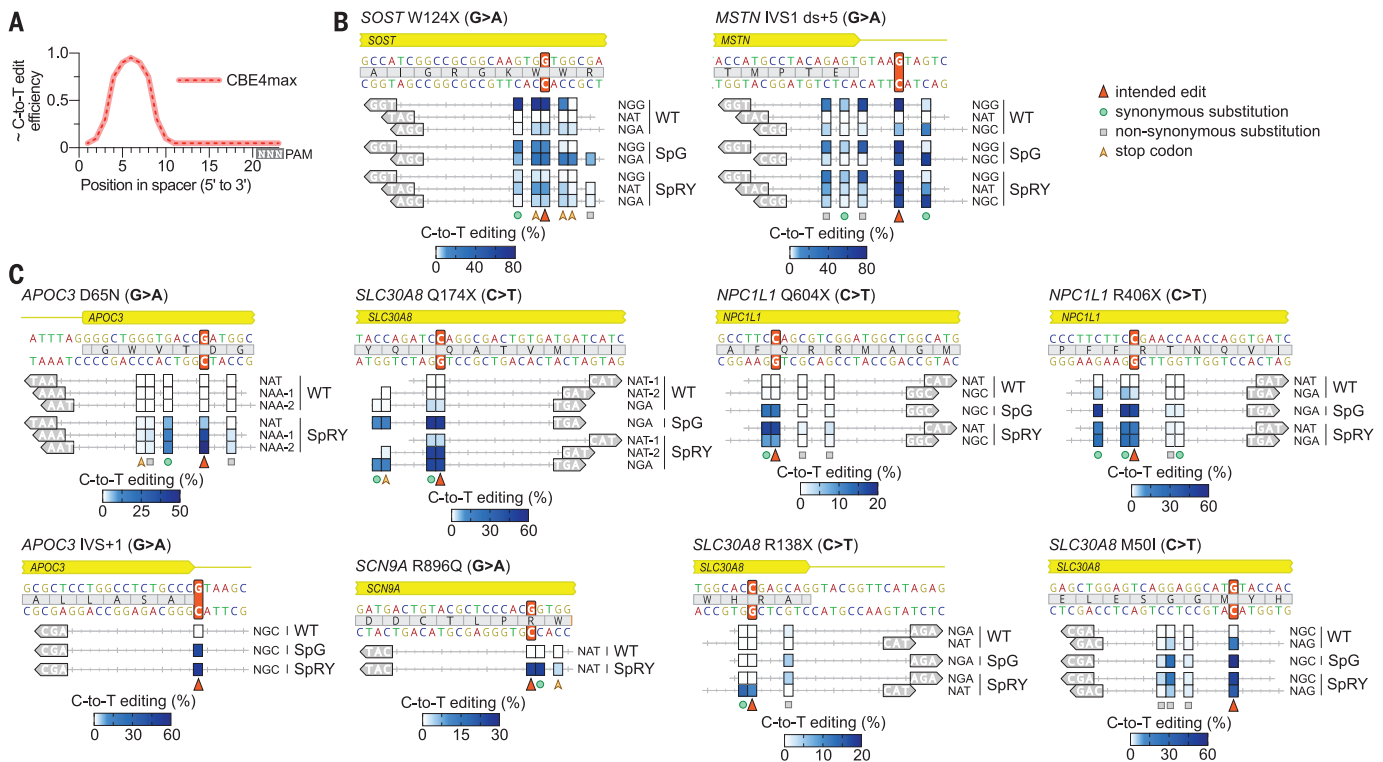


Fig. 4. Expanded capabilities of C-to-T base editors with SpG and SpRY to generate protective genetic variants. (A) Illustration of the relative C-to-T edit activity of CBE4max constructs depending on the position of the cytosine in the spacer [as reviewed in (28)]. (B and C) Comparison of the C-to-T editing activities of WT SpCas9, SpG, and SpRY CBE4max constructs across 22 target sites covering 10 previously described protective genetic variants accessible or inaccessible with target sites harboring NGG PAMs [(B) and (C), respectively]. The intended edit is

highlighted with a dark-orange arrow. C-to-T editing for cytosines within the spacer that are edited above 1% by any variant is plotted for all appropriate variant and guide combinations. SpG was tested only on sites harboring NGN PAMs. Editing of cytosines assessed by targeted sequencing with mean C-to-T editing is shown for n = 3. The bystander synonymous, nonsynonymous, and stop codon C-to-T edits are indicated. The PAMs for each target site are shown in the gray arrow annotation. For raw data, see table S5.

substitutions implicated to protect individuals against coronary heart disease, type 2 diabetes, osteoporosis, chronic pain, and other pathologies (32–38). We first selected two genetic variants (*SOST* W124X and *MSTN* IVS1) with nearby NGG PAMs that might appropriately position the CBE edit window (Fig. 4B). We assessed the activities of WT-, SpG-, and SpRY-CBE constructs against target sites with a variety of PAMs and, as expected, observed the most-robust editing with WT-CBE on sites with NGG PAMs. However, for *MSTN* IVS1, we also observed potentially deleterious bystander editing of a nearby cytosine with WT-CBE; this collateral edit was avoided or reduced when using SpG- and SpRY-CBEs targeted to nearby sites bearing NGC and NAT PAMs (Fig. 4B).

Next, we systematically evaluated the capability to generate eight additional protective variants that lack nearby canonical NGG PAMs (Fig. 4C). We examined target sites harboring NRN PAMs using WT-, SpG-, and SpRY-CBEs that would position the intended C-to-T edit within the high-activity CBE edit window (Fig. 4A). With WT-CBE, we were unable to efficiently generate the intended edit for seven of eight substitutions, owing to the absence of nearby canonical PAMs, which reinforces the need for variants with expanded targeting capabilities. With SpG- and SpRY-CBEs, we screened additional target sites for each substitution and observed that we could efficiently introduce the intended C-to-T edit across all eight targets (Fig. 4C). For most genetic variants, we were able to avoid deleterious bystander editing with SpG and SpRY by selecting from multiple targetable sites that produce silent or tolerable collateral edits instead of those that cause nonsynonymous C-to-T changes. These results demonstrate the utility of SpG and SpRY for higher-resolution targeting of previously uneditable genomic sites and the capability to examine additional target sites to avoid detrimental bystander edits.

Outlook

While the PAM requirement of CRISPR systems enables bacteria to distinguish self from non-self, for genome editing applications, the necessity of PAM recognition constrains CRISPR-Cas systems for use across genomic loci that lack or only sparsely encode PAMs. The SpG and SpRY variants circumvent this limitation by relaxing or almost entirely removing the dependence of SpCas9 on a requisite PAM, extending targeting to sites with NGN and NAN PAMs and to many sites with NCN or NTN PAMs, albeit at a reduced relative efficiency. These variants should enable unconstrained targeting for a variety of applications that require precise DNA breaks, nicks, deamination, or binding events. Beyond the experiments presented here in HEK 293T cells, the utility of SpG and SpRY across different applications and delivery contexts requires

additional investigation (e.g., for tiling putative regulatory elements in various cell types).

In principle, the strategy we used to reduce or eliminate the PAM requirement should be applicable to other native or engineered CRISPR-Cas9 and CRISPR-Cas12a orthologs for which structural information is available. Although future studies are needed to more precisely elucidate the molecular roles of the amino acid substitutions in SpG and SpRY, we speculate that SpRY achieves its expanded targeting range through the removal of the canonical base-specific interactions, displacement of the PAM DNA to facilitate interactions in the major groove of the PAM, and energetic compensation by the addition of novel nonspecific protein–DNA contacts. More practically, regarding which enzyme to use for experiments requiring on-target activity, we suggest WT SpCas9 for sites harboring NGG PAMs, SpG for NGH PAMs, and SpRY for targets encoding the remaining NHN PAMs (with NAN being preferable to NCN or NTN).

The potential for undesirable off-target effects requires methods to mitigate them. As observed when developing engineered CRISPR-Cas12a and CRISPR-Cas9 enzymes with expanded PAM tolerances, relaxation of the PAM can reduce specificity (22, 39). However, both enAsCas12a and SpCas9-NG were compatible with substitutions that enhance genome-wide specificity. Similarly, SpG and SpRY are compatible with SpCas9-HF1 substitutions, which eliminate nearly all detectable off-target effects as determined by GUIDE-seq, enabling applications that require higher fidelity.

By developing SpCas9 variants capable of high-resolution editing, we demonstrate that protein engineering can eliminate biological constraints that limit applications of CRISPR-Cas enzymes. With SpRY supporting the editing of many sites containing NRN>NYN PAMs, nearly all majority of the genome is now targetable.

REFERENCES AND NOTES

1. L. A. Marraffini, E. J. Sontheimer, *Nature* **463**, 568–571 (2010).
2. R. Heler et al., *Nature* **519**, 199–202 (2015).
3. H. Deveau et al., *J. Bacteriol.* **190**, 1390–1400 (2008).
4. F. J. M. Mojica, C. Díez-Villaseñor, J. García-Martínez, C. Almendros, *Microbiology* **155**, 733–740 (2009).
5. M. Jinek et al., *Science* **337**, 816–821 (2012).
6. S. H. Sternberg, S. Redding, M. Jinek, E. C. Greene, J. A. Doudna, *Nature* **507**, 62–67 (2014).
7. W. Jiang, D. Bikard, D. Cox, F. Zhang, L. A. Marraffini, *Nat. Biotechnol.* **31**, 233–239 (2013).
8. B. P. Kleinstiver et al., *Nature* **523**, 481–485 (2015).
9. K. M. Esvelt et al., *Nat. Methods* **10**, 1116–1121 (2013).
10. I. Fonfara et al., *Nucleic Acids Res.* **42**, 2577–2590 (2014).
11. T. Karvelis et al., *Genome Biol.* **16**, 253 (2015).
12. B. Zetsche et al., *Cell* **163**, 759–771 (2015).
13. B. Elliott, C. Richardson, J. Winderbaum, J. A. Nickoloff, M. Jasin, *Mol. Cell Biol.* **18**, 93–101 (1998).
14. G. M. Findlay, E. A. Boyle, R. J. Hause, J. C. Klein, J. Shendure, *Nature* **513**, 120–123 (2014).
15. M. C. Canver et al., *Nature* **527**, 192–197 (2015).
16. J. Shi et al., *Nat. Biotechnol.* **33**, 661–667 (2015).
17. A. C. Komor, Y. B. Kim, M. S. Packer, J. A. Zuris, D. R. Liu, *Nature* **533**, 420–424 (2016).
18. N. M. Gaudelli et al., *Nature* **551**, 464–471 (2017).

19. Y. Kan, B. Ruis, T. Takasugi, E. A. Hendrickson, *Genome Res.* **27**, 1099–1111 (2017).
20. C. Anders, O. Niewoehner, A. Duerst, M. Jinek, *Nature* **513**, 569–573 (2014).
21. B. P. Kleinstiver et al., *Nature* **529**, 490–495 (2016).
22. H. Nishimasu et al., *Science* **361**, 1259–1262 (2018).
23. J. H. Hu et al., *Nature* **556**, 57–63 (2018).
24. C. Anders, K. Bargsten, M. Jinek, *Mol. Cell* **61**, 895–902 (2016).
25. S. Hirano, H. Nishimasu, R. Ishitani, O. Nureki, *Mol. Cell* **61**, 886–894 (2016).
26. See supplementary materials.
27. K. Suzuki et al., *Nature* **540**, 144–149 (2016).
28. H. A. Rees, D. R. Liu, *Nat. Rev. Genet.* **19**, 770–788 (2018).
29. L. W. Koblan et al., *Nat. Biotechnol.* **36**, 843–846 (2018).
30. I. M. Slaymaker et al., *Science* **351**, 84–88 (2016).
31. S. Q. Tsai et al., *Nat. Biotechnol.* **33**, 187–197 (2015).
32. W. Balemans et al., *Hum. Mol. Genet.* **10**, 537–543 (2001).
33. M. Schuelke et al., *N. Engl. J. Med.* **350**, 2682–2688 (2004).
34. J. J. Cox et al., *Hum. Mutat.* **31**, E1670–E1686 (2010).
35. J. Flannick et al., *Nat. Genet.* **46**, 357–363 (2014).
36. TG and HDL Working Group of the Exome Sequencing Project, National Heart, Lung, and Blood Institute, *N. Engl. J. Med.* **371**, 22–31 (2014).
37. A. R. Harper, S. Nayee, E. J. Topol, *Nat. Rev. Genet.* **16**, 689–701 (2015).
38. Myocardial Infarction Genetics Consortium Investigators, *N. Engl. J. Med.* **371**, 2072–2082 (2014).
39. B. P. Kleinstiver et al., *Nat. Biotechnol.* **37**, 276–282 (2019).
40. K. Clement et al., *Nat. Biotechnol.* **37**, 224–226 (2019).
41. R. T. Walton, B. P. Kleinstiver, Scripts for analyzing High-Throughput PAM Determination Assay (HT-PAMDA) experimental data for CRISPR enzymes, Version 1, Zenodo (2020); <http://doi.org/10.5281/zenodo.3710516>.

ACKNOWLEDGMENTS

We thank S. Tsai and J. Lopez for advice on GUIDE-seq data analysis; J. Hsu for assistance with the PAMDA scripts; J. Grünwald for advice on NextSeq sequencing; Z. Hebert and the Molecular Biology Core Facilities (MBCF) at Dana-Farber Cancer Institute (DFCI) for support with NextSeq sequencing; K. Clement for guidance with CRISPResso2; S. Johnstone and B. Bernstein for assistance with and access to their Covaris E220; D. Gao for bioinformatic support; M. Prew and M. Welch for providing guide RNA plasmids; S. Katherisan for advice on protective variants; and J. K. Joung for suggestions on the manuscript. **Funding:** Research in the Kleinstiver lab was supported by NIH R00-CA218870, NIH P01-HL142494, a Career Development Award from the American Society of Gene & Cell Therapy, and the Margaret Q. Landenberger Research Foundation. **Author contributions:** R.T.W. and B.P.K. conceived of the study. R.T.W., K.A.C., and M.N.W. performed experiments. All authors analyzed data and interpreted results. R.T.W. and B.P.K. wrote the manuscript with input from all authors. **Competing interests:** R.T.W. and B.P.K. are inventors on various patents and patent applications that describe gene editing and epigenetic editing technologies. B.P.K. is a consultant for Avectas Inc. and an adviser for Acrigen Biosciences. **Data and materials availability:** Plasmids generated in this study are available through Addgene (www.addgene.org/Benjamin_Kleinstiver/; see also table S2). All data are available in the manuscript, in the supplementary materials, or in the following databases: High-throughput sequencing datasets from nuclease, CBE, ABE, HT-PAMDA, HT-PAMDA-CBE, and GUIDE-seq experiments are available through the National Center for Biotechnology Information Sequence Read Archive (NCBI SRA) under BioProject ID PRJNA605711 (www.ncbi.nlm.nih.gov/bioproject/605711). The commands for visualizing crystal structures in PyMOL are available in (26). CRISPResso2 (40) was used to analyze nuclease and base editor data (with nonstandard parameters detailed in the methods section of the supplementary materials). Custom Python scripts used to analyze HT-PAMDA and HT-PAMDA-CBE data are available through Zenodo (41).

SUPPLEMENTARY MATERIALS

science.sciencemag.org/content/368/6488/290/suppl/DC1
Materials and Methods
Supplementary Text
Figs. S1 to S12
Tables S1 to S7
References (42–46)

25 January 2020; accepted 16 March 2020
Published online 26 March 2020
10.1126/science.aba8853

GAS STORAGE

Balancing volumetric and gravimetric uptake in highly porous materials for clean energy

Zhijie Chen^{1*}, Penghao Li^{1*}, Ryther Anderson^{2*}, Xingjie Wang¹, Xuan Zhang¹, Lee Robison¹, Louis R. Redfern¹, Shinya Moribe^{1,3}, Timur Islamoglu¹, Diego A. Gómez-Gualdrón², Taner Yildirim⁴, J. Fraser Stoddart^{1,5,6}, Omar K. Farha^{1,7†}

A huge challenge facing scientists is the development of adsorbent materials that exhibit ultrahigh porosity but maintain balance between gravimetric and volumetric surface areas for the onboard storage of hydrogen and methane gas—alternatives to conventional fossil fuels. Here we report the simulation-motivated synthesis of ultraporous metal–organic frameworks (MOFs) based on metal trinuclear clusters, namely, NU-1501-M (M = Al or Fe). Relative to other ultraporous MOFs, NU-1501-Al exhibits concurrently a high gravimetric Brunauer–Emmett–Teller (BET) area of 7310 m² g^{−1} and a volumetric BET area of 2060 m² cm^{−3} while satisfying the four BET consistency criteria. The high porosity and surface area of this MOF yielded impressive gravimetric and volumetric storage performances for hydrogen and methane: NU-1501-Al surpasses the gravimetric methane storage U.S. Department of Energy target (0.5 g g^{−1}) with an uptake of 0.66 g g^{−1} [262 cm³ (standard temperature and pressure, STP) cm^{−3}] at 100 bar/270 K and a 5- to 100-bar working capacity of 0.60 g g^{−1} [238 cm³ (STP) cm^{−3}] at 270 K; it also shows one of the best deliverable hydrogen capacities (14.0 weight %, 46.2 g liter^{−1}) under a combined temperature and pressure swing (77 K/100 bar → 160 K/5 bar).

In 2017, for the first time in history, the U.S. petroleum-based transportation sector, which includes cars, trucks, planes, trains, and boats, overtook power plants as the largest source of greenhouse gas emissions in the country (1). This progression continued in 2018 as the transportation sector emitted 1.86 billion metric tons of CO₂ and power plants emitted 1.76 billion metric tons of CO₂, and this trend is projected to continue (1). This shift in CO₂ emissions makes finding alternative sources of cleaner energy for transportation even more important and judicious.

Methane and hydrogen are both alternatives to gasoline for potential use as fuel for the transportation sector (2, 3). Methane is envisioned as a transitional fuel, as its combustion still emits CO₂, but the amount of CO₂ released is less than that of gasoline (4). Hydrogen, by contrast, is envisioned as the “fuel of the future,” as hydrogen-powered fuel cell vehicles are zero-emission automobiles (2). However, the transportation, storage, and operations of hydrogen- and methane-powered vehicles

currently require high-pressure compression (i.e., 700 bar for H₂ and 250 bar for CH₄), which is both costly and potentially unsafe (2, 5). To encourage research in this important field, the U.S. Department of Energy (DOE) established metrics for the development of onboard storage and delivery systems for alternative fuels for the transportation sector (2, 6). For methane, these targets include a gravimetric storage capacity of 0.5 g g^{−1} and a volumetric storage capacity of 263 cm³ (standard temperature and pressure, STP) cm^{−3}. For hydrogen, these targets (for 2020) include a gravimetric storage capacity of 4.5 weight (wt) % and a volumetric storage capacity of 30 g liter^{−1}.

Developing new adsorbent materials is one of the strategies to reach these targets for the safe and cost-effective storage of methane and hydrogen. In particular, high-surface area porous materials (3, 7–9)—often thought of as having a surface area of 2000 m²/g or greater—such as metal–organic frameworks (MOFs) (3, 5, 8, 10–16), porous carbons (5, 17), covalent organic frameworks (18), and porous organic polymers (19–22) have been investigated intensively as candidate adsorbents for the onboard storage of clean-energy gases. The properties of these adsorbents could enable gas loadings to power vehicles under less extreme loading pressure (e.g., 100 bar) than that currently needed by the storage systems used in methane- and hydrogen-powered vehicles. Among these adsorbents, MOFs, constructed from inorganic nodes and organic linkers, have gained prominence as appealing materials for gas storage (23–27) because of their tailorable pore chemistry, pore geometry, and amenability for rational design, facilitated by clear-cut structure-property relationships. Furthermore, surface areas in

MOFs have been reported to reach ultrahigh values (28–30).

When these adsorbents are used, the tank pressure goes down as fuel is consumed until there is no longer a gradient driving the flow of methane or hydrogen to the engine, which typically occurs at 5 bar (2, 26). At this pressure, a substantial fraction of gas may still be adsorbed. Therefore, the deliverable capacity—the amount of stored gas delivered to the engine during operation—becomes a critical design parameter when designing adsorbents. The deliverable capacity for the 100 bar → 5 bar pressure swing has received exceptional interest because 100 bar is the highest refueling pressure for which all-metal Type I pressure tanks can be safety-compliant, circumventing the need for more expensive carbon fiber–reinforced composite vessels for hydrogen storage (2, 31). As both size and weight requirements for the onboard tank must be met to make the storage system feasible, it is crucial to consider the optimization of volumetric and gravimetric deliverable capacities in MOFs as concurrent objectives rather than separate ones (13, 32–34).

As the existence of a trade-off between gravimetric and volumetric capacities has become apparent (33), there is a great challenge in providing satisfactory volumetric and gravimetric capacities within a single material. For example, microporous HKUST-1 (5, 35), with a relatively low gravimetric Brunauer–Emmett–Teller (BET) area of 1980 m² g^{−1} (a volumetric BET area of 1740 m² cm^{−3}), exhibits high volumetric storage but moderate gravimetric CH₄ uptake [281 cm³ (STP) cm^{−3} and 0.23 g g^{−1} at 100 bar/ 298 K], whereas mesoporous MOF-210 (7), with a comparatively high gravimetric BET area of 6240 m² g^{−1} (a volumetric BET area of 1560 m² cm^{−3}), shows high gravimetric storage capacity yet low volumetric CH₄ uptake [0.48 g g^{−1} and 168 cm³ (STP) cm^{−3} at 80 bar/ 298 K]. Typically, ultraporous MOF materials—i.e., MOF-210 (7), NU-110 (28), and DUT-60 (30)—with high gravimetric BET areas, though containing high pore volumes and large pore sizes, show relatively low volumetric areas, which limits their applications in gas storage that requires a balance of volumetric and gravimetric capacities. Clearly, one key step toward a satisfactory trade-off between volumetric and gravimetric capacities would be to impart a single material with both high volumetric and gravimetric surface areas.

Results and discussion

To pursue both high gravimetric and volumetric surface areas in a single material, we used NU-1500 (36) as a starting point (Fig. 1). This class of material has several appealing characteristics, including (i) high porosity and surface area with a relatively small pore size of ~1.4 nm; (ii) a broad degree of designability—the combination of rigid trigonal prismatic linkers

¹Department of Chemistry and International Institute for Nanotechnology, Northwestern University, 2145 Sheridan Road, Evanston, IL 60208, USA. ²Department of Chemical and Biological Engineering, Colorado School of Mines, Golden, CO 80401, USA. ³Future Mobility Research Department, Toyota Research Institute of North America, Ann Arbor, Michigan 48105, USA. ⁴NIST Center for Neutron Research, National Institute of Standards and Technology, Gaithersburg, MD 20899, USA. ⁵Institute for Molecular Design and Synthesis, Tianjin University, 92 Weijin Road, Tianjin 300072, China. ⁶School of Chemistry, University of New South Wales, Sydney, NSW 2052, Australia. ⁷Department of Chemical and Biological Engineering, Northwestern University, 2145 Sheridan Road, Evanston, IL 60208, USA.

*These authors contributed equally to this work.

†Corresponding author. Email: o-farha@northwestern.edu

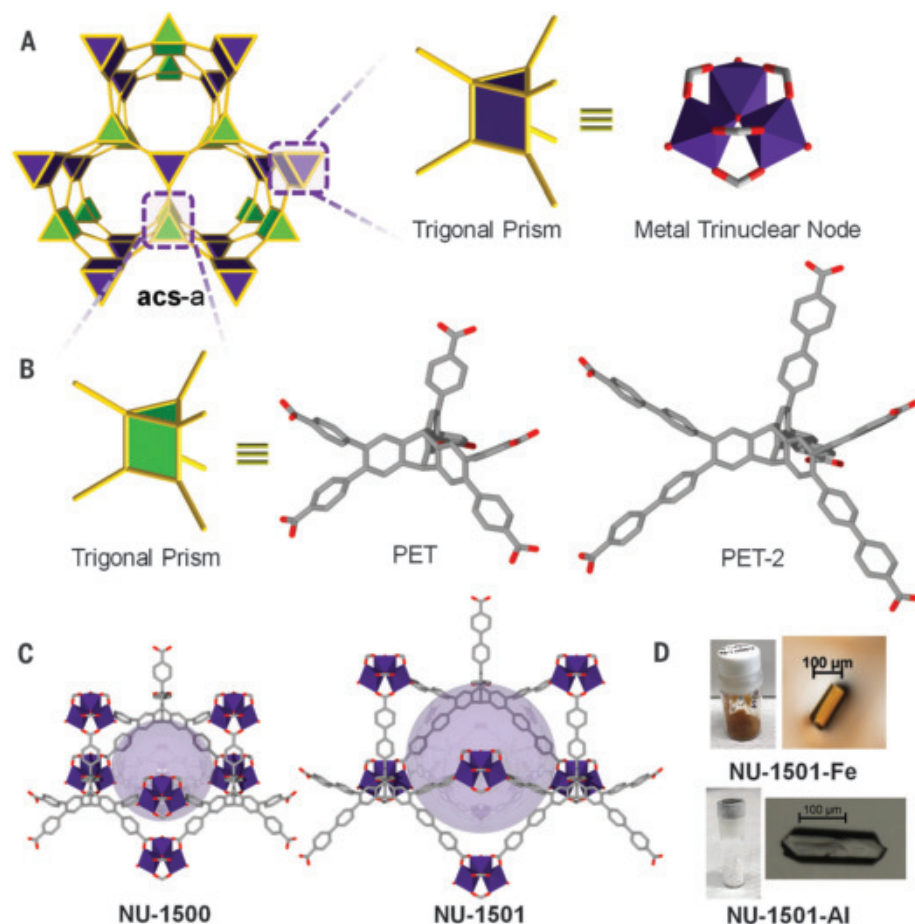


Fig. 1. Design and synthesis of NU-1501. (A to C) Schematic representation of **NU-1501-M** (M = Fe and Al) with the 6-c *acs* net. Atom color scheme: carbon, Gray; metal polyhedron, Northwestern University (NU) purple; O, red. H atoms are omitted for the sake of clarity. (D) Optical images of the single crystals of NU-1501.

and M_3O metal trimers will form MOFs with the *acs* net; (iii) good moisture stability for ease of processing; and finally, (iv) the versatility of metal trimers that allow it to be synthesized from M^{3+} metals, including abundant metals such as aluminum and iron. To start, we synthesized a new aluminum MOF, NU-1500-Al, $[Al_3(\mu_3-O)(H_2O)_2(OH)(PET)]$, which exhibits 6-c *acs* topology and has rigid trigonal prismatic triptycene-based organic ligands—i.e., peripherally extended triptycene (37) (H_6PET)—and aluminum μ_3 -oxo-centered trinuclear clusters (38) (figs. S5 and S10). We confirmed the permanent microporosity of activated NU-1500-Al by nitrogen (N_2) adsorption isotherm at 77 K, which exhibited an apparent BET area of $3560 \text{ m}^2 \text{ g}^{-1}$ —satisfying the four BET consistency criteria (39, 40)—and which also had an experimental total pore volume of $1.46 \text{ cm}^3 \text{ g}^{-1}$, in good agreement with the value for the simulated structure and previously reported (36) NU-1500-Fe (figs. S15 to S17). The volumetric BET area of NU-1500-Al is estimated to be $\sim 1770 \text{ m}^2 \text{ cm}^{-3}$, based on the crystallographic density from the simulated structure. The pore-size distribution from a density func-

tional theory (DFT) model with slit pore geometry revealed one type of pore centered at 1.4 nm, which agrees with the previous values from other NU-1500 analogs (36) (fig. S19).

On account of its high micropore volume and surface area, high-pressure H_2 and CH_4 sorption studies were conducted on NU-1500-Al at the National Institute for Standards and Technology (NIST) (figs. S31 to S36). At 100 bar, NU-1500-Al adsorbed $\sim 0.34 \text{ g g}^{-1}$ [237 cm^3 (STP) cm^{-3}] and $\sim 0.39 \text{ g g}^{-1}$ [273 cm^3 (STP) cm^{-3}] of CH_4 at 296 and 270 K, respectively, with deliverable capacities of $\sim 0.29 \text{ g g}^{-1}$ [202 cm^3 (STP) cm^{-3}] and $\sim 0.32 \text{ g g}^{-1}$ [224 cm^3 (STP) cm^{-3}] between 5 and 100 bar. The volumetric deliverable capacities of 5 to 100 bar for NU-1500-Al are comparable to those of benchmark methane-storage materials, such as MOF-905 (25) [203 cm^3 (STP) cm^{-3} ; 5 to 80 bar at 298 K], HKUST-1 (5) [207 cm^3 (STP) cm^{-3} ; 5 to 100 bar at 298 K], and Al-*soc*-MOF-1 (13) [201 cm^3 (STP) cm^{-3} ; 5 to 80 bar at 298 K] (table S6). NU-1500-Al adsorbed $\sim 8.6 \text{ wt } \%$ ($46.8 \text{ g liter}^{-1}$) of H_2 at 100 bar and 77 K, with a deliverable capacity of $8.2 \text{ wt } \%$ ($44.6 \text{ g liter}^{-1}$) under combined temperature and pressure swing condi-

tions: 77 K/100 bar \rightarrow 160 K/5 bar, which agrees with the tank design conditions proposed (41) by the DOE (table S7).

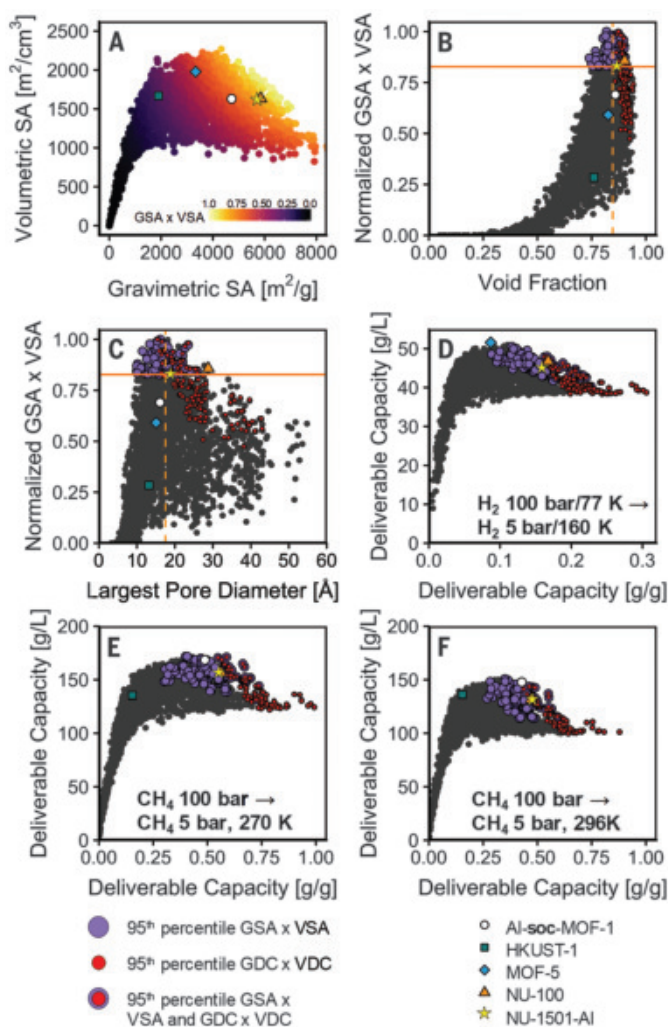
Motivated by the results from NU-1500, we first set out to understand the trade-off between gravimetric and volumetric surface area (GSA and VSA, respectively). To accomplish this task, we created a topologically diverse (58 topologies) 2800-MOF database, including 50 MOFs isorecticular to NU-1500, using the ToBaCCo (42) code (figs. S50 to S54). Both gravimetric and volumetric surface areas were calculated geometrically for the created structures. Plotting these two quantities against each other (Fig. 2A) reveals their trade-off, which can be quantified by their normalized product ($GSA \times VSA$).

The $GSA \times VSA$ product shows a volcano-type relationship between MOF helium void fraction (VF) and largest pore diameter (LPD) (Fig. 2, B and C), with MOFs at the top of the volcano presenting the ideal trade-off ($GSA \times VSA$ product in the 95th percentile). The intermediate MOFs in this database that still exhibit these ideal qualities display an average VF of 0.85 and an average LPD of 17.2 Å. By comparison, NU-1500 presents values of 0.76 and 12.7 Å, respectively, indicating opportunities to improve the trade-off by refining the MOF design. Indeed, the obtained structure-property relationships revealed the value of extending the rigid triptycene-based ligand of the NU-1500 by one phenyl ring, going from PET to PET-2 (43) (Fig. 1C).

We named the PET-2-based structure “NU-1501” and noticed that it presents properties (VF = 0.87, LPD = 18.8 Å) closer to the average of the MOFs in the ideal trade-off region. Simply meeting either property value does not guarantee an ideal trade-off. For instance, MOFs with “ideal” VFs cover a wide range for the $GSA \times VSA$ product. Thus, NU-1501 has other complementary features that boost its $GSA \times VSA$ product such as low metal atom-to-organic atom ratio. For example, figs. S51E and S51F show that MOFs with lower metal atom-to-organic atom ratios tend to have higher $GSA \times VSA$ products. This is because organic atom moieties (e.g., aromatic rings) tend to provide large adsorption surfaces while being light compared to metals.

To understand the implications of an ideal VSA versus GSA trade-off, we predicted methane and hydrogen deliverable capacities for the MOFs in the database (Fig. 2, D, E and F). Notably, there is broader peak in the gravimetric deliverable capacity (GDC) versus volumetric deliverable capacity (VDC) than in the VSA versus GSA trade-off, meaning that MOFs with maximally high GDC (and thus generally maximally high GSA) are included in the ideal trade-off region. From fig. S54, we see that there are many MOFs within the ideal trade-off region for deliverable capacity that have a GSA too high to

Fig. 2. Trade-offs of gravimetric and volumetric properties predicted by molecular simulation. (A) VSA versus GSA, colored by the product of the two. NU-1501-Al lies in the ideal trade-off region, characterized as being just past the peak of volumetric SA. Al-soc-MOF-1, HKUST-1, MOF-5, and NU-100 are shown for comparison. **(B)** The product of GSA and VSA versus void fraction. The horizontal orange line shows the cutoff for being in the 95th percentile of GSA \times VSA. The dashed, vertical orange line shows the average void fraction for MOFs in the 95th percentile. **(C)** Analogous to (B) except plotting GSA \times VSA versus MOF largest pore diameter. **(D)** Volumetric deliverable capacity (VDC) versus gravimetric deliverable capacity (GDC) for hydrogen. Purple points show MOFs in the ideal region (95th percentile of GSA \times VSA) of the GSA/VSA trade-off. Red points show MOFs in the 95th percentile of GDC \times VDC. Red points outlined in purple show MOFs in both regions. **(E)** Analogous to (D) except for methane VDC and GDC at 270 K. **(F)** Analogous to (D) except for methane VDC and GDC at 296 K.



be in the ideal trade-off region for surface area. NU-1501 lies exactly at the boundary of MOFs in the ideal trade-off region for deliverable capacity and MOFs in the ideal trade-off region for surface area (in all cases), meaning that NU-1501-Al maintains maximally high VSA for MOFs with GDC \times VDC in the 95th percentile (whereas most other MOFs have higher GSA and lower VSA).

Inspired by the computational results above, we decided to synthesize expanded versions of **acs**-MOFs—i.e., NU-1501, which features an extended ligand design, H_6PET-2 (figs. S1 to S4). Solvothermal reactions of H_6PET-2 with $AlCl_3 \cdot 6H_2O$ and $FeCl_3 \cdot 6H_2O$ yielded (Fig. 1D) colorless and yellow-orange hexagonal block crystals. Single-crystal x-ray diffraction (SCXRD) studies of these materials (NU-1501-Al and NU-1501-Fe) revealed noncatenated structures crystallizing in a hexagonal space group ($P6m2$) (tables S1 and S2). The μ_3 -oxo-centered trinuclear metal inorganic clusters are linked

by the fully deprotonated trigonal prismatic ligands, H_6PET-2 , to yield a 3-periodic **acs**-MOF having one type of open hexagonal channel with a pore size of ~ 2.2 nm. We predicted the formula to be $[M_3(\mu_3O)(H_2O)_2(OH)(PET-2)]$ ($M = Al$ or Fe), with the terminal anionic groups on the trinuclear node being $-OH$, as supported by the absence of chloride signals from energy-dispersive x-ray analysis (figs. S11 to S13). We confirmed the phase purities of the bulk NU-1501-Al and NU-1501-Fe, based on similarities (fig. S6) between the simulated and as-synthesized powder x-ray diffraction (PXRD) patterns.

The permanent porosity of NU-1501-Al and NU-1501-Fe after supercritical CO_2 activation has been confirmed by reversible N_2 and Ar adsorption and desorption isotherms at 77 and 87 K, respectively. Both materials have very similar isotherms (Fig. 3 and figs. S18 to S24). The experimental total pore volumes of NU-1501-Al, calculated from the N_2 and Ar adsorption isotherms, are 2.91 and 2.93 $cm^3 g^{-1}$,

respectively, which agree well with the simulated values from the single-crystal structure. The pore-size distribution based on a DFT model revealed that NU-1501-Al has pore sizes ranging from 1.5 to 2.5 nm, with two types of pores centered at ~ 1.7 and 2.2 nm, which agrees well with the two pores from the single-crystal structure. The apparent BET area of NU-1501-Al based on the N_2 adsorption isotherm is estimated to be 7310 $m^2 g^{-1}$ after satisfying all four BET consistency criteria (39, 40). If only the first two BET consistency criteria are fulfilled—as in the recently reported (30) ultraporous material, DUT-60—the apparent BET area is estimated to reach 9150 $m^2 g^{-1}$ (table S3). Moreover, the apparent BET area of NU-1501-Al, based on the Ar adsorption isotherm, attains 7920 $m^2 g^{-1}$ after satisfying the first three BET consistency criteria, which is in line with the simulated BET area of 7760 $m^2 g^{-1}$ from the simulated Ar adsorption isotherm (table S4). The deviation from the BET criteria should be minimized when it is not possible to select a region fulfilling all four consistency criteria, as in the case of the BET area calculation (40) from the Ar adsorption isotherm of NU-1501-Al. To the best of our knowledge, the gravimetric BET area (7310 $m^2 g^{-1}$) of NU-1501-Al is the highest reported value for all porous materials after satisfying all four BET criteria, despite the pore volume (about 2.90 $cm^3 g^{-1}$) being lower than those of ultraporous materials having BET areas larger than 7000 $m^2 g^{-1}$ (table S5). Notably, the volumetric BET area of NU-1501-Al reaches 2060 $m^2 cm^{-3}$, based on the crystallographic density. This volumetric BET area is among the highest of all reported porous materials with gravimetric BET areas higher than 5000 $m^2 g^{-1}$, and is much higher than that of similar ultraporous MOFs such as NU-110 (28) (1585 $m^2 cm^{-3}$), MOF-210 (7) (1560 $m^2 cm^{-3}$), and DUT-60 (30) (1466 $m^2 cm^{-3}$). The isotherm is highly reproducible, as illustrated by the similarities of isotherms taken from four different batches at Northwestern University and at NIST (fig. S18).

As revealed by the geometrical calculation of the pore size distribution from the crystal structures (fig. S49), there are two main features that allow NU-1501-Al to maintain a higher volumetric surface area over other MOFs—i.e., MOF-210 (7), NU-100 (8), NU-110 (28), and DUT-60 (30)—with similar gravimetric surface areas and higher pore volumes: (i) The largest pore of NU-1501-Al is much smaller than those of MOF-210 (7), NU-100 (8), NU-110 (28), and DUT-60 (30); and (ii) NU-1501-Al has only one dominant pore.

The iron-based analog of NU-1501 (NU-1501-Fe) shows gravimetric and volumetric BET areas (7140 $m^2 g^{-1}$ and 2130 $m^2 cm^{-3}$) similar to those of the aluminum-based NU-1501 and also features an experimental pore volume (2.90 $cm^3 g^{-1}$) similar to that of NU-1501-Al, illustrating the versatility of this MOF design and synthetic

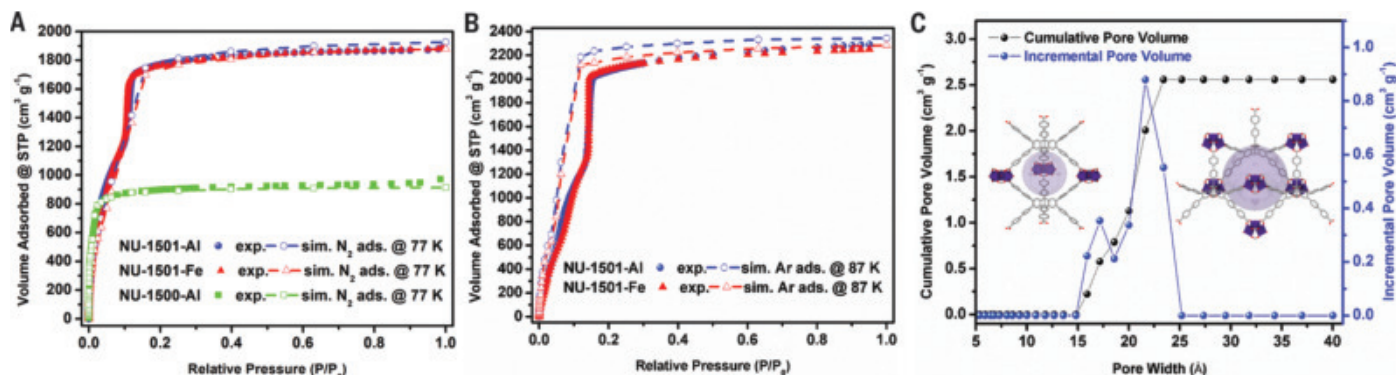


Fig. 3. Porosity measurements of NU-1501. (A) Experimental and simulated N₂ (77 K) adsorption isotherms of NU-1501 and NU-1500-Al. (B) Experimental and simulated Ar (87 K) adsorption isotherms of NU-1501. (C) DFT pore size distribution of NU-1501-Al from N₂ (77 K) adsorption isotherm. The dashed lines are a guide to the eye for simulated data.

strategy (fig. S20). Molecular simulations further revealed that NU-1501-Al and NU-1501-Fe have higher geometric surface areas (5714 and 5513 m² g⁻¹, respectively), when calculated with the N₂ sized probe, than that of NU-1500-Al (3634 m² g⁻¹) (table S8). Additionally, the trivalent metal-based trimer (i.e., Al₃O or Fe₃O) of NU-1501 produces a relatively more stable framework than the traditional ultraporous MOFs with BET areas larger than 6000 m² g⁻¹ based on Zn₄O or copper paddlewheel building units (7, 28, 30, 36). The overall stability of NU-1501 was tested by SCXRD, PXRD, and N₂ sorption measurements after soaking in liquid water, and by variable-temperature PXRD studies (table S2 and figs. S7 to S9, S14, and S25 to S27). To this end, NU-1501 represents an ultraporous material balancing both gravimetric and volumetric BET areas simultaneously—i.e., larger than 7000 m² g⁻¹ and 2000 m³ cm⁻³—making them promising candidates for clean energy-related gas storage (i.e., H₂ and CH₄).

Considering the exceptional gravimetric and volumetric surface areas, methane and hydrogen high-pressure sorption experiments were performed on activated NU-1501 at NIST (Fig. 4 and figs. S37 to S48). NU-1501-Al displays one of the top gravimetric methane uptakes among MOF materials at 80 bar—0.60 g g⁻¹ at 270 K and 0.48 g g⁻¹ at 296 K. The 5- to 80-bar methane working capacities of NU-1501-Al are ~0.44 g g⁻¹ [174 cm³ (STP) cm⁻³; 296 K] and ~0.54 g g⁻¹ [214 cm³ (STP) cm⁻³; 270 K]. These methane capacities are comparable to those of other MOF materials such as MOF-210 (7), Al-soc-MOF-1 (13), ST-2 (44), and MOF-905 (25). At room temperature, the gravimetric deliverable methane capacity of NU-1501-Al at working pressure between 80 bar (adsorption) and 5 bar (desorption) is comparatively similar to that of the benchmark Al-soc-MOF-1, whereas the volumetric deliverable capacity is slightly lower (Fig. 5). Notably, NU-1501-Al adsorbed ~0.54 g g⁻¹

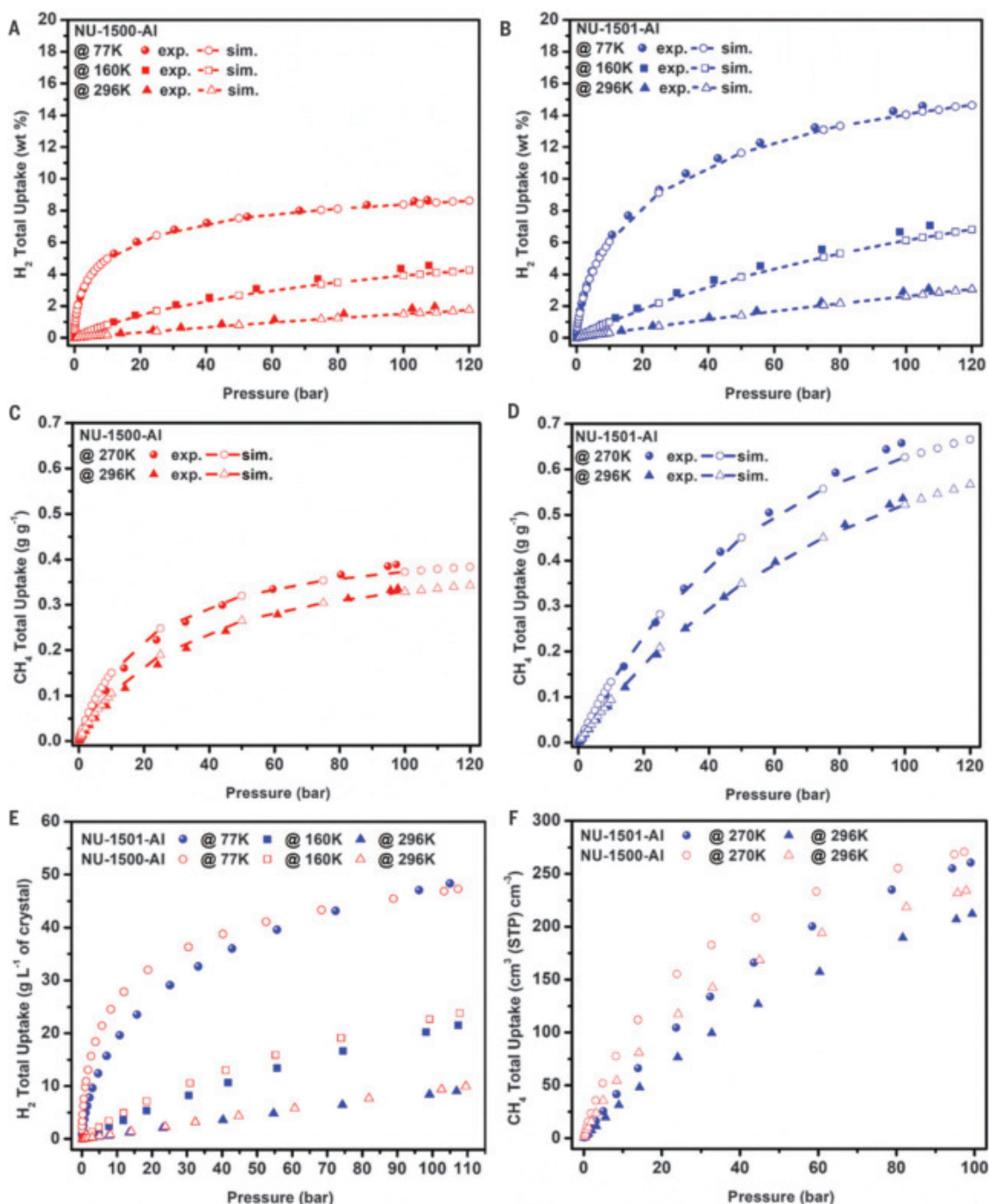
[214 cm³ (STP) cm⁻³] and ~0.66 g g⁻¹ [262 cm³ (STP) cm⁻³] of CH₄ at 100 bar and at 296 and 270 K, respectively. Deliverable capacities between 5 and 100 bar are 0.50 g g⁻¹ [198 cm³ (STP) cm⁻³; 296 K] and ~0.60 g g⁻¹ [238 cm³ (STP) cm⁻³; 270 K], suggesting that NU-1501-Al is among the best porous crystalline materials for methane storage (table S6). The uptake capacities of NU-1501-Al surpass the materials-level gravimetric CH₄ storage DOE target (0.5 g g⁻¹) at 100 bar at both room temperature and 270 K (6, 9, 25). The gravimetric deliverable capacity at 270 K and 5- to 100-bar—i.e., 0.60 g g⁻¹—is even higher than that of the recently reported record MOF materials (table S6). The gravimetric methane uptakes at 100 bar at 296 and 270 K are also much higher than those of the microporous isostructural NU-1500-Al (0.34 g g⁻¹ at 296 K and 0.39 g g⁻¹ at 270 K; at 100 bar), despite similar volumetric uptake [214 versus 237 cm³ (STP) cm⁻³ at 296 K; 262 versus 273 cm³ (STP) cm⁻³ at 270 K]. This suggests that the isoreticular extension of NU-1500 to NU-1501 substantially increases gravimetric methane capacity without sacrificing volumetric performance (Fig. 5). Additionally, at near-freezing temperatures, NU-1501-Al shows (Fig. 5F) a higher volumetric 5- to 100-bar deliverable methane capacity than HKUST-1 [238 cm³ (STP) cm⁻³ at 270 K versus 195 cm³ (STP) cm⁻³ at 273 K] because of the much lower unused methane uptake at 5 bar while having a considerably better gravimetric 5- to 100-bar deliverable capacity (0.60 g g⁻¹ at 270 K versus 0.16 g g⁻¹ at 273 K). NU-1501-Fe, compared to NU-1501-Al, adsorbed slightly less CH₄ (~0.52 g g⁻¹ at 296 K and ~0.63 g g⁻¹ at 270 K; at 100 bar) under the same conditions because of the slightly lower surface area and pore volume (figs. S45 to S48).

The isosteric heats of adsorption (Q_{st}) of NU-1501-Al for CH₄ (figs. S42) were calculated from the isotherms and found to be 9.7 and 10.9 kJ mol⁻¹ at low and high loading, re-

spectively. The experimental Q_{st} of NU-1501-Al is close to the enthalpy of adsorption calculated from the grand canonical ensemble Monte Carlo (GCMC) simulations at low pressure—10.3 kJ mol⁻¹ (table S9). These data suggest that moderate host-guest interactions occur between the framework and methane gas, which is ideal for achieving high deliverable capacities. The Q_{st} value of NU-1501 is slightly less than that for NU-1500-Al (13.7 kJ mol⁻¹) and is most likely due to the smaller pore size of NU-1500. The simulated adsorption isotherms at various temperatures and pressures closely resemble the experimental isotherms, further validating the successful activation of the materials and the high-pressure adsorption results of NU-1501.

NU-1501-Al and NU-1501-Fe are among the best MOFs for hydrogen storage under combined temperature and pressure swing conditions (77 K/100 bar → 160 K/5 bar) (Fig. 5B and table S7) (33, 34, 41, 45). H₂ adsorption isotherms revealed that NU-1501-Al adsorbs ~14.5 wt % (47.9 g liter⁻¹) of H₂ at 100 bar and 77 K, with a high deliverable capacity of 14.0 wt % (46.2 g liter⁻¹) under the conditions 77 K/100 bar → 160 K/5 bar. NU-1501-Fe shows a slightly lower deliverable capacity (13.2 wt %; 45.4 g liter⁻¹) than NU-1501-Al under the same conditions. The experimental H₂ adsorption isotherms closely match the simulated isotherms at various temperatures, which confirmed the near complete activation of the MOFs. In addition, both the absolute uptake at 77 K/100 bar and the deliverable capacities of NU-1501-Al for H₂ are much higher than those of NU-1500-Al while maintaining nearly identical volumetric uptake and capacities (14.0 versus 8.2 wt % and 46.2 g liter⁻¹ versus 44.6 g liter⁻¹ under the aforementioned operational condition), further demonstrating the effectiveness of extension of this **acs**-MOF platform in balancing the gravimetric and volumetric performance of H₂ storage. In agreement with the simulated results, the experimental

Fig. 4. High-pressure hydrogen and methane adsorption performance of NU-1500-Al and NU-1501-Al. (A and B) Experimental and simulated hydrogen adsorption uptake for NU-1501-Al and NU-1500-Al at 77, 160, and 296 K. (C and D) Experimental and simulated methane adsorption uptake for NU-1501-Al and NU-1500-Al at 270 and 296 K. In this work, the capacity (in wt %) of H₂ is calculated according to wt % = (mass of H₂)/(mass of H₂ + mass of MOF) × 100%. The dashed lines are a guide to the eye for simulated data. (E and F) Volumetric adsorption uptake of hydrogen and methane for NU-1501-Al and NU-1500-Al, calculated on the basis of crystallographic density.



gravimetric uptake of H₂ for NU-1501-Al at 100 bar and 296 K is ~2.9 wt % (volumetric uptake: 8.4 g liter⁻¹), which far exceeds the values of reported MOFs (generally between 1 and 2 wt % at 100 bar at room temperature) (11, 12, 46).

Additionally, the Q_{st} values from the H₂ adsorption isotherms at various temperatures indicated that NU-1501-Al exhibits small Q_{st} values of 4 and 2.6 kJ mol⁻¹ at low and high loading, respectively. The Q_{st} for H₂ of NU-1501 at low loading is close to the enthalpy of adsorption

from GCMC simulations at low pressure and slightly less than the Q_{st} of NU-1500-Al—i.e., 4.9 kJ mol⁻¹ (table S9). These values indicate that the MOFs have modest host-guest interactions and that the large hydrogen capacities observed experimentally are driven by adsorbate-adsorbate interactions and the frameworks' substantial porosities. The combination of the experimentally obtained high-pressure hydrogen adsorption studies and GCMC molecular simulations demonstrate that the NU-1501 series are promising candidate materials for the on-

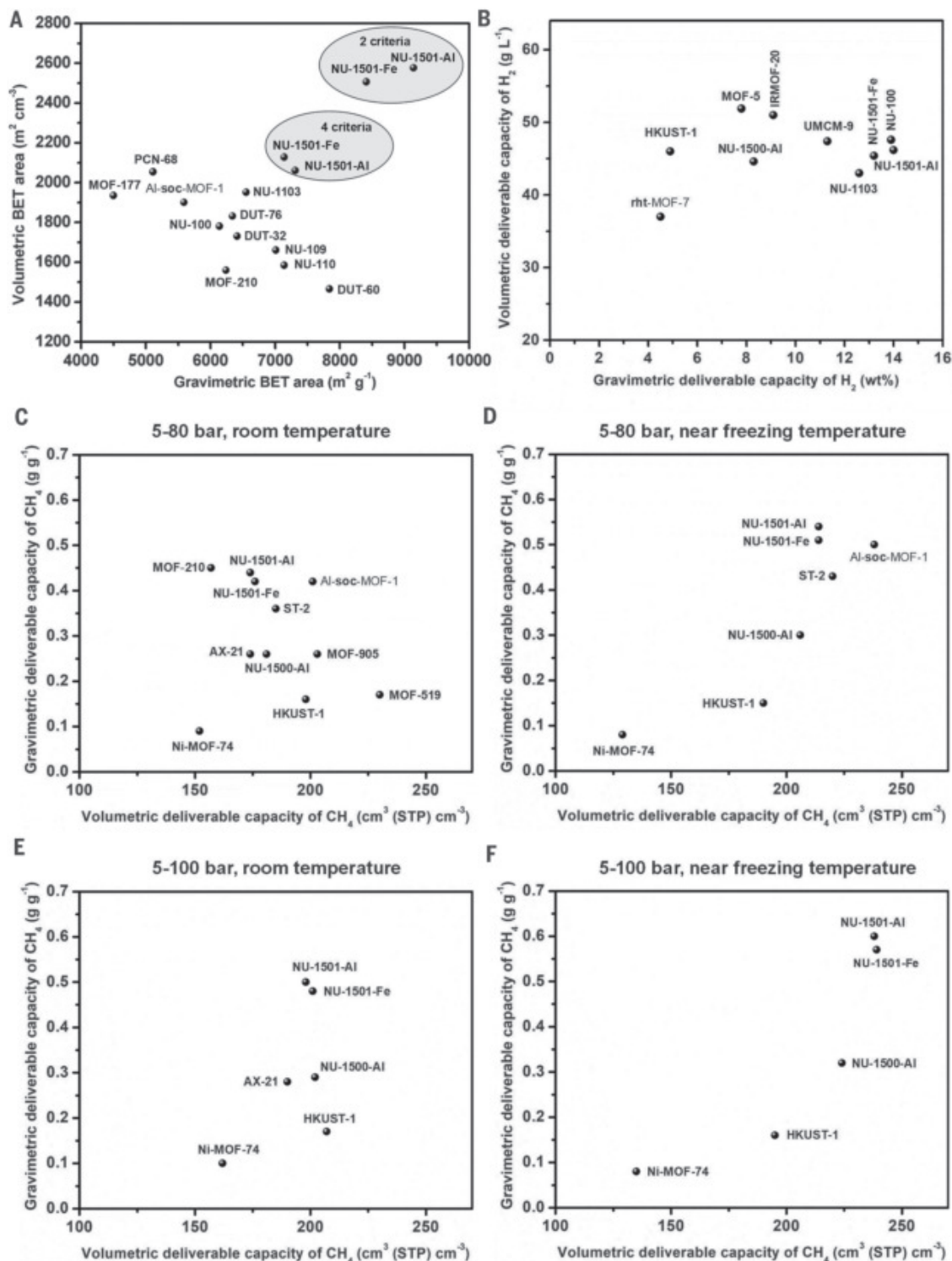
board storage of hydrogen gas, owing to their ultrahigh gravimetric and volumetric surface areas and moderate pore volumes of ~2.90 cm³ g⁻¹ (in comparison to traditional ultraporous MOFs) that balance both volumetric and gravimetric capacity.

Conclusions

In conclusion, we have rationally designed and synthesized a class of ultraporous MOFs, NU-1501, with narrow mesoporosity which exhibit pore diameters of less than 2.5 nm. These

Fig. 5. Trade-offs of gravimetric and volumetric properties suggested by experimental adsorption studies. (A) Trade-off between gravimetric and volumetric BET area for selected ultrahigh porous materials. (B) Trade-off between gravimetric and volumetric deliverable hydrogen capacity under combined temperature and pressure swing conditions: 77 K/100 bar \rightarrow 160 K/5 bar.

(C to F) Trade-off between gravimetric and volumetric deliverable methane capacity of MOFs for 5 to 80 bar and 5 to 100 bar at room temperature and near freezing temperature. Methane adsorption isotherms of MOFs in this work were performed at 296 and 270 K, and methane adsorption isotherms of other materials for comparison were performed at 298 and 273 K. For details of comparison, see tables S6 and S7 and figs. S28 to S30.



MOFs balance both gravimetric and volumetric BET areas, which make them ideal candidate adsorbent materials in onboard storage tanks for safe and effective storage of methane and hydrogen gases. In particular, NU-1501 has the highest apparent gravimetric BET areas among porous materials after satisfying all four BET consistency criteria. With a moderate pore vol-

ume compared to the conventional ultraporous materials such as MOF-210 (7), NU-110 (28), and DUT-60 (30), NU-1501 exhibits impressive volumetric BET areas. The combination of experiment and molecular simulation reveals that NU-1501 achieves outstanding gravimetric uptake, volumetric uptake, and deliverable capacities of methane and hydrogen simultaneously

under practical operational conditions, making these materials a new class of promising MOF adsorbent candidates for the storage and delivery of methane and hydrogen—clean energy carriers related to the carbon-neutral energy system. Finally, the unambiguous structure-property relationship derived from the performance of this material, high-throughput computational

modeling, and experimental results will fuel the design and synthesis of the next generation of ultraporous sorbents for storage and delivery of clean fuel sources.

REFERENCES AND NOTES

1. U.S. Energy Information Administration (EIA), Monthly Energy Review, DOE/EIA-0035(2019/7), July 2019.
2. M. D. Allendorf *et al.*, *Energy Environ. Sci.* **11**, 2784–2812 (2018).
3. A. Schoedel, Z. Ji, O. M. Yaghi, *Nat. Energy* **1**, 16034 (2016).
4. U.S. Energy Information Administration (EIA), Carbon Dioxide Emissions Coefficients (https://www.eia.gov/environment/emissions/co2_vol_mass.php), release date 2 February 2016.
5. J. A. Mason, M. Veenstra, J. R. Long, *Chem. Sci.* **5**, 32–51 (2014).
6. Y. Peng *et al.*, *J. Am. Chem. Soc.* **135**, 11887–11894 (2013).
7. H. Furukawa *et al.*, *Science* **329**, 424–428 (2010).
8. O. K. Farha *et al.*, *Nat. Chem.* **2**, 944–948 (2010).
9. B. Li, H.-M. Wen, W. Zhou, J. Q. Xu, *Chem* **1**, 557–580 (2016).
10. M. Eddaoudi *et al.*, *Science* **295**, 469–472 (2002).
11. D. Zhao, D. Yuan, H.-C. Zhou, *Energy Environ. Sci.* **1**, 222–235 (2008).
12. M. P. Suh, H. J. Park, T. K. Prasad, D.-W. Lim, *Chem. Rev.* **112**, 782–835 (2012).
13. D. Alezi *et al.*, *J. Am. Chem. Soc.* **137**, 13308–13318 (2015).
14. M. T. Kapelowski *et al.*, *Chem. Mater.* **30**, 8179–8189 (2018).
15. T. Tian *et al.*, *Nat. Mater.* **17**, 174–179 (2018).
16. Y. Yan, S. Yang, A. J. Blake, M. Schröder, *Acc. Chem. Res.* **47**, 296–307 (2014).
17. K. V. Kumar, K. Preuss, M.-M. Titirici, F. Rodríguez-Reinoso, *Chem. Rev.* **117**, 1796–1825 (2017).
18. H. Furukawa, O. M. Yaghi, *J. Am. Chem. Soc.* **131**, 8875–8883 (2009).
19. D. Yuan, W. Lu, D. Zhao, H.-C. Zhou, *Adv. Mater.* **23**, 3723–3725 (2011).
20. J. Jia *et al.*, *Chem* **5**, 180–191 (2019).
21. C. D. Wood *et al.*, *Chem. Mater.* **19**, 2034–2048 (2007).
22. V. Roznyev *et al.*, *Nat. Energy* **4**, 604–611 (2019).
23. S. i. Noro, S. Kitagawa, M. Kondo, K. Seki, *Angew. Chem. Int. Ed.* **39**, 2081–2084 (2000).
24. P. L. Llewellyn *et al.*, *Langmuir* **24**, 7245–7250 (2008).
25. J. Jiang, H. Furukawa, Y.-B. Zhang, O. M. Yaghi, *J. Am. Chem. Soc.* **138**, 10244–10251 (2016).
26. F. Gándara, H. Furukawa, S. Lee, O. M. Yaghi, *J. Am. Chem. Soc.* **136**, 5271–5274 (2014).
27. R. Grönkner *et al.*, *Chem. Commun.* **50**, 3450–3452 (2014).
28. O. K. Farha *et al.*, *J. Am. Chem. Soc.* **134**, 15016–15021 (2012).
29. S. B. Kalidindi *et al.*, *Angew. Chem. Int. Ed.* **54**, 221–226 (2015).
30. I. M. Hönigke *et al.*, *Angew. Chem. Int. Ed.* **57**, 13780–13783 (2018).
31. D. J. Durbin, C. Malardier-Jugroot, *Int. J. Hydrogen Energy* **38**, 14595–14617 (2013).
32. Y. Peng *et al.*, *Chem. Commun.* **49**, 2992–2994 (2013).
33. D. A. Gómez-Gualdrón *et al.*, *ACS Appl. Mater. Interfaces* **9**, 33419–33428 (2017).
34. A. Ahmed *et al.*, *Energy Environ. Sci.* **10**, 2459–2471 (2017).
35. S.-Y. Chui, S. M.-F. Lo, J. P. H. Charmant, A. G. Orpen, I. D. Williams, *Science* **283**, 1148–1150 (1999).
36. Z. Chen *et al.*, *J. Am. Chem. Soc.* **141**, 2900–2905 (2019).
37. P. Li *et al.*, *Angew. Chem. Int. Ed.* **58**, 1664–1669 (2019).
38. T. Devic, C. Serre, *Chem. Soc. Rev.* **43**, 6097–6115 (2014).
39. P. Llewellyn, F. Rodríguez-Reinoso, J. Rouquerol, N. Seaton, “Characterization of Porous Solids VII” in *Studies in Surface Science and Catalysis*, Eds. (Elsevier, 2007), vol. 160, pp. 49–56.
40. D. A. Gómez-Gualdrón, P. Z. Moghadam, J. T. Hupp, O. K. Farha, R. Q. Snurr, *J. Am. Chem. Soc.* **138**, 215–224 (2016).
41. P. García-Holley *et al.*, *ACS Energy Lett.* **3**, 748–754 (2018).
42. Y. J. Colón, D. A. Gómez-Gualdrón, R. Q. Snurr, *Cryst. Growth Des.* **17**, 5801–5810 (2017).
43. Z. Chen *et al.*, *J. Am. Chem. Soc.* **141**, 12229–12235 (2019).
44. C.-C. Liang *et al.*, *J. Am. Chem. Soc.* **139**, 13300–13303 (2017).
45. A. Ahmed *et al.*, *Nat. Commun.* **10**, 1568 (2019).
46. K. Sumida, M. R. Hill, S. Horike, A. Dailly, J. R. Long, *J. Am. Chem. Soc.* **131**, 15120–15121 (2009).
47. B. J. Bucior *et al.*, *Cryst. Growth Des.* **19**, 6682–6697 (2019).

ACKNOWLEDGMENTS

Funding: O.K.F. gratefully acknowledges research support from the U.S. Department of Energy’s Office of Energy Efficiency and Renewable Energy (EERE) under award no. DE-EE0008816. P.L. and J.F.S. acknowledge the Joint Center of Excellence in Integrated Nano-Systems (JCIN) at King Abdulaziz City for Science and Technology (KACST) and Northwestern University (NU). D.A.G.-G. acknowledges funding from NSF CAREER (award CBET 1846707). Simulations were performed at the Mio supercomputer cluster

maintained by the Colorado School of Mines. L.R.’s contribution to this work is based on work supported by the U.S. Department of Energy (DOE), Office of Science, Office of Workforce Development for Teachers and Scientists, Office of Science Graduate Student Research (SCGSR) program. The SCGSR program is administered by the Oak Ridge Institute for Science and Education (ORISE) for the DOE. ORISE is managed by ORAU under contract DE-SC0014664. This work made use of the EPIC facility of Northwestern University’s NUANCE Center, which has received support from the Soft and Hybrid Nanotechnology Experimental (SHyNE) Resource (NSF ECCS-1542205); the MRSEC program (NSF DMR-1720139) at the Materials Research Center; the International Institute for Nanotechnology (IIN); the Keck Foundation; and the State of Illinois, through the IIN. This work made use of the IMSEC at Northwestern University, which has received support from the Soft and Hybrid Nanotechnology Experimental (SHyNE) Resource (NSF ECCS-1542205), the State of Illinois, and the International Institute for Nanotechnology (IIN). **Author contributions:** O.K.F. supervised the project; Z.C. and O.K.F. conceived and designed the experiments; P.L. synthesized the ligand under the supervision of J.F.S.; Z.C. synthesized MOF materials; R.A. conducted molecular simulation under the supervision of D.A.G.; X.W. and Z.C. performed activation and low-pressure sorption at Northwestern University; Z.C. collected and analyzed the single-crystal data with help from X.Z.; Z.C. characterized MOF materials with help from X.W., L.R., L.R.R., S.M., and T.Y.; T.Y. conducted the low-pressure and high-pressure sorption studies at NIST with the samples sent from Northwestern University; Z.C. analyzed low-pressure and high-pressure sorption

data with help from O.K.F., R.A., D.A.G., and T.Y.; Z.C., L.R., and O.K.F. wrote the manuscript, and all authors commented and revised on the manuscript. **Competing interests:** O.K.F. has a financial interest in NuMat Technologies, a startup company that is seeking to commercialize MOFs. **Data and materials availability:** The x-ray crystallographic data for NU-1501-Al and NU-1501-Fe have been deposited at the Cambridge Crystallographic Data Centre (CCDC), under deposition no. CCDC 1909853, 1909854, and 1945113. These data can be obtained free of charge from the CCDC via www.ccdc.cam.ac.uk. Crystallographic information for NU-1501-Al and NU-1501-Fe can also be found in the supplementary data. MOFkey (47): AlPZUNVLJATCTESM.MOFkey-v1.acs (NU-1500-Al), FeGKGWJFNTVGTJMJR.MOFkey-v1.acs (NU-1501-Fe), AlGKGWJFNTVGTJMJR.MOFkey-v1.acs (NU-1501-Al). All other relevant data supporting the findings of this study are presented in the paper or the supplementary materials.

SUPPLEMENTARY MATERIALS

science.sciencemag.org/content/368/6488/297/suppl/DC1
Materials and Methods
Supplementary Text
Figs. S1 to S54
Tables S1 to S10
Captions for Data S1 to S3
References (48–83)
Data S1 to S3

17 October 2019; accepted 17 March 2020
10.1126/science.aaz8881

REPORTS

SEX DETERMINATION

Temperature-dependent sex determination is mediated by pSTAT3 repression of *Kdm6b*

Ceri Weber¹, Yingjie Zhou², Jong Gwan Lee¹, Loren L. Looger³, Guoying Qian², Chutian Ge^{2*}, Blanche Capel^{1*}

In many reptiles, including the red-eared slider turtle *Trachemys scripta elegans* (*T. scripta*), sex is determined by ambient temperature during embryogenesis. We previously showed that the epigenetic regulator *Kdm6b* is elevated at the male-producing temperature and essential to activate the male pathway. In this work, we established a causal link between temperature and transcriptional regulation of *Kdm6b*. We show that signal transducer and activator of transcription 3 (STAT3) is phosphorylated at the warmer, female-producing temperature, binds the *Kdm6b* locus, and represses *Kdm6b* transcription, blocking the male pathway. Influx of Ca²⁺, a mediator of STAT3 phosphorylation, is elevated at the female temperature and acts as a temperature-sensitive regulator of STAT3 activation.

The sex of many reptiles is determined by the temperature at which the egg develops in the nest. For example, in the red-eared slider turtle, *Trachemys scripta elegans* (*T. scripta*), the embryonic bipotential gonad differentiates into an ovary at 31°C [the female-producing temperature (FPT)] but into a testis at 26°C [the male-producing temperature (MPT)]. However, the molecular mechanisms underlying this temperature-

dependent developmental switch have remained elusive (1–4). A recent advance was made by our discovery that an epigenetic regulator, KDM6B (JMJD3, a histone demethylase), is required for expression of a conserved, male sex-determination gene, *Dmrt1*, at 26°C (5, 6); in the absence of KDM6B, male genes are not activated, and the female pathway is initiated, leading to formation of an ovary (6). KDM6B itself is not inherently responsive to temperature, indicating that a thermosensitive regulator upstream must provide the missing link between temperature and sex-specific gene expression (6).

One candidate for such a regulator is STAT3 (signal transducer and activator of transcription 3), a transcription factor that controls *Kdm6b*

¹Department of Cell Biology, Duke University Medical Center, Durham, NC 27710, USA. ²College of Biological and Environmental Sciences, Zhejiang Wanli University, Ningbo 315100, China. ³Janelia Research Campus, Howard Hughes Medical Institute, Ashburn, VA 20147, USA.

*Corresponding author. Email: blanche.capel@duke.edu (B.C.); cge@zww.edu.cn (C.G.)

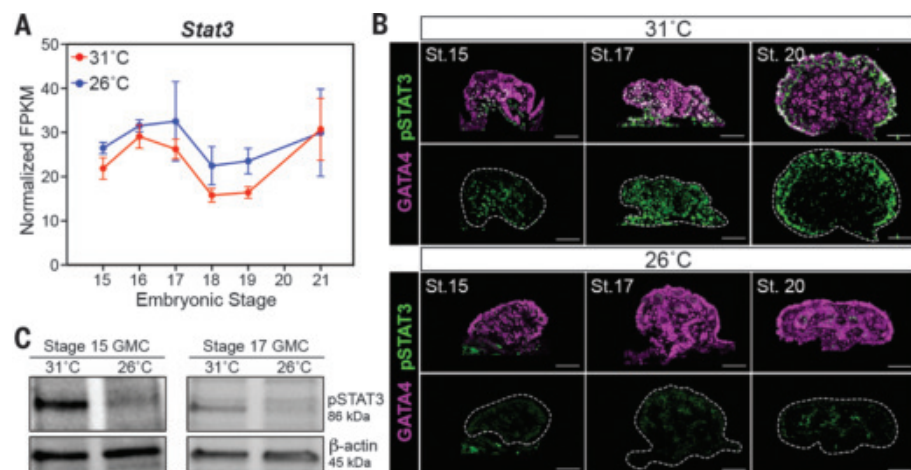


Fig. 1. STAT3 phosphorylation is temperature-dependent and sexually dimorphic. (A) RNA-sequencing measurements of STAT3 expression over the temperature-sensing period at both 26°C (blue) and 31°C (red) (15). FPKM, fragments per kilobase of exon per million fragments mapped. (B) Immunofluorescent images of pSTAT3 (green) and GATA4 (magenta; somatic gonad marker) in gonadal cross sections from embryos at stages 15, 17, and 20. pSTAT3 expression is nuclear and restricted to the sex cords and cortical domain. Scale bars, 50 μ m; $n > 3$ biological replicates. (C) Western blot analysis of pSTAT3 levels at stage 15 and stage 17 in GMCs, with β -actin control; $n > 3$ biological replicates.

expression (7, 8). Dimerization and translocation of STAT3 to the nucleus are dependent on phosphorylation, which can occur through several signaling pathways in response to environmental or physiological stimuli (9–12). Our analysis shows that in *T. scripta* embryos, transcript and protein levels of STAT3 are similar at both 26° and 31°C throughout the temperature-sensing window (stages 14 to 20) (Fig. 1A and fig. S1) (13–15). Immunofluorescence with a phosphospecific antibody showed elevated levels of phosphorylated STAT3 (pSTAT3) at 31°C throughout the embryonic gonad at stages 15 and 17, becoming mostly restricted to the cortex by stage 20 (Fig. 1B). These results were confirmed by means of Western blot analysis of gonad-mesonephric complexes at stages 15 and 17 (Fig. 1C). On the basis of these results, we hypothesized that pSTAT3 binds the *Kdm6b* locus at 31°C and acts as an inhibitor of *Kdm6b* transcription.

To test whether pSTAT3 binds the *Kdm6b* locus, we collected gonads at stage 16 and performed chromatin immunoprecipitation (ChIP) for pSTAT3 followed by quantitative polymerase chain reaction (qPCR) using primers for two conserved pSTAT3 binding sites in the 5' end of the *Kdm6b* locus (fig. S2). pSTAT3 is enriched at the *Kdm6b* locus at 31°C, and its binding is blocked by HO-3867, an inhibitor of STAT3 phosphorylation and DNA binding (Fig. 2A).

To determine whether pSTAT3 functions as a repressor of *Kdm6b*, we explanted stage-14 whole gonad-mesonephros complexes (GMCs) to organ culture at 31° or 26°C. GMCs were

exposed to one of two pSTAT3 inhibitors with different mechanisms of action, HO-3867 or NSC 74859 (S31-201, inhibitor of STAT3 phosphorylation and dimerization), and collected after 24 hours for analysis (16, 17). Levels of pSTAT3 declined in response to both inhibitor treatments, according to immunofluorescence and Western blot analysis (Fig. 2, B and C, and fig. S3A). Reverse transcription followed by qPCR (RT-qPCR) showed that expression of both *Kdm6b* and its downstream target *Dmrt1* was up-regulated at 31°C after exposure to either inhibitor of STAT3 phosphorylation (Fig. 2D). *Kdm6b* expression was not significantly affected by either pSTAT3 inhibitor at 26°C (fig. S3B). This supports a model in which pSTAT3 represses *Kdm6b* transcription at the FPT.

To determine whether pSTAT3 inhibition had a similar effect in vivo, we injected increasing doses of HO-3867 (25, 50, and 100 μ M) into eggs at stage 14 and collected gonads at stages 16 and 21 (Fig. 3A). Consistent with organ culture results, pSTAT3 inhibition led to up-regulation of *Kdm6b* and *Dmrt1* in eggs incubated at 31°C (Fig. 3B). Consequently, 16 of 23 (69.6%) HO-3867-treated eggs exhibited an ovary-to-testis shift in sexual trajectory (table S1), as determined by the ectopic expression of SOX9 protein in gonads at stage 21 (Fig. 3C). However, the up-regulation of *Dmrt1* after inhibition of pSTAT3 at 31°C could be prevented by knocking down *Kdm6b* expression with *Kdm6b*-RNAi (RNA interference) (Fig. 3B), which restored ovarian development in 92.9% (13 of 14) of HO-3867-treated gonads at 31°C (Fig. 3C and table S1). These data further support the model that pSTAT3 binds the *Kdm6b*

locus to repress activation of the male pathway at 31°C.

Phosphorylation of STAT3 can be regulated by calcium signaling pathways that respond to environmental signals, including temperature (18). To investigate a possible relationship between temperature-driven calcium signaling and sex determination, we derived primary cells from stage 15 *T. scripta* gonads. A single-wavelength calcium indicator dye, Cal-520 acetoxymethyl ester (Cal-520 AM) (AAT Bioquest) (19, 20), was introduced into these cells in culture to measure the relative calcium levels at either 26° or 31°C (diagrammed in fig. S4). Cells grown at 31°C showed more fluorescent activity than cells at 26°C, suggesting that Ca^{2+} influx is elevated at FPT (Fig. 4A). Cells were imaged live as the temperature was quickly shifted from 26° to 31°C. Significantly higher fluorescence was recorded almost immediately after the temperature was increased (Fig. 4B, figs. S5A and S6, and movie S1). This effect could be mimicked by exposing cells at 26°C to the calcium ionophore A23187 (Fig. 4C and fig. S5B). Conversely, cells treated with the calcium chelator 1,2-bis(2-aminophenoxy)ethane-*N,N,N',N'*-tetraacetic acid (BAPTA)-AM reported diminished levels of fluorescence over time, despite a shift to 31°C (Fig. 4C and fig. S5B). Western blot analysis of A23187- or BAPTA-AM-treated cells showed that exposure to the ionophore A23187 drives phosphorylation of STAT3 at 26°C, whereas chelation of calcium with BAPTA-AM during the shift from 26° to 31°C leads to diminished activation of STAT3 (Fig. 4, D to F). Collectively, these results show that higher calcium levels at 31°C promote STAT3 phosphorylation.

Taken together, our findings support a new model for sex determination in *T. scripta* (Fig. 4G). According to this model, at warmer temperatures (31°C), ovary development is initiated by a robust influx of calcium into gonadal cells. This promotes phosphorylation of STAT3 and repression of *Kdm6b*, a required activator of the testis-determining pathway. A critical question is therefore how calcium flux is regulated by temperature. Potential effectors for this step are transient receptor potential (TRP) cation channels, well-known environmental sensors that can initiate calcium signaling in response to temperature stimuli (21). TRP channel activity is reported to activate STAT3 in mammalian cell systems and may mediate thermoregulatory responses during inflammation (18). In another reptile with temperature-dependent sex determination, the American alligator, pharmacological manipulation of TRPV4 led to changes in expression of male pathway genes *Sox9* and *Amh* (22). In *T. scripta* gonads, several TRP channels were up-regulated early in the temperature-sensitive period at 31°C (15), including TRPV4, and this may contribute to additional biases in Ca^{2+} flux. When

Fig. 2. pSTAT3 binds *Kdm6b* at 31°C and represses transcription.

(A) ChIP-qPCR analysis shows enrichment of bound pSTAT3 at two sites in the *Kdm6b* locus in gonads at 31°, 26°, and 31°C with HO-3867 treatment. Values are shown as a percentage of the input. IgG, immunoglobulin G control; $n = 3$ pooled biological replicates; data are means \pm SD.

(B) Immunofluorescent images of pSTAT3 (green) and GATA4 (magenta) in gonad sections from cultured GMCs treated with dimethyl sulfoxide (DMSO), NSC 74859, or HO-3867 at 31° or 26°C. Scale bars, 50 μ m.

(C) Western blot analysis of pSTAT3 levels in GMCs treated with DMSO, NSC 74859, or HO-3867 at 31° or 26°C. Western blot band intensity was quantified after normalization to β -actin.

(D) mRNA levels of *Kdm6b* and *Dmrt1* in GMCs cultured at 31°C with DMSO, NSC 74859, or HO-3867. Expression levels of DMSO-treated GMCs were set as 1 after normalization to *Gapdh*. DMSO, $n = 9$ biological replicates; HO-3867, $n = 5$ biological replicates; NSC 74859, $n = 6$ biological replicates. Data are means \pm SD; * $P < 0.05$, ** $P < 0.005$, Mann-Whitney nonparametric t test.

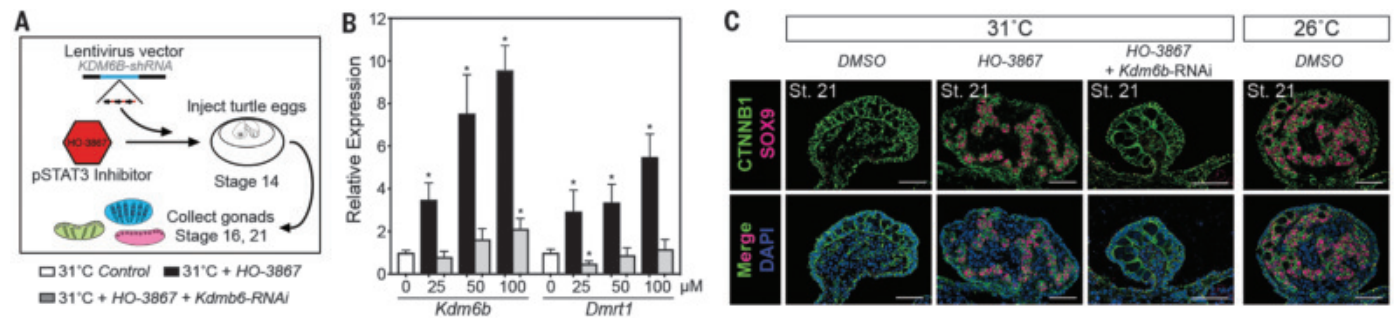
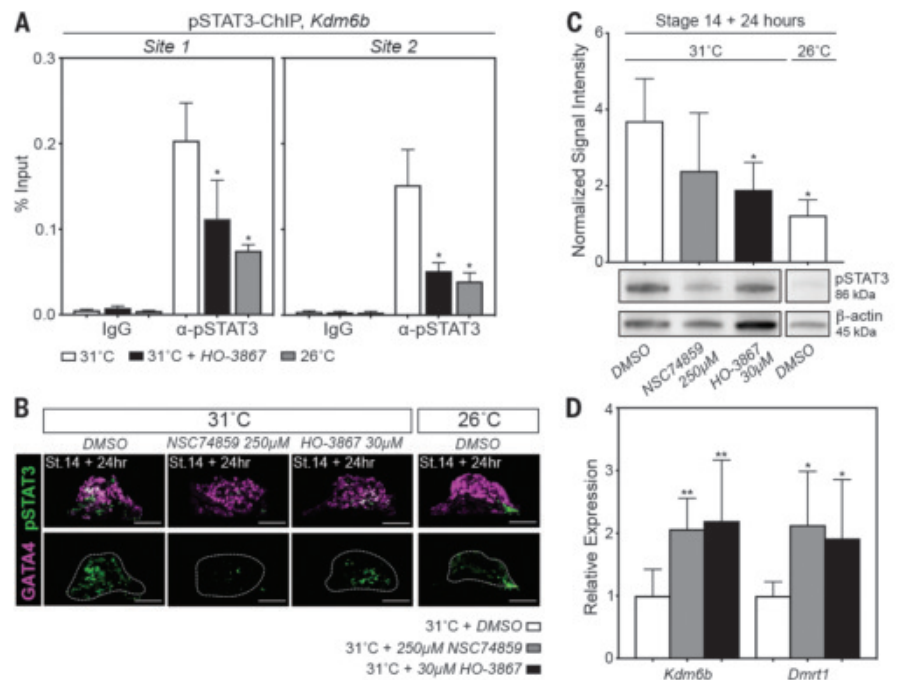


Fig. 3. The switch from the ovary to the testis pathway induced by pSTAT3 inhibition can be reversed by knockdown of *Kdm6b*.

(A) Experimental overview. Eggs raised at 31°C were injected at stage 14 with pSTAT3 inhibitor HO-3867 or co-injected with HO-3867 and *Kdm6b*-RNAi and collected at stage 16 and stage 21 to capture the effect of pSTAT3 inhibition early and late in the sex-determination window.

(B) mRNA levels of *Kdm6b* and *Dmrt1* in stage-16 gonads from 31°C eggs injected with increasing concentrations

conditional approaches become feasible in *T. scripta*, we anticipate that a targeted knockdown of candidate cation channels individually and in combination will be informative. Although TRP channel activity and intracellular calcium are indicated in STAT3 activation, it is unclear whether STAT3 is phosphorylated through canonical signaling (Janus kinase/STAT), other kinases such as calcium/calmodulin-dependent protein kinase II (CaMKII) or Src, or even TRP channels directly (18, 23, 24). Although we propose a calcium-mediated mechanism, it is possible that other well-characterized thermoregulatory responses such as heat shock

protein activity also contribute to STAT3 phosphorylation and sex determination in *T. scripta* (25). Sex determination is likely a cumulative process, and other conserved factors—such as anti-Müllerian hormone (AMH), doublesex and mab-3 related transcription factor 1 (DMRT1), (sex determining region Y)-box 9 (SOX9), or aromatase—likely feed into the Ca²⁺-pSTAT3-*Kdm6b* regulatory loop to stabilize ovary or testis development.

Any model of temperature-dependent sex determination must account for natural nests experiencing oscillating temperatures, unlike the constant temperature experienced by eggs

of HO-3867, or HO-3867 and *Kdm6b*-RNAi. Control 31°C gonads were set as 1 after normalization to *Gapdh*. Data are means \pm SD; $n = 3$ pooled biological replicates. * $P < 0.05$, Mann-Whitney nonparametric t test. (C) Immunofluorescence of SOX9 (pink) and CTNNB1 (β -catenin, green) in stage-21 gonads from 31°C eggs injected with 100 μ M HO-3867 alone or in combination with *Kdm6b*-RNAi compared with gonads from 26°C eggs. Scale bars, 50 μ m. DAPI, 4',6-diamidino-2-phenylindole.

in the laboratory. Broad temperature fluctuations are sufficient to feminize developing turtle embryos, indicating that regular exposures to warmer temperatures are sufficient to initiate and maintain female development (26). Through temperature-shifting experiments, Wibbels *et al.* hypothesized that the magnitude and duration of temperature exposure exerts an effect on sex determination by driving the accumulation of a sex factor in sufficient quantities; a pulse of 26°C MPT lasting at least three embryonic stages or a pulse of 31°C FPT lasting 1.5 embryonic stages was sufficient to affect sex determination (27).

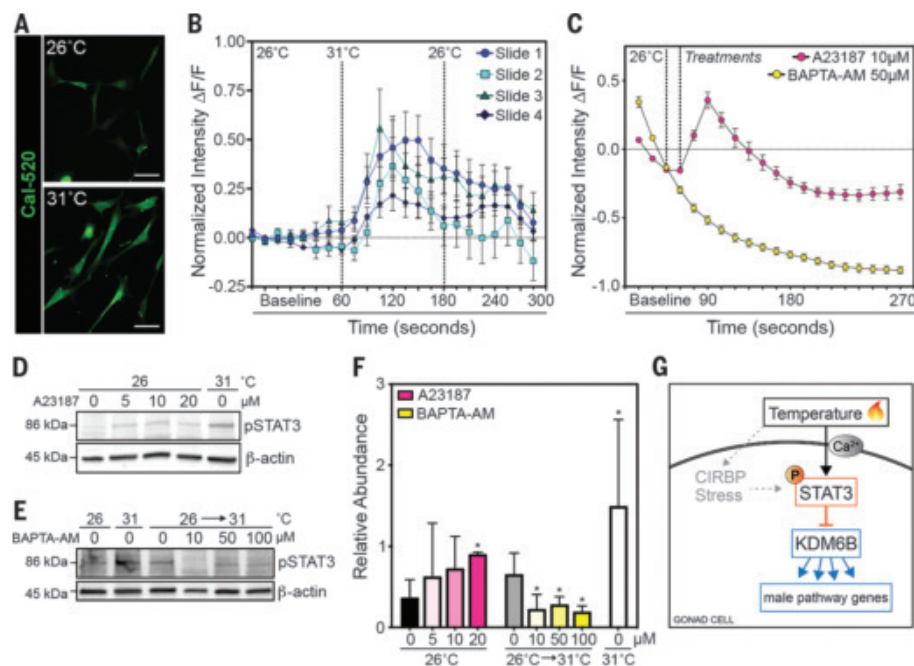


Fig. 4. Intracellular $[Ca^{2+}]$ increases at 31°C are associated with temperature-dependent phosphorylation of STAT3. (A) Gonad-derived primary cells display higher levels of fluorescence at 31°C. (B) Fluorescence (F) was recorded in cells exposed to a temperature shift from 26° to 31°C. Data are means \pm SE; $n = 4$ slides. (C) Cells were stimulated with ionophore A23187 and maintained at 26°C or treated with chelator BAPTA-AM and then shifted to 31°C. (D) pSTAT3 was present in primary cells at 26°C after treatment with increasing concentrations of A23187 for 5 min. (E) STAT3 phosphorylation was diminished when cells at 26°C were treated with increasing concentrations of BAPTA-AM and then switched to 31°C for 5 min. (F) pSTAT3 levels in treated cells were compared with control cells grown at 26° or 31°C. Western blot band intensity was quantified after normalization to β -actin. Data are means \pm SD; $n = 3$ biological replicates. (G) A molecular model for temperature-dependent sex determination in *T. scripta*. Warm temperatures initiate a rise in intracellular calcium that promotes STAT3 phosphorylation. pSTAT3 binds *Kdm6b* to repress activation of *Dmrt1* and the male pathway. Temperature may also activate CIRBP and/or stress response pathways, which can also activate STAT3.

Our data show that a rapid, calcium-mediated response to 31°C leads to phosphorylation of STAT3. Because STAT3 is reported to be stable for at least 8 hours (28), intermittent exposure to high temperature may be sufficient to repress the male pathway in the face of fluctuating temperatures.

In other organisms, a variety of physiological changes other than temperature can regulate the sex-determining pathway, but we argue that these may nevertheless converge on the differential activation of STAT3 and its downstream target, *Kdm6b*. For example, in sequentially hermaphroditic fish, cortisol and the hypothalamus-pituitary-adrenal axis are thought to mediate the social and hormonal changes that transform the identity of the gonad (29). STAT3 can be activated by cortisol through the adenosine 3',5'-monophosphate (cAMP)-cAMP-dependent protein kinase (PKA)-Src pathway (11, 24). Proopiomelanocortin (POMC)—the precursor to adrenocorticotrophic hormone (ACTH), which stimulates the release of cortisol—is up-regulated in temperature-

driven sex-reversed female Australian bearded dragons, suggesting that POMC-mediated stress modulates gonadal fate in some reptiles (30). Other pathways involved in homeostasis have also been implicated in STAT3 activation. Cold-inducible RNA-binding protein (CIRBP) is activated in response to a number of environmental stimuli, including hypothermia (<32°C), and has been associated with female specification in another turtle species with temperature-dependent sex determination (31). CIRBP is a reported activator of STAT3 by way of a number of signaling pathways (12), including calcium and TRPV4 signaling (32). Taken together, these observations support a unifying concept in which pSTAT3 repression of the epigenetic regulator *Kdm6b* is a conserved cassette in multiple environmental sex-determination networks.

REFERENCES AND NOTES

- M. Charnier, *C. R. Seances Soc. Biol. Fil.* **160**, 620–622 (1966).
- J. J. Bull, R. C. Vogt, *J. Exp. Zool.* **218**, 435–440 (1981).

- M. W. J. Ferguson, T. Joanen, *Nature* **296**, 850–853 (1982).
- C. Pieau, M. Dorizzi, N. Richard-Mercier, *Cell. Mol. Life Sci.* **55**, 887–900 (1999).
- C. Ge et al., *Development* **144**, 2222–2233 (2017).
- C. Ge et al., *Science* **360**, 645–648 (2018).
- P. Przanowski et al., *J. Mol. Med. (Berl.)* **92**, 239–254 (2014).
- M. M. Sherry-Lynes, S. Sengupta, S. Kulkarni, B. H. Cochran, *PLOS ONE* **12**, e0174775 (2017).
- Z. Zhong, Z. Wen, J. E. Darnell Jr., *Proc. Natl. Acad. Sci. U.S.A.* **91**, 4806–4810 (1994).
- J. Si, S. J. Collins, *Cancer Res.* **68**, 3733–3742 (2008).
- M. B. Ernst et al., *J. Neurosci.* **29**, 11582–11593 (2009).
- T. Sakurai et al., *Cancer Sci.* **106**, 352–358 (2015).
- H. Merchant-Larios, S. Ruiz-Ramirez, N. Moreno-Mendoza, A. Marmolejo-Valencia, *Gen. Comp. Endocrinol.* **107**, 373–385 (1997).
- E. Greenbaum, *Can. J. Zool.* **80**, 1350–1370 (2002).
- M. Czerwinski, A. Natarajan, L. Barske, L. L. Looger, B. Capel, *Dev. Biol.* **420**, 166–177 (2016).
- K. Siddiquee et al., *Proc. Natl. Acad. Sci. U.S.A.* **104**, 7391–7396 (2007).
- K. S. Rath et al., *Cancer Res.* **74**, 2316–2327 (2014).
- A. Yoshida et al., *Sci. Rep.* **6**, 26088 (2016).
- L. Albantakis, C. Lohmann, *J. Neurosci. Methods* **184**, 206–212 (2009).
- M. Tada, A. Takeuchi, M. Hashizume, K. Kitamura, M. Kano, *Eur. J. Neurosci.* **39**, 1720–1728 (2014).
- M. Gees, B. Colson, B. Nilius, *Cold Spring Harb. Perspect. Biol.* **2**, a003962 (2010).
- R. Yatsu et al., *Sci. Rep.* **5**, 18581 (2015).
- M. Hulsurkar, A. P. Quick, X. H. Wehrens, *J. Clin. Invest.* **128**, 5219–5221 (2018).
- W. Wang et al., *Sci. Signal.* **8**, ra106 (2015).
- S. Kohno et al., *Sex Dev.* **4**, 73–87 (2010).
- N. Valenzuela et al., *Sci. Rep.* **9**, 4254 (2019).
- T. Wibbels, J. J. Bull, D. Crews, *J. Exp. Zool.* **260**, 371–381 (1991).
- E. Siwert, W. Müller-Esterl, R. Starr, P. C. Heinrich, F. Schaper, *Eur. J. Biochem.* **265**, 251–257 (1999).
- A. Goikotxea, E. V. Todd, N. J. Gemmell, *Reproduction* **154**, R149–R160 (2017).
- I. W. Deveson et al., *Sci. Adv.* **3**, e1700731 (2017).
- A. L. Schroeder, K. J. Metzger, A. Miller, T. Rhen, *Genetics* **203**, 557–571 (2016).
- T. Fujita et al., *Sci. Rep.* **7**, 2295 (2017).

ACKNOWLEDGMENTS

We thank B. L. M. Hogan for advice on the manuscript and members of the Capel laboratory for their support. We are also grateful to J. Grandl and the Duke Light Microscopy Core Facility for their assistance with the calcium imaging experiments. We thank A. Lemire, K. Aswath, and D. Kao (Janelia Quantitative Genomics) for assistance with *T. scripta* genome sequence collection and assembly. **Funding:** This work was supported by the NSF (IOS-1256675), Duke University School of Medicine (4511579), NSFC (31922084, 31872960), NSF (LR19C190001), and NKRD (2018YFD0900203). **Author contributions:** C.W., C.G., and B.C. designed the study; C.W., Y.Z., J.G.L., L.L.L., G.Q., C.G., and B.C. performed research and analyzed data; and C.W. and B.C. wrote the paper. **Competing interests:** The authors declare no conflict of interest. **Data and materials availability:** The accession number for *Kdm6b* upstream sequence is MN810324. All data needed to reproduce and evaluate the conclusions in this paper are present in the main text and supplementary materials.

SUPPLEMENTARY MATERIALS

science.sciencemag.org/content/368/6488/303/suppl/DC1
Materials and Methods
Figs. S1 to S6
Tables S1 to S3
References (33, 34)
Movie S1

6 September 2019; accepted 16 March 2020
10.1126/science.aaz4165

CORAL REEFS

Meeting fisheries, ecosystem function, and biodiversity goals in a human-dominated world

Joshua E. Cinner^{1*}, Jessica Zamborain-Mason¹, Georgina G. Gurney¹, Nicholas A. J. Graham^{1,2}, M. Aaron MacNeill³, Andrew S. Hoey¹, Camilo Mora⁴, Sébastien Villéger⁵, Eva Maire^{1,2,5}, Tim R. McClanahan⁶, Joseph M. Maina^{6,7}, John N. Kittinger⁸, Christina C. Hicks^{1,2}, Stephanie D'agata^{5,6,7,9}, Cindy Huchery¹, Michele L. Barnes¹, David A. Feary¹⁰, Ivor D. Williams¹¹, Michel Kulbicki⁹, Laurent Vigliola⁹, Laurent Wantiez⁹, Graham J. Edgar¹², Rick D. Stuart-Smith¹², Stuart A. Sandin¹³, Alison L. Green¹⁴, Maria Beger¹⁵, Alan M. Friedlander¹⁶, Shaun K. Wilson¹⁷, Eran Brokovich¹⁸, Andrew J. Brooks¹⁹, Juan J. Cruz-Motta²⁰, David J. Booth²¹, Pascale Chabanet⁹, Mark Tupper²², Sebastian C. A. Ferse²³, U. Rashid Sumaila²⁴, Marah J. Hardt²⁵, David Mouillot^{1,5}

The worldwide decline of coral reefs necessitates targeting management solutions that can sustain reefs and the livelihoods of the people who depend on them. However, little is known about the context in which different reef management tools can help to achieve multiple social and ecological goals. Because of nonlinearities in the likelihood of achieving combined fisheries, ecological function, and biodiversity goals along a gradient of human pressure, relatively small changes in the context in which management is implemented could have substantial impacts on whether these goals are likely to be met. Critically, management can provide substantial conservation benefits to most reefs for fisheries and ecological function, but not biodiversity goals, given their degraded state and the levels of human pressure they face.

At the forefront of ongoing efforts to sustain coral reef ecosystems in the current period of intense social and environmental change is an increasing need to simultaneously manage for multiple goals, including fisheries, ecosystem functioning, and biodiversity (1, 2). However, critical gaps remain in our capacity to effectively implement this type of ecosystem-based management approach in which multiple goals are pursued simultaneously (3). In particular, little is known about the context under which key goals can be simultaneously met and the degree to which local management efforts can help to meet them.

Here, we compiled data from ~1800 tropical reef sites across 41 countries, states, and ter-

ritories to examine the conditions under which reefs simultaneously support three ecological metrics reflecting key fisheries, ecological function, and biodiversity goals (4) (Fig. 1 and tables S1 and S2). These are, respectively: (i) potential stocks available for multispecies coral reef fisheries, calculated as the biomass of fishes >20 cm in total length (4) (Fig. 1 and table S2); (ii) scraping potential, reflecting a specialized ecological function performed by parrotfish that is critical for the removal of algal biomass and the provision of bare substrate for coral settlement (4, 5) (table S2); and (iii) the diversity of species traits (i.e., home range, body size, diet, diurnal activity, schooling behavior, and position in the water column), which can underpin aspects of biodiversity such as community assembly processes, ecosystem productivity, and stability (6). We measured trait diversity using a generalization of the Shannon entropy index accounting for both the dissimilarity of trait values present in a reef fish community and the spread of biomass across these trait values (4, 7) (table S2). Our analysis shows that the three metrics are not strongly related to each other ($r < 0.54$; fig. S1).

To elucidate the capacity of reefs to simultaneously support multiple goals, we first developed reference conditions for each metric to serve as benchmarks. Reference conditions (also called reference points) are a key concept in fisheries and conservation (8, 9) but are nascent in coral reef science (10). As key reference conditions, we used the top 10% value for each metric (corrected for sampling) but also included additional reference conditions (i.e., the top 5 and 20%) in the supplementary materials (4). We then set aspirational targets of 25, 50, and 75% of reference conditions. When looking

at these aspirational targets across multiple goals, we found that only 5% of reef sites simultaneously had fish biomass, parrotfish scraping, and trait diversity at 75% of reference conditions (Fig. 1D). These sites, although reasonably rare, were geographically spread throughout the Indian, Pacific, and Atlantic Ocean basins (Fig. 1D). We found that 12.5% of sites simultaneously met the 50% target, and 29.3% of sites met the 25% target (Fig. 1D).

To examine the context under which key goals can be met, we first developed a series of Bayesian hierarchical models that quantify how the three ecological metrics are related to key socioeconomic drivers of resource exploitation while controlling for environmental conditions and sampling techniques (4, 11, 12) (fig. S2 and table S3). We then used the posterior distributions from these models to calculate how the probability of simultaneously meeting multiple goals changes along a gradient of human pressure while holding other covariates constant (4) (Fig. 2 and figs. S3 and S4). We measured human pressure as the size of human populations in the surrounding seascape divided by the accessibility (in minutes of travel time squared) of our reef sites to them, an adaptation of the economic gravity model used to measure the “gravitational pull” of interactions such as trade and migration (4, 13). Human pressure displayed the most consistent negative relationships to our response variables (fig. S2). The distribution of human pressure and other key socioeconomic and environmental covariates among our surveyed reefs closely matched that of reefs globally (fig. S5). The probability of openly fished reef sites simultaneously having all three metrics declined with our measure of human pressure and the ambitiousness of the conservation target (Fig. 2A). In other words, on openly fished reefs, it is extremely unlikely that all three goals will be simultaneously met where human pressure is intense but this likelihood increases where human pressure is low, particularly for the 25 and 50% targets. There was considerable variability in how the probability of meeting individual goals changed along a gradient of human pressure (Fig. 2, B to D).

A critical gap remains in understanding the context in which different local management tools can help to simultaneously achieve key goals (14, 15). To address this, we first examined the probability of reef sites in both fully protected Marine Protected Areas (MPAs) (where fishing is prohibited) and restricted fishing areas (where there are limitations on the fishing gear used and who can access the fishing grounds) in achieving key targets for the individual and combined ecological metrics (Fig. 2, E to L). We then calculated the conservation gains from using these different forms of management along a gradient of human pressure (15) (Fig. 2, M to X). By “conservation

¹ARC Centre of Excellence for Coral Reef Studies, James Cook University, Townsville, Queensland, Australia. ²Lancaster University, Lancaster, Lancashire, UK. ³Dalhousie University, Halifax, Nova Scotia, Canada. ⁴University of Hawai'i at Manoa, Honolulu, HI, USA. ⁵University of Montpellier, Montpellier, France. ⁶Wildlife Conservation Society, Bronx, NY, USA. ⁷Macquarie University, Sydney, NSW, Australia. ⁸Conservation International, Arlington, VA, USA. ⁹ENTROPIC, IRD-UR-UNC-CNRS-IFREMER, La Réunion/New Caledonia, France. ¹⁰MRAG Ltd., London, UK. ¹¹National Oceanic and Atmospheric Administration, Washington, DC, USA. ¹²University of Tasmania, Hobart, Tasmania, Australia. ¹³University of California, San Diego, CA, USA. ¹⁴The Nature Conservancy, Carlton, Victoria, Australia. ¹⁵University of Leeds, Leeds, West Yorkshire, UK. ¹⁶National Geographic Society, Washington, DC, USA. ¹⁷Department of Biodiversity, Conservation and Attractions, Kensington, WA, Australia. ¹⁸Ministry of Energy, Jerusalem, Israel. ¹⁹University of California, Santa Barbara, CA, USA. ²⁰Universidad de Puerto Rico, Mayagüez, Puerto Rico. ²¹University of Technology, Sydney, NSW, Australia. ²²University of Portsmouth, Portsmouth, Hampshire, UK. ²³Leibniz Centre for Tropical Marine Research (ZMT), Bremen, Germany. ²⁴University of British Columbia, Vancouver, BC, Canada. ²⁵Future of Fish, Bethesda, MD, USA.

*Corresponding author. Email: joshua.cinner@jcu.edu.au

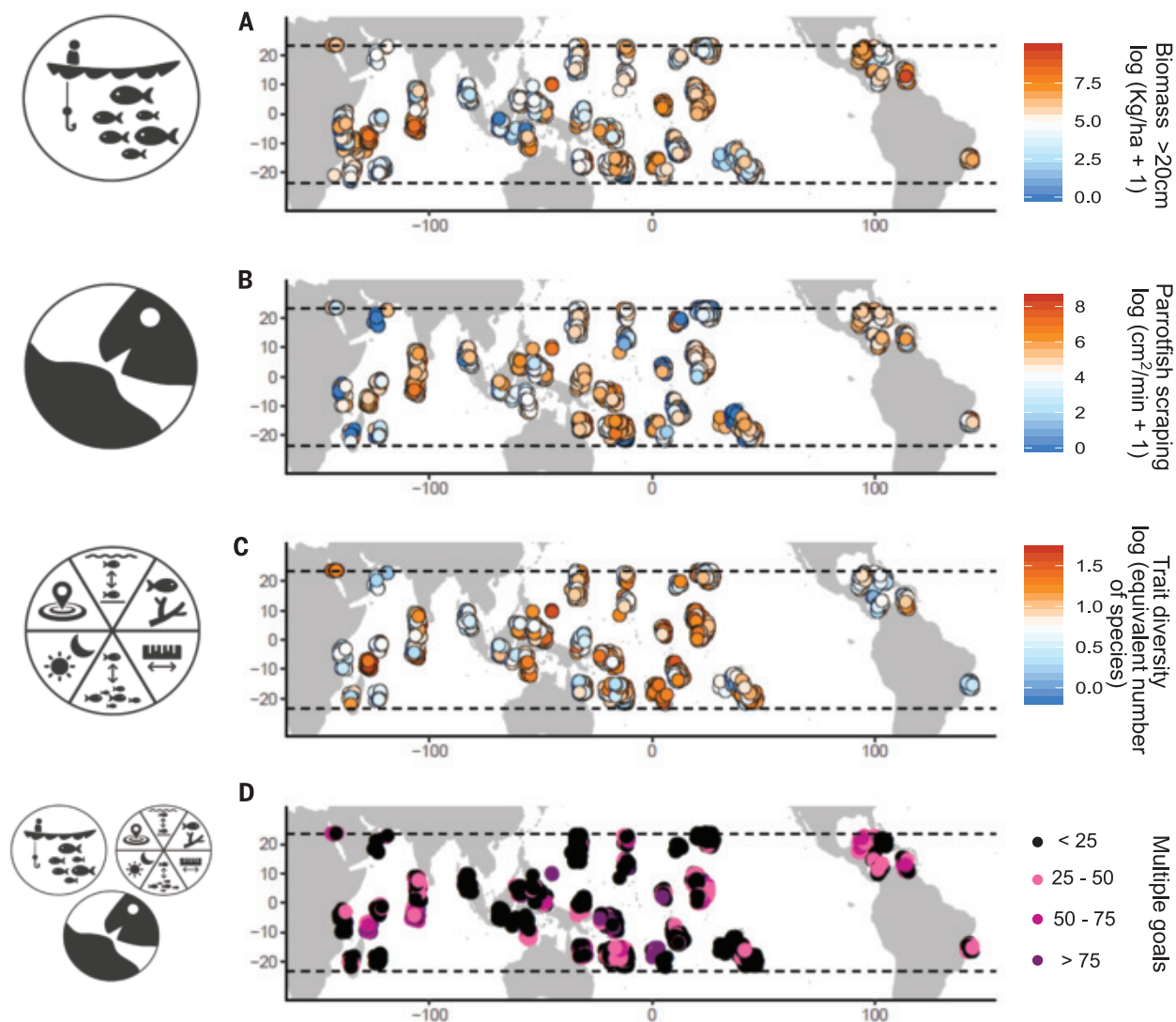


Fig. 1. Meeting multiple goals on coral reefs. Shown is the distribution of (A) the biomass of reef fish >20 cm ($n = 1798$), (B) the parrotfish scraping potential ($n = 1662$), and (C) the trait diversity ($n = 1662$), all in natural log and corrected for sampling (4). Differences in the number of sites are because one data provider collected data at the family level, which could not be used in

calculating parrotfish scraping potential or trait diversity. Parrotfishes were not detected at 31% of our reef sites (fig. S1). (D) Sites that simultaneously have fish biomass, parrotfish scraping potential, and trait diversity at >75% (purple), 50 to 75% (dark pink), 25 to 50% (light pink), and <25% (black) of reference conditions (4). Points are jittered to allow for visualization of overlapping reef sites.

gains,” we refer to the difference in probability of achieving a specific target (e.g., 25% of reference condition biomass) when fully protected MPAs or fishery restrictions are implemented relative to openly fished areas. This concept addresses the idea that contexts with maximal conservation gains highlight the best opportunities for management to have the biggest impact; conversely, implementing management in contexts with minimal conservation gains (either because goals are already being met or because they are unlikely to be met regardless of management) provides few returns for limited conservation resources (16).

Critically, we found that both fully protected MPAs and restricted fishing areas have the potential to provide conservation gains but

the context under which these gains can be maximized is highly variable depending on both the goal and target (Fig. 2, M to X). For simultaneously meeting fisheries, function, and biodiversity, maximal conservation gains are from fully protected MPAs in the lowest human pressure locations for the most ambitious target (75% of reference conditions) but as targets become less ambitious, conservation gains peak where human pressure is more intermediate (Fig. 2M). For all three targets, there are minimal conservation gains in locations where human pressure is most intense, which means that in this context, management is unlikely to help meet these goals. For each independent goal, the context under which conservation gains can be maximized varies

considerably (Fig. 2). Trait diversity is the least responsive to management, with conservation gains never reaching above 0.4.

We then simulated how the number of our openly fished sites achieving key conservation targets would change if a fully protected MPA (Fig. 3) or fisheries restrictions (Fig. S6) were implemented, given the other conditions at our reef sites. Our analysis reveals both key opportunities and constraints in the capacity for local management to simultaneously meet multiple goals. For >50% of our fished sites, the implementation of a fully protected MPA is predicted to help achieve multiple goals (Fig. 3A). Conversely, <1% of the sites starting below 25% of reference conditions are predicted to achieve the 75% of reference conditions target,

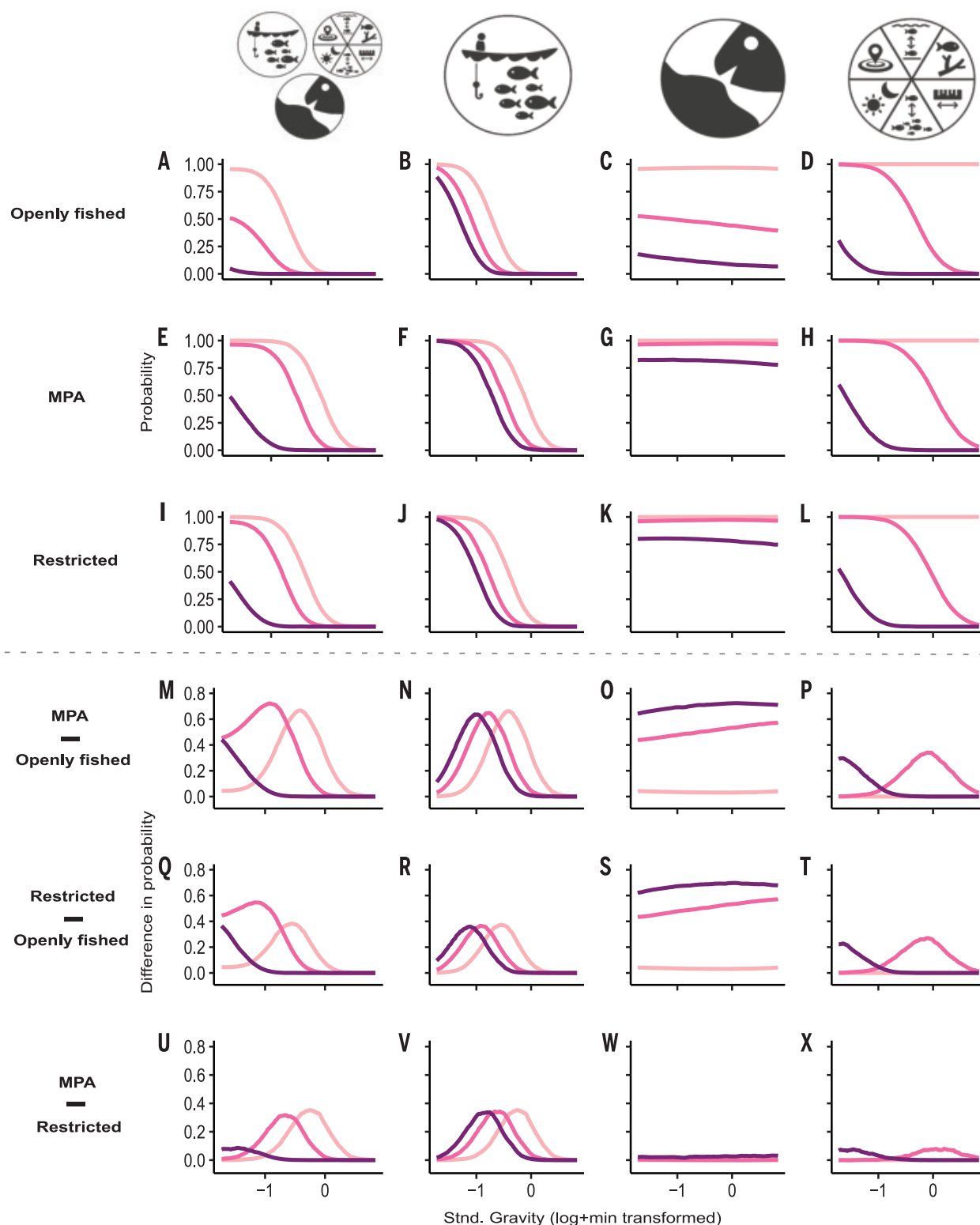


Fig. 2. Estimated probability of reef sites having 25, 50, and 75% of reference conditions (light, medium, and dark purple, respectively). Shown are the combination of fish biomass (>20 cm), parrotfish scraping potential, and trait diversity (A) and each metric (B to D, respectively) for openly fished sites along a gradient of human pressure (gravity). Separate estimates are provided for reef sites in fully protected MPAs, where fishing is prohibited (E to H), and with restricted fishing (I to L). To highlight how the potential benefits of management change along a gradient of

human pressure (gravity), we extracted the difference in the probability of achieving each target between MPAs and openly fished sites (M to P), restricted and openly fished areas (Q to T), and MPAs and restricted areas (U to X). We plotted the partial effect of the relationship between gravity and each target by setting all other continuous covariates to 0 (because they were all standardized) and all categorical covariates to their most common category (i.e., 4 to 10 m for depth, slope for habitat, standard belt transect for census method). Gravity (x axis) is standardized, with an average of 0.

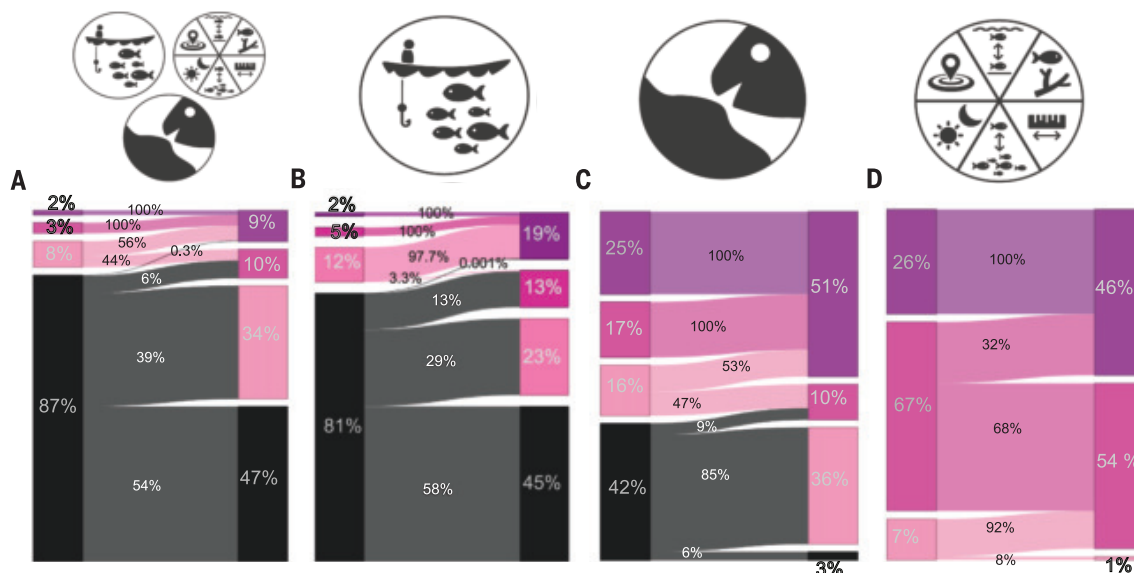


Fig. 3. Conservation target outcomes from simulating the implementation of fully protected MPAs in openly fished sites. Alluvial plots show the change in the number of sites expected to achieve key conservation targets if MPAs were implemented in our openly fished sites for (A) simultaneously meeting fish biomass,

parrotfish scraping potential, and trait diversity and (B to D) each goal, respectively. The left side of each plot shows the current conditions and the right side shows the expected conditions if MPAs were implemented. Black, <25%; light pink, 25 to 50%; dark pink, 50 to 75%; and purple, >75% of reference conditions.

highlighting how the broader seascape context may stunt MPA potential in degraded reefs (15). Indeed, more than half of the 87.4% of openly fished reefs starting at <25% of reference conditions are predicted to remain in that same category (Fig. 3A). Additionally, our analysis showed that even where fishable biomass is very low, scraping potential and trait diversity are often >25% of reference conditions (Fig. 3, B to D), a finding supported by previous research showing that herbivores and a diversity of traits can still persist on degraded reefs (17).

In situations in which fishing prohibitions are in direct conflict with achieving certain fisheries goals, other forms of management may be necessary (18). We found that fisheries restrictions provide a similar, but typically lower magnitude, pattern of conservation gains than fully protected MPAs, particularly for achieving the combined goal and fisheries goal (Fig. 2, Q to X, and fig S6). For parrotfish scraping potential, fishing restrictions provide the same conservation gains as MPAs, providing multiple ways to achieve that specific goal (Fig. 2W).

Our findings provide guidance on what can be realistically achieved with various forms of local management regarding key fisheries, ecological function, and biodiversity goals on coral reefs. We highlight key pros and cons of placing management in different areas by demonstrating how potential conservation gains not only vary by goal, but are also strongly dependent on both the ambitiousness of the target and the context (Fig. 2 and figs. S3 and S4). In particular, the potential for local manage-

ment to help in meeting goals is strongly related to the amount of human pressure in the surrounding seascape (Fig. 2 and S2). A key finding is that conservation gains tend to change nonlinearly with human pressure, which means that relatively small changes in the context in which management is implemented could have big impacts on whether key goals are likely to be met (Fig. 2, M to X). This not only has important implications for the placement of new MPAs, but is also relevant to how future socioeconomic changes such as infrastructure development and population growth may affect the efficacy of reef conservation. However, the impacts of these changes could potentially be buffered by making management more effective, for example, by leveraging insights about using social norms and cognitive biases to improve compliance (19, 20) and learning lessons about key practices and processes from locations that have defied expectations of global reef degradation (12, 21). Our global analysis makes clear the limitations of local management, especially in promoting certain aspects of biodiversity such as trait diversity. Although international action on climate change will be crucial for ensuring a future for coral-dominated reefs (1, 2), effective management will also be crucial for sustaining reefs and the millions of livelihoods that depend on them.

REFERENCES AND NOTES

1. T. P. Hughes *et al.*, *Nature* **546**, 82–90 (2017).
2. A. V. Norström *et al.*, *Front. Ecol. Environ.* **14**, 490–498 (2016).
3. E. K. Pikitch *et al.*, *Science* **305**, 346–347 (2004).
4. Materials and methods are available as supplementary materials.

5. Y.-M. Bozec, S. O'Farrell, J. H. Bruggemann, B. E. Luckhurst, P. J. Mumby, *Proc. Natl. Acad. Sci. U.S.A.* **113**, 4536–4541 (2016).
6. J. E. Duffy, J. S. Lefcheck, R. D. Stuart-Smith, S. A. Navarrete, G. J. Edgar, *Proc. Natl. Acad. Sci. U.S.A.* **113**, 6230–6235 (2016).
7. A. Chao *et al.*, *Ecol. Monogr.* **89**, e01343 (2019).
8. M. A. MacNeil, *Environ. Conserv.* **40**, 297–301 (2013).
9. G. M. Mace, R. Lande, *Conserv. Biol.* **5**, 148–157 (1991).
10. T. R. McClanahan *et al.*, *Proc. Natl. Acad. Sci. U.S.A.* **108**, 17230–17233 (2011).
11. H. J. Geist, E. F. Lambin, *Bioscience* **52**, 143–150 (2002).
12. J. E. Cinner *et al.*, *Nature* **535**, 416–419 (2016).
13. J. E. Anderson, *Annu. Rev. Econ.* **3**, 133–160 (2011).
14. R. S. Steneck, P. J. Mumby, C. MacDonald, D. B. Rasher, G. Stoyle, *Sci. Adv.* **4**, eaao5493 (2018).
15. J. E. Cinner *et al.*, *Proc. Natl. Acad. Sci. U.S.A.* **115**, E6116–E6125 (2018).
16. P. J. Ferraro, S. K. Pattanayak, *PLOS Biol.* **4**, e105 (2006).
17. J. P. W. Robinson *et al.*, *Nat. Ecol. Evol.* **3**, 183–190 (2019).
18. R. Hilborn *et al.*, *Ocean Coast. Manage.* **47**, 197–205 (2004).
19. B. J. Bergseth, M. Roscher, *Mar. Policy* **89**, 132–141 (2018).
20. J. Cinner, *Science* **362**, 889–890 (2018).
21. G. Post, J. Geldmann, *Conserv. Biol.* **32**, 576–583 (2018).
22. J. Cinner, Data for: Meeting fisheries, ecosystem function, and biodiversity goals in a human-dominated world. James Cook University (2020); <https://doi.org/10.25903/5e61a7f08ae39>.
23. J. Zamborain-Mason, Code for: Meeting fisheries, ecosystem function, and biodiversity goals in a human-dominated world. Zenodo (2020); <https://zenodo.org/record/3697928#.Xnu-VdLtwkw>.

ACKNOWLEDGMENTS

We thank S. Pardede and Blue Ventures for data contributions. **Funding:** J.E.C. is supported by the Australian Research Council (CE140100020, FT160100047), the Pew Charitable Trust, and the CGIAR Research Program on Fish Agri-Food Systems (FISH) led by WorldFish. N.A.J.G. is supported through a Royal Society University Research Fellowship (UF140691). This research was partly funded through the 2017–2018 Belmont Forum and BiodivErsA REEF-FUTURES project under the BiodivScen ERA-Net COFUND program and with the funding organizations ANR, DFG, NSF, and NSERC. This study has been partly funded by the PRISTINE and APEX Total Foundation, Government of New Caledonia projects, and associated French Oceanographic Cruises (<https://doi.org/10.17600/14004500>, <https://doi.org/10.17600/14003600>, <https://doi.org/10.17600/13100060>, and <https://doi.org/10.17600/13100070>). **Author contributions:** J.E.C. conceived

of the study with support from D.M., C.M., E.M., N.A.J.G., T.R.M., J.N.K., C.C.H., M.L.B., M.A.M., and C.C.H.; J.Z.-M., G.G.G., J.E.C., D.M., and E.M. developed and implemented the analyses; J.E.C. led the writing of the manuscript. All other authors contributed to data collection and made substantive contributions to the text.

Competing interests: The authors declare no competing interests.

Data and materials availability: Data are permanently archived

on the James Cook University Tropical Data Hub (22) and the code is archived at Zenodo (23).

SUPPLEMENTARY MATERIALS

science.sciencemag.org/content/368/6488/307/suppl/DC1
Materials and Methods

Tables S1 to S7

Figs. S1 to S4

References (24–59)

13 May 2019; accepted 18 March 2020

10.1126/science.aax9412

TOPOLOGICAL OPTICS

Topological funneling of light

Sebastian Weidemann^{1*}, Mark Kremer^{1*}, Tobias Helbig², Tobias Hofmann², Alexander Stegmaier², Martin Greiter², Ronny Thomale², Alexander Szameit^{1†}

Dissipation is a general feature of non-Hermitian systems. But rather than being an unavoidable nuisance, non-Hermiticity can be precisely controlled and hence used for sophisticated applications, such as optical sensors with enhanced sensitivity. In our work, we implement a non-Hermitian photonic mesh lattice by tailoring the anisotropy of the nearest-neighbor coupling. The appearance of an interface results in a complete collapse of the entire eigenmode spectrum, leading to an exponential localization of all modes at the interface. As a consequence, any light field within the lattice travels toward this interface, irrespective of its shape and input position. On the basis of this topological phenomenon, called the “non-Hermitian skin effect,” we demonstrate a highly efficient funnel for light.

For any physical system, the exchange of energy with the environment is inevitable. For this reason, non-Hermiticity is a ubiquitous property. Although such an exchange is often considered undesirable, recent work (1–3) has shown that tailored gain and loss distributions within a non-Hermitian system can lead to intriguing features such as nonorthogonal eigenmodes (4), exceptional points (5, 6), and peculiar transport transitions (7). Several promising applications have been proposed, such as exceptional-point enhanced sensing (8) or mode-selective laser cavities (9, 10). In photonics, the successful integration of optical gain and loss has enabled the experimental demonstration of a plethora of promising non-Hermitian features (11–13) such as loss-induced transparency (14) or unidirectional invisibility (5), providing a route to develop a new generation of optical devices. When dealing with periodic systems, the approximation of infinitely expanded settings is often used, although it is never fulfilled in any experiment. This approximation is commonly justified because in sufficiently large systems, any distant boundaries are expected to introduce only minor and especially local changes in the mode spectrum, hence not causing appreciable deviations from the infinite system. A prominent example of this approximation is the topological boundary mode in the Hermitian Su-

Schrieffer-Heeger (SSH) model (15). Besides the possible appearance of this mode, the eigenmode spectrum of the bulk in an SSH lattice does not change substantially when introducing a boundary. However, it has been proposed that in certain lattices where the source of non-Hermiticity derives not from gain and loss but from anisotropic coupling, the presence of an interface can cause all eigenmodes to localize at this interface. This phenomenon, known as the “non-Hermitian skin effect” (16–20), is currently the key element in a lively debate about the validity of the bulk-boundary correspondence (BBC) in non-Hermitian topological systems (16, 17, 21–23). The BBC demands the coexistence of a bulk and a boundary, where quantities derived from the bulk can be used to predict properties of the boundary, which is a crucial concept of topological physics.

Here, we demonstrate the non-Hermitian skin effect in a photonic lattice. Our experimental implementation is based on light propagation in coupled optical fiber loops (24) and relies on the fact that light propagation in this setup obeys the same equations that describe a linear one-dimensional photonic lattice. The ability to control the optical properties of the fiber loops allows us to realize the required anisotropic coupling, also referred to as nonreciprocal coupling. By connecting lattices with different directions of the anisotropy, a funneling effect for light occurs (Fig. 1A), which relies on the non-Hermitian skin effect and its nontrivial topological properties induced by the anisotropic coupling.

In our work, we compare two models. The Hermitian SSH model, which consists of a chain of nearest-neighbor coupled lattice sites with alternating coupling constants (15), is shown in Fig. 1B. Every second coupling is chosen to be different but isotropic, as indicated by the different shades of the orange arrows. The skin effect model (Fig. 1C) also features an alternating coupling, but this coupling is anisotropic, as the hopping from one site to its neighbor is different from the hopping from its neighbor back to itself. This anisotropy, indicated by differently sized black arrows, causes a non-Hermiticity, even though there is neither gain nor loss in the model.

Because of translational invariance, the eigenmodes in both lattices are delocalized when periodic boundary conditions are applied (see supplementary materials). When introducing an interface in the SSH lattice

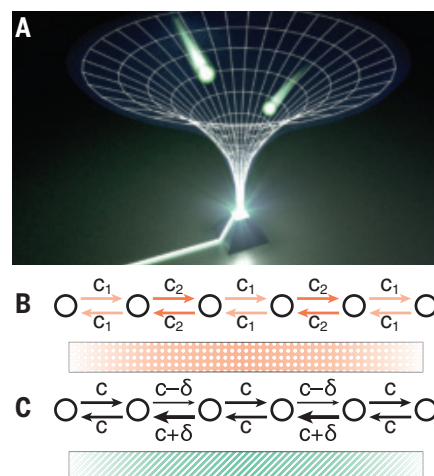


Fig. 1. General model. (A) Illustration of the light-gathering concept, which reassembles a funnel for light. A lattice guides wave packets toward a funnel opening, where light is collected. (B) Linear chain of nearest-neighbor coupled sites with coupling strengths c_1 and c_2 . The modulation of coupling strength is indicated by the dotted orange ribbon below the chain. (C) Linear chain of nearest-neighbor coupled sites with coupling strength $c + \delta$ in the left direction and $c - \delta$ in the right direction for every second coupling. This anisotropic modulation is indicated by the ribbon with angled green stripes.

¹Institute of Physics, University of Rostock, 18059 Rostock, Germany. ²Department of Physics and Astronomy, Julius-Maximilians-Universität Würzburg, Am Hubland, 97074 Würzburg, Germany.

*These authors contributed equally to this work.

†Corresponding author. Email: alexander.szameit@uni-rostock.de

by inverting the ratio c_1/c_2 at some position (illustrated in Fig. 2A, where the inverted ribbon indicates the inverted coupling ratio), only one mode localizes at the interface, which is well known as a topological SSH mode (15). All other modes, however, remain delocalized; that is, far away from the interface, the modal amplitudes on the individual sites remain essentially unchanged (Fig. 2B).

The situation changes when an interface is introduced in the non-Hermitian lattice with anisotropic hopping. The interface is created by flipping the direction of the anisotropy at some position, illustrated by the mirrored pattern in Fig. 2C. The entire eigenmode spectrum

is found to collapse, and all eigenmodes are exponentially localized at the interface (Fig. 2D). All former bulk modes transform into boundary modes, making the notion of bulk, in relation to edge modes, invalid, and hence making less certain the applicability of the BBC. This behavior is in stark contrast to the Hermitian case, where sufficiently far from an interface its influence on the bulk mode structure is negligible. The localization of the eigenmodes in the non-Hermitian lattice has further profound consequences: No matter where the lattice is excited, every signal travels toward the interface. In the context of photonics, this means that any light signal that impinges on

the lattice is guided toward the interface and remains there. These findings suggest the opportunity to realize a non-Hermitian light funnel, which may form the basis for intriguing applications. Note that the presence of an interface does not change the propagation until the light field reaches the interface.

Here, we study the non-Hermitian skin effect by using a modified version of a one-dimensional discrete-time quantum walk, also called a light walk (24). The dynamics are governed by the evolution in Eqs. 1 and 2,

$$u_n^{m+1} = G_u[\cos(\beta)u_{n+1}^m + i\sin(\beta)v_{n+1}^m]\exp(i\varphi_u) \quad (1)$$

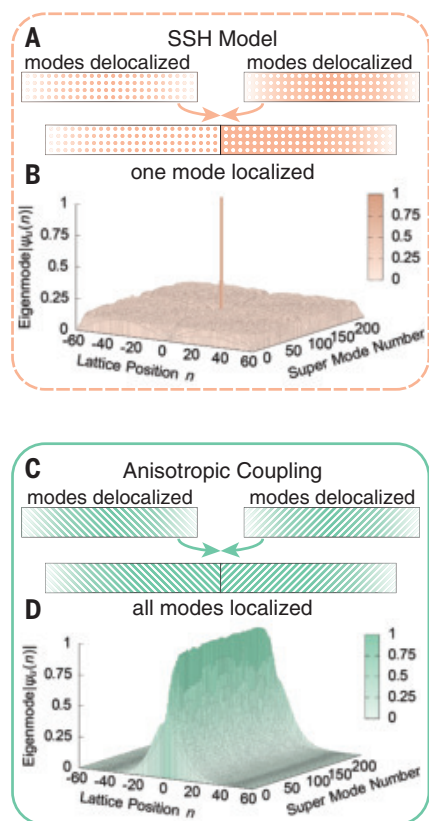


Fig. 2. Eigenmodes of systems with interfaces.

(A) An interface is formed with two lattices with SSH modulation (as in Fig. 1C), where the inverted ribbon indicates the inverted coupling ratio. (B) The eigenmodes of the system shown in (A) are plotted for a lattice with 120 lattice sites. (C) An interface is formed with two lattices with anisotropic modulation (as in Fig. 1D), where the inverted ribbon indicates the inverted anisotropy $\delta \rightarrow -\delta$. (D) The eigenmodes of the system shown in (C) are plotted for a lattice with 120 lattice sites. For the calculation of both spectra, we used periodic boundary conditions to avoid terminations. Note that for the case of the SSH modulation, the topological boundary mode appearing at the other boundary is not shown for the sake of clarity.

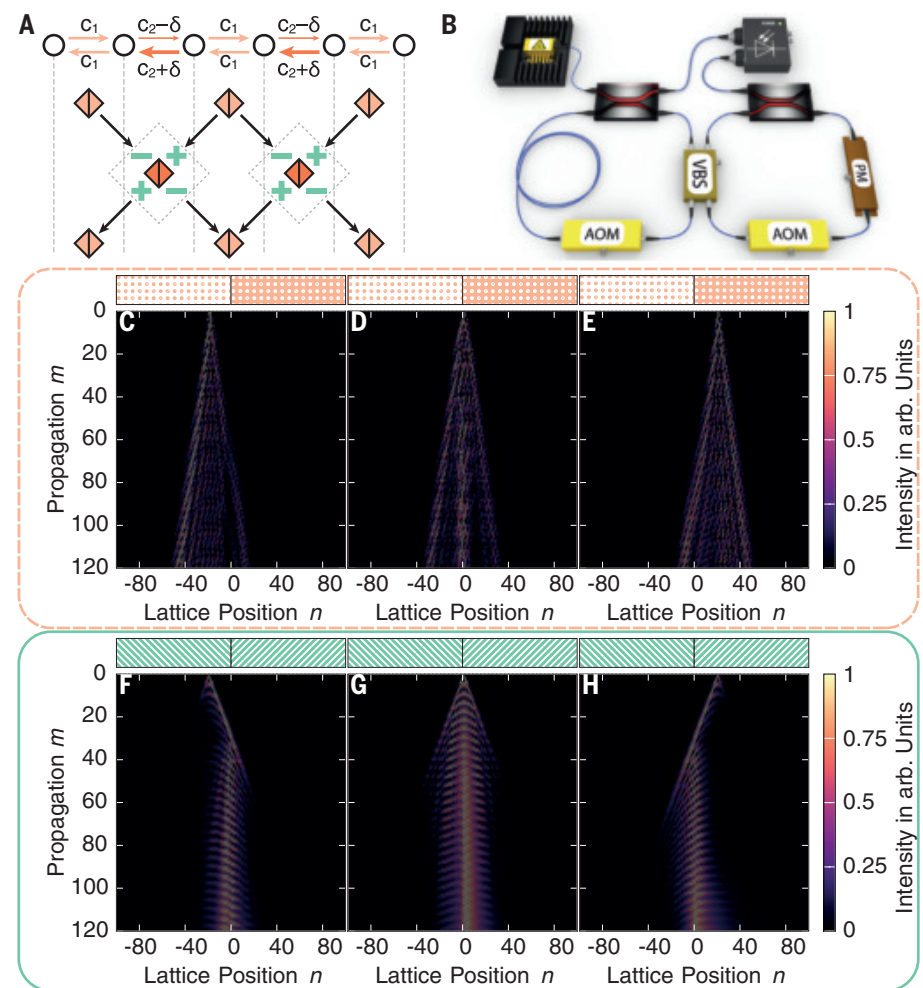


Fig. 3. Experimental setup and measurements. (A) Mapping from the models shown in Fig. 1, B and C, to a light walk. The different shades of orange represent different coupling strengths (coupling ratios); the green plus and minus signs represent amplitude modulations. Note that in the experiments, either the coupling modulation (SSH) or the amplitude modulation (skin effect) is applied; the two are never combined. (B) The experimental setup consists of two fiber loops connected by a variable beamsplitter (VBS). One loop is connected to a pulsed laser source. The propagation of pulses through the loop arrangement can be mathematically mapped to a propagation through a mesh lattice of beamsplitter cubes (A). An acousto-optical modulator (AOM) and a phase modulator (PM) respectively manipulate the amplitudes and phases of the pulses. (C to E) Propagation through the photonic lattice with the SSH modulation for three different excitations, which are at the interface and to its left and right. (F to H) Propagation through the photonic lattice with the anisotropic modulation for three different excitations, which are at the interface and to its left and right.

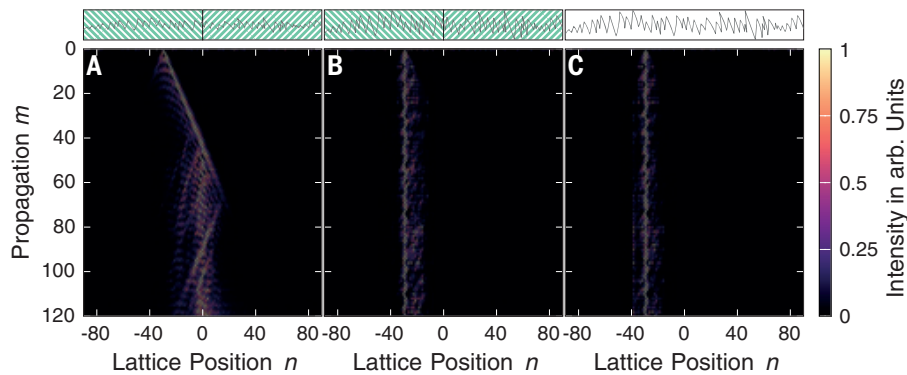


Fig. 4. Propagation in the presence of disorder. (A) Propagation in the photonic lattice with the anisotropic modulation and weak phase disorder $W = 0.1\pi$, with the excitation on the left side of the interface. (B) Same as in (A) but with strong phase disorder $W = 0.74\pi$. (C) Same as in (B) but without the anisotropic modulation.

$$v_n^{m+1} = G_v[i \sin(\beta) u_{n-1}^m + \cos(\beta) v_{n-1}^m] \quad (2)$$

where u_n^m denotes the amplitude at lattice position n and time step m on left-moving paths, and v_n^m denotes the corresponding amplitude on right-moving paths. The parameter $\beta = \beta(n, m)$ characterizes the splitting ratio of the beamsplitter. The beamsplitter mediates the hopping between lattice sites, as depicted in Fig. 3A. For instance, $\beta = \pi/4$ corresponds to a homogeneous lattice of 50:50 beamsplitter. The ability to adjust the splitting β at will allows us to control the coupling between individual sites. In the evolution described by Eqs. 1 and 2, the common quantum walk dynamics are extended by $G_{u,v} = G_{u,v}(n, m)$, which captures a non-Hermitian attenuation and amplification within the lattice, which in turn enables the realization of an anisotropic coupling as described below. Additionally, a phase modulation $\exp(i\varphi_u)$ allows the implementation of arbitrary real parts of the potential. In our experiments, optical pulses propagate in two unequally long fiber loops connected by a variable beamsplitter, with which we control the splitting β (Fig. 3B). We use acousto-optical modulators (AOM) to manipulate amplitudes via $G_{u,v}$ and a phase modulator (PM) to control $\exp(i\varphi_u)$. The phase modulation is used for studying the non-Hermitian skin effect in the presence of disorder. (See supplementary materials for a detailed treatment of how the light propagation in the fiber loops maps onto the SSH model and the non-Hermitian skin effect model.)

We start our experiments by probing the Hermitian SSH model that is realized by implementing two different coupling ratios β_1 and β_2 , as indicated in Fig. 3A by the different shades of the orange arrows and beamsplitter cubes. To characterize the transport in the lattice, we excite it at three different positions: left from the interface (Fig. 3C), directly at the interface (Fig. 3D), and right from the inter-

face (Fig. 3E). Clearly, any excitation populates extended modes that lead to a spreading of the wave packet, even at the interface. This is consistent with the spectrum of eigenmodes of this lattice shown in Fig. 2B, where only one localized (topological) mode exists at the interface, whereas all other modes remain delocalized and spread over the entire lattice.

However, this situation changes when turning to non-Hermitian contributions. To experimentally realize the non-Hermitian skin effect model, we require anisotropic coupling that is achieved by the introduction of amplification or attenuation depending on the hopping direction, as shown by the green plus and minus signs, respectively, in Fig. 3A. This modulation is equivalent to replacing an isotropic beamsplitter with its anisotropic counterpart (see supplementary materials). Such a modulation was already used in previous works to study PT-symmetric Bloch oscillations (25). Moreover, it reassembles the Hatano-Nelson model (26), where an imaginary vector potential translates to an anisotropic coupling. To realize the interface, we combine two lattices with inverted modulation with respect to the amplification and attenuation (see supplementary materials). In contrast to the Hermitian case, a substantial change in the propagation dynamics can be observed when probing the non-Hermitian lattice: Because all eigenmodes are localized at the interface (Fig. 2D), any excitation results in a light flow that is directed toward the interface. This is true when exciting left from the interface (Fig. 3F), at the interface (Fig. 3G), and right from the interface (Fig. 3H). This is exactly the manifestation of the non-Hermitian skin effect. The presence of an interface forces the eigenmodes to collapse at the interface, and no delocalized modes remain in the bulk of the lattice. Consequently, any light excitation somewhere in the lattice shows a funnel-like behavior,

such that light localizes exclusively along the interface. This behavior can be linked to the topological properties of the underlying lattice, as the direction of the anisotropic coupling is connected to a winding number (see supplementary materials) (27). Therefore, the interface between the lattices is connecting two regions of different winding, thereby serving as an explanation for the localization.

In the next set of experiments, we explore the robustness of non-Hermitian skin effect in the presence of disorder (26). It is interesting to study the interplay of these two effects, as disorder induces Anderson localization (28), which—as a long-range interference effect—might be suppressed by the non-Hermitian modulation. We address this problem by adding a uniformly distributed phase disorder $\varphi_u \in [-W, W]$ in space n upon the amplitudes u_n^m , which is experimentally realized by using a fiber-based phase modulator (Fig. 3B). In a first step, we combine the anisotropic modulation with a weak disorder $W = 0.1\pi$ (Fig. 4A). In this case, the light still moves toward the interface, demonstrating the robustness of the non-Hermitian skin effect against a certain degree of disorder. If, on the other hand, strong disorder $W = 0.74\pi$ is applied, one can observe that the wave packet is arrested and no movement toward the interface occurs (Fig. 4B). This behavior is equivalent to disorder-induced Anderson localization without anisotropic coupling (29), as shown in Fig. 4C. These results clearly show that the non-Hermitian modulation in our lattice does not prevent Anderson localization as an interference effect. In other words, a continuous transition from skin effect localization at the funnel opening to Anderson localization at the excitation site takes place (see supplementary materials). This behavior can be explained in topological terms using the winding number. Whereas for low disorder the winding number can still be defined, for strong disorder a topological transition occurs because the winding number vanishes (27). In other words, the funneling effect is robust against disorder until a topological transition occurs. The transition from the skin effect localization at the interface toward Anderson localization at the injection site does clearly show that, counterintuitively, anisotropic coupling and the presence of a boundary do not necessarily lead to a funneling effect.

Our findings provide a route for using anisotropic coupling and nonreciprocity for unusual non-Hermitian phenomena in sophisticated applications, such as light harvesting and enhanced optical sensitivity. In this vein, coupled optical fiber loops are a flexible and scalable platform for investigating nonreciprocal lattices with anisotropic coupling. Because our approach is not limited to

the specific experimental platform and is based only on the wavelike properties of light, it might also be applicable to other areas of research using different experimental environments.

REFERENCES AND NOTES

- C. M. Bender, S. Boettcher, *Phys. Rev. Lett.* **80**, 5243–5246 (1998).
- R. El-Ganainy *et al.*, *Nat. Phys.* **14**, 11–19 (2018).
- R. El-Ganainy, K. G. Makris, D. N. Christodoulides, Z. H. Musslimani, *Opt. Lett.* **32**, 2632–2634 (2007).
- C. E. Rüter *et al.*, *Nat. Phys.* **6**, 192–195 (2010).
- A. Regensburger *et al.*, *Nature* **488**, 167–171 (2012).
- M. A. Miri, A. Alù, *Science* **363**, eaar7709 (2019).
- T. Eichelkraut *et al.*, *Nat. Commun.* **4**, 2533 (2013).
- H. Hodaei *et al.*, *Nature* **548**, 187–191 (2017).
- L. Feng, Z. J. Wong, R.-M. Ma, Y. Wang, X. Zhang, *Science* **346**, 972–975 (2014).
- H. Hodaei, M.-A. Miri, M. Heinrich, D. N. Christodoulides, M. Khajavikhan, *Science* **346**, 975–978 (2014).
- M. Kremer *et al.*, *Nat. Commun.* **10**, 435 (2019).
- F. Klauck *et al.*, *Nat. Photonics* **13**, 883–887 (2019).
- L. Xiao *et al.*, *Nat. Phys.* **13**, 1117–1123 (2017).
- A. Guo *et al.*, *Phys. Rev. Lett.* **103**, 093902 (2009).
- W. P. Su, J. R. Schrieffer, A. J. Heeger, *Phys. Rev. Lett.* **42**, 1698–1701 (1979).
- C. H. Lee, R. Thomale, *Phys. Rev. B* **99**, 201103 (2019).
- S. Yao, Z. Wang, *Phys. Rev. Lett.* **121**, 086803 (2018).
- A. Ghatak, M. Brandenbourger, J. van Wezel, C. Coullais, arXiv 1907.11619 [cond-mat.mes-hall] (26 July 2019).
- T. Helbig *et al.*, arXiv 1907.11562 [cond-mat.mes-hall] (26 July 2019).
- L. Xiao *et al.*, *Nat. Phys.* **10**, 1038/s41567-020-0836-6 (2020).
- A. Ghatak, T. Das, *J. Phys. Condens. Matter* **31**, 263001 (2019).
- Y. Xiong, *J. Phys. Commun.* **2**, 035043 (2018).
- T. E. Lee, *Phys. Rev. Lett.* **116**, 133903 (2016).
- A. Schreiber *et al.*, *Phys. Rev. Lett.* **104**, 050502 (2010).
- M. Wimmer, M.-A. Miri, D. Christodoulides, U. Peschel, *Sci. Rep.* **5**, 17760 (2015).
- N. Hatano, D. R. Nelson, *Phys. Rev. Lett.* **77**, 570–573 (1996).
- Z. Gong *et al.*, *Phys. Rev. X* **8**, 031079 (2018).
- P. W. Anderson, *Phys. Rev.* **109**, 1492–1505 (1958).
- A. Schreiber *et al.*, *Phys. Rev. Lett.* **106**, 180403 (2011).
- S. Weidemann, M. Kremer, A. Szameit, Data Set for Topological Funneling of Light, Rostock University Publication Server (2020); doi:10.18453/rosdok_id00002571.

ACKNOWLEDGMENTS

We thank M. Wimmer for very useful discussions. **Funding:** The authors acknowledge funding from the Deutsche Forschungsgemeinschaft (BL 574/13-1, SZ 276/19-1, SZ 276/20-1, SZ 276/9-2, and 258499086-SFB 1170), the Würzburg-Dresden Cluster of Excellence on Complexity and Topology in Quantum Matter *ct.qmat* (39085490-EXC 2147), and the Alfred Krupp von Bohlen und Halbach Foundation. **Author contributions:** M.K. developed the theory and S.W. performed the experiments on the photonic mesh lattice. R.T. and A.S. supervised the project. All authors discussed the results and co-wrote the paper. The manuscript reflects the contributions of all authors. **Competing interests:** The authors declare that they have no competing interests. **Data and materials availability:** All experimental data and any related experimental background information not mentioned in the text can be found at the Rostock University Publication Server repository (30).

SUPPLEMENTARY MATERIALS

science.sciencemag.org/content/368/6488/311/suppl/DC1
Materials and Methods
Supplementary Text
Figs. S1 to S9

16 October 2019; accepted 3 February 2020
Published online 26 March 2020
10.1126/science.aaz8727

DROUGHT

Large contribution from anthropogenic warming to an emerging North American megadrought

A. Park Williams^{1*}, Edward R. Cook¹, Jason E. Smerdon¹, Benjamin I. Cook^{1,2}, John T. Abatzoglou^{3,4}, Kasey Bolles¹, Seung H. Baek^{1,5}, Andrew M. Badger^{6,7,8}, Ben Livneh^{6,9}

Severe and persistent 21st-century drought in southwestern North America (SWNA) motivates comparisons to medieval megadroughts and questions about the role of anthropogenic climate change. We use hydrological modeling and new 1200-year tree-ring reconstructions of summer soil moisture to demonstrate that the 2000–2018 SWNA drought was the second driest 19-year period since 800 CE, exceeded only by a late-1500s megadrought. The megadrought-like trajectory of 2000–2018 soil moisture was driven by natural variability superimposed on drying due to anthropogenic warming. Anthropogenic trends in temperature, relative humidity, and precipitation estimated from 31 climate models account for 47% (model interquartiles of 35 to 105%) of the 2000–2018 drought severity, pushing an otherwise moderate drought onto a trajectory comparable to the worst SWNA megadroughts since 800 CE.

Southwestern North America (SWNA; western United States and northern Mexico: 30°N to 45°N, 105°W to 125°W) has been anomalously dry and warm in the 21st century relative to the 20th century (*1–3*). The 21st-century drought severity has been reflected in reduced snowpack (*4*), reduced river flow and lake levels (*5*), declines in ground-water availability (*6, 7*), shifts in agricultural activities (*8*), forest drought stress (*9*), increased wildfire activity (*10*), and reduced vegetation carbon uptake (*11*).

Paleoclimatic proxies indicate that SWNA experienced many severe swings in hydroclimate before the observed period. In particular, tree-ring records reveal several megadrought events during the Medieval era and subsequent centuries (~850–1600 CE) that dwarfed all droughts in the following 400 years in intensity and duration (*12*). These megadroughts were likely associated with cool eastern tropical Pacific sea surface temperatures, which promote an atmospheric wave train that blocks Pacific storms from reaching SWNA (*13–15*). Any attribution of recent drought to anthropogenic climate change must consider this region's capacity for large internal hydroclimatic variability (*16, 17*). Although 21st-century drought conditions have been clearly promoted by natural Pacific Ocean variability (*18–20*), certain

elements are also consistent with projected drying due to anthropogenic radiative forcing (*21–23*). Cold-season precipitation deficits across the southwestern United States and northern Mexico are consistent with modeled poleward expansion of the subtropics, albeit with large uncertainties in models and observations (*24, 25*). Observed warming since the early 1900s is more uniformly consistent with model simulations of anthropogenic trends, decreasing SWNA runoff and warm-season soil moisture by reducing snowpack and increasing evaporative demand (*26–28*). Models project that 21st-century SWNA summer droughts will intensify owing to declining spring precipitation in the southern portion of the region and continued warming-induced reductions of summer runoff and soil moisture (*22–24, 29*).

Here, we use 1586 tree-ring chronologies to reconstruct 0- to 200-cm summer (June to August) soil moisture and snow water equivalent (hereinafter termed “soil moisture” collectively) anomalies on a 0.5° latitude-longitude grid back to 800 CE across western North America [*(30)*; Fig. 1]. Soil-moisture anomalies are standardized relative to the entire 800–2018 CE period, and the magnitude of negative anomalies indicates drought severity. The soil-moisture record targeted in the reconstruction covers 1901–2018 and is referred to as Noah-calibrated soil moisture (*31*). Because true observations of soil moisture do not exist, this soil-moisture record is modeled based on observed climate. Monthly precipitation, temperature, humidity, wind speed, and radiation data are used to force a bucket-type water-balance model with intermonthly persistence tuned to emulate the Community Noah land-surface model (*32*) (fig. S1). The reconstruction method is the same method that has been used to develop previous continental drought atlases (*16*). Reconstruction skill is evaluated

¹Lamont-Doherty Earth Observatory of Columbia University, Palisades, NY 10964, USA. ²NASA Goddard Institute of Space Studies, New York, NY 10025, USA. ³Department of Geography, University of Idaho, Moscow, ID 83844, USA. ⁴Management of Complex Systems Department, UC Merced, Merced, CA 95343, USA. ⁵Department of Earth and Environmental Sciences, Columbia University, New York, NY 10027, USA. ⁶Cooperative Institute for Research in Environmental Sciences, University of Colorado Boulder, Boulder, CO 80302, USA. ⁷Universities Space Research Association, Columbia, MD 21046, USA. ⁸NASA Goddard Space Flight Center, Greenbelt, MD, USA 20771, USA. ⁹Civil, Environmental, and Architectural Engineering, University of Colorado Boulder, Boulder, CO 80309, USA.

*Corresponding author. Email: williams@ldeo.columbia.edu

as the squared Pearson's correlation (R^2) between observations during the 1901–1983 calibration period and out-of-sample reconstruction values that were calculated by using leave-10-out cross-validation (30). Reconstruction skill is highly significant ($P < 0.01$) across much of SWNA (Fig. 1A). The cross-validated R^2 for the SWNA regionally averaged reconstruction is 0.86 back to 1700 CE (Fig. 1B). Skill reduces back in time owing to loss of tree-ring chronologies but remains above 0.73, even when using the subset of tree-ring chronologies extending back to 800 CE (Fig. 1B).

We evaluated 19-year running means of reconstructed and observed soil-moisture anomalies for explicit contextualization of the dry 2000–2018 period. Running-mean values are assigned to the final year in each 19-year window. During 800–2018 CE, there were 40 prolonged drought events with more than one negative SWNA 19-year running-mean soil-moisture anomaly. We rank the severity of each prolonged drought event based on the event's most negative 19-year soil-moisture anomaly. Definitions of megadrought vary, but in North America, they generally refer to multidecade drought events that contained

periods of very high severity and were longer lasting than any event observed in the 19th or 20th centuries (12). Here we identify the strongest SWNA megadroughts in the reconstruction as the prolonged drought events that contained at least one 19-year anomaly that was 0.25 standard deviations (σ) more negative than any observed in the 20th century. The regionally averaged SWNA reconstruction (Fig. 1C) reveals four megadroughts that satisfy this criterion in the late 800s, mid-1100s, 1200s, and late 1500s.

The 21st-century prolonged drought event (still ongoing as of 2020 given our definition) registered its first negative SWNA 19-year anomaly in 1996–2014, and its most negative anomaly (2000–2018) was -0.74σ ; the late-1500s megadrought was the only reconstructed event with a more negative 19-year soil-moisture anomaly than that in 2000–2018 (Fig. 1C). The most severe SWNA 19-year soil moisture anomaly during the late-1500s megadrought was -0.80σ in 1575–1593. The 2000–2018 drought severity was nevertheless within the uncertainty ranges of several other 19-year drought severities, and the late-1500s event contained six 19-year anomalies more nega-

tive than that in 2000–2018. Within SWNA, local drought rankings during the 21st-century event were generally not as high as the ranking of the regionally averaged drought (Fig. 1D). Only 37% of SWNA experienced a local 19-year drought severity that ranked among the top five since 800 CE, a smaller aerial extent of high-ranking drought than occurred during any of the four most severe reconstructed megadroughts (Fig. 1D). Notably, the four megadroughts in Fig. 1 were longer than the 21st-century drought thus far, giving grid cells more chances to register high-ranking 19-year drought severities. Conversely, the 21st-century drought is the only event in which all SWNA grid cells registered at least one below-average 19-year soil-moisture anomaly.

The above results are consistent across alternate reconstructions with longer calibration periods that extend beyond 1983 (using fewer tree-ring records), with 2000–2018 always ranking second driest (fig. S2A). The above results are also consistent with alternate reconstructions of the self-calibrated Palmer Drought Severity Index [scPDSI; (33)] and soil moisture simulated by the Variable Infiltration Capacity hydrological model [VIC; (34)], but

Fig. 1. Summer soil-moisture reconstruction for SWNA. (A) Cross-

validated reconstruction skill (R^2) using tree-ring records that extend to 800 and 1700 CE (green contour: $R^2 \geq 0.5$; gray: reconstruction does not extend to 800 CE; yellow box: SWNA). (B) Time-resolved cross-validated R^2 of the SWNA regional reconstruction. The inset shows observations versus cross-validated reconstructions during the 1901–1983 calibration interval using tree-ring records extending back to 800 and 1700 CE. (C) Time series of reconstructed (red) and observed (blue) 19-year running-mean standardized SWNA soil moisture (gray: 95% reconstruction confidence interval; blue horizontal line: 2000–2018 mean; pink and green shading: the five drought and pluvial periods with the most-negative and most-positive 19-year soil-moisture anomalies, respectively).

(D) Maps of the local rank of the most negative 19-year anomaly to occur during each of the five drought events highlighted in (C). In the maps, the aqua color indicates no negative 19-year anomaly, and numbers in the top left corners indicate the rank of the most negative regionally averaged 19-year anomaly during each drought event.

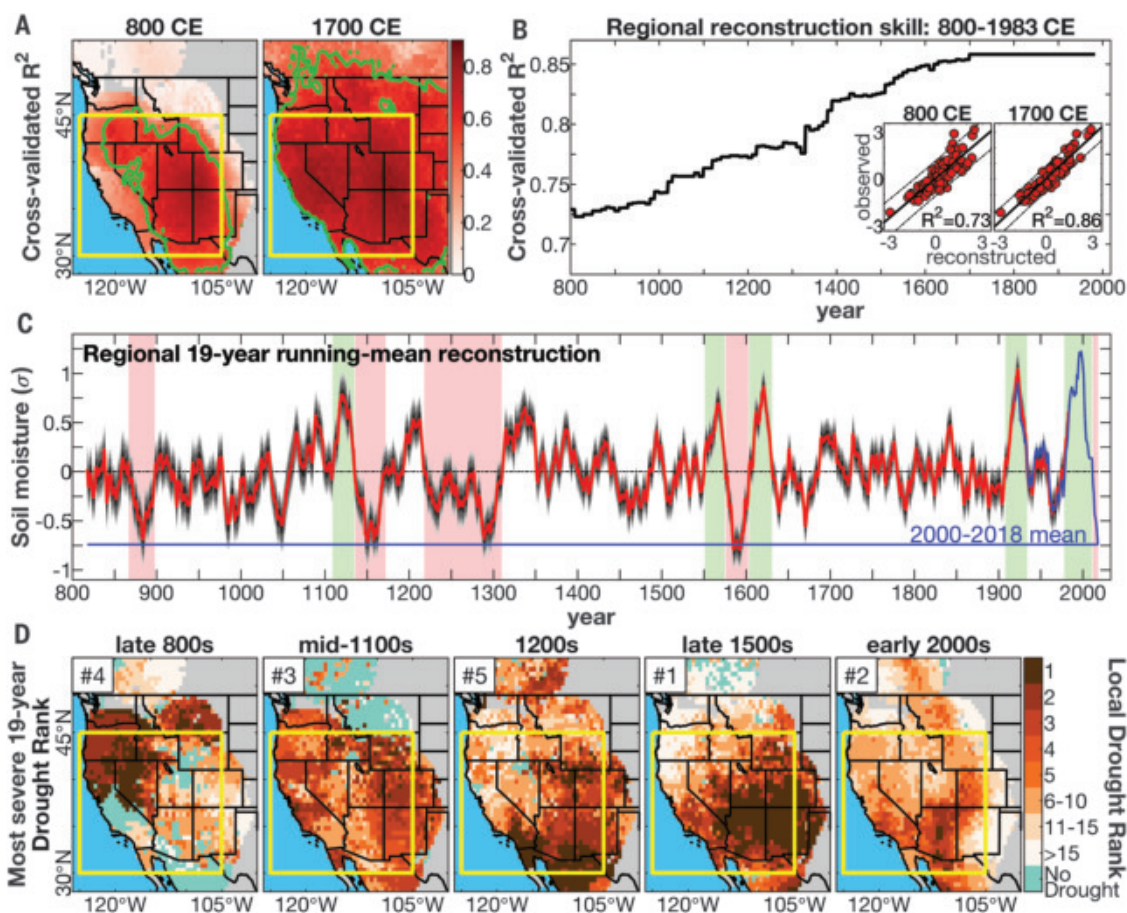
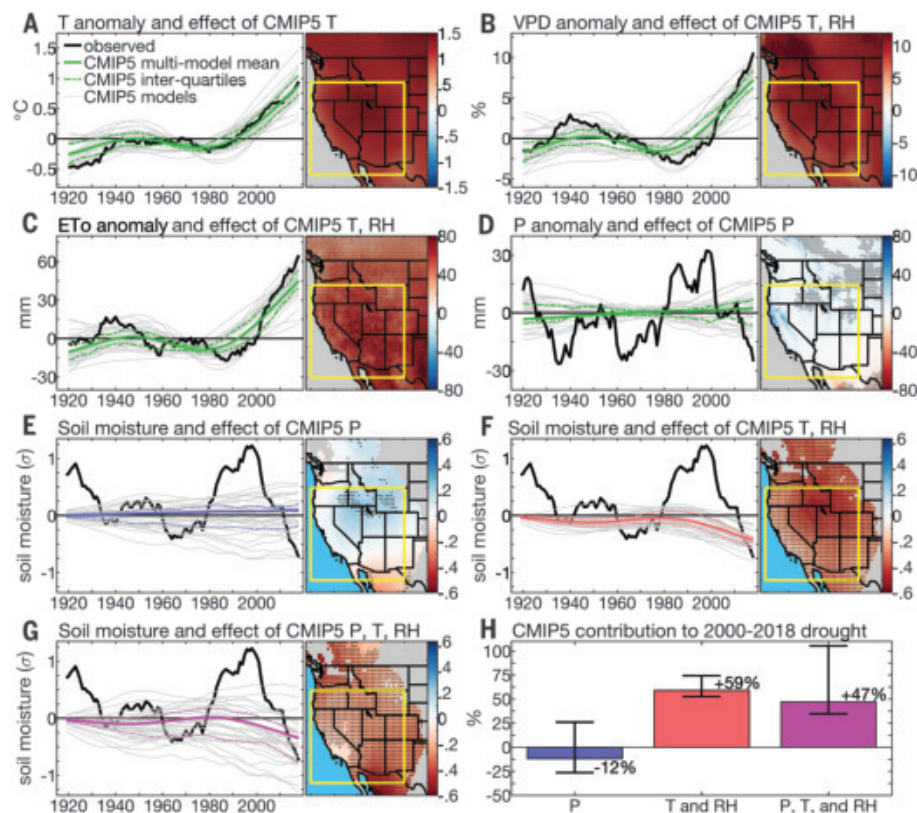
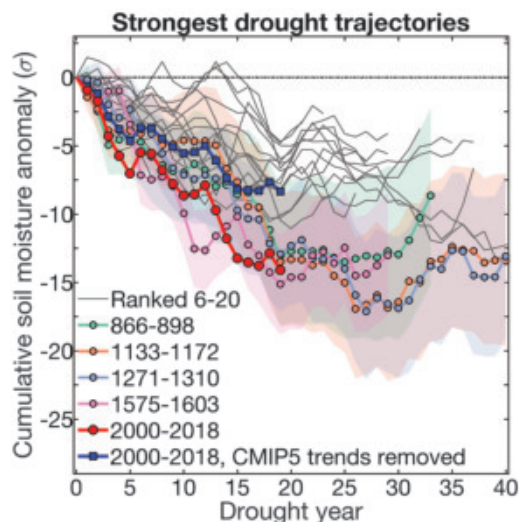


Fig. 2. Effects of anthropogenic climate trends.

(A to G) Time series plots showing the 19-year running-mean observed anomalies (black lines) in SWNA (yellow box in maps) for mean annual temperature (T) (A), mean annual vapor pressure deficit (VPD) (B), annual reference evapotranspiration (ET_o) (C), annual precipitation (P) (D), and soil moisture [(E) to (G)]. Solid and dotted colored lines represent 19-year running-mean CMIP5 multimodel mean and IQ trends, respectively (gray lines: trends from 31 models). CMIP5 trends are evaluated for T, T, and relative humidity (RH). In (E) to (G), CMIP5 trends show contributions to observed soil-moisture anomalies since 1901. The maps show CMIP5 multimodel mean contributions to 2000–2018 anomalies (dots: >75% model agreement on sign; gray: masked out because reconstruction does not extend to 800 CE). (H) Percent contribution of CMIP5 (bars) multimodel mean climate trends to the 2000–2018 SWNA soil-moisture anomaly (whiskers: model IQs). Anomalies are relative to 1921–2000 in (A) to (D) and 800–2018 CE in (E) to (G).

**Fig. 3. Development of the most severe 19-year droughts since 800 CE.**

Time series of cumulative SWNA summer soil-moisture anomalies for the 20 prolonged droughts with the most-negative 19-year soil-moisture anomalies. The drought periods analyzed here begin 18 years before the most-negative 19-year anomaly. The dark blue line shows 2000–2018 cumulative anomalies after removing CMIP5 multimodel mean climate trends. The shaded regions represent 95% confidence intervals for the four reconstructed megadroughts shown with the light colored lines.



the reconstruction targeting VIC soil moisture has considerably less skill than the reconstructions targeting Noah-calibrated soil moisture or scPDSI [(30); fig. S2, B and C]. The alternate reconstructions of scPDSI and VIC soil moisture agree with our primary reconstruction in placing 2000–2018 within the two most severe prolonged SWNA droughts in at least 1200 years (fig. S2, B and C).

To address the contribution of anthropogenic climate change, we evaluated 1901–2018 trends in precipitation, temperature, and relative humidity simulated with 31 climate mod-

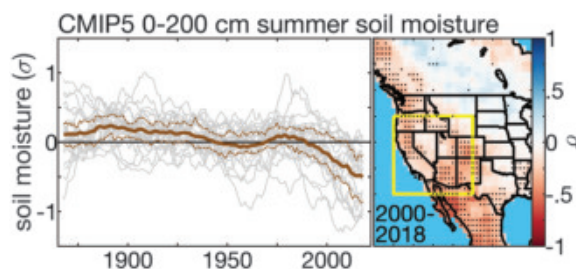
els in the fifth phase of the Coupled Model Intercomparison Project (CMIP5). During 2000–2018, the multimodel mean anthropogenic warming in SWNA was 1.2°C [model interquartiles (IQs): 1.0° to 1.5°C], with all models simulating warming (Fig. 2A). Anthropogenic warming increased the annual mean atmospheric vapor-pressure deficit by 9.6% (IQs: 8.4 to 11.3%), which increased the mean annual total evaporative demand (as estimated by the Penman-Monteith reference evapotranspiration) by 59 mm, or 4.5% (IQs: 53 to 73 mm, 4.1 to 5.5%) (Fig. 2, B and C). Models disagree

on anthropogenic precipitation trends, with a slight multimodel mean increase in the SWNA annual total (6 mm, 1.2%; IQs: –6 to 12 mm, –2.5 to 2.2%) (Fig. 2D).

In Fig. 2, E to H, we estimate the effect of these anthropogenic climate trends on soil moisture as the difference between observed soil-moisture anomalies and those recalculated after removing model-estimated anthropogenic trends from the observed climate records [e.g., (3, 10)]. The positive effect of the slight multimodel mean precipitation increase in northern SWNA (Fig. 2E) is overwhelmed by the spatially ubiquitous drying effect of increasing vapor-pressure deficit simulated by all models (Fig. 2F). Notably, the high intermodel spread in anthropogenic precipitation trends causes high spread among estimated soil-moisture trends (Fig. 2, D and E), and the true uncertainty may be even larger than suggested here owing to systematic model biases (25, 35). Combined, the multimodel mean estimates of anthropogenic trends in precipitation, temperature, and humidity force a 2000–2018 SWNA regionally averaged summer soil-moisture anomaly of –0.35 σ (IQs: –0.26 to –0.78 σ) (Fig. 2G). This accounts for 47% (IQs: 35 to 105%) of the observed anomaly (Fig. 2H). Of the 31 CMIP5 models considered, 28 (90%) simulated climate trends that promoted SWNA drought during 2000–2018 based on our water-balance estimates. Twenty-five models (81%) indicated that this altered baseline in mean climate

Fig. 4. Trends in summer soil moisture simulated directly from coupled models. (Left) CMIP5

19-year running-mean 0- to 200-cm summer soil-moisture anomalies for historical (1850–2005) and 21st-century (2006–2018) scenarios (standardization relative to 1850–2018; gray represents 26 models; brown represents multi-model mean, IQs). **(Right)** Multimodel mean anomalies in 2000–2018 (dots represent >75% model agreement on sign; yellow box indicates SWNA).



accounted for >25% of the observed 2000–2018 SWNA soil-moisture anomaly. This net anthropogenic drying effect is corroborated by the tree-ring records themselves. Reconstruction of an alternate summer soil-moisture record recalculated after removal of CMIP5 ensemble mean temperature and relative humidity trends reduces validation skill because the recalculated soil moisture is too wet relative to the reconstruction in recent decades (fig. S3).

When repeated for scPDSI and VIC soil moisture, the CMIP5 multimodel mean contribution to SWNA 2000–2018 drought severity was 47 and 30%, respectively (fig. S4). The weaker anthropogenic drying effect in the VIC simulation was primarily due to desert areas: (i) In high desert, warming reduces winter snow sublimation and increases infiltration; (ii) where vegetation is sparse, increased winter precipitation and minimal transpiration enhance deep moisture storage; and (iii) in more vegetated desert areas, soils dry to the wilting point in summer regardless of anthropogenic climate trends, erasing all soil-moisture memory of warming-induced drying in spring (supplementary text S1 and figs. S5 to S10). Outside of deserts, and particularly in forested areas, the VIC model simulates summer soil drying driven by anthropogenic warming through enhanced evapotranspiration and early loss of snowpack (fig. S11).

Given known disagreement among land-surface models in deserts where small anomalies are substantial relative to dry climatologies (36) and the inherently better representation of forested areas by the tree-ring network, we repeated our reconstructions to target forested areas only. All forest-only reconstructions still estimate 2000–2018 to be among the two driest 19-year drought periods since 800 CE for SWNA (fig. S12, A to C). Considering SWNA forested areas only, the contribution of anthropogenic climate trends to 2000–2018 drought severity increased slightly for Noah-calibrated soil moisture and scPDSI (to 57 and 51%, respectively) and dramatically (to 83%) for VIC soil moisture (fig. S12, D to F). This stronger anthropogenic effect in the VIC simulation is likely due to the additional effect of warming-driven snowpack loss, which

is not accounted for directly in the Noah-calibrated soil moisture or scPDSI. The VIC simulations indicate a steady warming-driven reduction to SWNA spring snowpack over the past century that accounts for the majority of the simulated spring snowpack anomaly in 2000–2018 (fig. S13).

The 2000–2018 drought was preceded by the wettest 19-year period (1980–1998) in at least 1200 years (Fig. 1C). Climate models project enhanced precipitation variability across much of the globe as a result of anthropogenic climate change, and this includes a slight 21st-century trend toward greater decadal precipitation swings in SWNA (37). This tendency is also apparent in model simulations of summer 0- to 200-cm soil moisture, but this simulated effect does not emerge until the second half of the 21st century (fig. S14). Regardless of the anthropogenic impact on multidecadal variability, the 1980–2018 wet-to-dry transition was hastened by the background drying forced from anthropogenic warming.

Figure 3 shows that the 2000–2018 drought was on a megadrought-like trajectory throughout its development. In the absence of anthropogenic climate trends, 2000–2018 would still rank among the 11 most severe prolonged droughts in the reconstruction (dark blue line in Fig. 3), but anthropogenic warming was critical for placing 2000–2018 on a trajectory consistent with the most severe past megadroughts. These results are robust regardless of the drought metric used or whether only forested areas are considered (fig. S15).

The results above do not account for the possibility that increased atmospheric carbon dioxide concentration ($[CO_2]$) has ameliorated soil-water loss by allowing plants to reduce stomatal conductance and use water more efficiently through increased surface resistance (r_s) to transpiration (38). Although the effects of enhanced $[CO_2]$ on vegetation and surface water fluxes are highly uncertain (39), we explore how our results would be affected by a r_s response to $[CO_2]$ as simulated by current Earth system models. Repeating our study with an adjusted calculation of reference evapotranspiration that assumes the CMIP5 multimodel mean r_s response to $[CO_2]$ (40) reduces 2000–2018 drought severity by about 20% (to -0.61σ).

This prolonged drought ranks fifth in the revised reconstruction, still in line with the megadroughts (fig. S16). Even with the assumed increase in r_s , 30% of the 2000–2018 drought's severity is attributed to anthropogenic climate trends, with 81% of models simulating some degree of anthropogenic drying. Importantly, the potency of the $[CO_2]$ effect on r_s varies by a factor of three among CMIP5 models (40), highlighting considerable uncertainty in this effect.

Our relatively simple hydrological modeling approach also does not account for coupled land-atmosphere interactions or dynamic vegetation responses to climate. It has been argued that hydrological effects of anthropogenic climate change are better addressed with coupled Earth system models that directly simulate land-atmosphere coupling and vegetation responses to changes in climate and $[CO_2]$ (38, 41). Figure 4 shows that, of the 26 CMIP5 models with soil-moisture data available for historical and 21st-century climate scenarios, 23 (88%) simulate negative soil-moisture anomalies in SWNA during 2000–2018, with a multimodel mean of -0.50σ (IQs: -1.38 to -0.17σ) relative to a 1850–2018 CE baseline. Because each model simulation has its own internal climate variability, intermodel agreement on dry soil during 2000–2018 arises from the common anthropogenic forcing. The multimodel mean 2000–2018 anomaly derived directly from CMIP5 soil-moisture simulations is somewhat larger than the anthropogenic effect of -0.41σ found when the previously calculated anthropogenic effect shown in Fig. 2G is rescaled relative to 1850–2018 CE. The stronger anthropogenic soil drying simulated by the CMIP5 models is likely due to reduced spring-summer mountain snowpack and enhanced vegetation water use caused by lengthened growing seasons and increased leaf area due to CO_2 fertilization (39). Notably, the simulated ability for vegetation to survive and perpetuate these modeled soil-moisture declines may be unrealistic because current Earth system models inadequately represent nutrient and moisture limitations on vegetation activity (42–44).

The tree-ring record serves as an ominous reminder that natural climate variability can drive SWNA megadroughts that are as severe and longer than the 21st-century drought thus far. The atmosphere and ocean anomalies that drove past megadroughts very likely dwarfed those that occurred during 2000–2018, but superposition of the 2000–2018 climate dynamics on background anthropogenic soil drying put an otherwise moderately severe soil-moisture drought onto a trajectory characteristic of the megadroughts of 800–1600 CE. Critical to the megadrought-like trajectory of the 21st-century event were enhanced evaporative demand, early snowpack loss, and a broad spatial extent, all promoted by anthropogenic

warming. Natural variability may very well end the early 21st-century drought in the coming years, and this transition may be under way after a wet 2019. However, our work demonstrates that the magnitude of background anthropogenic soil drying is already substantial relative to the range of natural multidecadal variability. Furthermore, anthropogenic global warming and its drying influence in SWNA are likely still in their infancy. The magnitude of future droughts in North America and elsewhere will depend greatly on future rates of anthropogenic greenhouse gas emissions globally. The effects of future droughts on humans will be further dependent on sustainable resource use because buffering mechanisms such as ground water and reservoir storage are at risk of being depleted during dry times.

REFERENCES AND NOTES

- K. M. Andreadis, E. A. Clark, A. W. Wood, A. F. Hamlet, D. P. Lettenmaier, *J. Hydrometeorol.* **6**, 985–1001 (2005).
- M. Hoerling *et al.*, *Bull. Am. Meteorol. Soc.* **95**, 269–282 (2014).
- A. P. Williams *et al.*, *Geophys. Res. Lett.* **42**, 6819–6828 (2015).
- P. W. Mote, S. Li, D. P. Lettenmaier, M. Xiao, R. Engel, *NPJ Clim. Atmos. Sci.* **1**, 2 (2018).
- M. Xiao, B. Udall, D. P. Lettenmaier, *Water Resour. Res.* **54**, 6739–6756 (2018).
- M. Rodell *et al.*, *Nature* **557**, 651–659 (2018).
- C. C. Faunt, M. Sneed, J. Traum, J. T. Brandt, *Hydrogeol. J.* **24**, 675–684 (2016).
- R. Howitt, J. Medellín-Azuara, D. MacEwan, J. Lund, D. A. Sumner, “Economic analysis of the 2014 drought for California agriculture” (UC Davis Center for Watershed Sciences, Davis, CA, 2014).
- A. P. Williams *et al.*, *Nat. Clim. Change* **3**, 292–297 (2013).
- J. T. Abatzoglou, A. P. Williams, *Proc. Natl. Acad. Sci. U.S.A.* **113**, 11770–11775 (2016).
- C. R. Schwalm *et al.*, *Nat. Geosci.* **5**, 551–556 (2012).
- B. I. Cook *et al.*, *Wiley Interdiscip. Rev. Clim. Change* **7**, 411–432 (2016).
- R. Seager *et al.*, *Quat. Sci. Rev.* **26**, 2322–2336 (2007).
- B. I. Cook *et al.*, *J. Geophys. Res. Atmos.* **123**, 11307–11320 (2019).
- N. J. Steiger *et al.*, *Sci. Adv.* **5**, eaax0087 (2019).
- E. R. Cook *et al.*, *J. Quaternary Sci.* **25**, 48–61 (2010).
- C. A. Woodhouse, D. M. Meko, G. M. MacDonald, D. W. Stahle, E. R. Cook, *Proc. Natl. Acad. Sci. U.S.A.* **107**, 21283–21288 (2010).
- T. L. Delworth, F. Zeng, A. Rosati, G. A. Vecchi, A. T. Wittenberg, *J. Clim.* **28**, 3834–3845 (2015).
- R. Seager, M. Ting, *Curr. Clim. Change Rep.* **3**, 141–149 (2017).
- F. Lehner, C. Deser, I. R. Simpson, L. Terray, *Geophys. Res. Lett.* **45**, 6251–6261 (2018).
- R. Seager *et al.*, *Science* **316**, 1181–1184 (2007).
- B. I. Cook, T. R. Ault, J. E. Smerdon, *Sci. Adv.* **1**, e1400082 (2015).
- T. R. Ault, J. S. Mankin, B. I. Cook, J. E. Smerdon, *Sci. Adv.* **2**, e1600873 (2016).
- M. Ting, R. Seager, C. Li, H. Liu, N. Henderson, *J. Clim.* **31**, 4265–4279 (2018).
- R. Seager *et al.*, *Nat. Clim. Change* **9**, 517–522 (2019).
- P. Barnett *et al.*, *Science* **319**, 1080–1083 (2008).
- G. J. McCabe, D. M. Wolock, G. T. Pederson, C. A. Woodhouse, S. McAffee, *Earth Interact.* **21**, 1–14 (2017).
- P. C. D. Milly, K. A. Dunne, *Science* **367**, 1252–1255 (2020).
- D. R. Cayan *et al.*, *Proc. Natl. Acad. Sci. U.S.A.* **107**, 21271–21276 (2010).
- Materials and methods are available as supplementary materials.
- A. P. Williams *et al.*, *J. Geophys. Res. Atmos.* **122**, 10888–10905 (2017).
- M. B. Ek *et al.*, *J. Geophys. Res. Atmos.* **108**, 8851 (2003).
- N. Wells, S. Goddard, M. J. Hayes, *J. Clim.* **17**, 2335–2351 (2004).
- X. Liang, D. P. Lettenmaier, E. F. Wood, S. J. Burges, *J. Geophys. Res. Atmos.* **99**, 14415–14428 (1994).
- I. R. Simpson, R. Seager, M. Ting, T. A. Shaw, *Nat. Clim. Change* **6**, 65–70 (2016).
- R. D. Koster *et al.*, *J. Clim.* **22**, 4322–4335 (2009).
- A. G. Pendergrass, R. Knutti, F. Lehner, C. Deser, B. M. Sanderson, *Sci. Rep.* **7**, 17966 (2017).

- A. L. S. Swann, F. M. Hoffman, C. D. Koven, J. T. Randerson, *Proc. Natl. Acad. Sci. U.S.A.* **113**, 10019–10024 (2016).
- J. S. Mankin, R. Seager, J. E. Smerdon, B. I. Cook, A. P. Williams, *Nat. Geosci.* **12**, 983–988 (2019).
- Y. Yang, M. L. Roderick, S. Zhang, T. R. McVicar, R. J. Donohue, *Nat. Clim. Change* **9**, 44–48 (2019).
- A. Berg, J. Sheffield, *Curr. Clim. Change Rep.* **4**, 180–191 (2018).
- W. K. Smith *et al.*, *Nat. Clim. Change* **6**, 306–310 (2015).
- W. R. Wieder, C. C. Cleveland, W. K. Smith, K. Todd-Brown, *Nat. Geosci.* **8**, 441–444 (2015).
- W. Yuan *et al.*, *Sci. Adv.* **5**, eaax1396 (2019).
- P. Williams, Large contribution from anthropogenic warming to an emerging North American megadrought (NCEI Accession 0209529), NOAA National Centers for Environmental Information (2020); doi:10.25921/2vbe-8092.

ACKNOWLEDGMENTS

This work would not be possible without the tree-ring data from many gracious contributors, largely through the International Tree-Ring Databank hosted by the National Oceanic and Atmospheric Administration (NOAA). Thanks to R. Seager for helpful feedback. **Funding:** Funding came from NSF AGS-1703029 (A.P.W., E.R.C., and K.B.), AGS-1602581 (J.E.S., A.P.W., and E.R.C.), AGS-1805490 (J.E.S.), and AGS-1243204 (J.E.S.); NASA 16-MAP16-0081 (A.P.W.

and B.I.C.); NOAA NA15OAR4310144 and NA16OAR4310132 (A.M.B. and B.L.); and Columbia University’s Center for Climate and Life (A.P.W.). This work utilized the Summit supercomputer, which is supported by the National Science Foundation (awards ACI-1532235 and ACI-1532236), the University of Colorado Boulder, and Colorado State University. **Author contributions:** The study was conceived by A.P.W., E.R.C., J.E.S., B.I.C., J.T.A., and S.H.B. Methods were developed by all authors. Analysis was carried out by A.P.W., J.T.A., K.B., and A.M.B. The original manuscript was written by A.P.W., and all authors edited subsequent drafts. **Competing interests:** The authors declare no competing interests. **Data and materials availability:** The observed and reconstructed climate and drought data are available at (45). LDEO contribution number is 8392.

SUPPLEMENTARY MATERIALS

science.sciencemag.org/content/368/6488/314/suppl/DC1
Materials and Methods
Supplementary Text
Figs. S1 to S21
Tables S1 and S2
References (46–90)

23 October 2019; accepted 10 March 2020
10.1126/science.aaz9600

CATALYSIS

A dual light-driven palladium catalyst: Breaking the barriers in carbonylation reactions

Gerardo M. Torres*, Yi Liu*, Bruce A. Arndtsen†

Transition metal-catalyzed coupling reactions have become one of the most important tools in modern synthesis. However, an inherent limitation to these reactions is the need to balance operations, because the factors that favor bond cleavage via oxidative addition ultimately inhibit bond formation via reductive elimination. Here, we describe an alternative strategy that exploits simple visible-light excitation of palladium to drive both oxidative addition and reductive elimination with low barriers. Palladium-catalyzed carbonylations can thereby proceed under ambient conditions, with challenging aryl or alkyl halides and difficult nucleophiles, and generate valuable carbonyl derivatives such as acid chlorides, esters, amides, or ketones in a now-versatile fashion. Mechanistic studies suggest that concurrent excitation of palladium(0) and palladium(II) intermediates is responsible for this activity.

The capacity of transition metals to cleave and forge covalent bonds via the fundamental operations of oxidative addition and reductive elimination is a cornerstone of catalysis. Examples with palladium or nickel alone include such prominent reactions as cross coupling (1, 2), C–H bond functionalization (3), hydrogenation (4), reduction (5), or oxidation (6, 7) and are exploited across the spectrum of pharmaceutical and fine chemical synthesis. By manipulating the features that govern the basic steps (Fig. 1A), researchers over the past several decades have optimized catalysts for each of these reactions. Unfortunately, there are also intrinsic limitations to this cycle that diminish its utility. These arise from the forward and reverse sequences of the successive operations at the metal, in which steric or electronic features of the catalyst that favor one half-cycle often inhibit the

other. Balancing these steps is thus a critical feature of reaction design that may lower overall catalyst activity or constrain substrate scope. Moreover, it is often not possible to perform catalysis that requires both difficult oxidative addition and reductive elimination steps (8), which blocks direct routes to many important classes of products.

These features are well illustrated in palladium-catalyzed carbonylation reactions. Carbonylation offers, at least in principle, one of the most efficient routes to assemble valuable carbonyl compounds from feedstock reagents, including such ubiquitous functionalities as esters, amides, or ketones (9, 10). However, the inhibitory influence of CO coordination to palladium on oxidative addition requires increased temperatures relative to the analogous cross-coupling chemistry and restricts the use of many key substrates, such as less-reactive, simple alkyl halides (11). These issues can be partially addressed by catalyst design. For example, efforts to promote the use of alkyl halides in carbonylations have been described

Department of Chemistry, McGill University, 801 Sherbrooke St. W., Montreal, QC H3A 0B8, Canada.

*These authors contributed equally to this work.

†Corresponding author. Email: bruce.arndtsen@mcgill.ca

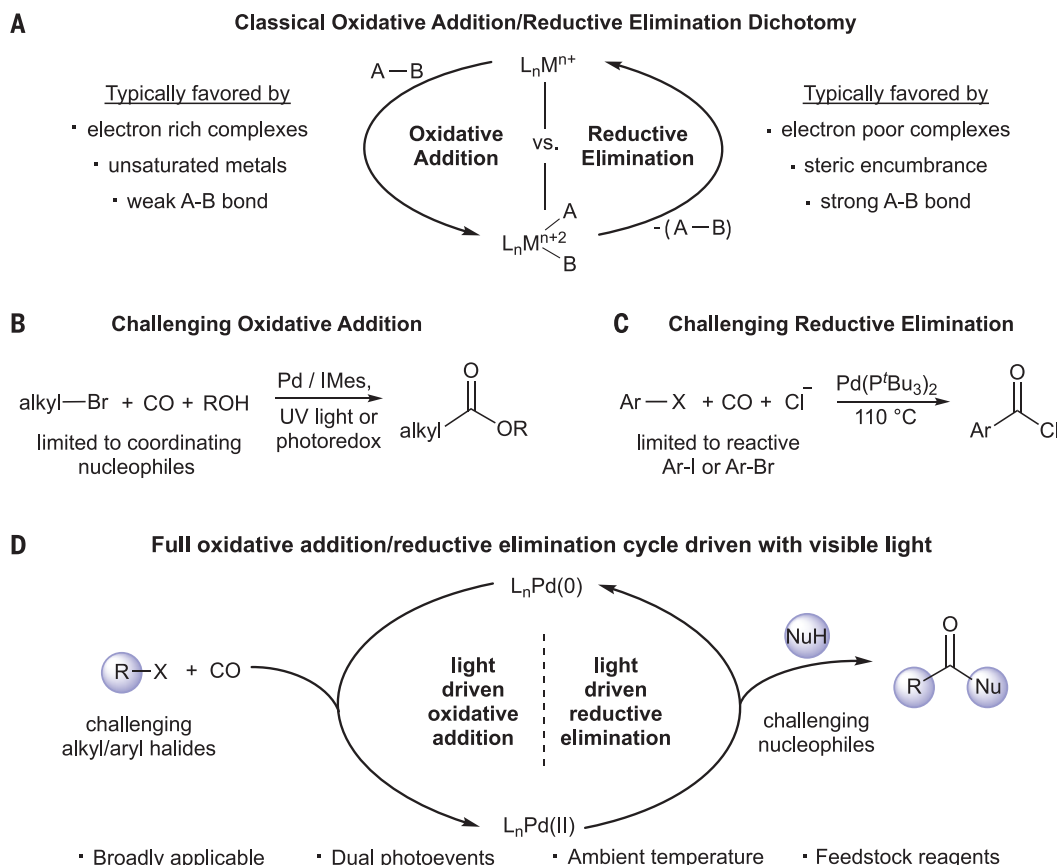


Fig. 1. A light-based strategy for the oxidative addition–reductive elimination cycle. (A) Opposing influences on these operations. L, ligand; M, metal. (B and C) Their limiting use in carbonylations. IMes, 1,3-dimesitylimidazol-2-ylidene; Ar, aryl. (D) Concept: Exploiting multiple photoevents to access potent, broadly applicable palladium catalysts. X, halogen; Nu, nucleophile.

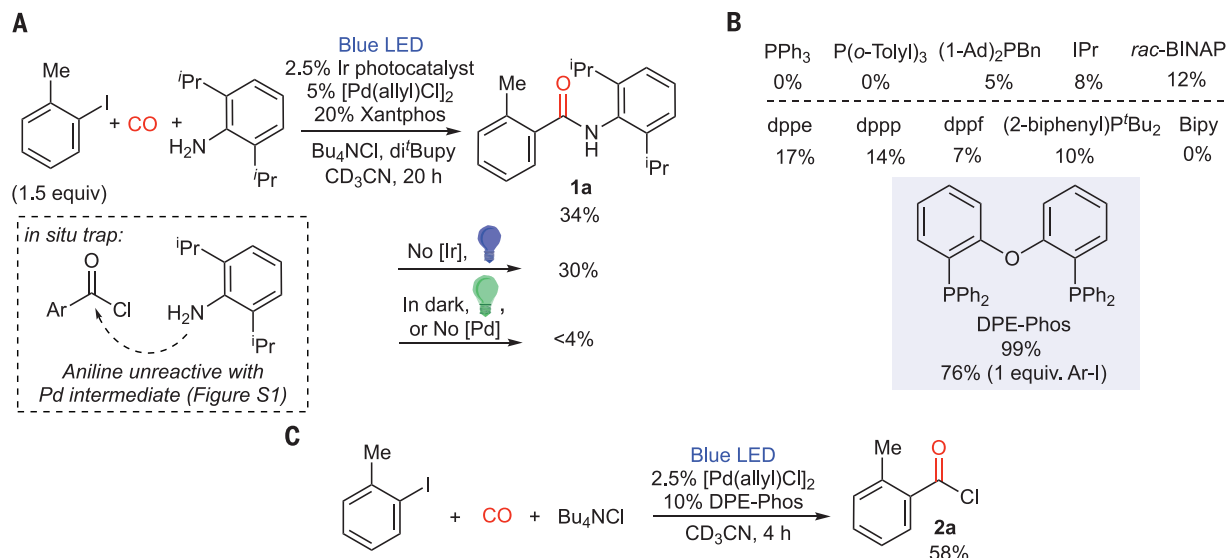


Fig. 2. Light and ligand effects on the Pd-catalyzed carbonylation of aryl iodides to acid chlorides. (A) Unusual effect of light on *in situ* acid chloride generation. di^tBupy, 2,6-di-*t*-butylpyridine; ⁱPr, isopropyl. (B) Accelerated coupling with DPEphos instead of Xantphos in reaction A (with collidine base in benzene). Ph, phenyl; 1-Ad, 1-adamantyl; Bn, benzyl; Pr, propyl; BINAP, 2,2'-bis(diphenylphosphino)-1,1'-binaphthyl; dppe, 1,2-bis(diphenylphosphino)ethane; dppp, 1,3-bis(diphenylphosphino)propane; dppf, 1,1'-bis(diphenylphosphino)ferrocene; Bipy, 2,2'-bipyridine. (C) Catalytic synthesis of acid chloride with light.

by Alexanian and Ryu with electron-rich catalysts or ultraviolet (UV) light, respectively, but the factors strongly favoring oxidative addition often necessitate the use of strong nucleophilic partners for elimination (Fig. 1B) (12, 13).

Carbonylations also often require nucleophiles that can readily associate to palladium for reductive elimination (14–16). Research here has also been reported using sterically hindered ligands to favor the formation of acyl halides

that react with an array of nucleophiles (Fig. 1C) (17–19). However, the catalyst features needed to favor the challenging reductive elimination now restrict this chemistry to substrates that can undergo facile oxidative addition.

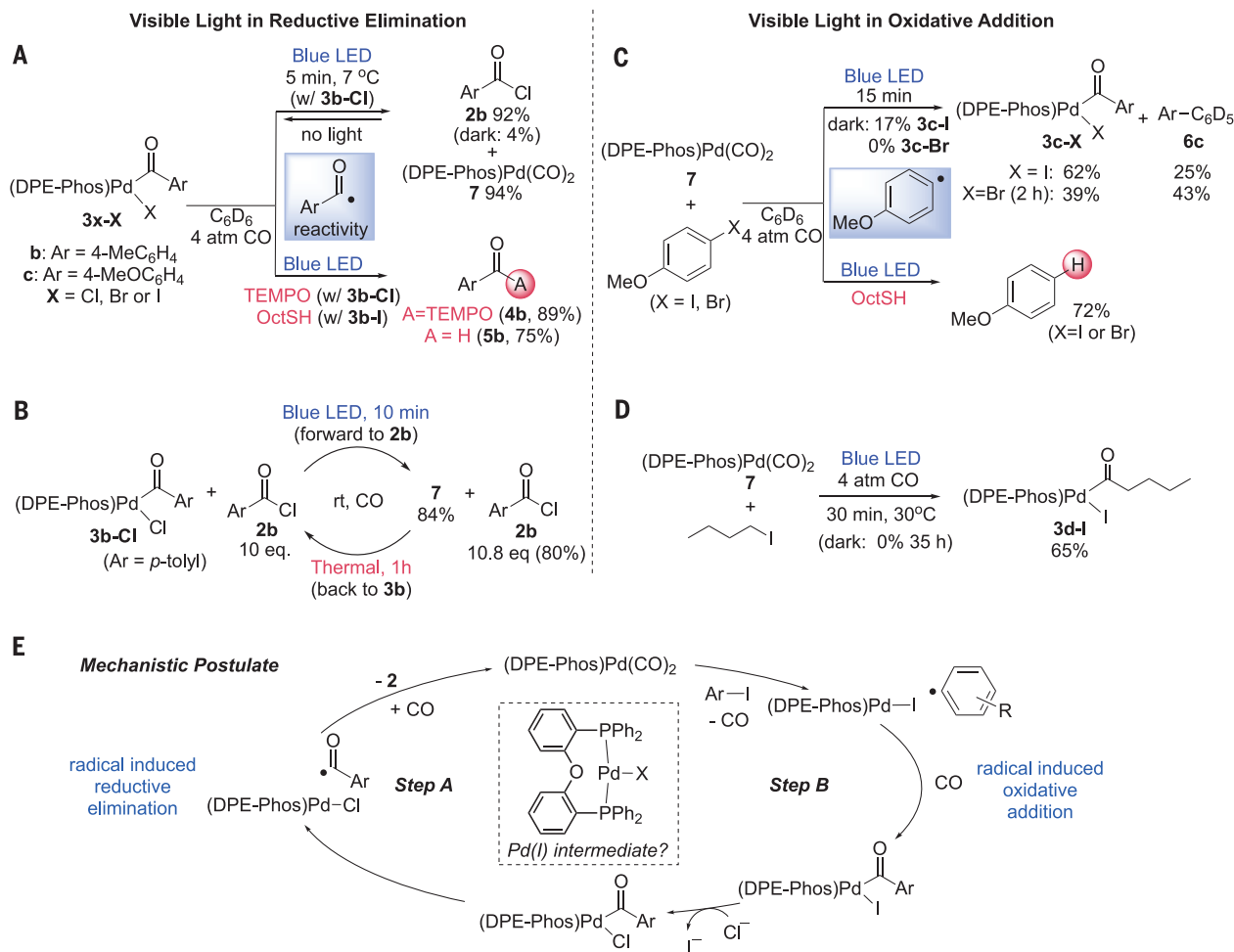


Fig. 3. Mechanistic insights into the role of visible light in catalysis. (A) Photoinduced acid chloride reductive elimination, wherein trapping hints at the intermediacy of acyl radicals. OctSH, 1-C₈H₁₇SH. (B) Reversibility of light-driven reductive elimination. eq., equiv. (C) Light-driven aryl halide oxidative addition. (p-MeOC₆H₄I/Br was used because it is easily monitored by ¹H NMR analysis.) (D) Alkyl iodide activation with light. (E) Potential mechanisms for the catalytic chemistry.

An intriguing alternative approach to metal catalysis that is of growing prominence is to exploit external factors to drive these reactions. For example, seminal reports from a number of labs have shown that pairing a visible-light photocatalyst with a more conventional nickel or palladium catalyst can accelerate a challenging step in coupling reactions (20–27). These can even be performed through the direct excitation of palladium catalysts (28–32) and have been applied to carbonylative Suzuki coupling with alkyl halides (33). Although such strategies expand the scope of products available via catalysis, the other steps in the catalytic cycle do still rely on the classic steric and electronic factors of the metal and can be limited by the thermal barriers inherent to these operations.

In considering these features, we questioned if light might play a greater role in catalysis. For example, could visible light offer a pathway to completely eliminate the need to balance

oxidative addition and reductive elimination steps and drive both in the same transformation? Because photoreactions can proceed with low barriers, such a system could offer the exciting opportunity to perform reactions without having to compromise with ligand effects in each step of the cycle and thus access exceptionally potent and versatile catalysts. The use of two different photoredox events to accelerate opposing operations such as these poses a substantial challenge of balancing two reverse redox events and their highly plausible mutual quenching (34). Nevertheless, light has been shown to have multiple influences on catalysis beyond photoredox chemistry that might be exploited in this design. We describe herein our studies toward such a system.

Our initial approach to this catalyst system focused on the use of light to favor the palladium-catalyzed formation of acid chlorides. As noted above, though the buildup of

acid chlorides offers a route to apply carbonylations to an array of nucleophiles, the ligands needed to favor this challenging elimination (P^tBu₃ and CO; ^tBu, *tert*-butyl) limit oxidative addition to reactive substrates such as aryl iodides and bromides at high temperatures (Fig. 1C). In these, in situ halogen exchange with a chloride source leads to acid chlorides, but less reactive reagents such as alkyl halides are not viable substrates. We postulated that photoredox chemistry could oxidize in situ generated Pd(II)-acyl complexes to a transient Pd(III) intermediate to induce the reductive elimination, in analogy to recent reports in nickel catalysis (23, 24). Nevertheless, it was unclear if photoredox chemistry could drive reductive elimination from a stable Pd(II) center or if such a catalyst might also undergo light-driven oxidative addition.

To test for this potential, the carbonylation of *o*-tolyl iodide was performed in the presence of 1 equiv Bu₄NCl, to allow the formation

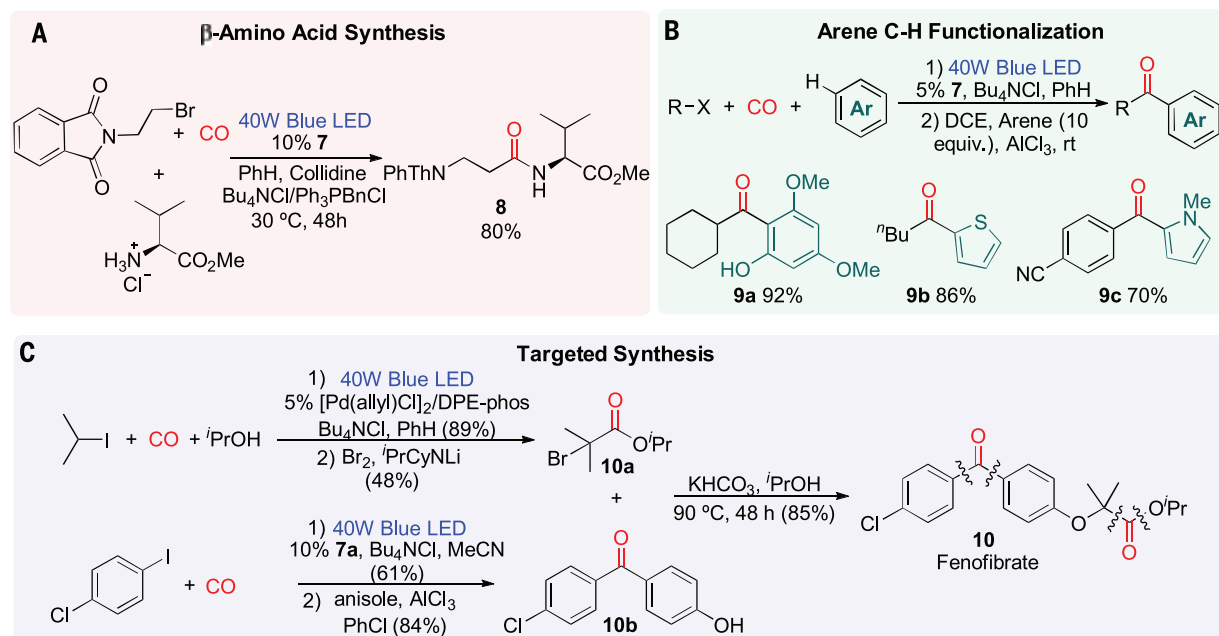


Fig. 5. Application of light-driven carbonylations to new classes of products. (A to C) Applications include β amino acids (A), ketones via C–H bond functionalization (B), and targeted synthesis via sequential carbonylation (C). See supplementary materials for experimental details. DCE, 1,2-dichloroethane; rt, room temperature.

to the organic halide (28–32). However, the capacity to induce the room-temperature buildup of a reactive acid chloride, and to do so without an added photocatalyst, suggests that light plays a distinct role in this system, because the reductive elimination typically requires pressing thermal conditions (>100 °C, high CO pressure). To more closely interrogate this product-forming step, the DPEphos-ligated Pd(II)-acyl complex **3b-Cl** was generated (see supplementary materials for synthesis). Complex **3b-Cl** absorbs blue light [absorption range (λ_{abs}) = 330 to 460 nm, fig. S4], and its irradiation even at low temperature leads to the near-quantitative reductive elimination of acid chloride **2b** within 5 min (Fig. 3A). The reaction mixture reverts back to a near 1:1 equilibrium mixture of **3b-Cl** and acid chloride **2b** in the absence of light (fig. S4A). The excitation of **3b** therefore appears to create an unusual photostationary state that drives the generation of acid chloride.

Stoichiometric reactivity studies provided further insights into this reductive elimination step. For example, the irradiation of complex **3b-Cl** in the presence of 1 equiv (2,2,6,6-tetramethylpiperidin-1-yl)oxyl (TEMPO) leads to the rapid formation of the acyl-radical trapping product **4b** (Fig. 3A). A similar transformation with a thiol leads to acyl-radical hydrogen-atom abstraction and aldehyde **5b** generation even faster than the known thioester formation from the reaction at palladium (10). These and other control experiments (see fig. S4 for full mechanistic study) are consistent with the formation of acyl radicals upon excita-

tion of **3**, which could lead to acid chloride formation by subsequent chlorine abstraction (step A of Fig. 3E; see fig. S5 for other pathways to acyl radical reactivity and the potential role of the DPEphos ligand) (36–38). Metal-acyl bonds have been reported to undergo light-driven homolysis, although not in palladium catalysis (39, 40). As shown in Fig. 3B, the accelerating influence of light on this radical-induced reductive elimination is sufficient to drive acid chloride formation even in the presence of a large excess of product, which quantitatively regenerates **3b-Cl** within 1 hour when light is removed.

In addition to favoring reductive elimination, light also appeared to be involved in oxidative addition chemistry through the excitation of the Pd(0) complex (DPEphos)Pd(CO)₂ (**7**) (Fig. 3) (41). Initial indications were noted upon closer analysis of the catalytic reaction mixture, where we observed the low-yield formation of a second product: the biaryl *o*-CH₃C₆H₄-C₆H₅ (**6a**, 8%; see fig. S6A). The latter formally arises from *o*-tolyl radical addition to the C₆H₅ solvent (42). Pd(0) complex **7** is formed upon acid chloride elimination, can be independently generated (see supplementary materials for synthesis), and also absorbs blue light (λ_{abs} = 300 to 420 nm). Moreover, its irradiation in the presence of aryl iodide leads to the rapid reverse oxidative addition to form **3c-I** together with biaryl *p*-CH₃OC₆H₄-C₆D₅ (**6c**; Fig. 3C). Performing the reaction in the presence of a thiol as hydrogen-atom donor inhibits oxidative addition and leads instead to radical trapping product anisole (Fig. 3C). These

data support the previously reported role of light-induced single-electron transfer from Pd(0) to aryl iodide opening a low-barrier, radical-induced oxidative addition pathway (step B in Fig. 3E; see fig. S7 for the full study of oxidative addition) (28–32) and are similar to the radical carbonylations pioneered by Ryu (43, 44). Although aryl iodides can also undergo a slow thermal reaction with **7**, similar light-induced reactivity is observed with aryl bromides and even alkyl iodides (Fig. 3, C and D), neither of which reacts thermally under these conditions, clearly demonstrating the role of visible light in oxidative addition.

Together, the data suggest a combination of two different roles of light acting in this system. The participation of Pd(0) and visible light in radical-induced oxidative addition has been described (32), but the capacity of light excitation to facilitate catalytic reductive elimination from Pd(II), and to do so in concert with Pd(0) photochemistry, is, to our knowledge, unknown. Evidence for the influence of light in catalysis can also be seen. As noted above, biaryl **6a** is generated in addition to amide **1a** (fig. S6A), suggesting the catalytic role of photoreduction of aryl iodide by Pd(0) in oxidative addition (Fig. 3A). Alternatively, performing the catalytic reaction in the presence of a TEMPO radical trap inhibits catalysis and leads to the formation of the acyl radical trapping product **4**, which arises from the in situ excitation of the Pd(II) intermediate **3** (fig. S6B). Nuclear magnetic resonance (NMR) analysis of the catalytic reaction shows that complex **7** is the catalyst resting state (fig. S6C),

which contrasts with thermal chemistry (**18**) but is consistent with the relative rates of the two individual photolytic steps (Fig. 3).

From a synthetic perspective, this visible light-based catalytic system offers a route to perform carbonylations in broad fashion, at ambient temperature, and with challenging electrophiles and nucleophiles. Catalysis proceeded with an array of aryl iodides, including those with electron withdrawing or donating substituents in the para, meta, and ortho positions (**1a** to **1i**, Fig. 4). The reaction proved compatible with potentially coordinating groups such as aldehydes (**1i**), protected amines (**1h**), esters (**1c** and **1d**), nitriles (**1f**), thioethers (**1e**), or even heterocyclic substrates (**1j**). Aryl bromides, which have to date required high temperatures for carbonylation to acid chlorides (100° to 120°C), could also undergo carbonylations to generate in situ acid chlorides at temperatures as low as -3°C (table SI). As with aryl iodides, a variety of functionalized aryl bromides could undergo carbonylation to generate in situ acid chlorides, including those with methoxy (**1p**), nitrile (**1q**), trifluoromethyl (**1s**), or ketone (**1r**) substituents, as well as heterocycles (**1t**).

This light-driven system also enabled a distinctive carbonylative pathway to convert simple alkyl halides into valuable alkyl acid chloride products (**2d** to **2i**). The latter are heavily exploited electrophilic building blocks in synthesis (**45**) and can be generated with both alkyl iodide and bromide reagents at catalyst loadings as low as 1 mol % palladium. The efficiency is presumably a result of the low reduction potential of alkyl halides (**46**). A diverse array of primary (**1w** and **1ff** to **1hh**), secondary (**1u** and **1dd**), and even tertiary (**1bb** and **1ii**) alkyl halides can be incorporated into this reaction, as well as those with various ester (**1cc**), ketone (**1kk**), nitrile (**1gg**), or alkyl chloride (**1z**) substituents. Alkyl chlorides, which are more challenging to reduce, are not reactive under these conditions. The reaction of cyclopropylmethyl iodide affords the ring-opened alkene product **1x**, supporting the role of electron transfer in oxidative addition.

Because each of these transformations leads to the formation of acid chlorides, a broad array of nucleophiles can at the same time be incorporated into this chemistry, such as substituted anilines (**1n** to **1r**), sterically hindered secondary amines (**1k** and **1l**), tertiary alcohols (**1dd**), or even weakly nucleophilic *N*-heterocycles (**1m**). In reactions where the nucleophile is not compatible with the reaction conditions, it can be added after the catalytic buildup of acid chlorides. The latter has allowed the coupling of challenging substrate combinations (**1y** to **1aa**, **1ii**) and the generation of structurally more elaborate products (terpenes, **1kk**; β -acetals, **1ff**; and steroidal acid chlorides, **2i**), none of

which are viable via classical carbonylation chemistry.

The versatility of this dual light-driven catalyst suggests an opportunity to access various useful classes of products from carbon monoxide. For example, β amino acids are important reagents in the preparation of peptoids but are often generated by multistep protocols (**47**). By contrast, this visible light-based catalyst opens a direct route to β peptide derivatives via carbonylations (Fig. 5A). Alternatively, the electrophilic reactivity of acid chlorides can be applied to Friedel-Crafts acylations for synthesis of alkyl-substituted ketones from feedstock reagents such as arenes or heteroarenes, alkyl halides, and carbon monoxide (Fig. 5B) (**48**). This approach can also open routes to targeted synthesis, such as the cholesterol-lowering drug fenofibrate (Fig. 5C) (**49**). The power to convert both alkyl and aryl halides to acid chlorides is on display in this synthesis, where the initial functionalization of the 2-iodopropane to form an acid chloride for coupling with isopropanol, followed by an aryl halide carbonylative Friedel-Crafts reaction, affords **10** from 2 equiv carbon monoxide.

These results illustrate an alternative strategy to access versatile palladium catalysts for carbonylative coupling reactions, wherein visible-light excitation of palladium can drive oxidative addition and reductive elimination with low barriers. Considering the range of carbonylation and related catalytic transformations where this cycle plays a critical role, we anticipate that this approach will prove important as a pathway to create potent catalyst systems.

REFERENCES AND NOTES

1. A. Biffis, P. Centomo, A. Del Zotto, M. Zecca, *Chem. Rev.* **118**, 2249–2295 (2018).
2. C. C. Johansson Seechurn, M. O. Kitching, T. J. Colacot, V. Snieckus, *Angew. Chem. Int. Ed.* **51**, 5062–5085 (2012).
3. J. F. Hartwig, *J. Am. Chem. Soc.* **138**, 2–24 (2016).
4. O. King, R. D. Larsen, E.-I. Negishi, "Palladium-catalyzed hydrogenolysis" in *Handbook of Organopalladium Chemistry for Organic Synthesis*, E.-I. Negishi, Ed. (Wiley, 2002), vol. 2, pp. 2719–2752.
5. M. Holmes, L. A. Schwartz, M. J. Krische, *Chem. Rev.* **118**, 6026–6052 (2018).
6. W. Shi, C. Liu, A. Lei, *Chem. Soc. Rev.* **40**, 2761–2776 (2011).
7. D. Wang, A. B. Weinstein, P. B. White, S. S. Stahl, *Chem. Rev.* **118**, 2636–2679 (2018).
8. M. R. Uehling, R. P. King, S. W. Kraska, T. Cernak, S. L. Buchwald, *Science* **363**, 405–408 (2019).
9. M. Beller et al., "Carbonylation" in *Applied Homogeneous Catalysis with Organometallic Compounds*, B. Cornils, W. A. Herrmann, M. Beller, R. Paciello, Eds. (Wiley, 2018), pp. 91–190.
10. J.-B. Peng, H.-Q. Geng, X.-F. Wu, *Chem* **5**, 526–552 (2019).
11. L. Wu et al., *ACS Catal.* **4**, 2977–2989 (2014).
12. S. Sumino, A. Fusano, T. Fukuyama, I. Ryu, *Acc. Chem. Res.* **47**, 1563–1574 (2014).
13. M. R. Kwiatkowski, E. J. Alexanian, *Acc. Chem. Res.* **52**, 1134–1144 (2019).
14. J. R. Martinelli, T. P. Clark, D. A. Watson, R. H. Munday, S. L. Buchwald, *Angew. Chem. Int. Ed.* **46**, 8460–8463 (2007).
15. M. N. Burhardt, R. H. Taaning, T. Skrydstrup, *Org. Lett.* **15**, 948–951 (2013).
16. S. M. A. Donald, S. A. Macgregor, V. Settels, D. J. Cole-Hamilton, G. R. Eastham, *Chem. Commun.* **2007**, 562–564 (2007).

17. R. Garrison Kinney et al., *Nat. Chem.* **10**, 193–199 (2018).
18. J. S. Quesnel, B. A. Arndtsen, *J. Am. Chem. Soc.* **135**, 16841–16844 (2013).
19. T. Ueda, H. Konishi, K. Manabe, *Org. Lett.* **15**, 5370–5373 (2013).
20. M. Osawa, H. Nagai, M. Akita, *Dalton Trans.* **2007**, 827–829 (2007).
21. D. Kalyani, K. B. McMurtrey, S. R. Neufeldt, M. S. Sanford, *J. Am. Chem. Soc.* **133**, 18566–18569 (2011).
22. J. C. Tellis, D. N. Primer, G. A. Molander, *Science* **345**, 433–436 (2014).
23. Z. Zuo et al., *Science* **345**, 437–440 (2014).
24. S. Z. Tasker, T. F. Jamison, *J. Am. Chem. Soc.* **137**, 9531–9534 (2015).
25. E. B. Corcoran et al., *Science* **353**, 279–283 (2016).
26. M. D. Levin, S. Kim, F. D. Toste, *ACS Cent. Sci.* **2**, 293–301 (2016).
27. K. L. Skubi, T. R. Blum, T. P. Yoon, *Chem. Rev.* **116**, 10035–10074 (2016).
28. M. Parasram, P. Chuentragool, D. Sarkar, V. Gevorgyan, *J. Am. Chem. Soc.* **138**, 6340–6343 (2016).
29. M. A. Fredricks, M. Drees, K. Köhler, *ChemCatChem* **2**, 1467–1476 (2010).
30. G.-Z. Wang, R. Shang, W.-M. Cheng, Y. Fu, *J. Am. Chem. Soc.* **139**, 18307–18312 (2017).
31. R. Kancherla et al., *Angew. Chem. Int. Ed.* **58**, 3412–3416 (2019).
32. P. Chuentragool, D. Kurandina, V. Gevorgyan, *Angew. Chem. Int. Ed.* **58**, 11586–11598 (2019).
33. S. Roslin, L. R. Odell, *Chem. Commun.* **53**, 6895–6898 (2017).
34. For an example of a postulated two photon role in nickel catalysis see (50).
35. R. D. Costa et al., *Angew. Chem. Int. Ed.* **51**, 8178–8211 (2012).
36. P. W. N. M. van Leeuwen, P. C. J. Kamer, *Catal. Sci. Technol.* **8**, 26–113 (2018).
37. T. L. Andersen, S. Kramer, J. Overgaard, T. Skrydstrup, *Organometallics* **36**, 2058–2066 (2017).
38. C. M. Fafard, D. Adhikari, B. M. Foxman, D. J. Mendiola, O. V. Ozerov, *J. Am. Chem. Soc.* **129**, 10318–10319 (2007).
39. J. Demarteau, A. Debuigne, C. Detrembleur, *Chem. Rev.* **119**, 6906–6955 (2019).
40. K. I. Goldberg, R. G. Bergman, *J. Am. Chem. Soc.* **111**, 1285–1299 (1989).
41. F. M. Miloserdov et al., *Organometallics* **33**, 736–752 (2014).
42. I. Ghosh, L. Marzo, A. Das, R. Shaikh, B. König, *Acc. Chem. Res.* **49**, 1566–1577 (2016).
43. I. Ryu, N. Sonoda, *Angew. Chem. Int. Ed.* **35**, 1050–1066 (1996).
44. C. Chatgililoglu, D. Crich, M. Komatsu, I. Ryu, *Chem. Rev.* **99**, 1991–2070 (1999).
45. C. A. G. N. Montalbetti, V. Falque, *Tetrahedron* **61**, 10827–10852 (2005).
46. H. G. Roth, N. A. Romero, D. A. Nicewicz, *Synlett* **27**, 714–723 (2016).
47. C. Cabrele, T. A. Martinek, O. Reiser, L. Berlicki, *J. Med. Chem.* **57**, 9718–9739 (2014).
48. X.-F. Wu, H. Neumann, M. Beller, *Chem. Soc. Rev.* **40**, 4986–5009 (2011).
49. K. McKeage, G. M. Keating, *Drugs* **71**, 1917–1946 (2011).
50. L. K. G. Ackerman, J. I. Martinez Alvarado, A. G. Doyle, *J. Am. Chem. Soc.* **140**, 14059–14063 (2018).

ACKNOWLEDGMENTS

We thank S. Bohle and R. Stein for helpful discussions on electron paramagnetic resonance analysis. **Funding:** We thank the Natural Sciences and Engineering Research Council of Canada, McGill University (James McGill Research Fund), and the Centre for Green Chemistry and Catalysis (supported by Fonds de recherche du Québec – Nature et Technologies) for funding this research. G.M.T. thanks the CONACYT (Mexican National Council of Science and Technology) for providing funding for doctoral studies. **Author contributions:** G.M.T. and Y.L. performed the research described in the paper and helped conceive the idea with B.A.A. B.A.A., G.M.T., and Y.L. prepared the manuscript. **Competing interests:** The authors declare no competing interests. **Data and materials availability:** All data are available in the main text or the supplementary materials.

SUPPLEMENTARY MATERIALS

science.sciencemag.org/content/368/6488/318/suppl/DC1
Materials and Methods
Figs. S1 to S31
Table SI
References (51–89)

17 December 2019; accepted 16 March 2020
10.1126/science.aba5901



Light Sheet Fluorescence Microscope

The high stability of ZEISS Lightsheet 7 enables researchers to observe living samples with subcellular resolution over extended periods of time—even days—with less phototoxicity than ever before. Specimens up to 2 cm in size with a refractive index between

1.33 and 1.58 and in almost any clearing solution can be accommodated, such as organoids, spheroids, organs, and brains. ZEISS Lightsheet 7 features the high-quantum efficiency of pco.edge sCMOS detectors to enable observations of the fastest processes at the lowest-illumination light levels. The sample holder makes mounting larger specimens easy. Smart software tools assist in defining imaging parameters, such as light sheet and sample positions; correct zoom settings, tiles, and positions; as well as data processing parameters. All these new features work with the reliable ZEISS combination of cylindrical lens optics and laser scanning to generate the illumination light sheet. The patented Pivot Scan technology delivers artifact-free optical sections for the best possible image quality.

ZEISS

For info: +49-(0)-7364-20-0

www.zeiss.com

Semiautomatic Tube Rack Sealing Device

Ziath announces ImpressiOn—a versatile, semiautomatic device designed to take the strain out of applying friction sealing mats or septum sealing caps to Society for Biomolecular Screening (SBS)-format tube racks. Using ImpressiOn is quick and easy—just place your rack or plate with its attendant friction mat or septum cap web in the drawer and push it firmly shut. Sealing is initiated using the large, single-action start button; then sophisticated electronics take over, applying reproducible and even pressure every time to force the septum seals down into each tube. The compact unit requires only a 110-V or 220-V power supply to operate and is small enough to fit on most lab benches. The ImpressiOn will work with most commercially available septum cap mats and most 2D-coded and uncoded tubes in SBS-format racks. As standard, the unit is also supplied with two rack adaptors to enable sealing of shallow and deep racks. Alternative rack adaptors are available to suit specific manufacturers' tube racks.

Ziath

For info: 858-880-6920

ziath.com/index.php/products/tube-devices/impression

Coronavirus-COVID-19 Research Products

AMS Biotechnology announces the availability of recombinant proteins and antibodies for detection of coronavirus disease 2019 (COVID-19) and related RNA viruses. Coronaviruses are a group of enveloped, positive-stranded RNA viruses that contain four structural proteins: spike (S) glycoprotein, envelope (E) protein, membrane (M) protein, and nucleocapsid (N) protein. The spike glycoprotein includes two regions, S1 and S2, where S1 is for host-cell receptor binding via angiotensin-converting enzyme 2 (ACE2), and S2 is for membrane fusion. Spike glycoprotein is a key target for vaccines, therapeutic antibodies, and diagnostics. To facilitate research in these areas, we supply high-quality COVID-19 full-length S protein, S1 protein, and human ACE2 protein based on the HEK293 human

cell expression platform. The binding activity of these products has been verified by surface plasmon resonance and biolayer interferometry technologies. Also available are antibodies, including antibody pairs against coronavirus for ELISA; a PCR detection kit for severe acute respiratory syndrome coronavirus 2 (SARS-CoV-2), ACE2 expression vectors, and short hairpin RNA vectors; and CRISPR kits.

AMS Biotechnology

For info: 617-945-5033

www.amsbio.com/coronavirus.aspx

Biological and Aqueous Sample Extraction

Porvair Sciences offers Microlute SLE 96-well plates and cartridges to enable you to quickly and easily extract a wide range of acidic, basic, and neutral analytes from samples with greater reproducibility. Designed to provide a superior method of liquid extraction, Microlute SLE products use selectively sourced diatomaceous earth as the solid support to maximize absorption of the aqueous solvent, enabling greater and simpler separation and elution of organic analytes from biological samples such as plasma, serum, and aqueous solutions. With no inversions, shaking, or tedious pipetting required, Microlute SLE overcomes sample handling issues commonly associated with traditional liquid-liquid extraction (LLE). It is also lab friendly and uses significantly less solvent and glassware than LLE protocols.

Porvair Sciences

For info: +44-(0)-1978-666222

www.microplates.com/microlute-sle

3-Position Clamp

Produced for chemists undertaking parallel syntheses, the Asynt DrySyn 3-Position Clamp allows secure clamping of up to three round bottom flasks or condensers to a standard boss head. There are three sizes of the 3-Position Clamp available—to suit the DrySyn MULTI-E, MULTI-M, and MULTI-S heating block systems—and these devices are also perfect to use with the Asynt CondenSyn range of waterless air condensers. Each clamp features a novel, fast grip/release mechanism that minimizes setup time, and its unique design enables easy, simultaneous removal of all three reactions from the heat source should the need arise. Durably constructed from aluminum and stainless steel, with a replaceable rubber covering, the compact, affordably priced 3-Position Clamp is available in sizes from 5 mL to 500 mL, to securely hold condensers and round bottom flasks.

Asynt

For info: +44-(0)-1638-781709

www.asynt.com/product/drysyn-multi-clamp

Compound Libraries

The Tocriscreen range of compound libraries are collections of compounds for use in screening assays for receptor deorphaning, target validation, drug reprofiling, tool-compound identification, and assay development. Comprising biologically active compounds selected from the Tocris catalog, these libraries provide wide coverage of cellular targets, including G protein-coupled receptors, ion channels, kinases, enzymes, nuclear receptors, and transporters. Tocriscreen 2.0 Max, Mini, and Micro Compound Libraries include 1,280 compounds covering multiple pharmacological targets and research areas. Collections of compounds for specific research areas or targets, such as epigenetics and kinases, are also available.

Tocris

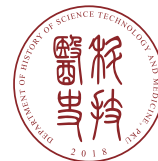
For info: 800-343-7475

www.tocris.com

Electronically submit your new product description or product literature information! Go to www.sciencemag.org/about/new-products-section for more information.

Newly offered instrumentation, apparatus, and laboratory materials of interest to researchers in all disciplines in academic, industrial, and governmental organizations are featured in this space. Emphasis is given to purpose, chief characteristics, and availability of products and materials. Endorsement by *Science* or AAAS of any products or materials mentioned is not implied. Additional information may be obtained from the manufacturer or supplier.

Multiple Positions Open in The Department of History of Science, Technology and Medicine, Peking University



The Department of History of Science, Technology and Medicine (DHSTM) at Peking University is currently inviting applications for multiple positions at the ranks of full professor with tenure, associate professor with tenure, assistant professor on tenure track, and post-doctoral fellow respectively. Given the department's current engagement in the historical study of science in modern and contemporary China as well as related explorations based on big data, candidates with relevant experience are especially encouraged to apply. Successful applicants must demonstrate their enthusiasm and vision about the future of the DHSTM and the development of the history of science in China. The appointees will teach undergraduate and graduate courses across the history of science and technology, science culture, etc. They must also actively participate in the department's academic and educational activities. Peking University will provide all the appointees internationally competitive salaries and benefit package, matching their academic rank and experience. In addition, the university will provide appointees start-up funds for research and endeavor to create satisfied working conditions for them. The DHSTM was established in November 2018 and has been headed by Professor Qide Han, a medical scientist and an academician of the Chinese Academy of Sciences, as its founding chairman. The mission of this department is to work with scholars around the world to advance the harmonious development of science, humanity, and society. It concentrates on teaching and studying the history of modern and contemporary science, technology and medicine, aiming at creating a collaboration platform with cutting-edge ideas and global vision.

Specific Qualification:

1. Full Professor with tenure

Applicants should be highly influential scholars with significant publications in their own field and working experience in a top academic institution, either in China or overseas. Candidates should have strategic vision for the discipline's development, rich teaching experience, extensive academic connections, as well as excellent peer review.

2. Associate Professor with tenure

Applicants should be reputable scholars with high-quality publications in their own field and working experience in a top academic institution, either in China or overseas. Candidates should have rich teaching experience, extensive academic connections, as well as excellent peer review. Preferred candidates are those specializing in the twentieth-century history of science, technology, and Medicine (including both Chinese and Western) or in the philosophy of science.

3. Assistant Professor on tenure track

Applicants must have a Ph.D. degree in hand; preferred candidates are those who have done some postdoctoral research. Candidates must have some academic publications in the field, good peer review, and demonstrated outstanding potential. Preferred candidates are those specializing in the twentieth-century history of science, technology, and Medicine (including both Chinese and Western) or in the philosophy of science.

4. Postdoctoral Fellows

Applicants should have demonstrated outstanding academic potential as well as a doctorate in any of the following specialties: the history of science and technology, the philosophy of science, the STS (science, technology and society), science communication and Big Data research in the history of science, history, or sociology.

Application materials:

1. A personal statement, specifying the position applied, research and teaching plan, as well as expected beginning date at the DHSTM.
2. A Curriculum Vitae
3. A list of publications and forthcoming works, and three representative works;
4. A personal plan of academic study in the next 3 to 5 years;
5. For postdoctoral and junior positions, at least three letters of recommendation from academic professionals, in addition to the references from the applicants' mentors;
6. Applicants for tenured senior positions (full or associate professor) will be subjected to peer review according to the requirements for tenure evaluation. Applicants may provide a list of suggested referees who will be contacted directly by the department;
7. A copy of Ph.D. diploma and other certificates of awards, honors, appointments, etc.

Contacts:

Mr. Zheng

Email: hstm@pku.edu.cn

Address: Peking University,
NO 5 Yiheyuan Road, Haidian District, Beijing 100871



HIGH-LEVEL GLOBAL TALENTS RECRUITMENT

2020 Global Online Job Fair (www.edu.cn/cv)

April 17, 2020 South Area of East China Doctoral Talents Recruitment

April 24, 2020 Specialty Session (Science & Engineering)

May 08, 2020 North Area of East China Doctoral Talents Recruitment

May 09, 2020 Hong Kong, Macao, Taiwan and the China Great Bay Area
Doctoral Talents Recruitment

May 15, 2020 High-level Global Talents Recruitment

Qualification for Applicants

Global scholars, Doctor and Post-doctor

Key Disciplines

Life Sciences, Health Sciences and Physical Sciences

Participating Approach

Please send your CV to consultant@acabridge.edu.cn for
2020 Global Online Job Fair



Scan to check the sessions

EVEN SEPARATED BY MOUNTAINS AND RIVERS, WE HAVE OUR BLOOD TIGHTLY CONNECTED

The Coronavirus pandemic has forced many of us to consider different ways of working and communicating. Chinese universities and colleges are now holding online job fairs to help overseas scholars explore career options in China.

Fight with One Heart to Combat COVID-19

In these challenging times, Chinese universities and colleges have shot videos, sending greetings and wishes to their overseas compatriots. Please scan below QR code to receive messages of love and well wishes from high schools in your motherland.



Overseas **Chinese Scholars'** Visit to Top Chinese Universities

Check the Details from www.edu.cn/zgx

- 10,000+ academic job vacancies in China
- Free one-to-one consultation service

Send your CV to consultant@acabridge.edu.cn

海外學者
中國行



西安交通大學



中國石油大學



中南民族大學



SPECIAL JOB FOCUS:

Biotechnology

Issue date: May 22

Book ads by May 7

Ads accepted until May 15 if space allows



Deliver your message to a global audience of targeted, qualified scientists.

129,566

subscribers in print every week

33,295

yearly unique active job seekers searching for biotechnology jobs

16,250

yearly applications submitted for biotechnology positions

To book your ad, contact:
advertise@sciencecareers.org

The Americas
202 326 6577

Europe
+44 (0) 1223 326527

Japan
+81 3 6459 4174

**China/Korea/Singapore/
Taiwan**
+86 131 4114 0012

**Science
Careers**
AAAS

SCIENCECAREERS.ORG

What makes *Science* the best choice for recruiting?

- Read and respected by 400,000 readers around the globe
- Your ad dollars support AAAS and its programs, which strengthens the global scientific community.

Why choose this job focus for your advertisement?

- Relevant ads lead off the career section with a special biotechnology banner.

Expand your exposure by posting your print ad online:

- Additional marketing driving relevant job seekers to the job board.

Produced by the *Science*/AAAS Custom Publishing Office.



FOR RECRUITMENT IN SCIENCE, THERE'S ONLY ONE SCIENCE.

Improving the World Through Plant Science Innovation

Research teams at NC State are at the forefront of crop resilience research. Tommy Carter, a USDA-ARS professor, has spent decades incorporating genetic diversity into U.S. soybeans to improve drought tolerance. Amy Grunden, a Distinguished professor, is leading a \$30 million study on the wheat microbiome to make the staple more resilient.

Learn how NC State and USDA are tackling the grand challenges facing agriculture through team-based plant science innovation.

go.ncsu.edu/drought

NC STATE



ScienceCareers

FROM THE JOURNAL SCIENCE  AAAS

Confused about your next career move?



**Download Free Career
Advice Booklets!**

ScienceCareers.org/booklets



By Caitlyn A. Hall

My career earthquake

During my first few years in grad school, I proudly told colleagues that my research on earthquake hazard mitigation technology would save countless lives and help prevent trillions of dollars of infrastructure damage. I wasn't lying. My adviser and I truly felt as though we were about to deliver a technological breakthrough. But our confidence came crashing down one afternoon, when we met with representatives of a state agency to discuss moving our work beyond the pilot scale. "The risk of using a brand new technology is too high. The approval and implementation process can take decades," one official told us. I left the meeting feeling deflated.

I went home and thought deeply about my priorities. I saw real problems in the world: natural hazards, environmental injustice, social inequity—the list goes on. I went to grad school because I wanted to make a difference. I felt that the world was burning, and I wanted to help people in the here and now, not decades in the future. Suddenly, it became clear that wasn't going to happen.

I tried to pivot my project so that it could be implemented more quickly. But my Ph.D. committee was unenthusiastic. One committee member went so far as to tell me that if I went in that direction, I would be wasting time.

I was discouraged. I seriously considered quitting, and I wavered for months about whether my work was worthwhile. But I had sunk years into grad school at that point, so I tried to stick with it.

One day, it occurred to me that research might not be the only way I could make a difference. I started to brainstorm activities outside academia that would marry my interests in science, policy, and communication. But I had no idea how to get started. So, I attended a workshop in Washington, D.C., that taught scientists how to communicate with legislators and their staff. I met other graduate students and postdocs from across the country who were disenchanted with academic work and wanted to have an impact on science policy. It was a relief to discover that I wasn't alone.

When I returned to my graduate program in Arizona, I used my spare time to start a statewide science policy network with the goal of helping early-career scientists engage with policymakers and the general public. As part of that work, I organized a "Science Day" at the Arizona State Capitol, which drew 12 state politicians and roughly 60 early-career scientists. During a panel discussion, one



**"I've come to realize that ...
my scientific expertise
is valuable in other arenas."**

student asked, "We see important issues in Arizona! What can we do?" A congressperson responded, "Call your representative! We want to hear from you." That response was unsatisfying to me. I raised my hand and pointed out we wanted to do more. Later, the congressperson reached out and agreed to partner with our network to bring more scientific expertise into decision-making. We started to meet with lawmakers regularly, submit written briefs, and testify to committees—work that we've continued to do remotely during the COVID-19 pandemic.

My role with the network has brought me a renewed sense of joy and accomplishment. I'm still pursuing my Ph.D. research, and I hope that the technology we're

developing will be implemented one day. But I've come to realize that I can make an impact in other ways—and that my scientific expertise is valuable in other arenas.

By stepping outside academia, I've also developed a network of professionals who work in industry, nonprofit organizations, and the government. Some of those people have given me helpful feedback on my Ph.D. research. And the connections I'm making will be invaluable for my future career, when I hope to work in science policy.

I went to grad school brimming with enthusiasm. Over the years, I learned that my academic research by itself wouldn't satisfy my eagerness to make a difference in the world. It was a painful realization, but I'm grateful for the times of doubt because they pushed me in a new direction. Now, I'm back to feeling proud of all of the work that I do. ■

Caitlyn A. Hall is a Ph.D. student at Arizona State University, Phoenix. Do you have an interesting career story to share? Send it to SciCareerEditor@aaas.org.

PUT YOUR RESEARCH OUT IN FRONT

Submit your research:
[cts.ScienceMag.org](https://cts.science.org)



PINS

RESTORING HOPE



Beijing PINS Medical Equipment Co. Ltd. was established in 2008.

As an innovative high-tech enterprise with focus on neuromodulation, PINS Medical has developed a variety of clinical products, which include stimulators for deep brain, vagus nerve, spinal cord, and sacral nerve stimulation therapies. PINS Medical devotes itself to providing cutting-edge treatments for patients who suffer from neurological disorders, such as Parkinson's disease, epilepsy, chronic pain, and uroclepsia.

The name of PINS is derived from a Chinese word with the original meaning of "Magic Pin," the ability to cure disease. PINS is also an abbreviation of "Patient Is No. 1 always." This message clearly represents the goal of PINS Medical for "restoring hope," not simply as an innovation company but also across society to citizens.

www.pinsmedical.com/html/en/

info@pinsmedical.com